

# SURFACE ROUGHNESS GENERATED BOUNDARY LAYER NOISE



**Yu Liu**

SIDNEY SUSSEX COLLEGE  
UNIVERSITY OF CAMBRIDGE

A dissertation submitted to  
the DEPARTMENT OF ENGINEERING  
for the DEGREE OF DOCTOR OF PHILOSOPHY

MAY 2008



*Dedicated to my parents and Yi,  
for their constant support ...*





# Abstract

Aircraft noise has been an increasing urgent environment issue especially for people living near airports. In recent years, airframe noise has been comparable to engine noise particularly for landing aircraft. This thesis addresses a previously neglected source, surface roughness generated boundary-layer noise, with the aim of developing a prediction model to assess the potential contribution of surface roughness to airframe noise.

The thesis is focused on the sound scattering mechanism. The generation of sound by turbulent boundary-layer flow over a rough wall is investigated by applying a theoretical model which describes the scattering of turbulence near field into sound by roughness elements. Models for the source statistics are obtained by scaling smooth-wall data by the increased friction velocity and boundary-layer thickness for a rough surface. Attention is focused on a numerical method to predict the absolute level of far-field radiated roughness noise. Direct numerical integration is used to obtain the prediction model which is able to reproduce the spectral characteristics of the available empirical formula and experimental data.

Acoustic experiments are conducted for two rough plates in an open jet. The reasonable agreement between measured and predicted noise spectra is observed, and beamforming source maps by phased microphone arrays exhibit satisfactory similarities between measurement and simulation in source pattern and source strength. The dipole directivity features are demonstrated. However, the prediction model underestimates the streamwise gradient of source strength and overestimates the sound radiation in the high-frequency region. Hot-wire measurement is performed and it determines the applicable wake strength and skin friction coefficient that account for the roughness effects of turbulence enhancement.

Numerical estimates for a current aircraft wing and a conceptual “silent aircraft” design with idealized roughness levels show that in the high-frequency region the sound radiated from surface roughness may exceed that from trailing edge. A parametric study indicates that roughness height and roughness density significantly affect the noise radiation with roughness height having the dominant effect. The noise directivity pattern varies with different levels of surface roughness. The maximum allowable roughness levels on the surface of the silent aircraft are studied to achieve an aggressive noise target.

An alternative method to the scattering of near-field turbulence is that large roughness elements shed vorticity resulting in unsteady drag. This drag dipole mechanism is extended to consider very large roughness elements by modifying a previous model for spheres to determine the unsteady drag on the hemispherical elements and then the radiated sound. The preliminary prediction shows that this noise source can be comparable to the scattering roughness noise.

Finally, a beamforming correction for dipole measurement using phased microphone arrays is presented. A new beamforming algorithm for identifying dipoles is developed and validated by numerical and experimental implementation.

In conclusion, the validated theoretical model shows that it is capable of approximately predicting the far-field radiated roughness noise. The assessment of the contribution of surface roughness to airframe noise suggests that surface roughness noise was underestimated and needs to be carefully considered in the design of a low-noise airframe.

**KEYWORDS:** Silent Aircraft Initiative, surface roughness noise, airframe noise, sound scattering, rough-wall turbulent boundary layer, wavenumber-frequency spectrum, hairpin vortex, aeroacoustic dipole, phased microphone array, beamforming algorithm.

# Declaration

Except where otherwise stated in the text, this dissertation is the result of my own work carried out at the University of Cambridge and is not the outcome of work done in collaboration.

The beamforming codes used for the phased microphone array system were developed and upgraded by P. Sijtsma of the National Aerospace Laboratory (NLR), the Netherlands, provided to the University of Cambridge under the terms of the collaborative project, "Silent Aircraft Initiative" (SAI). The experimental work of beamforming correction for dipole measurements was carried out in collaboration with A. R. Quayle, and the noise propagation algorithm, providing corrections from the source to the ground for the SAI conceptual design, was developed by D. Crichton of the SAI team.

This dissertation is not substantially the same as any that I have submitted or am currently submitting for a degree, diploma or any other qualification at any other university. No part of this dissertation has already been or is being concurrently submitted for any such degree, diploma or any other qualification.

This dissertation does not exceed sixty-five thousand words, including appendices, figures, tables, equations, footnotes and bibliography. It also contains seventy-nine figures and fifteen tables.

SIDNEY SUSSEX COLLEGE  
UNIVERSITY OF CAMBRIDGE

YU LIU  
MAY 2008



# Acknowledgements

Above all, I would like to express my sincere gratitude to my supervisor, Professor Dame Ann Dowling, who has provided me with invaluable advice and guidance throughout my doctoral studies. This thesis could not have been completed without her numerous support. I am especially grateful for her precise attitude towards scientific study and her encouragement to conduct independent research.

I also wish to thank my advisor, Dr Will Graham, for several fruitful discussions and reviews of my work, and the validation codes of wavenumber-frequency spectrum models at the initial stage of my research. In addition, my appreciation to Dr Ho-Chul Shin of the SAI team, whose expertise and kind tutorial in phased array measurements and the analysis software were very helpful.

The realisation of my studies in University of Cambridge may never have been possible without the financial support from the Overseas Research Students Awards Scheme (ORSAS) of the British Government and the Gates Cambridge Scholarship, both of which I am greatly grateful to. Additional funding to this research was also provided by the Department of Engineering, Sidney Sussex College and the Cambridge-MIT Institute (CMI).

My sincere thanks go to Dr Pieter Sijtsma of NLR for his continued support and interest in results obtained from the phased array in Cambridge, and my colleague in the Acoustics Laboratory, Mr Alexander Quayle, for lots of beneficial discussions on the phased array system and his assistance to the experiments on the dipole beamforming algorithm.

Special thanks also to the technicians of the Acoustics Laboratory and the Aerodynamics Laboratory, especially Mr John Hazlewood and Mr John Clark, for

providing the technical support and fabricating the models examined in the course of the experimental work.

I would also like to thank everyone in the Acoustics Laboratory, many members of the SAI team, and other friends in the University and elsewhere for their friendship and help during my studies in Cambridge.

Finally, I wish to thank my wife, Yi Liu, for her love and constant support, especially during the writing of this thesis. I am indebted to my parents and family, for their support and encouragement over the past years.

YU LIU  
MAY 2008

# Contents

<b>Abstract</b>	<b>i</b>
<b>Declaration</b>	<b>iii</b>
<b>Acknowledgements</b>	<b>v</b>
<b>List of Figures</b>	<b>xi</b>
<b>List of Tables</b>	<b>xvii</b>
<b>List of Publications</b>	<b>xix</b>
<b>Nomenclature</b>	<b>xxi</b>
<b>1 Introduction</b>	<b>1</b>
1.1 Background . . . . .	1
1.1.1 Aircraft noise sources . . . . .	1
1.1.2 The Silent Aircraft Initiative . . . . .	3
1.2 Motivations and Objectives . . . . .	4
1.3 Thesis Outline . . . . .	8
<b>2 Literature Review</b>	<b>11</b>
2.1 Wave Scattering from Rough Surfaces . . . . .	11
2.1.1 Overview . . . . .	11
2.1.2 Perturbation theory . . . . .	13
2.1.3 Kirchhoff theory . . . . .	14
2.1.4 Comparison and further considerations . . . . .	16
2.2 Rough-Wall Turbulent Boundary-Layer Flow . . . . .	18
2.2.1 Flow effects over rough walls . . . . .	18

2.2.2	Turbulent wall pressures . . . . .	20
2.3	Sound Generation by Surface Roughness . . . . .	24
2.3.1	General introduction . . . . .	24
2.3.2	Experimental measurements . . . . .	25
2.3.3	Theoretical modelling . . . . .	27
<b>3</b>	<b>Theoretical Modelling</b>	<b>35</b>
3.1	Introduction . . . . .	35
3.2	Diffraction Theory of Surface Roughness Noise . . . . .	36
3.2.1	Formulation of the diffraction problem . . . . .	36
3.2.2	Acoustic spectrum of the radiated sound . . . . .	39
3.3	Rough-Wall Turbulent Boundary-Layer Pressures . . . . .	41
3.3.1	Modelling turbulence Reynolds stress sources . . . . .	41
3.3.2	Wall pressure wavenumber-frequency spectrum . . . . .	42
3.3.3	Determinations of $u_\tau$ and $\delta$ . . . . .	44
3.4	Evaluation of the Rough-Wall Acoustic Spectrum . . . . .	46
3.4.1	Asymptotic approximation and empirical model . . . . .	46
3.4.2	Direct numerical integration . . . . .	47
3.4.3	Comparison of empirical model with numerical method . . . . .	50
3.5	Summary . . . . .	52
<b>4</b>	<b>Experimental Validation</b>	<b>53</b>
4.1	Introduction . . . . .	53
4.2	Acoustic Spectrum Measurement . . . . .	54
4.2.1	Experimental setup . . . . .	54
4.2.2	Modifications of the numerical method . . . . .	58
4.2.3	Results and discussion . . . . .	60
4.3	Phased Array Measurement . . . . .	63
4.3.1	Introduction and survey . . . . .	63
4.3.2	Experimental setup . . . . .	65
4.3.3	Results and discussion . . . . .	68
4.3.4	Theoretical simulation . . . . .	73
4.3.5	Comparison of measurement and simulation . . . . .	80
4.4	Hot-Wire Measurement . . . . .	84








---

4.4.1	Experimental setup . . . . .	84
4.4.2	Results and discussion . . . . .	86
4.5	Summary . . . . .	89
<b>5</b>	<b>Numerical Prediction and Analysis</b>	<b>91</b>
5.1	Introduction . . . . .	91
5.2	Boeing-757 Sized Aircraft Wing . . . . .	92
5.2.1	Roughness noise from an aircraft wing . . . . .	92
5.2.2	Idealized test cases . . . . .	95
5.2.3	Parametric study . . . . .	99
5.2.4	Directivity . . . . .	102
5.3	SAI Design SAX-40 . . . . .	106
5.3.1	Methodology . . . . .	106
5.3.2	Noise assessment . . . . .	109
5.3.3	Candidate surface roughness . . . . .	116
5.4	Summary . . . . .	119
<b>6</b>	<b>Drag Dipole Mechanism</b>	<b>121</b>
6.1	Introduction and Survey . . . . .	121
6.1.1	Lift and drag fluctuations of a sphere . . . . .	121
6.1.2	Hairpin vortices . . . . .	124
6.1.3	Motivation and structure of the chapter . . . . .	126
6.2	Howe <i>et al.</i> 's Sphere Model of Unsteady Forces . . . . .	126
6.2.1	Analytical model of vortex shedding . . . . .	126
6.2.2	The lift and drag spectra . . . . .	130
6.2.3	Comparison of prediction and measurement . . . . .	132
6.3	Drag Dipole Noise . . . . .	134
6.3.1	Theoretical formulation . . . . .	134
6.3.2	Glegg <i>et al.</i> 's drag model . . . . .	137
6.3.3	Wall-mounted hemisphere model . . . . .	140
6.4	Numerical Prediction . . . . .	144
6.4.1	Small-time approximation . . . . .	144
6.4.2	Noise spectrum . . . . .	150
6.5	Summary . . . . .	153

<b>7</b>	<b>Beamforming Correction for Dipole Measurement</b>	<b>155</b>
7.1	Introduction . . . . .	155
7.2	Theoretical Formulation . . . . .	157
7.2.1	The monopole source . . . . .	157
7.2.2	The dipole source . . . . .	158
7.3	Beamforming Algorithm . . . . .	159
7.3.1	Conventional beamforming . . . . .	159
7.3.2	Signal correction . . . . .	160
7.3.3	Beamforming correction . . . . .	161
7.4	Numerical Simulation . . . . .	162
7.4.1	Simulation setup . . . . .	162
7.4.2	Signal correction . . . . .	164
7.4.3	Beamforming correction . . . . .	168
7.5	Experiment . . . . .	170
7.5.1	Experimental setup . . . . .	170
7.5.2	Noise spectra . . . . .	172
7.5.3	Beamforming correction . . . . .	173
7.6	Summary . . . . .	178
<b>8</b>	<b>Conclusions and Future Work</b>	<b>179</b>
8.1	Summary and Conclusions . . . . .	179
8.2	Suggestions for Future Work . . . . .	183
<b>A</b>	<b>Empirical Models for Smooth-Wall Wavenumber-Frequency Spectrum</b>	<b>187</b>
A.1	Empirical Models . . . . .	187
A.2	Prediction . . . . .	190
<b>B</b>	<b>Discrete Power Spectral Density</b>	<b>193</b>
<b>C</b>	<b>Derivation of Skin Friction Coefficient from Hot-Wire Measurement</b>	<b>195</b>
<b>D</b>	<b>Derivations Related to the Wall-Mounted Hemisphere Model</b>	<b>199</b>
D.1	The Image-Vortex Effects . . . . .	199
D.2	Small-Time Approximations . . . . .	201
	<b>Bibliography</b>	<b>205</b>

# List of Figures

1.1	Aircraft noise sources [149]. . . . .	2
1.2	Typical modern aircraft noise levels [161]. . . . .	2
1.3	Airframe noise sources [54]. . . . .	3
1.4	The Silent Aircraft eXperimental design SAX-40 and the Cambridge-MIT Silent Aircraft team. . . . .	4
1.5	Airfoil self noise normalized by wing area and height as a function of velocity (measured data from Fink [54]). Straight lines correspond to the 5 <sup>th</sup> power variation predicted by Lilley’s TE noise theory [97]. Comparison of self noise models (Faszer and Hileman [50, 51]):  red, Lilley semi-empirical airframe model [97];  purple, ESDU empirical airframe model [27] – conventional wing;  orange, modified volume Lilley semi-empirical airframe model [99];  blue, ESDU empirical airframe model [27] – glider wing;  green, Brooks <i>et al.</i> self noise model [21]. . . . .	5
1.6	The rough surface of a transport aircraft. . . . .	6
2.1	$h$ as a function of roughness Reynolds number, $Re_\tau = k_s u_\tau / \nu$ (Duncan <i>et al.</i> [42]). . . . .	18
2.2	Turbulent boundary layer and wall pressure wavenumber-frequency spectrum at low Mach numbers when $\omega\delta/U \gg 1$ (Howe [82]). . . . .	20
2.3	Boundary-layer velocity profile regions and their relationships with the source mechanisms of surface roughness noise. Regions: I – viscous sublayer, II – logarithmic layer, III – outer region. Source mechanisms: (i) sound scattering and (ii) drag dipole. . . . .	28
2.4	Rough surfaces with different values of $\nabla\xi$ . . . . .	32
3.1	Schematic illustration of the diffraction problem. . . . .	36

3.2	Sound radiation from a region of area $A$ of the rough wall. . . . .	41
3.3	Curve fits of the frequency spectrum of wall pressure fluctuations (Ahn [4]). . . . .	49
3.4	Comparison of roughness noise spectra predicted by the empirical model [82] and the present numerical method. $\nabla$ $\circ$ $\triangle$ Previous experimental data obtained by Hersh [71]. . . . .	51
4.1	Schematic of the experimental setup for acoustic spectrum measurement. The rectangular region on the test plate is the effective rough region. . . . .	55
4.2	Test rough panels of Rough1 and Rough2 with rigid hemispherical roughness elements formed by plastic beads. . . . .	56
4.3	Schematic of the rough region at a distance from the leading edge. . . . .	59
4.4	Comparison between experimental and predicted roughness noise spectra. Smooth-wall experimental results are shown for comparison. $U = 30$ m/s. . . . .	61
4.5	Schematic of the experimental setup for phased array measurement. . . . .	64
4.6	Microphone positions of the HF and LF arrays. . . . .	66
4.7	Schematic of the acoustic measurement by a phased microphone array. . . . .	67
4.8	Measured source maps by the HF array: (a) Rough1, (b) Rough2, (c) Smooth. $U = 30$ m/s. . . . .	69
4.9	Measured source maps by the LF array: (a) Rough1, (b) Rough2, (c) Smooth. $U = 30$ m/s. . . . .	70
4.10	Measured source maps at Locations 1–3: (a) Rough1, (b) Rough2. HF array, $f = 2000$ Hz, $U = 30$ m/s. . . . .	72
4.11	Predicted SPL of $P_R(\omega)/A$ with streamwise distance $x_1$ for chosen frequencies: $\blacksquare$ 1250 Hz, $\bullet$ 1600 Hz, $\blacktriangle$ 2000 Hz. $U = 30$ m/s. . . . .	73
4.12	Schematic of the theoretical simulation. . . . .	76
4.13	Comparison of source maps between measurement and simulation: (a) measurement, (b) simulation. Rough1, HF array, $U = 30$ m/s. . . . .	81
4.14	Comparison of source maps between measurement and simulation: (a) measurement, (b) simulation. Rough1, LF array, $U = 30$ m/s. . . . .	81
4.15	Comparison of source maps between measurement and simulation: (a) measurement, (b) simulation. Rough2, HF array, $U = 30$ m/s. . . . .	82

4.16	Comparison of source maps between measurement and simulation: (a) measurement, (b) simulation. Rough2, LF array, $U = 30$ m/s. . . .	82
4.17	Schematic of the hot-wire experimental setup and measurement stations A–D. . . . .	84
4.18	The hot-wire probe above hemispherical roughness elements. . . . .	85
4.19	Comparison of the predicted and measured boundary-layer thickness $\delta$ on a rough plate with streamwise distance $x_{le} + x_1$ . $U = 20$ m/s. . .	87
5.1	3-view drawing of a commercial airplane type, the Boeing 757 family [19]. . . . .	93
5.2	Evolution of the approximation of a Boeing-757 sized aircraft wing to a flat plate model. Dimensions are in metres and are estimated from Figure 5.1. . . . .	93
5.3	Frequency response of the A-weighting filter for the dBA scale. . . .	94
5.4	Predicted spectra of roughness noise and TE noise for Cases 1–3. . .	96
5.5	Effects of roughness height $R$ and roughness density $\sigma$ on predicted roughness noise spectra. . . . .	100
5.6	Effects of roughness height $R$ and roughness density $\sigma$ on predicted roughness noise OASPL. . . . .	101
5.7	Predicted directivities of roughness noise OASPL for Cases 1–3, $ \mathbf{x}  =$ $500$ m, $\phi = -\pi/2$ . . . . .	103
5.8	$J$ , as defined in Equation (5.6), as a function of $\kappa$ and $\alpha$ . . . . .	103
5.9	Predicted ground contours of roughness noise OASPL for Cases 1–3. . .	104
5.10	Evolution of the approximation of the SAX-40 planform. . . . .	106
5.11	Hypothetical airport dimensions used for the noise assessment of SAX-40 during approach. . . . .	108
5.12	Predicted ground contours of roughness noise OASPL for Cases 1–3 of SAX-40. . . . .	110
5.13	Effects of $R$ and $\sigma$ on roughness noise OASPL of SAX-40 during approach. Maximum OASPL on the eastward axis at $(H, 0)$ . . . . .	111
5.14	Effects of $R$ and $\sigma$ on roughness noise OASPL of SAX-40 during approach. Maximum OASPL on both northward and eastward axes at $(H, 0)$ or $(0, H)$ . . . . .	111
5.15	Distribution of roughness noise sources (dBA) on the SAX-40 surface. . .	113

5.16	Predicted ground contours of TE noise OASPL for Cases 1–4. . . . .	115
5.17	Comparison of displacement boundary-layer thickness $\delta^*$ at the trailing edge of SAX-40 planform along lateral coordinate $y$ . . . . .	116
5.18	Ground noise footprints (dBA) for two candidate rough surfaces: top, ground contour; middle, noise level at flyover; bottom, noise level along sideline. . . . .	118
6.1	Vortex shedding from a sphere modelled by a sequence of randomly orientated vortex rings (Howe <i>et al.</i> [83]). . . . .	123
6.2	Hairpin vortex shapes at different Reynolds number ( $500 < Re_\theta < 17500$ ) flows (Head and Bandyopadhyay [69]). . . . .	124
6.3	View from downstream and above of a vortex ring separating from the sphere at A and B when $\varphi_n = 0$ . The angle $\xi_n(t)$ determines the total arc length $2a\xi_n(t)$ of the shed vortex during separation (Howe <i>et al.</i> [83]). . . . .	128
6.4	Measured and predicted (a) lift spectrum and (b) drag spectrum. ●●● averaged measured values for $Re = 6680, 10020, 13360, 16700$ . — — —, ○ ⊕ predictions for the two cases $\langle \theta \rangle = 10^\circ, 30^\circ$ when averaging is performed over $0.9 < \theta_n / \langle \theta \rangle < 1.1$ and $a = 0.7R$ , $U_c = 0.7U$ , $C_D = 0.4$ (reproduced from Howe <i>et al.</i> [83]). . . . .	133
6.5	Schematic of vortex shedding from a wall-mounted hemisphere modelled by a sequence of vortex semi-circular arcs. . . . .	140
6.6	View from downstream and above of a vortex loop separating from the hemisphere at the intersection points A and B, $\varphi_n \equiv 0$ (modified from Figure 6.3). . . . .	141
6.7	Variation of the nondimensional lift and drag during shedding from the sphere and hemisphere, respectively, when $a = 0.7R$ , $\theta_n = \pi/8$ . Important time points: A – full vortex ring released from the sphere, and B – half vortex ring released from the hemisphere. . . . .	145
6.8	Variation of $\xi_n(t)/\pi$ (□□□) and the integrands $\dot{\mathcal{F}}_n$ (●●●), $\dot{\mathcal{G}}_n$ (○○○) of Equations (6.13) and (6.15) with the nondimensional time $U_c(t-t_n)/R$ for the sphere model and hemisphere model, respectively, when $a = 0.7R$ , $\theta_n = \pi/8$ . . . . .	146

6.9	Comparison of approximated and integrated predictions of the lift and drag spectra for the two cases $\langle\theta\rangle = 10^\circ, 30^\circ$ when averaging is performed over $0.9 < \theta_n/\langle\theta\rangle < 1.1$ and $a = 0.7R, U_c = 0.7U, C_D = 0.4$ . Small-time approximations: $\circ \circ \circ \langle\theta\rangle = 30^\circ, \square \square \square \langle\theta\rangle = 10^\circ$ . Numerical integrations: $\text{—} \langle\theta\rangle = 30^\circ, \text{---} \langle\theta\rangle = 10^\circ$ . Also shown are $\bullet \bullet \bullet$ the averaged measured values for $Re = 6680, 10020, 13360, 16700$ by Howe <i>et al.</i> [83]. The sphere model. . . .	149
6.10	Approximated and integrated drag spectra for the two cases $\langle\theta\rangle = 10^\circ, 30^\circ$ over the interval $0.9 < \theta_n/\langle\theta\rangle < 1.1$ and $a = 0.7R, U_c = 0.7U, C_D = 0.4$ . Small-time approximations: $\circ \circ \circ \langle\theta\rangle = 30^\circ, \square \square \square \langle\theta\rangle = 10^\circ$ . Numerical integrations: $\text{—} \langle\theta\rangle = 30^\circ, \text{---} \langle\theta\rangle = 10^\circ$ . The hemisphere model. . . . .	150
6.11	Nondimensional drag dipole noise spectra of the sphere and hemisphere models for the case $\langle\theta\rangle = 45^\circ$ over the interval $0.75 < \theta_n/\langle\theta\rangle < 1.25$ and $a = 0.7R, U_c = 0.7U, C_D = 0.4$ . . . . .	151
6.12	Comparison of noise spectra between the drag dipole mechanism and the scattering mechanism. For the drag dipole noise spectrum, $R = 2$ cm, $\sigma = 0.01$ for the case $\langle\theta\rangle = 45^\circ$ over the interval $0.75 < \theta_n/\langle\theta\rangle < 1.25$ and $a = 0.7R, U_c = 0.7U, C_D = 0.4$ . For the scattering noise spectra, Cases 1–3 are defined in Section 5.2.2. . . . .	153
7.1	Schematic of the simulation for a dipole source. . . . .	163
7.2	Dipole directivities for test cases 1 and 2. . . . .	163
7.3	Simulated source maps for Case 1: (a) dipole without correction, (b) dipole with signal correction, (c) reference monopole. HF array, $f = 8000$ Hz; LF array, $f = 2000$ Hz. Colour bars are in dB. . . . .	164
7.4	Simulated source maps for Case 2: (a) dipole without correction, (b) dipole with signal correction, (c) reference monopole. HF array, $f = 8000$ Hz; LF array, $f = 2000$ Hz. Colour bars are in dB. . . . .	165
7.5	Variation of peak source power $S$ with 1/3 octave-band centre frequency $f$ for Cases 1 and 2. Dipole without correction: $\blacksquare$ HF array, $\bullet$ LF array; dipole with signal correction: $\square$ HF array, $\circ$ LF array; $\text{---} S \sim f^3, \text{—} S \sim f$ . . . . .	167

7.6	Simulated source maps by the D-Beam algorithm: (a) Case 1 and (b) Case 2. HF array, $f = 8000$ Hz; LF array, $f = 2000$ Hz. Colour bars are in dB. . . . .	168
7.7	Simulated multiple dipole by the D-Beam algorithm: (a) 2 Y (0, 1, 0) dipoles located at $(-0.1, 0.0)$ and $(0.1, 0.0)$ ; (b) 3 Z (0, 0, 1) dipoles located at $(0.0, 0.1)$ , $(-0.1, -0.1)$ and $(0.1, -0.1)$ . HF array, $f = 12500$ Hz; LF array, $f = 4000$ Hz. Colour bars are in dB. . . . .	170
7.8	Experimental setup for aeolian-tone dipoles in two different directions: Z (0, 0, 1) and Y (0, 1, 0). . . . .	171
7.9	Measured cross spectra for dipoles in two different directions: Z (0, 0, 1) and Y (0, 1, 0) with measured cross spectra of overhead and side supports for comparison. $\Delta f = 117.2$ Hz. . . . .	173
7.10	Comparison of simulated source maps by the M-Beam and D-Beam algorithms for dipoles in two different directions: (a) Z (0, 0, 1) and (b) Y (0, 1, 0). HF array, $f = 6300$ Hz. Colour bars are in dB. . . . .	174
7.11	Variation of simulated peak source power $S$ with $1/3$ octave-band centre frequency $f$ for the Z and Y dipoles. M-Beam algorithm: ■ HF array, ● LF array; D-Beam algorithm: □ HF array, ○ LF array; ---, — $S \sim f^3$ . . . . .	175
7.12	Comparison of measured source maps by the M-Beam and D-Beam algorithms for dipoles in two different directions: (a) Z (0, 0, 1) and (b) Y (0, 1, 0). HF array, $f = 6300$ Hz. Colour bars are in dB. . . . .	176
A.1	Predicted wavenumber-frequency spectra that are plotted against streamwise wavenumber $\kappa_1$ non-dimensionalized on the convective wavenumber $\omega/U_{cr}$ and thus peak round one. . . . .	191
A.2	Predicted spanwise wavenumber-frequency spectra. . . . .	192
C.1	Schematic of the derivation of $\bar{c}_f$ from measured mean velocity profiles at two stations along a flat plate. . . . .	195
D.1	End view of a vortex loop separating from the hemisphere at the intersection points A and B. Also shown are the images of the vortex loop and the hemisphere (dashed lines). $\varphi_n \equiv 0$ . . . . .	200



# List of Tables

4.1	Surface conditions to be tested in the experiment. . . . .	56
4.2	Overall dimensions and the maximum and minimum values of $d$ for each array. . . . .	66
4.3	Locations of the array centre. . . . .	71
4.4	Streamwise locations of measurement stations A–D. . . . .	86
4.5	Comparison of the average skin friction coefficient $\bar{c}_f$ between measurement and predictions by Formula (3.31) (Prandtl and Schlichting [124]) and Formula (3.33) (Mills and Hang [106]). Rough surfaces: (a) Rough1 and (b) Rough2. . . . .	88
5.1	Test case parameters. . . . .	95
5.2	Equivalent roughness heights $k_s$ for common surfaces [44]. . . . .	98
5.3	Predicted roughness noise and TE noise OASPL for test cases 1–3. . . . .	98
5.4	Reduced forms of expressions for observers on the $x_1$ - and $x_3$ -axis. . . . .	105
5.5	Approximate configuration of the SAX-40 planform. . . . .	107
7.1	Source location $\xi$ and dipole vector $l$ for test cases 1 and 2. . . . .	163
7.2	Simulated peak source power $S$ (dB) by the M-Beam and D-Beam algorithms for Cases 1 and 2. HF array, $f = 8000$ Hz; LF array, $f = 2000$ Hz. . . . .	169
7.3	Comparison of elapsed CPU time (s) between the signal correction ( $t_s$ ) and beamforming correction ( $t_b$ ). HF array, $f = 8000$ Hz; LF array, $f = 2000$ Hz. . . . .	169
7.4	Dipoles in two different directions. . . . .	171
7.5	Peak source power $S$ (dB) of measurement and simulation for the Z and Y dipoles. (a) HF array, $f = 6300$ Hz; (b) LF array, $f = 3150$ Hz. . . . .	177



# List of Publications

## Journal Articles

- [1] LIU, Y., QUAYLE, A. R., DOWLING, A. P., AND SIJTSMA, P. Beamforming Correction for Dipole Measurement Using Two-Dimensional Microphone Arrays. *Journal of the Acoustical Society of America* 124, 1 (2008), 182–191.
- [2] LIU, Y., DOWLING, A. P., AND SHIN, H.-C. Measurement and Simulation of Surface Roughness Noise Using Phased Microphone Arrays. *Journal of Sound and Vibration* 314, 1–2 (2008), 95–112.
- [3] LIU, Y., AND DOWLING, A. P. Assessment of the Contribution of Surface Roughness to Airframe Noise. *AIAA Journal* 45, 4 (2007), 855–869.

## Conference Proceedings

- [4] LIU, Y., DOWLING, A. P., AND QUAYLE, A. R. Numerical Simulation of Beamforming Correction for Dipole Source Identification. *Proceedings of the 2<sup>nd</sup> Berlin Beamforming Conference (BeBeC)*. Paper No. 22, Berlin, Germany, 19–20 February, 2008.
- [5] QUAYLE, A. R., GRAHAM, W. R., DOWLING, A. P., BABINSKY, H., AND LIU, Y. Mitigation of Beamforming Interference from Closed Wind Tunnels Using CLEAN-SC. *Proceedings of the 2<sup>nd</sup> Berlin Beamforming Conference (BeBeC)*. Paper No. 16, Berlin, Germany, 19–20 February, 2008.
- [6] LIU, Y., DOWLING, A. P., HILEMAN, I. J., AND QUAYLE, A. R. Surface Roughness Noise Prediction for Silent Aircraft eXperimental Design SAX-40.

- Proceedings of the 46<sup>th</sup> AIAA Aerospace Sciences Meeting and Exhibit*. AIAA Paper 2008-0845, Reno, Nevada, USA, 7–10 January, 2008.
- [7] QUAYLE, A. R., DOWLING, A. P., BABINSKY, H., GRAHAM, W. R., AND LIU, Y. Mechanisms for Model Scale Landing Gear Noise Generation. *Proceedings of the 46<sup>th</sup> AIAA Aerospace Sciences Meeting and Exhibit*. AIAA Paper 2008-0845, Reno, Nevada, USA, 7–10 January, 2008.
- [8] LIU, Y., DOWLING, A. P., AND SHIN, H.-C. Experimental Study of Surface Roughness Noise. *Proceedings of the 13<sup>th</sup> AIAA/CEAS Aeroacoustics Conference*. AIAA Paper 2007-3449, Rome, Italy, 21–23 May, 2007.
- [9] QUAYLE, A. R., DOWLING, A. P., BABINSKY, H., GRAHAM, W. R., AND LIU, Y. Phased Array Measurements from Landing Gear Models. *Proceedings of the 13<sup>th</sup> AIAA/CEAS Aeroacoustics Conference*. AIAA Paper 2007-3463, Rome, Italy, 21–23 May, 2007.
- [10] LIU, Y., DOWLING, A. P., AND SHIN, H.-C. Application of Phased Arrays in the Study of Surface Roughness Noise. *Proceedings of the 1<sup>st</sup> Berlin Beamforming Conference (BeBeC)*. Paper No. 16, Berlin, Germany, 21–22 November, 2006.
- [11] LIU, Y., DOWLING, A. P., AND SHIN, H.-C. Effects of Surface Roughness on Airframe Noise. *Proceedings of the 12<sup>th</sup> AIAA/CEAS Aeroacoustics Conference*. AIAA Paper 2006-2510, Cambridge, Massachusetts, USA, 8–10 May, 2006.

# Nomenclature

The Nomenclature lists symbols used in the main body of the thesis: Chapters 3–7. Definitions of symbols are also incorporated in the Literature Review of Chapter 2 and the Appendices.

## Roman Symbols

$a$	monopole source strength
$a$	radius of vortex ring, Chapter 6
$A$	area of the rough region
$A$	frontal area of the sphere or hemisphere, Chapter 6
$A$	source auto-power of monopole strength $a$ , Equation (7.24)
$A$	expected aspect ratio of roughness elements, Equation (6.50)
$A_j$	the $j$ th equal subarea of the rough region, $A/N_A$
$A_{\text{gro}}$	gross area of the SAX-40 planform
$A_{\text{ref}}$	reference area for calculating source distribution on SAX-40
$B$	empirical constant for the profile of $u$ on a rough wall, Equation (3.35)
$c$	speed of sound in free field
$c_f$	local skin friction coefficient, $\tau_w / \frac{1}{2} \rho_0 U^2$
$c_{f0}$	$c_f$ at a distance $x_{le}$ from the leading edge
$\mathbf{C}$	cross-power matrix
$C_F$	overall skin friction coefficient, $\frac{1}{L} \int_0^L c_f dx_1$
$C_A$	A-weighting factor
$C_D$	mean drag coefficient of the sphere
$d$	distance between microphones and their nearest neighbour
$d_m, U_m$	width and local velocity of each roughness element, Section 6.3.2
$d_n$	nominal depth of flow above roughness elements in a wind tunnel
$D$	directivity function

$D$	sphere diameter, Chapter 6
$\mathcal{D}'$	fluctuating part of unsteady drag $\mathcal{D}$
$\overline{\mathcal{D}}_m$	steady drag on each roughness element, Section 6.3.2
DPL	dipole characteristic term, Equation (7.18)
$\mathcal{E}, \mathcal{H}$	auxiliary terms, Equations (6.70) and (6.68)
$f$	frequency
$f_0$	quasi-periodic vortex shedding frequency
$f_i$	force per unit area externally applied on fluid by roughness bosses
$F$	net force exerted on the sphere, Section 6.2.1.1
$\mathbf{F}$	dipole source strength vector, Section 7.2.2
$F(St)$	loading spectrum as a function of $St$ , Section 6.3.2
$\mathcal{F}_n, \mathcal{G}_n$	functions to determine the lift and drag, Equations (6.13) and (6.15)
$\dot{\mathcal{F}}_n, \dot{\mathcal{G}}_n$	integrands of $\mathcal{F}_n, \mathcal{G}_n$
$g$	function of Strouhal number $Sh^*$ , Equation (3.52)
$\mathbf{g}$	transfer vector
$g_n$	components of $\mathbf{g}$ , Equation (7.21)
$G$	Green's function
$G_L, G_D$	normalized lift and drag spectra, Equation (6.31)
$h_m$	roughness height of each element, Section 6.3.2
$H$	aircraft altitude
$i$	unit imaginary number $\sqrt{-1}$
$I_1-I_3$	integrals with respect to polar coordinates $\kappa\delta^*$ and $\alpha$ , Equation (3.49)
$J$	function of $\kappa$ , Equation (5.6)
$J$	term related to the minimization problem, Equation (7.22)
$J_1$	Bessel function of order unity
$k, k_0$	acoustic wavenumber, $\omega/c$
$k_s$	equivalent roughness height
$l$	distance between two coherent monopoles of a dipole
$L$	length of the flat plate
$L_c, L_s$	equivalent chord and span of an aircraft wing
$\mathcal{L}, \mathcal{D}$	lift and drag on the sphere
$M$	free-stream Mach number, $U/c$

$n$	normal to the rough surface, Sections 3.2.1 and 6.3.1
$n$	empirical coefficient in $\Phi_R$ , Equation (3.42)
$n$	number of frequency intervals, Section 4.3.4.5
$\tilde{\mathbf{n}}$	unit observer vector
$\mathbf{n}_n$	normal to the plane of the $n$ th vortex ring
$N$	average number of roughness bosses per unit area
$N$	number of roughness elements on the surface, Section 6.3
$N$	number of array microphones, Section 7.3
$N_A$	number of subareas in the rough region
$p$	pressure fluctuation
$\hat{p}$	acoustic pressure spectrum
$\mathbf{p}$	vector of measured pressure amplitude by array microphones
$p_0$	static pressure
$p_s$	hypothetical smooth-wall pressure fluctuation
$p_{ij}$	surface compressive stress tensor
$p_{\text{ref}}$	reference sound pressure, $2 \times 10^{-5}$ Pa
$P$	power spectral density of $\hat{p}$
$P_R$	acoustic frequency spectrum of far-field radiated roughness noise
$P_s$	smooth-wall wavenumber-frequency spectrum
$q(t)$	monopole source strength in time domain
$Q$	turbulence Reynolds stress source
$r$	propagation distance from source to observer
$R$	roughness height
$R$	sphere radius, Chapter 6
$Re$	Reynolds number
$Re_L$	Reynolds number based on the whole plate, $UL/\nu$
$Re_{le}$	Reynolds number based on $x_{le}$ , $Ux_{le}/\nu$
$Re_x$	Reynolds number based on $x_1$ , $Ux_1/\nu$
$Re_\tau$	roughness Reynolds number, $k_s u_\tau/\nu$
$s$	curvilinear distance along the axis of vortex core, Section 6.2.1.1
$S$	boundary surface, Sections 3.2.1 and 6.3.1
$S$	cross-spectral density of turbulence Reynolds stress, Equation (3.17)

---

$S$	surface area, Section 6.3.2
$S$	peak source power, Chapter 7
$S_F$	expected loading spectrum, $\text{Ex}[F(St)]$
$Sh$	Strouhal number based on $\delta$ and $u_\tau$ , $\omega\delta/u_\tau$
$Sh^*$	Strouhal number based on $\delta^*$ and $U$ , $\omega\delta^*/U$
$St$	Strouhal number based on $d_m$ and $U_m$ , $\omega d_m/2\pi U_m$ , Section 6.3.2
$St$	Strouhal number based on $R$ and $U$ , $fR/U$ , Section 6.4.2.2
$t$	observer time
$t$	vortex shedding time, Chapter 6
$t_n$	shedding starting time for the $n$ th vortex ring
$t_s, t_b$	CPU time of signal correction or beamforming correction, Section 7.4.3
$u$	streamwise mean velocity in a boundary layer
$u_\tau$	friction velocity
$U$	free-stream velocity
$U_c$	eddy convection velocity
$U_m$	maximum value of $u$
$v$	$x_2$ -component of perturbation velocity $\boldsymbol{v}$
$\boldsymbol{v}$	perturbation velocity
$\boldsymbol{v}$	fluid velocity, Section 6.2.1.1
$V$	bounded volume, Section 3.2.1
$w$	wake function
$\boldsymbol{x}$	observer position, $(x_1, x_2, x_3)$
$\boldsymbol{x}$	position of integration point on vortex ring, Equations (6.10) and (6.61)
$x_0$	hypothetical extension of the rough region
$x_1$	streamwise distance from the front edge of the rough region
$x_{le}$	distance between the rough region and the leading edge
$x_n$	position of the centre of the $n$ th vortex ring on the $x$ -axis, Chapter 6
$x, y, z$	Cartesian coordinates
$X$	velocity potential of an ideal flow past the sphere with unit speed
$\boldsymbol{y}$	source position, $(y_1, y_2, y_3)$
$\boldsymbol{Y}$	velocity potential of an ideal incompressible flow over the rough wall



## Greek Symbols

$\alpha$	polar angle of the wavenumber plane, first used in Equation (3.44)
$\alpha$	aircraft approach path angle, Section 5.3.1.2
$\beta$	empirical coefficient in $\Phi_R$ , Equation (3.42)
$\beta$	$\sqrt{1 - M^2}$ , Chapter 7
$\gamma$	$(k_0^2 - \kappa^2)^{\frac{1}{2}}$
$\Gamma$	vortex circulation
$\delta$	local boundary-layer thickness
$\delta^*$	displacement boundary-layer thickness
$\delta_0$	$\delta$ at the front edge of the rough region
$\delta_{99}$	99% free-stream velocity boundary-layer thickness, Equation (6.56)
$\delta_{ij}$	Kronecker delta
$\delta t_n$	shedding duration of the $n$ th vortex ring
$\delta(\cdot)$	Dirac delta function
$\Delta$	space separation vector
$\Delta f$	frequency bandwidth
$\Delta t$	difference in observer time of two microphones, Equation (4.2)
$\Delta t_e$	emission time delay, Equation (7.4)
$\Delta x, \Delta y$	longitudinal and lateral increments when dividing the SAX-40 planform
$\varepsilon$	power law exponent for the OASPL variation with $R$
$\eta$	fluid shear viscosity
$\theta$	orientation of vortex ring, Chapter 6
$\theta, \phi$	directivity angles
$\Theta$	auxiliary term determined by $M$ and $r$ , Equation (7.13)
$\kappa$	wavenumber vector, $(\kappa_1, 0, \kappa_3)$
$\kappa_0$	Kármán constant, $\approx 0.41$
$\lambda$	acoustic wavelength, $2\pi c/\omega$
$\Lambda$	power spectral density of monopole strength $a$
$\mu$	roughness density factor, $1/(1 + \frac{1}{4}\sigma)$
$\nu$	kinematic viscosity
$\xi$	definition of the rough surface, Sections 3.2.1 and 6.3.1
$\xi$	angle from the intersection of vortex ring and $(x, y)$ -plane, Chapter 6

$\xi$	point source location, Section 7.2
$\pi$	constant, $\approx 3.14159 \dots$
$\Pi$	rough-wall acoustic power spectrum
$\Pi_0$	wake strength
$\rho_0$	mean fluid density in free field
$\sigma$	roughness density, $N\pi R^2$
$\sigma_p$	peak value of $\sigma$ where OASPL achieves the maximum
$\sigma_{ij}$	surface viscous stress tensor
$\sigma_{sq}$	$\sigma$ for a square close packing, $\sim 0.78$
$\sigma_{max}$	maximum value of $\sigma$ for a hexagonal close packing, $\sim 0.91$
$\tau$	source time
$\tau$	interval of vortex shedding, $1/f_0$ , Chapter 6
$\tau_0$	roughness parameter, Equation (3.43)
$\tau_w$	mean wall shear stress, $\rho_0 u_\tau^2$
$\varphi$	azimuthal angle of vortex ring, Section 6.2.1
$\Phi$	point pressure frequency spectrum
$\Phi_B$	Blake's frequency spectrum of wall pressures, Equation (3.52)
$\Phi_E$	Efimtov's frequency spectrum of wall pressures, Equation (3.53)
$\Phi_L, \Phi_D$	frequency spectra of unsteady lift and drag, Equations (6.27) and (6.30)
$\tilde{\Phi}_p$	models for smooth-wall wavenumber-frequency spectrum
$\Phi_R$	empirical model for rough-wall acoustic frequency spectrum
$\chi$	non-dimensionalized term in $I_1-I_3$ , Equation (3.50)
$\Psi$	term related to $\sigma$ , Equation (3.18)
$\omega$	radian frequency, $2\pi f$
$\omega$	fluid vorticity curl $\mathbf{v}$ , Section 6.2.1.1
$\omega_\tau$	friction frequency, Equation (6.50)
$\Omega$	nondimensional frequency, $\omega R/u_\tau$
$\Omega_\tau$	nondimensional frequency, $\omega/\omega_\tau$

## Subscripts

+, -	with regard to monopoles with opposite phase
1, 2	with regard to two microphones, Section 4.2.2

1, 2	with regard to dipoles $DPL_1, DPL_2$ , Section 4.3.4.5
$i$	with regard to the $i$ -direction, Chapter 6
$i, j$	general summation variable
$m$	roughness element index
$m, n$	microphone indices, Equation( 7.25)
$m, s$	with regard to measurement or simulation, Section 7.5.3
$n$	vortex ring index, Chapter 6
$x, y, z$	with regard to the $x$ -, $y$ - or $z$ -direction, Chapter 6
$\iota$	summation variable over $x_1$ and $x_3$ in plane directions
max	maximum value
min	minimum value
rms	root mean square
tot	total

### Superscripts

'	different values of the same variable
*	complex conjugate or Hermitian transpose when applied to a vector
-	mean value or average
^	Fourier transform
~	normalized value

### Other Symbols

$\nabla$	Del operator
$\nabla^2$	Laplacian operator
$\text{curl}(\cdot)$	$\nabla \times (\cdot)$
$\text{Ex}[\cdot]$	Expected value
$\cdot$	scalar product
$\wedge$	vector product
$\langle \cdot \rangle$	ensemble average
$\oint_S$	integration over boundary surface $S$
$\int_V$	integration over bounded volume $V$

**Acronyms**

2D	two-dimensional
B&K	Brüel & Kjær
BWB	blended-wing-body
CFD	Computational Fluid Dynamics
CFT	continuous Fourier transform
CMI	Cambridge-MIT Institute
CTA	Constant Temperature Anemometer
CUED	Cambridge University Engineering Department
DAMAS	Deconvolution Approach for the Mapping of Acoustic Sources
D-Beam	dipole-beamforming
DFT	discrete Fourier transform
DNS	Direct Numerical Simulation
DPL <sub>1</sub>	dipole in flow direction
DPL <sub>2</sub>	dipole normal to flow direction
FAA	Federal Aviation Administration
FFT	fast Fourier transform
FW-H	Ffowcs Williams-Hawkings
HF	high-frequency
ICAO	International Civil Aviation Organization
LES	Large Eddy Simulation
LF	low-frequency
M-Beam	monopole-beamforming
OASPL	overall sound pressure level (dBA)
SAI	Silent Aircraft Initiative
SAX	Silent Aircraft eXperimental
SPL	sound pressure level
TE	trailing edge

# Chapter 1

## Introduction

### 1.1 Background

#### 1.1.1 Aircraft noise sources

**N**OISE has been one of the most important pollution sources in modern industrial society, and is often cited as the most undesirable feature of life in the urban community. One significant contribution to the noise pollution is from aircraft noise, which is second only to traffic noise in the city in its unsociable levels, frequency, and time of occurrence, and is often at the top of the list in rural areas [138]. Along with the increasing growth of civil transport aircraft from the 1960s, aircraft noise has drawn worldwide concerns and become one of the important criteria for aircraft navigability. Federal Aviation Administration (FAA) and International Civil Aviation Organization (ICAO) issued the Code of Federal Regulations, Part 36 (CFR Part 36)<sup>†</sup> [48] and Annex 16 to the Convention on International Civil Aviation [85], respectively, with strict certification setting maximum permissible noise for each type of aircraft. It is pointed out definitely that no aircraft is allowed to operate until it satisfies the certification requirements.

The noise from an aircraft may be broadly classified into two categories: (i) *Propulsive Noise*: noise from aircraft engines; and (ii) *Airframe Noise*: noise from high-lift devices, trailing edges, landing gear, cavities, *etc.*, defined as the noise generated by flow over the airframe and/or the non-propulsive noise of an aircraft

---

<sup>†</sup>Originally called Federal Air Regulations, Part 36 (FAR Part 36).

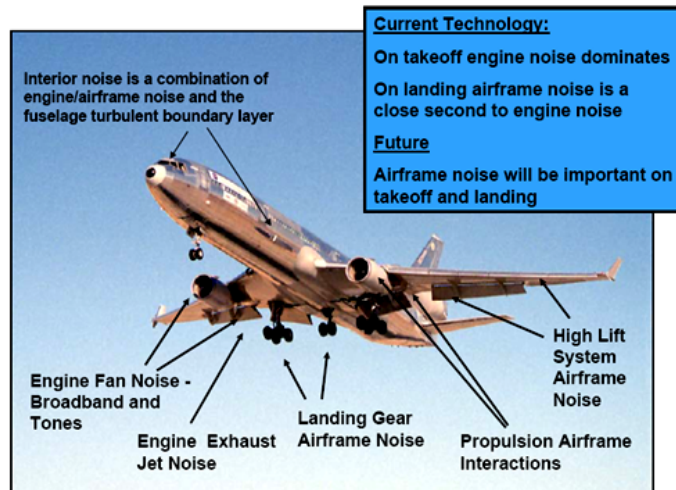


Figure 1.1: Aircraft noise sources [149].

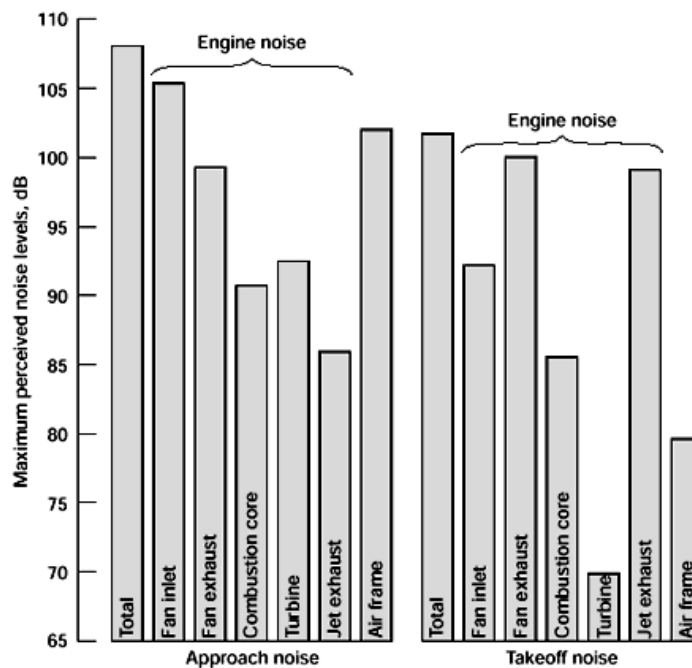


Figure 1.2: Typical modern aircraft noise levels [161].

in flight. Figure 1.1 displays the typical aircraft noise sources. Engine noise has been significantly reduced with the introduction of high-bypass-ratio engines; currently, airframe noise is comparable to engine noise for landing/approaching aircraft. Typical levels showing the relative importance of various noise sources are shown in Figure 1.2. Therefore any further noise reduction can only be achieved by reducing both the airframe noise and propulsive noise.

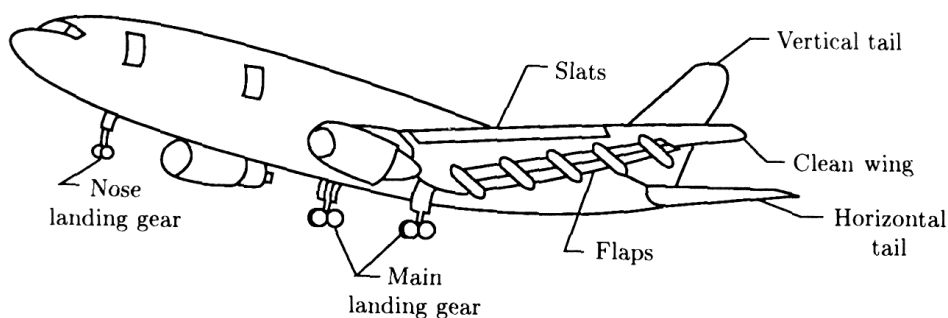


Figure 1.3: Airframe noise sources [54].

Airframe noise derives from various sources, as shown in Figure 1.3, among which flaps, leading-edge devices and landing gear are three main components. The relative contributions of individual airframe noise sources seem to be highly design dependent, varying greatly with aircraft design, geometry, and configuration. In a “clean” configuration (landing gear and high-lift devices stowed), airframe noise is primarily due to trailing-edge (TE) noise and protrusions around the airframe; whereas in a “dirty” configuration (landing gear and high-lift devices deployed), the major contributors of airframe noise are extended high-lift devices on the wing and deployed landing gear.

### 1.1.2 The Silent Aircraft Initiative

The work described in this thesis is part of a wider project, “Silent Aircraft Initiative” (SAI) [40, 41, 101, 145], funded by the Cambridge-MIT Institute (CMI). The project is carried out in a partnership between the University of Cambridge and MIT as part of an extensive network of aerospace partners which includes industry, airline and airport operators, policy makers and academics, such as Boeing, Rolls-Royce, British Airways and NASA.

The project aims to develop a conceptual aircraft design whose noise impact would be below the daytime ambient levels around a typical urban airport. The outcome of this research effort has been a Silent Aircraft eXperimental design SAX-40, as shown in Figure 1.4, designed to carry 215 passengers with a range of 5000 nm in a blended-wing-body (BWB) type airframe [72] and a predicted

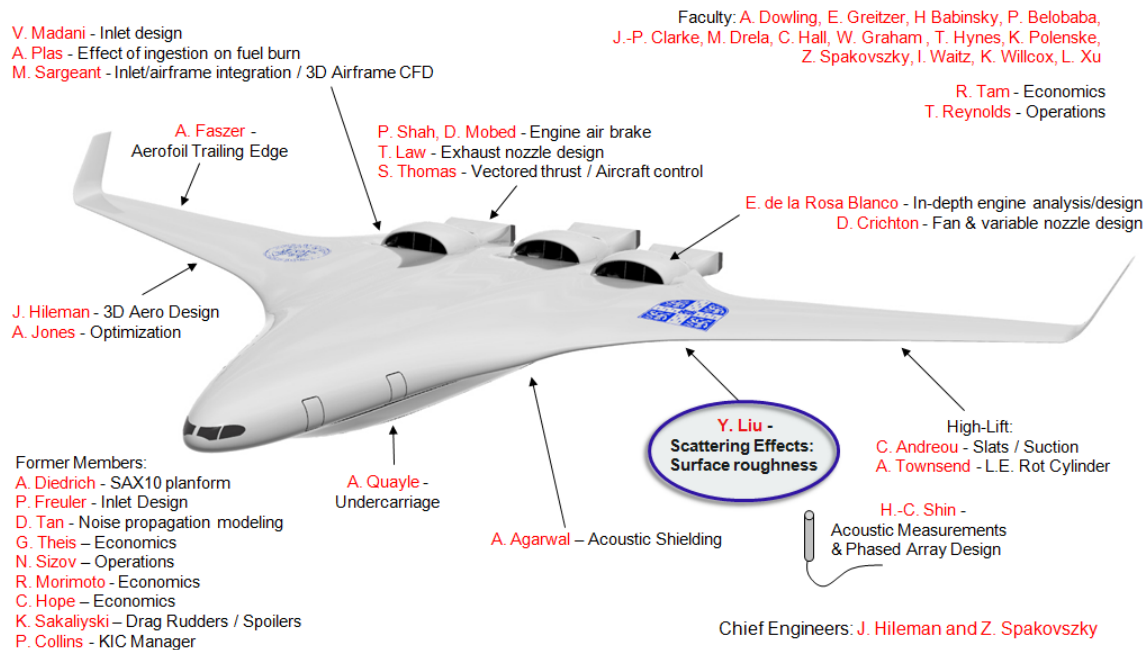


Figure 1.4: The Silent Aircraft eXperimental design SAX-40 and the Cambridge-MIT Silent Aircraft team.

maximum noise level below 63 dBA outside the airport perimeter. Many technical challenges still need to be overcome before the conceptual design could become a reality in the 2030 time frame, but the project has clearly identified these challenges and thus provided a direction for the work needed to address them.

The research team consists of the engine noise, airframe noise, operations and economics groups with about 35 researchers, and the work of this thesis is affiliated within the airframe noise group. Figure 1.4 shows the Cambridge-MIT Silent Aircraft team and the specific work undertaken by the team members. Details of the SAI research can be found in a collection of papers presented in the “Special Session – Towards A Silent Aircraft” [7, 32, 37, 40, 72, 73, 123, 126, 142, 147] at the 45<sup>th</sup> AIAA Aerospace Sciences Meeting and Exhibit, Reno, USA, January 2007.

## 1.2 Motivations and Objectives

Following the TE noise theory of Lilley [97], in a recent research Faszer and Hileman [50, 51] compared previous airfoil self noise models [21, 27, 97, 99] and they found that there is a significant gap of approximately 15–20 dB in noise levels



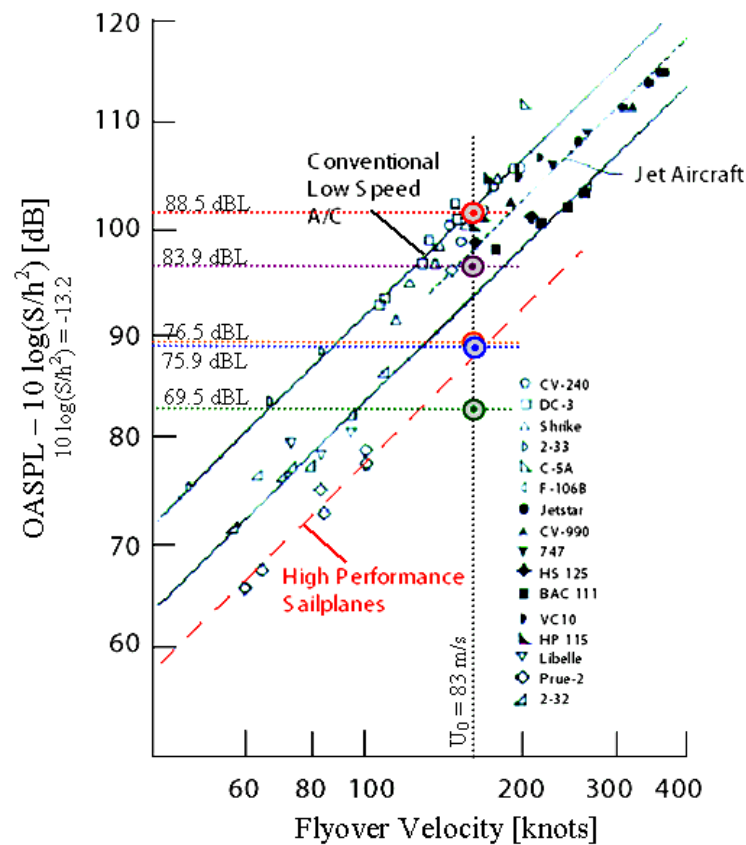


Figure 1.5: Airfoil self noise normalized by wing area and height as a function of velocity (measured data from Fink [54]). Straight lines correspond to the 5<sup>th</sup> power variation predicted by Lilley’s TE noise theory [97]. Comparison of self noise models (Faszer and Hileman [50, 51]):  $\odot$  red, Lilley semi-empirical airframe model [97];  $\ominus$  purple, ESDU empirical airframe model [27] – conventional wing;  $\odot$  orange, modified volume Lilley semi-empirical airframe model [99];  $\ominus$  blue, ESDU empirical airframe model [27] – glider wing;  $\odot$  green, Brooks *et al.* self noise model [21].

between the TE noise and the airfoil self noise generated by a “clean” configuration of jet aircraft. As shown in Figure 1.5, the Brooks *et al.* self noise model [21] (green circle) considers TE noise only, whereas the models marked by the red and purple circles [27, 97] are empirical fits for “clean” configurations and agree well with measurement (Fink [54]). The orange and blue circles [27, 99] almost coincide with the red dashed line which is for the measured data of high performance sailplanes without power equipments.

Figure 1.5 demonstrates a discrepancy between prediction and measurement of self noise from a “clean” configuration. According to previous studies [54],

TE noise was supposed to be the only significant noise source under the “clean” condition, and hence it should be slightly lower than the overall self noise of a “clean” configuration. Consequently, this means increasing interest in other features that may contribute to the 15–20 dB discrepancy.

Panel vibration may give noticeable noise levels [57] in addition to other noise sources that could arise from wing tips and horizontal and vertical tails. In this work, however, we look at another source mechanism, surface roughness noise, whereby energy in the turbulent boundary layer may scatter into radiated sound due to the presence of small surface irregularities. Surface roughness noise has been previously discounted [33], but it may become a potential contributor as major advances have been made in reducing the main sources of airframe noise.

According to Lighthill’s theory of aerodynamic sound [95], turbulent boundary-layer sound from a perfectly smooth flat surface is acoustically equivalent to a distribution of quadrupole sources, and is therefore not important at aircraft approach Mach numbers. However, it has been known that the sound level will be enhanced by turbulent boundary-layer flow over nominally plane surfaces (or over surfaces of large radius of curvature) [77, 78], *e.g.* ship hulls, aircraft wings and fuselages, as illustrated in Figure 1.6. Such surfaces are inevitably not perfectly



Figure 1.6: The rough surface of a transport aircraft.

smooth due to the presence of small surface irregularities, which might arise from discontinuities (rivets, ribs, joints, *etc.*), environmental contamination, paint finishes or imprecise machining during manufacture.

Relatively small amount of surface roughness can produce substantial increases in drag compared to that predicted for the corresponding perfectly smooth boundary [100, 130]. Howe [77] has speculated that surface roughness would also lead to large increases in the strength of the boundary-layer generated noise. Moreover, it is likely that a substantial fraction of the airframe noise of a wide-bodied jet transport airplane flying in the “clean” configuration is associated with the surface roughness generated noise [77].

The overall aim of this research, therefore, is to assess the contribution of surface roughness to airframe noise. We seek to determine whether surface roughness is a significant noise source comparable to TE noise in the far field, and if it is how to quantify the roughness noise for a specific aircraft.

The major objectives of this thesis are:

- To understand the sound generation mechanisms of surface roughness noise through a theoretical approach;
- To develop a theoretical prediction model to approximately quantify the surface roughness noise radiated to the far field;
- To design and conduct experiments to validate the prediction model including some roughness effects on turbulent boundary-layer parameters;
- To apply the validated prediction model to the assessment of surface roughness noise from current aircraft and the SAI design SAX-40;
- To extend the theoretical model to very large roughness elements and obtain preliminary noise predictions;
- To develop a new beamforming algorithm for phased microphone array measurements of dipole sources.

## 1.3 Thesis Outline

The principle underpinning this research is the development of the prediction model for surface roughness noise, including theoretical formulation, numerical calculation, experimental validation and applications to a Boeing-757 sized aircraft wing and the SAX-40 airframe. A range of technical topics is covered in this work, such as sound diffraction, formulations for turbulent boundary-layer pressure fluctuations, flow effects over rough surfaces, wind tunnel experimentation, acoustic measurements in an open jet, and acoustic beamforming algorithm.

The structure of this thesis is as follows:

In Chapter 2, we introduce the classical theories of wave scattering from rough surfaces, and survey the literature relevant to rough-wall turbulent boundary-layer flow and sound generation by surface roughness, including flow effects of turbulent boundary layers over rough walls, turbulent boundary-layer wall pressures, and previous experimental and theoretical work on surface roughness noise.

Chapter 3 is a description of the theoretical modelling of the surface roughness noise of sound scattering. We first formulate the diffraction theory of turbulent boundary-layer roughness noise on the basis of a previous analytical model [77]. The frequency spectrum of far-field radiated roughness noise is derived as an infinite double integral in which the effects of roughness-enhanced turbulent fluctuations are considered. A numerical method is then applied to evaluate the integral and the predicted roughness noise spectrum is compared with those from a previous empirical model [82] and experimental data [71].

In Chapter 4, we present experimental results to validate this prediction model. Acoustic measurements are conducted to compare the measured and predicted roughness noise spectra. Phased microphone arrays are applied to identify the locations and strengths of roughness noise sources. In parallel with the array measurements, theoretical predictions of the noise are processed through the same beamforming algorithm to enable an indirect comparison of array results between measurement and prediction. Hot-wire measurement is also performed to

determine the value of wake strength for the rough-wall boundary-layer thickness formula proposed in Chapter 3, and to validate the skin friction formula [106] for a rough plate.

Following the experimental validation, in Chapter 5 we apply the prediction model to estimate the far-field radiated roughness noise from a Boeing-757 sized aircraft wing with different idealized levels of surface roughness. The relative levels of the roughness noise and TE noise are discussed and explained. A parametric study and a directivity study are also carried out to investigate more features of the roughness noise. We then perform similar roughness noise assessment for the SAX-40 airframe and investigate the maximum allowable roughness levels on the aircraft surface, if the aircraft is to achieve the aggressive noise target.

We then extend the prediction of surface roughness noise in Chapter 6 to model the noise generated by very large roughness elements that protrude out of the boundary layer and enhance the drag fluctuations due to additional vortex shedding from each element. From a brief literature survey on relevant work, a previous analytical model [83] is modified to determine the unsteady drag on the hemispherical element and hence the noise radiation. Based on the modified hemisphere model, the drag-dipole roughness noise is preliminarily predicted and compared with the scattering roughness noise which has been studied in detail in Chapters 3–5.

In Chapter 7, a beamforming correction for identifying dipole sources by means of phased microphone array measurements is proposed and implemented numerically and experimentally. Both the correction techniques to microphone signals and the beamforming algorithm are derived and compared. A new dipole-beamforming algorithm is developed by modifying the basic source definition used for beamforming. Numerical simulations are performed for validating its capability to recover ideal dipole sources. The beamforming correction is then applied to the experiments of realistic aeolian-tone dipoles.

Finally, a summary of the thesis and its conclusions are given in Chapter 8, and future work of improvements and interesting areas is suggested.



# Chapter 2

## Literature Review

**T**HIS chapter presents a review on three relevant topics: (i) wave scattering from rough surfaces, (ii) rough-wall turbulent boundary-layer flow, and (iii) sound generation by surface roughness published in the open literature. Emphasis is laid on the last topic, surface roughness generated boundary-layer noise, which is the primary purpose of this thesis. The source mechanisms of surface roughness noise, *i.e.* the sound scattering mechanism (incoherent and coherent) and the drag dipole mechanism, will be surveyed and discussed systematically. It is pointed out that the incoherent scattering mechanism will be selected for the theoretical modelling of turbulent boundary-layer roughness noise in Chapter 3 and verified experimentally in Chapter 4, and that the drag dipole mechanism will be extended to account for very large roughness elements in Chapter 6.

### 2.1 Wave Scattering from Rough Surfaces

#### 2.1.1 Overview

Real surfaces are never perfectly smooth. The extent to which surface roughness affects wave scattering behaviour is therefore of great interest. This problem has been the subject of study over the last few decades in many diverse branches of physics and engineering, including medical ultrasonics, radar imaging, sonar detection, solid-state physics, optics, astronomy and ultrasonic non-destructive testing [117]. So far the majority of wave scattering problems have concentrated on

two types of waves [116]: (i) electromagnetic wave scattering from rough surfaces for the design of radar systems; and (ii) acoustic wave scattering from rough surfaces for ultrasonic inspection of materials and sonar studies.

There are numerous research papers on wave scattering from rough surfaces, both theoretical and experimental. The most often quoted book on this subject is by Beckmann and Spizzichino [13]. This book concentrates on the Kirchhoff approximation as a method of solution to scalar wave scattering from periodic and random surfaces; and most of the results may equally well be applied to electromagnetic waves or acoustic waves. The second edition of this book discusses experimental observations of the effects of surface roughness, including reflections from the surfaces of the Earth, Moon, Sun and atmosphere layers.

A more recent book of Bass and Fuks [12] considers both perturbation and Kirchhoff theories and deals with more complicated effects such as surface self-shadowing and multiple scales of roughness. Multiple scattering is also considered, through integral equation techniques. A survey of literature specific to acoustic wave scattering from the sea surface was carried out by Fortuin [56], who discusses both random and periodic surfaces. Perturbation and Kirchhoff theories are discussed and model predictions compared with experimental observations of sea surface scattering.

The most recent review on this subject is probably that of Ogilvy [116, 117]. Although published over 15 years ago it is the first comprehensive summary, in one volume, of all the intensive studies up to 1991. The early theories developed for the study of acoustic, elastic and electromagnetic wave scattering from randomly rough surfaces are discussed, and emphasis is placed on those which lead to soluble equations and which are of practical interest, including the perturbation theory and Kirchhoff theory.

Despite the large volume of literature there has been no systematic development of the theory. Most of the theoretical work can be divided into two categories:

- Approximate but tractable, and hence of restricted applicability, *e.g.* the perturbation theory and Kirchhoff theory;



- More rigorous but formal, due to the complicated nature of the resulting expressions, such as integral equation techniques and variational methods.

The approaches easiest to understand physically are probably the perturbation and Kirchhoff approximations. For this reason these two theories are introduced briefly in turn and their strengths and weaknesses are identified and compared.

### 2.1.2 Perturbation theory

In perturbation theory [59] the rough surface is regarded as a perturbation to a smooth plane, and the consequent change in the scattering coefficient, due to the presence of roughness, is calculated. The scattering of waves from surfaces that are only slightly rough may be studied using perturbation theory, which necessitates restrictions on the height  $h(x, y)$  and gradient  $\nabla h(x, y)$  of the surface:

$$k|h(x, y)| \ll 1 \quad \text{and} \quad |\nabla h(x, y)| \ll 1, \quad (2.1)$$

where  $k$  is the modulus of the wavevector of the incident wave. This inequality requires that the height deviation of the surface is everywhere very small compared to the wavelength of the incident wave.

It is assumed that if Equation (2.1) is satisfied, and the surface profile is slowly varying with no discontinuities, then the total field in the presence of a scatterer may be expanded in an infinite series:

$$\psi(\mathbf{r}) = \psi^{\text{inc}}(\mathbf{r}) + \sum_{n=0}^{\infty} \psi^{\text{sc}}(\mathbf{r}), \quad (2.2)$$

where  $\psi^{\text{inc}}(\mathbf{r})$  is the incident wave field and  $\psi^{\text{sc}}(\mathbf{r})$  is the  $n$ th-order approximation to the scattered field. The term  $n = 0$  is given by the scattered field which would exist if the surface were smooth (the unperturbed solution). It is also assumed that if the boundary conditions obeyed on the rough surface are of the form

$$f(x, y, z)|_{z=h(x,y)} = 0, \quad (2.3)$$

then they may be expanded in a Taylor series about the mean plane  $z = 0$ , of the form

$$f(x, y, z)|_{z=h(x,y)} = f(x, y, z)|_{z=0} + h \frac{\partial f}{\partial z} \Big|_{z=0} + \frac{h^2}{2} \frac{\partial^2 f}{\partial z^2} \Big|_{z=0} + \dots, \quad (2.4)$$

where  $f(x, y, z)$  is, for example, the pressure (acoustics) or stress components (elasticity) on the rough surface.

The accuracy of perturbation theory depends on the validity of the restrictions given by Equation (2.1) and the order of terms retained in the expansion of Equation (2.4). The theory can take some account of multiple scattering effects if terms of order  $h^2$  are retained. However, other effects (*e.g.* shadowing and multiple scattering events of a higher order than the theory) will combine to reduce the accuracy of the perturbation approach. These effects will become more marked as the angles of incidence and scattering increase away from the mean surface normal. No applications of this theory go beyond the use of the second-order perturbation theory which is usually an adequate level of approximation. The range of surfaces for which this approximation is adequate is limited, due to the restrictions on height and gradient.

### 2.1.3 Kirchhoff theory

Kirchhoff theory, also known as tangent plane theory, is the most widely used theory in the study of wave scattering from rough surfaces. This is perhaps due primarily to two reasons: the theory has an easily understandable physical basis and leads to relatively simple analytical expressions for scattered field amplitudes.

A simple geometrical construction has been used to determine an inequality which must be satisfied by the surface (see, for example, Bass and Fuks [12]):  $ka \cos^3 \theta_1 \gg 1$ , where  $a$  is the radius of curvature of the surface and  $\theta_1$  is the incidence angle. This essentially states that the deviation of the surface from flat must be small compared with the wavelength of the incident wave. A restriction is therefore placed on the radius of curvature of the surface that must have a height profile with no rapid changes in the gradient. No explicit restrictions on the *magnitude* of the height or gradient are required.

When the surface of the scatterer,  $S_0$ , is closed (*i.e.* the surface encloses a finite volume) then the scattered field at any observation point  $r$  can be written in terms

of the field quantities on the surface using the Helmholtz scattering formula [117]

$$\begin{aligned}\psi^{\text{sc}}(\mathbf{r}) &= \psi(\mathbf{r}) - \psi^{\text{inc}}(\mathbf{r}) \\ &= \int_{S_0} \left[ \psi(\mathbf{r}_0) \frac{\partial G(\mathbf{r}, \mathbf{r}_0)}{\partial \mathbf{n}_0} - G(\mathbf{r}, \mathbf{r}_0) \frac{\partial \psi(\mathbf{r}_0)}{\partial \mathbf{n}_0} \right] dS_0,\end{aligned}\quad (2.5)$$

where the integral is over  $S_0$ , and  $\mathbf{n}_0$  is the unit outer normal to  $S_0$ .

All quantities in Equation (2.5) are known except for the total pressure (or potential)  $\psi(\mathbf{r}_0)$  and its gradient  $\partial\psi(\mathbf{r}_0)/\partial\mathbf{n}_0$  on the scattering surface. One of these is known from the boundary condition satisfied at the surface, and the other is specified with the aid of the Kirchhoff approximation. If the pressure is to be specified, the total pressure on the surface is then given by

$$\psi(\mathbf{r}_0) = [1 + R(\mathbf{r}_0)]\psi^{\text{inc}}(\mathbf{r}_0). \quad (2.6)$$

If the gradient of the pressure is to be specified, we have that

$$\frac{\partial\psi(\mathbf{r}_0)}{\partial\mathbf{n}_0} = [1 - R(\mathbf{r}_0)] \frac{\partial\psi^{\text{inc}}(\mathbf{r}_0)}{\partial\mathbf{n}_0}, \quad (2.7)$$

where the reflection coefficient  $R(\mathbf{r}_0)$  is assumed to depend on position along the surface. By substitution of Equation (2.6) or (2.7) into Equation (2.5), together with the boundary conditions, an expression is obtained for the scattered field at some point  $\mathbf{r}$  in terms of known quantities. This is the general solution to the scattering problem in the Kirchhoff approximation.

Kirchhoff theory provides an approximation to the scattered field on the surface of a scatterer. The physical basis for this approximation is obvious: any point on the rough surface is assumed to behave as if the surface were locally flat, so that the reflection coefficient is equal to that of an infinite plane passing through that point and parallel to the local surface tangent. Kirchhoff theory is therefore exact for surfaces that are infinite, smooth and planar. For all other scatterers the theory is approximate and suffers from two shortcomings: it is not self-consistent and does not conserve energy [117]. The former means that if Kirchhoff theory is used to calculate the field away from a scatterer and this field is then specialized to points on the scatterer then the surface fields do not satisfy the theory. Lack of energy conservation suggests that propagating modes such as surface waves are ignored

by Kirchhoff theory. The accuracy of Kirchhoff theory will be affected both by the roughness of the surface and by the shape and dimensions of the mean surface. Unlike the perturbation approach it is difficult to quantify the inherent accuracy of Kirchhoff approximation.

#### 2.1.4 Comparison and further considerations

The results from perturbation theory and Kirchhoff theory can be compared for those surfaces for which the limitations of both methods hold. It is generally stated in the literature that results from these two methods do not agree due to the very different physical principles on which they are based. However, the two theories can lead to the same predictions for coherent and diffuse field intensities. This would be for surfaces of small height and with a correlation length satisfying  $\lambda_0 > \lambda$ .

A good discussion on the comparison of the two theories is given by Chapman [24]. This piece of work has demonstrated neatly that the perturbation and Kirchhoff approaches generally do not lead to the same result for the reflected coherent signal except in the limit of surfaces with infinite correlation length (*i.e.* regular patterns or smooth surfaces). Furthermore, agreement between the two methods improves as the incident wave approaches the normal to the mean plane. In addition, the general forms of the diffusely scattered field agree for both first-order perturbation theory and Kirchhoff theory in the small roughness limit.

Despite being one of the early developed methods, Kirchhoff theory is undoubtedly still the most often quoted and applied theory in the literature of recent times, in both theoretical and experimental studies. The reason for this must lie in the obvious physical basis for the approximation and the ease with which the results may be calculated. Application of perturbation theory has been much more limited, probably due to the stricter conditions on the surface to which this theory is applicable. In addition the effects of roughness for these surfaces must be small due to the restrictions on height and gradient.

Since the early introduction of the above theories various refinements have been introduced, including self-shadowing (see, for example, Wangner [153]). Here an

estimate is obtained for the fraction of surface not insonified by the wave, due to other parts of the surface acting as a screen. The problem of multiple scale roughness is considered in a small portion of literature. In general it is assumed that the large scale may be treated using Kirchhoff theory and that perturbation theory may be used for the small scale roughness [12].

In addition, the effects of multiple scattering become important in the case that the surface roughness increases and the incidence angle increases away from the surface normal [75]. The boss (protuberance) model is probably the most promising multiple scattering theory in which the surface is modelled as a random array of bosses of known shape and known scattering behaviour. The advantage of this model, which does not appear to describe true rough surfaces realistically, lies in its ability to include the effects of multiple interactions between the bosses.

Other approaches describe a rough surface as an array of planar facets or randomly distributed point scatters with reflection properties known. Integral equations is then formulated, from the Helmholtz scattering formula, for the scattered field on the rough surface, which makes an improvement on Kirchhoff approximation [98]. Variational techniques have been used to obtain optimal estimates to the scattering coefficients [67].

However, the theories on wave scattering from rough surfaces are still far from complete. No model provides a full description of the processes involved, and each model is valid for certain regimes of surface roughness only. These models are, in general, a compromise between the need for accurate predictions and the requirement for reasonable mathematical simplicity.

More recently the use of numerical simulation methods has become feasible with the advantage of evaluating expressions which are analytically intractable, often those involving statistical averages. These methods may be applied both to examine the accuracy of approximate techniques and to simulate more realistic scattering experiments. While numerical simulation methods are necessarily computationally intensive they are probably the most hopeful way forward for further advances in solving rough surface scattering problems [117].

## 2.2 Rough-Wall Turbulent Boundary-Layer Flow

### 2.2.1 Flow effects over rough walls

The problem of turbulent boundary-layer flow over rough walls has been studied since the early works of Hagen [66] and Darcy [36], who were concerned with pressure losses in water conduits. Most fluid dynamics and turbulence books include material on surface roughness, and the ones by Schlichting [130] and Duncan *et al.* [42] are still useful references. The most recent survey is that of Jiménez [86] in 2004 who reviewed the experimental evidence on turbulent flow over rough walls.

The most important effect of surface roughness is the change of the mean velocity profile near the wall, with the consequent modification of the skin friction coefficient. The best known early experiments on this aspect are the ones by Nikuradse [115], who studied pipes roughened with carefully graded, closely packed sand grains. He found that the logarithmic velocity distribution for the mean velocity profile of smooth walls could still be used in the rough-wall boundary layer, with the same value of the Kármán constant,  $\kappa_0 = 0.4$ , and he expressed the velocity profile of rough walls as

$$\frac{u}{u_\tau} = \frac{1}{\kappa_0} \ln \left( \frac{y}{k_s} \right) + h \left( \frac{k_s u_\tau}{\nu} \right), \quad (2.8)$$

where  $u_\tau$  is the friction velocity, and  $h$  is some function of the roughness Reynolds

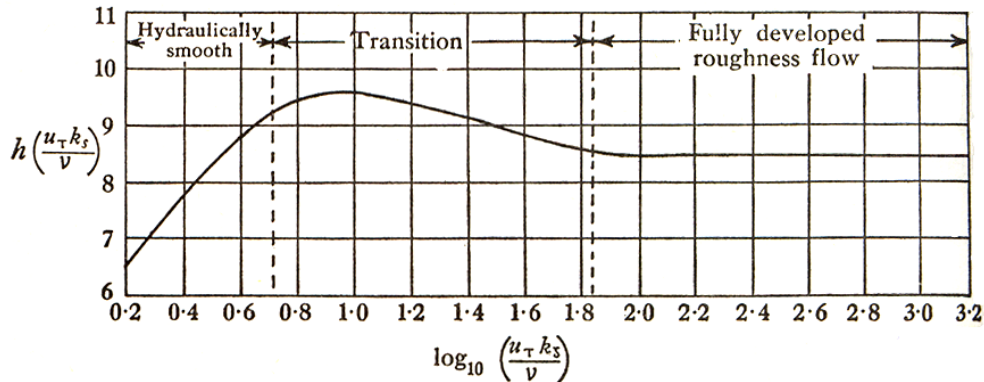


Figure 2.1:  $h$  as a function of roughness Reynolds number,  $Re_\tau = k_s u_\tau / \nu$  (Duncan *et al.* [42]).

number,  $Re_\tau = k_s u_\tau / \nu$ . Equation (2.8) has become the definition of the “equivalent” or “effective” sand roughness height  $k_s$ . The function  $h$  as determined by these experiments is shown in Figure 2.1.

It is found that for values of  $k_s u_\tau / \nu$  less than about 5,

$$h(k_s u_\tau / \nu) = 2.5 \ln(k_s u_\tau / \nu) + 5.5, \quad (2.9a)$$

$$\frac{u}{u_\tau} = 2.5 \ln\left(\frac{u_\tau y}{\nu}\right) + 5.5, \quad (2.9b)$$

as for a completely smooth pipe. This is because the surface roughness is entirely immersed in the viscous sublayer that it does not affect the flow in the pipe or the surface friction. The surface is then referred to as *hydraulically smooth* or *aerodynamically smooth*.

On the other hand, for values of  $k_s u_\tau / \nu$  greater than about 70,

$$h(k_s u_\tau / \nu) = \text{const.} = 8.5, \quad (2.10a)$$

$$\frac{u}{u_\tau} = 2.5 \ln\left(\frac{y}{k_s}\right) + 8.5. \quad (2.10b)$$

In this case the flow and surface friction are independent of the roughness Reynolds number. The flow is then referred to as *fully developed roughness flow*.

The intermediate region (*i.e.*  $5 < k_s u_\tau / \nu < 70$ ) is referred to as *transitional roughness* in which both viscous friction and roughness form drag contribute significantly to the surface drag.

The effects of rough walls on turbulent boundary layers are controlled by two dimensionless parameters [86]. The roughness Reynolds number  $Re_\tau$  quantifies the effect of the roughness on the buffer layer. The behaviour of transitionally rough surfaces with low  $Re_\tau \lesssim 50$  depends a lot on their geometries, ranging from the gradual transitions of irregular surfaces, to the sharper ones in more uniform geometries. A second parameter is the blockage ratio of the boundary-layer thickness to the roughness height,  $\delta/k_s$ , which determines whether a logarithmic layer survives. In flows with  $\delta/k_s \lesssim 50$ , the effect of surface roughness extends across the boundary layer, and is also variable.

## 2.2.2 Turbulent wall pressures

### 2.2.2.1 Wavenumber-frequency spectrum

A turbulent boundary layer induces a fluctuating pressure on the underlying wall. When the wall is locally plane and the fluctuations are regarded as statistically stationary in time, these characteristics are usually expressed in terms of the wall pressure wavenumber-frequency spectrum  $P(\boldsymbol{\kappa}, \omega)$ , which is the Fourier transform of the space-time correlation function of the wall pressure. Theoretical models of  $P(\boldsymbol{\kappa}, \omega)$  generally assume the flow to be homentropic of low Mach number over a flat, rigid wall with no mean pressure gradient.

Howe [81, 82] has discussed the wall pressure wavenumber-frequency spectrum and the significance of various “wavenumber domains”. Following his work, the characteristic shape of the wavenumber-frequency spectrum at low Mach numbers is illustrated in Figure 2.2 for a fixed frequency satisfying  $\omega\delta/U \gg 1$ . The strongest components occur in the neighbourhood of the “convective ridge” centred on  $\kappa_1 = \omega/U_c$ ,  $\kappa_3 = 0$ , where  $U_c$  is the convection velocity. For a homogeneous flexible

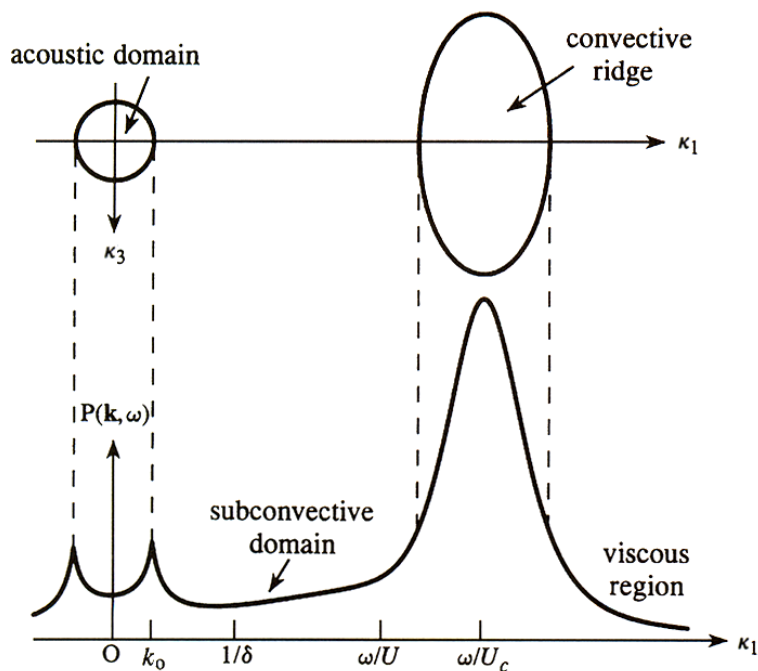


Figure 2.2: Turbulent boundary layer and wall pressure wavenumber-frequency spectrum at low Mach numbers when  $\omega\delta/U \gg 1$  (Howe [82]).



surface, however, the strongest coupling between the wall and flow is usually attributed to longer wavelength, “subconvective” components of the wall pressure. These occupy the low-wavenumber region

$$|k_0| < \kappa_1 \ll |\omega|/U_c, \quad (2.11)$$

where the spectral levels are typically 30–60 dB below the convective ridge at low March numbers [82]. Beyond the convective ridge, say for  $\kappa_1 > u_\tau/30\nu$ , the scale of the motion is small enough to be controlled by viscosity, which governs the ultimate decay of the spectrum [111]. The region  $\kappa_1 < |k_0|$  is called the “acoustic domain”, and the corresponding pressure fluctuations are actually sound waves which will be discussed in Section 2.3.1.

### 2.2.2.2 Empirical models

Present theoretical work on turbulent boundary-layer flows is still not adequate to calculate the wall pressure fluctuations directly. Immense numerical simulations have been carried out (Kim *et al.* [91], Choi and Moin [28], Spalart [141], Coleman [30], *etc.*) and they can provide accurate quantitative information for low-Reynolds-number flow in simple geometries. A review on the development of turbulence simulations until 1984 can be found in Rogallo and Moin [127], and the review by Moin and Mahesh [109] concentrated on changes in Direct Numerical Simulation (DNS) since that time. However, much work still remains before sufficiently reliable statistics for high-Reynolds-number flow and complicated geometries become realistic in the long term.

Therefore, the main information on wall pressure fluctuations of turbulent boundary layers is obtained through experimental measurements (Willmarth [157, 158], Willmarth and Wooldridge [160], Blake [17], Bhat [15], Bull and Thomas [22], Efimtsov [43], Schewe [129], *etc.*) which have been reviewed recently by Ahn [4]. There have been many attempts made to provide empirical models for the wavenumber-frequency spectrum of the pressure fluctuations which yield the best agreement with experiments. Several representative empirical models  $\tilde{\Phi}_p(\boldsymbol{\kappa}, \omega)$  for the smooth-wall wavenumber-frequency spectrum  $P(\boldsymbol{\kappa}, \omega)$  were developed by

Corcos [31], Efimtsov [43], Smol'yakov and Tkachenko [140], Ffowcs Williams [52] and Chase [25, 26]. These empirical models contain adjustable coefficients whose values are fixed by comparison with experimental data in both the convective and low-wavenumber domains. A brief description of these empirical models is provided in Appendix A, and detailed discussions can be found in Graham [63] and Ahn [4].

Sufficient data are available, derived principally from wind-tunnel experiments at low Mach numbers, to permit the formulation of empirical representations of the convective region. Nevertheless, so far there is no satisfactory theoretical understanding of the characteristics of the spectrum in the subconvective and acoustic domains [79] for which reported properties often vary significantly between different experiments. Therefore, there are discrepancies between the various models of  $\tilde{\Phi}_p(\boldsymbol{\kappa}, \omega)$ , especially in low wavenumber regions. Through comparison of the wavenumber-frequency spectra, these discrepancies have been examined by Graham [63] and then further analysed by Ahn [4].

To sum up, in spite of several decades of intensive experimental study, the reliability of the various models for the pressure fluctuations of turbulent boundary layers remains controversial, and no single accepted model covering all wavenumbers yet exists. As pointed out by Howe [81], the empirical representations of  $P(\boldsymbol{\kappa}, \omega)$  in the convective region can probably be used with confidence, but unqualified application of formulae in the low-wavenumber and acoustic domains cannot be recommended.

### 2.2.2.3 Effects of surface roughness

The above empirical models are for the turbulent boundary-layer flow over smooth walls. However, as pointed out by Blake [18], at low Mach numbers the validity of  $P(\boldsymbol{\kappa}, \omega)$  may be extended to rough wall boundary layers (provided the characteristic roughness height  $k_s \ll \delta$ ) by using suitably augmented values of the various coefficients (e.g. the friction velocity  $u_\tau$ ) in these models to compensate for the increased levels of Reynolds stress fluctuations. Howe [81] has discussed the

surface roughness effects on wall pressure wavenumber-frequency spectrum, and he commented that the above procedure gives satisfactory predictions in the convective region, but takes no account of modifications produced by scattering of convective pressures by the roughness elements, which can have a significant influence, however, on the form of the spectrum in the low-wavenumber and acoustic domains through the redistribution of wall pressures.

Indeed, it has been argued [71, 76–79] that, except at low frequencies, the aerodynamic sound generated by boundary-layer flow over a rough wall is produced primarily by scattering of the convective wall pressures. According to Hersh [71], the intensity of the roughness noise radiation can be expressed in terms of the values of  $P(\kappa, \omega)$  in the acoustic domain, and this implies that surface roughness must produce substantial differences between the smooth- and rough-wall pressure spectra at acoustic wavenumbers, and presumably also in the adjacent subconvective region.

Howe [79] then considered the influence of surface diffraction by the roughness elements beneath a turbulent boundary layer, and found that the rough-wall pressure spectrum differs from that on a smooth wall on two counts: (i) the strengths of the turbulence Reynolds stresses that are ultimately responsible for the pressure fluctuations are increased by the action of surface roughness; and (ii) the near fields produced by those enhanced pressure sources are redistributed in the wavenumber plane by diffraction by the roughness elements. His analysis indicates that surface diffraction is significant only in the low-wavenumber and acoustic domains, and is progressively more important as the frequency increases.

Based on the smooth-wall formula by Chase [26], an empirical model was also proposed by Howe [79] to formulate the rough-wall pressure spectrum, which incorporates the effects of interstitial flows and wake formation by large roughness elements. However, it is unable to fix the values of all adjustable parameters due to insufficient experimental data so far. The fixed parameters determine the shape of the spectrum, but not its absolute level. Further measurements are therefore needed to complete the specification of this empirical model.

## 2.3 Sound Generation by Surface Roughness

### 2.3.1 General introduction

Intense surface pressure fluctuations beneath a turbulent boundary layer generate sound and structural vibrations. Sound is produced directly by aerodynamic sources within the fluid and indirectly by the interaction of hydrodynamic pressures and the surface vibrations with discontinuities of the wall (ribs, rivets, joints, *etc.*) [18, 26]. At low subsonic Mach numbers, the phase velocity  $\omega/\kappa_1$  of surface pressures in the convective domain is subsonic, and these pressures therefore decay rapidly with distance from the wall and do not correspond to sound waves. However, convective pressures can generate sound (and structural vibrations) when the wall is rough or has other discontinuities at which convective energy is scattered. In the acoustic domain  $\kappa_1 < |k_0|$ , the phase velocity is supersonic; here disturbances propagate to the far field and wall pressure fluctuations are actually sound waves produced directly either by boundary-layer quadrupoles [95] or by the scattering of convective pressures and flow-induced structural motions.

Howe [81, 82] studied the sound produced by turbulent flow over a rigid wall (boundary-layer noise), and obtained the acoustic frequency spectrum of the smooth-wall boundary-layer noise. At low Mach numbers it is probable that the predicted levels by the smooth-wall formula will fall far below observed levels. Howe argued that this is because in practice the wall is inhomogeneous owing to the presence of small irregularities. In the absence of such irregularities, sound is generated by a relatively inefficient mechanism, “quadrupole” sound sources varying as  $U^8$  [18, 95], in which the wall behaves predominately as a passive reflector of the generated sound.

For an inhomogeneous wall, surface roughness first enhances the turbulence production especially in the near wall region [130] and presumably the intensity of quadrupole noise radiated directly from the flow. However, sound is also produced indirectly by “dipole” sources<sup>†</sup> associated with the scattering of energy from the

---

<sup>†</sup>The dipole source has a relative efficiency that is nominally of the order  $1/M^2 \gg 1$  to the quadrupole source [35].

convective (hydrodynamic) region of the wall pressure fluctuations and by the scattering of turbulence excited structural modes. This sound is therefore referred to as *surface roughness noise* in this thesis (or *rough-wall boundary-layer noise* in some literature).

Because the intensity of surface roughness noise varies as  $U^6$  it is likely to dominate in low-Mach-number applications (e.g. water flows). In such applications the acoustic wavelength will likely be large compared to the boundary layer scales, and these long wave motions can couple to the supporting structure of the flow surface and hence induce vibration [64]. This sound could become a potential source contributing to the noise from low-speed vehicles, such as ships, submarines and approaching aircraft. Therefore it is critical to understand surface roughness noise for prediction purposes in vehicle design and operation.

Below is a review and discussion on what is known about the fundamental characteristics of this noise source. Unlike the large amount of research efforts in wave scattering from rough surfaces and rough-wall turbulent boundary-layer flow, previous studies on sound generation by surface roughness are comparatively limited. Recently, Grissom *et al.* [64] reviewed the theoretical and experimental work on this topic, relying heavily on Blake [18] which covers much of the relevant literature in this area. They commented that in total only a handful of studies have been performed and their results do not paint a unified picture. There is a significant disagreement over its scaling and hence the source mechanisms. In the review we commence with a brief introduction on previous experimental measurements of surface roughness noise and then focus on the theoretical modelling of its possible source mechanisms. Detailed scaling analysis can be found in recent publications of Grissom *et al.* [64, 65] and Glegg *et al.* [61].

### 2.3.2 Experimental measurements

The experimental measurements of surface roughness noise are technically difficult because its spectral levels tend to be very low and thus difficult to detect from background noise or other sources. Few researchers have attempted to study

experimentally the far-field radiated noise from rough-wall boundary layers. One of the early work was published by Skudrzyk and Haddle [136] in 1960. In this study, they measured the noise generated by flow around a rotating cylinder immersed in a water tank using large-diameter hydrophones mounted on the tank wall. Increases in the overall sound pressure level (OASPL) with the cylinder speed raised to the power of 6, 10.3 and 12 were recorded for a painted cylinder surface and one coated with 60 and 180 grit roughness. The first of these results is consistent with a dipole source and is supported by subsequent studies.

Chanaud [23] then measured the noise generated in the flow around a spinning disk mounted inside an anechoic chamber. This study tested a smooth disk, along with disks roughened with 0.032 inch grain sandpaper on the edges and disks with roughened rings on the surface. Both roughened disks produced significantly greater high-frequency noise ( $> 3$  kHz) and the OASPL recorded from the roughened-ring disk was found to vary as the 6<sup>th</sup> power of the edge speed. Chanaud attributes part of the high-frequency noise to shear stress dipoles enhanced by the surface roughness, but his directivity measurements show evidence of a dipole perpendicular to the disk surface that is not easily accounted for from this mechanism.

Cole [29] studied the radiated noise from boundary-layer flow over smooth walls and walls roughened by strips and areas of 40 and 80 grit sandpaper in an anechoic chamber by using a directionally sensitive microphone system. Many of the noise spectra measured by Cole show the roughness enhanced noise levels by about 3 dB. Cole attempted to scale these results as a dipole or quadrupole and found that both scalings applied to some degree.

In 1983 Hersh [71] measured the sound radiated from the open ends of two internally roughened pipes produced by a low Mach number stream of turbulent air exhausting from the pipe. In the first experiment, measurements with a smooth pipe wall showed the OASPL to vary as the 8<sup>th</sup> power of the flow velocity, consistent with jet noise emitted from the pipe exhaust. Measurements with walls roughened with 40 grit sandpaper showed a 6<sup>th</sup> power variation, consistent with a dipole source. Hersh contends that this dipole source is produced specifically by the fluctuating

shear stress promoted by roughness. In the second and more comprehensive experiment, Hersh found that transitionally rough surfaces ( $k_s u_\tau / \nu < 50$ ) consisting of 80, 100 and 120 grit sandpaper produced fairly low amplitude sound at high frequencies ( $> 10$  kHz), while fully rough surfaces ( $k_s u_\tau / \nu > 400$ ) produced significantly more sound ( $\sim 15$  dB) over the full measured frequency range. Variations in the OASPL with flow speed suggest a dipole source and correlate well when normalized on  $(\rho/c)^2 u_\tau^6$ .

The most recent, and systematic experimental study was reported by Grissom *et al.* [65] in 2007 in which the noise generated by turbulent flow over rough surfaces was measured in a wall-jet facility. A number of surface roughness from standard aluminum oxide sandpaper (40–220 grit) and heavier duty floor sanding sheets (20–80 grit) was tested by using three microphones in a triangle. One of the objectives of this study was to infer the scaling through determining the form and intensity of the roughness noise spectrum. A nondimensional frequency based on outer flow variables,  $\omega \delta^* / U_c$ , was found to normalize all measurements of roughness noise, and the amplitude scaling revealed the presence of two regions split at  $\omega \delta^* / U_c = 20$ . In the low-frequency range the acoustic spectra are best modelled on the maximum turbulent velocity fluctuations to the 5<sup>th</sup> power, while the high frequency region is controlled by the convective velocity to the 7<sup>th</sup> power. Grissom *et al.* [65] contend that this suggests the existence of a low-frequency region controlled by a scattering, dipole-type source mechanism due to the surface roughness, while the high-frequency region is dominated by a quadrupole source due to the roughness-enhanced boundary-layer turbulence.

Apart from the above far-field studies, there were at least two studies of the near-field characteristics of surface roughness noise by Farabee and Geib [49] and Smol'yakov [139] which have been reviewed by Grissom *et al.* [64].

### 2.3.3 Theoretical modelling

The majority of the theoretical work on surface roughness noise and its source mechanisms was carried out by Howe who has developed a diffraction theory

distributed in a series of publications [76–79, 81, 82]. A very recent contribution to the roughness noise mechanism was made by Glegg *et al.* [61] in 2007. Basically, two alternative source mechanisms for the surface roughness generated boundary-layer noise have been identified:

- (i) **Sound Scattering:** The first mechanism is based on the concept that the hydrodynamic pressure fluctuations in the boundary layer are scattered into acoustic waves by the roughness elements. This mechanism can be divided into incoherent scattering and coherent scattering dependent on discrete or continuous surface roughness.
- (ii) **Drag Dipole:** The alternative theory is based on the concept that each individual roughness element radiates sound as a drag dipole source due to the enhanced shear stress at the wall or surface pressures.

These two mechanisms are dependent on the size of the roughness elements relative to the length scales of the boundary-layer velocity profile regions, as illustrated in Figure 2.3. Previous theoretical work on each mechanism will be introduced below separately.

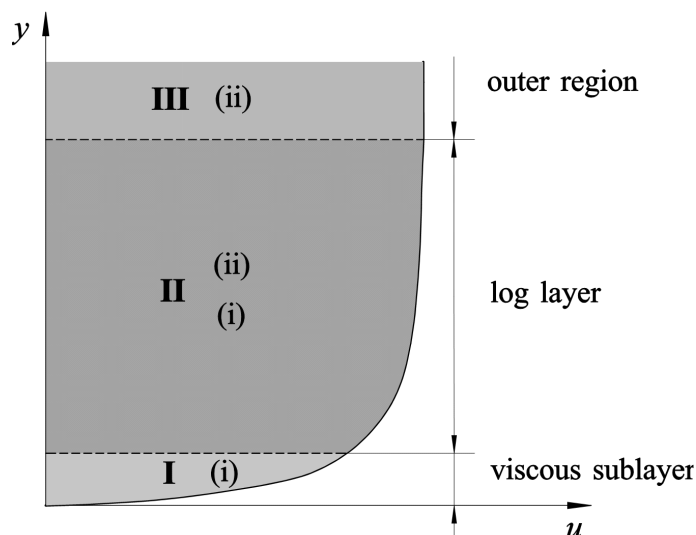


Figure 2.3: Boundary-layer velocity profile regions and their relationships with the source mechanisms of surface roughness noise. Regions: I – viscous sublayer, II – logarithmic layer, III – outer region. Source mechanisms: (i) sound scattering and (ii) drag dipole.



### 2.3.3.1 Sound scattering (incoherent)

The source mechanism of sound scattering (incoherent) was firstly proposed by Howe [77] in 1984 and applies to the roughness elements contained in the boundary-layer regions I and II (see Figure 2.3). It assumes that the near-field hydrodynamic disturbances in a turbulent boundary layer interact with the surface irregularities and produce radiated sound by scattering at the roughness elements in isolation. The turbulent near field on each roughness element would then be uncorrelated and the sound generation from multiple roughness elements is obtained by incoherently summing the contribution from each individual element. The sound power from this source is therefore proportional to the number of roughness elements per unit area.

Inspired by the measurements of Hersh [71] and his conclusion on the dipole nature of roughness generated noise, Howe [78, 79, 81, 82] developed a theory for the wall pressure spectrum and radiated noise generated by surface roughness. In the earliest work, Howe [77] presented an analytical model on the generation of sound by turbulent boundary-layer flow over a rough wall, and speculated that the roughness generated noise would be a substantial fraction of the airframe noise of an airplane flying in the “clean” configuration. In this theory and the subsequent work [78, 79, 81, 82], Howe considers the idealized case in which the rough surface is invariably modelled by randomly distributing rigid, hemispherical bosses over an otherwise smooth plane. It is assumed that the turbulent boundary-layer roughness noise is produced primarily by the diffraction of the turbulent hydrodynamic near field (pseudo-sound) by the roughness bosses.

The analysis is according to the classical, ideal fluid diffraction theory so that the viscous stresses on the wall can be disregarded. This approximation is likely to be adequate for the roughness Reynolds number  $Re_\tau = k_s u_\tau / \nu > 10$ , where the equivalent roughness height  $k_s$  is determined by fitting a conventional logarithmic curve to the mean boundary-layer velocity profile [130]. In this case the roughness bosses protrude beyond the viscous sublayer (Region II), and this is consistent with the usual criteria (namely  $Re_\tau > 5$ ) for a surface to be hydraulically rough.

An important limitation of the above theoretical approach [77] lies in the fact that it is unable to account for local effects such as the formation of wakes (vortex shedding) by the roughness elements, which creates new noise sources during the interaction of the turbulence with the wall. A first approximation is therefore obtained by assuming that all of the significant turbulent pressure sources lie above the roughness elements, and Howe anticipates that this approximation is only likely to be adequate for surfaces whose roughness elements do not penetrate beyond the buffer zone into the fully developed turbulent region of the flow<sup>†</sup>. In this case the acoustic frequency spectrum  $P_R(\boldsymbol{x}, \omega)$  of the far-field radiated roughness noise can be expressed as an infinite integral in terms of the smooth-wall wavenumber-frequency spectrum  $P_s(\boldsymbol{\kappa}, \omega)$  of the hydrodynamic pressure fluctuations on a control surface located at a distance  $R$  from the mean wall plane, where  $R$  is the characteristic height of the roughness elements.

There have been various published empirical models for the smooth-wall wavenumber-frequency spectrum  $\tilde{\Phi}_p(\boldsymbol{\kappa}, \omega)$ , as introduced in Section 2.2.2.2. These models can be related to  $P_s(\boldsymbol{\kappa}, \omega)$  that is directly connected to the cross-spectral density of the Reynolds stresses, and so can be expressed in terms of  $u_\tau$  and  $\delta$  since the fluctuating Reynolds stresses scale on  $\rho u_\tau^2$  and the distance they occupy from the wall scales on  $\delta$ . For moderately rough surfaces, we make the same assumption as Howe [77] in this thesis that the principal differences in the features of the wall pressure spectrum from those of the wall pressure spectrum on a smooth wall are accounted for by the differences in  $u_\tau$  and  $\delta$ . This is expected to be a good approximation especially in the vicinity of the convective ridge [25]. Therefore in this approach the rough-wall wavenumber-frequency spectrum may be approximated by a smooth-wall formula provided that  $u_\tau$  and  $\delta$  are increased to compensate for the enhanced surface drag and turbulence production [130].

The integral of  $P_R(\boldsymbol{x}, \omega)$  was conventionally evaluated by means of asymptotic approximation [77, 79] based on the wall pressure spectrum being sharply peaked in the vicinity of the convective ridge. A series of empirical formulae for  $P_R(\boldsymbol{x}, \omega)$  were

---

<sup>†</sup>In fact, Howe's theory of sound scattering can be applied to roughness elements that lie in the logarithmic layer (Region II). It has been confirmed [61] that the effect of shear stress fluctuations due to vortex shedding is negligible compared to the sound scattering mechanism (see Section 2.3.3.3).

also proposed by Howe [79, 81, 82] in which the values of adjustable coefficients were partially estimated by fitting to the noise spectra of a mixture of transitional and full roughness measured by Hersh [71]. These coefficients fix the shape of the roughness noise spectrum, but it was not possible to derive the absolute level of  $P_R(\boldsymbol{x}, \omega)$  from the Hersh data due to the unknown effects of acoustic refraction by the free-jet shear layers downstream of the nozzle exit. One primary objective of the theoretical work in this thesis, therefore, is to develop a reliable model to predict the far-field radiated roughness noise in both spectral shape and absolute level.

Howe [78] then extended the inviscid diffraction theory to ascertain the possible influence of viscous wall stresses on the diffraction mechanism. In these circumstances the roughness elements are assumed to be sufficiently small and contained entirely within the viscous sublayer (*i.e.* Region I,  $Re_\tau < 5$ ) that the viscous “no-slip” condition at the wall may be applied iteratively on the mean plane of the wall. By this means it is concluded that over the whole frequency range in which roughness noise is expected to be significant, viscous effects increase the levels of the radiated sound by 2 or 3 dB at the most.

### 2.3.3.2 Sound scattering (coherent)

If the surface roughness can be considered as a continuous field instead of composed of discrete roughness elements, the incoherent scattering mechanism may underestimate the total sound field. Morse and Ingard [112] presented a formulation for acoustic scattering by rough surfaces with continuous roughness elements. Grissom *et al.* [64] recently presented that this theory can be modified to apply to the scattering of hydrodynamic pressure fluctuations by a rough surface. The coherent scattering mechanism was then reworked by Glegg *et al.* [61] in 2007 for the roughness elements protruding into the logarithmic layer (Region II in Figure 2.3). Their work is based on Morse and Ingard’s theory and the primary change is that the incident acoustic wave is replaced by a hydrodynamic pressure perturbation.

In this theory, Glegg *et al.* focused on the formulation of the frequency scaling of radiated roughness noise spectrum, and hypothesized that the frequency

scaling should be based on the correlation length scale of the roughness element distribution instead of the roughness height as assumed by Howe [79, 81, 82]. The coherent scattering mechanism therefore has a different scaling from the incoherent one proposed by Howe, although Glegg *et al.* estimated that the dimensional peak frequency is approximately the same in both cases. However, the spectral peak levels of both incoherent and coherent mechanisms appear very similar.

Unlike Howe's diffraction theory [77–79, 81, 82] assuming hemispherical roughness elements, Glegg *et al.*'s theory [61] aims to include an arbitrary distribution of roughness elements. However, an important assumption in Morse and Ingard's theory [112] is that the rough surface defined by  $x_2 = \xi(x_1, x_3)$  with the mean plane at  $x_2 = 0$  should satisfy the condition  $\nabla_{1,3}\xi \ll 1$ , so that the gradient of the Green's function normal to the rough surface can be approximated by

$$\frac{\partial G}{\partial n} \approx \frac{\partial G}{\partial x_2} - \frac{\partial \xi}{\partial x_1} \frac{\partial G}{\partial x_1} - \frac{\partial \xi}{\partial x_3} \frac{\partial G}{\partial x_3}. \quad (2.12)$$

This implies that the theory by Glegg *et al.* only applies to rough elements with



Figure 2.4: Rough surfaces with different values of  $\nabla\xi$ .

sufficiently small curvature (see Figure 2.4(a)). For common surfaces on aircraft and ships, the roughness due to materials, paint finishes or imprecise machining during manufacture may fall into this category. However, the application of this theory is restricted in the case of rough surfaces with large slope of surface irregularities, *e.g.* discontinuities (rivets, ribs, joints, *etc.*) or environmental contamination (accretions caused by pollutants and organic matter), as shown in Figure 2.4(b).

### 2.3.3.3 Unsteady drag due to enhanced shear stress

The alternative source mechanism is the sound generated by enhanced shear stress fluctuations on the wall which are related to the unsteady forces due to local vortex shedding from each roughness element. In this mechanism the roughness elements

can also be regarded as individual incoherent sources and the radiated sound level increases in proportion to the number of roughness elements. As illustrated in Figure 2.3, this mechanism applies to large roughness elements that protrude far beyond the viscous sublayer in Region II (relatively large elements) or Region III (very large elements) and hence result in the additional shear stresses.

The mechanism of the shear stress noise has been discussed by Howe [76] and Smol'yakov [140] but not fully defined in the literature. It was argued that this source mechanism is negligible compared to the sound scattering mechanism. Glegg *et al.* [61] recently studied this mechanism for relatively large roughness elements in Region II in company with their work on the coherent scattering mechanism in 2007. The purpose was to clarify whether this assumption will hold as the roughness elements become large enough that they protrude out of the viscous sublayer. In this work, the physical process is assumed to be the same as noise from the unsteady loads on fixed objects in a steady flow and so each individual roughness element behaves as a drag dipole. Glegg *et al.* applied the Ffowcs Williams-Hawkings (FW-H) equation [53] to give the acoustic field radiated by the drag fluctuations and obtained the far-field acoustic spectrum in terms of the spectrum of the unsteady drag on each roughness element. The drag spectrum was then determined by using existing semi-empirical techniques [60, 114] for estimating the noise from bluff bodies, which will be introduced in Chapter 6.

As for the scattering mechanism, Glegg *et al.* [61] derived the formulation of the frequency scaling for the noise from the shear stress. They compared the scaling laws of both mechanisms and found that the two mechanisms have distinctly different scaling. The predicted peak frequency of the shear stress source is about half of the scattering mechanism. When the roughness elements do not protrude beyond the logarithmic layer, the spectral peak of the shear stress noise is lower than that of the scattering noise by  $\sim -46$  dB, which tends to confirm the assumption of Howe that roughness noise from shear stress enhancement is insignificant [76] and that the noise is dominated by the scattering of hydrodynamic pressure fluctuations into acoustic waves by the roughness elements [77–79].

When the roughness elements become larger that they protrude into the outer

region (Region III), it can be anticipated that the unsteady drag due to shear stress fluctuations will be further enhanced and produce stronger drag dipoles. Glegg *et al.* [61] also considered this case and attempted to similarly derive the frequency scaling by approximating the flow velocity in the outer region. They speculated that the spectral peak would occur at a frequency comparable to the noise generated by scattering. However, the classical scaling of boundary-layer parameters is not applicable to roughness elements this large, and thus they contended that it is probably unreasonable to estimate the spectral level in this case.

In this thesis, the drag dipole mechanism will be extended to very large hemispherical roughness elements that protrude far beyond the logarithmic layer (*i.e.* in the upper section of Region III). In this case the unsteady drag is produced principally owing to the fluctuation in surface pressures instead of enhanced shear stresses, and the free-stream flow parameters can be used to describe the incident flow onto a roughness element with confidence. The acoustic frequency spectrum is derived based on a recent analytical model [83] for the vortex shedding and hence the lift and drag fluctuations on a sphere in a nominally steady, high Reynolds number, incompressible flow. A modified model is developed from this sphere model to account for the unsteady drag spectrum of a wall-mounted hemisphere. Noise spectra of this source are predicted and compared with those of the scattering mechanism. Details of the modified drag model and noise prediction will be discussed in Chapter 6.

In conclusion, the three source mechanisms described above scale differently with the roughness height or the roughness correlation length scale. However, it has been confirmed that the sound scattering mechanism dominates for roughness elements contained in the logarithmic layer and the spectral peaks of both incoherent and coherent scattering are at similar levels. In the current research, we will focus our analysis on the incoherent scattering mechanism as the framework of this mechanism is relatively systematic and mature. Howe's work [77] on this mechanism is therefore applied as a baseline to formulate the diffraction problem of turbulent boundary-layer roughness noise of this thesis, and will be described in detail in Chapter 3.

# Chapter 3

## Theoretical Modelling

### 3.1 Introduction

IN the previous chapter, we determined to base the formulation of surface roughness noise on the incoherent sound scattering mechanism which is relatively systematic and mature compared to other source mechanisms. We derive a theoretical model in this chapter to predict the surface roughness noise radiated to the far field.

This chapter commences with a formulation of the diffraction theory of turbulent boundary-layer roughness noise in Section 3.2. This is based on the early analytical model of Howe [77], and the major derivations are presented here for the sake of completeness. The acoustic pressure frequency spectrum  $P_R(\boldsymbol{x}, \omega)$  is derived in terms of an infinite double integral and the final expression takes the form of a weighted integral over the smooth-wall wavenumber-frequency spectrum  $P_s(\boldsymbol{\kappa}, \omega)$  through modelling the turbulence Reynolds stress sources. In Section 3.3, we relate  $P_s(\boldsymbol{\kappa}, \omega)$  with the available empirical model  $\tilde{\Phi}_p(\boldsymbol{\kappa}, \omega)$ , and determine the increased boundary-layer properties  $u_\tau$  and  $\delta$  by means of a skin friction formula [106] for a rough wall to account for the enhanced mean drag and turbulence level.

Section 3.4 discusses alternative methods to evaluate the integral of the far-field acoustic spectrum  $P_R(\boldsymbol{x}, \omega)$ . Attention is focused on a generally more accurate method by direct numerical integration in the wavenumber space. The numerical method is then adopted in this work to predict the roughness noise spectrum and

it reproduces the spectral characteristics of both Howe's empirical model [82] and Hersh's experimental data [71].

## 3.2 Diffraction Theory of Surface Roughness Noise

### 3.2.1 Formulation of the diffraction problem

The general idea of the diffraction theory of roughness generated sound is introduced by considering turbulent boundary-layer flow over a rough, rigid wall defined by the surface  $x_2 = \xi(x_\iota)$ , where the Greek suffix  $\iota$  varies over the 1-direction and 3-direction parallel to the mean plane of the wall. The rough wall is formed by a random distribution ( $N$  per unit area) of rigid hemispherical bosses of radius  $R$  over the plane  $x_2 = 0$  (see Figure 3.1), and the fluid occupies the region  $x_2 > \xi(x_\iota)$ .

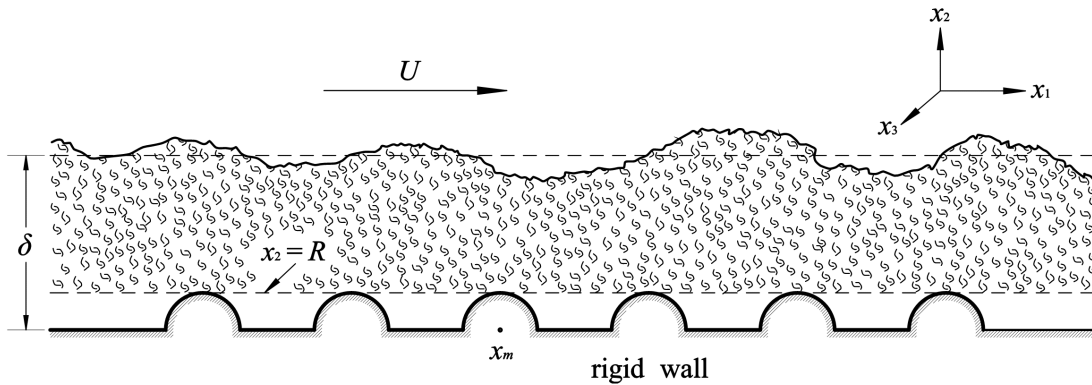


Figure 3.1: Schematic illustration of the diffraction problem.

The mean flow is in the positive  $x_1$ -direction, and is of uniform mean density  $\rho_0$  and sufficiently low Mach number. Pressure fluctuations  $p$  are related to turbulent fluctuations in the Reynolds stress by Lighthill's equation [95] in the reduced form:

$$\left( \frac{1}{c^2} \frac{\partial^2}{\partial t^2} - \nabla^2 \right) p = Q(\mathbf{x}, t), \quad (3.1)$$

where  $Q(\mathbf{x}, t)$  is the turbulence quadrupole source,

$$Q(\mathbf{x}, t) = \frac{\partial^2 (\rho_0 v_i v_j)}{\partial x_i \partial x_j}, \quad (3.2)$$

$v$  being the perturbation velocity. Here and henceforth it is implicitly assumed that the dominant Reynolds stress fluctuations  $\rho_0 v_i v_j$  occur in the region  $x_2 > R$  above the roughness elements.



Equation (3.1) is to be solved for the pressure in terms of the Reynolds stress fluctuation  $\rho_0 v_i v_j$ , subject to the inviscid, high-Reynolds-number, rigid boundary condition

$$\frac{\partial p}{\partial x_n} = 0 \quad \text{on} \quad x_2 = \xi(x_\iota), \quad (3.3)$$

where  $x_n$  is a local coordinate normal to the rough wall. In application, the roughness elements generally protrude beyond the viscous sublayer at the wall into the fully turbulent region of the boundary layer. Even when this is not the case, however, it appears that only a small error is incurred by using inviscid boundary conditions at the wall [78]. To solve this equation, a Green's function  $G(\mathbf{x}, \mathbf{y}, t, \tau)$  is introduced, which is the solution of wave equation (3.1) and boundary condition (3.3), with outgoing wave behaviour when the source term  $Q$  is replaced by the impulsive point source

$$\delta(\mathbf{x} - \mathbf{y})\delta(t - \tau), \quad x_2, y_2 > \xi(x_\iota). \quad (3.4)$$

$G(\mathbf{x}, \mathbf{y}, t, \tau)$  provides the response at observation point  $\mathbf{x}$  at time  $t$  to a pulse released at source point  $\mathbf{y}$  at time  $\tau$ .

An approximate Green's function was derived by Howe [77] that satisfies the boundary condition  $\partial G/\partial n = 0$  on an infinite number of hemispherical bosses of radius  $R$ , distributed randomly over the plane  $y_2 = 0$ . It is assumed that turbulence of low Mach number generates sound whose characteristic wavelength greatly exceeds the boundary-layer thickness  $\delta$ , and therefore the roughness height  $R$ . In these circumstances, Howe gave the Green's function in the form

$$G(\mathbf{x}, \mathbf{y}, t, \tau) = \frac{\delta(t - \tau - |\mathbf{x} - \mathbf{Y}|/c)}{2\pi|\mathbf{x} - \mathbf{Y}|}, \quad (3.5)$$

provided that the far-field point  $\mathbf{x}$  is situated at a distance much greater than  $R$  from the centre of the nearest boss, *i.e.*, attention is confined to components of the diffracted field whose length scales are much greater than  $R$ .

In the Green's function (3.5),  $\mathbf{Y}$  is defined by

$$\begin{cases} Y_2 = y_2 \\ Y_\iota = y_\iota + \sum_m \frac{\mu R^3 (y_\iota - x_{m\iota})}{2|\mathbf{y} - \mathbf{x}_m|^3}, \quad (\iota = 1, 3) \end{cases}, \quad (3.6)$$

where  $\mathbf{x}_m = (x_{m1}, 0, x_{m3})$  is the centre of the  $m$ th boss on the plane. The factor  $\mu$  is to take approximate account of mutual interactions between neighbouring bosses. It is not appreciably different from unity, and is given (to within a relative error of about 4%) by

$$\mu = \frac{1}{1 + \sigma/4}, \quad (3.7)$$

where

$$\sigma = N\pi R^2 \quad (3.8)$$

is the surface roughness density, *i.e.* the fractional area of the plane covered by roughness bosses. The function  $Y_\iota(\mathbf{y})$  is identical with the velocity potential describing an ideal incompressible flow in the  $\iota$ -direction over the rough wall. It satisfies

$$\frac{\partial Y_\iota}{\partial y_n} = 0 \quad \text{on} \quad y_2 = \xi(y_\iota), \quad (3.9)$$

and ensures that the Green's function satisfies  $\partial G/\partial n = 0$  when the acoustic wavelength is much larger than  $R$ .

Following routine applications of the Green's second theorem, we can specify the formal solution to Equation (3.1) as:

$$\begin{aligned} p(\mathbf{x}, t) = & \int_{-\infty}^{\infty} \int_{V(\mathbf{y})} G(\mathbf{x}, \mathbf{y}, t, \tau) Q(\mathbf{y}, \tau) d^3\mathbf{y} d\tau \\ & + \int_{-\infty}^{\infty} \oint_{S(\mathbf{y})} \left[ p(\mathbf{y}, \tau) \frac{\partial G(\mathbf{x}, \mathbf{y}, t, \tau)}{\partial n} - G(\mathbf{x}, \mathbf{y}, t, \tau) \frac{\partial p(\mathbf{y}, \tau)}{\partial n} \right] dS(\mathbf{y}) d\tau, \end{aligned} \quad (3.10)$$

which is an equation for  $p$  of the pressure wave within and on the surface bounding the medium, in terms of a volume integral of the source function  $Q$  over the bounded volume  $V$  and a surface integral of the boundary values of  $p$  and its outward normal gradient over the boundary surface  $S$  [112]. It states that the total acoustic field at the observer  $\mathbf{x}$  is the summation of the fields from the elementary sources  $Q d^3\mathbf{y}$  plus the waves reflected by the boundary surface. Because  $p$  and  $G$  both satisfy the vanishing normal derivative condition (3.3), the surface integral in Equation (3.10) vanishes, and thus the acoustic pressure  $p(\mathbf{x}, t)$  can be related to the Reynolds stress quadrupole source  $Q(\mathbf{y}, \tau)$  by

$$p(\mathbf{x}, t) = \int_{-\infty}^{\infty} \int_{V(\mathbf{y})} G(\mathbf{x}, \mathbf{y}, t, \tau) Q(\mathbf{y}, \tau) d^3\mathbf{y} d\tau. \quad (3.11)$$

### 3.2.2 Acoustic spectrum of the radiated sound

The far-field acoustic frequency spectrum will be derived concisely. A different Fourier transform from that of Howe [77, 79] is introduced according to the reciprocal relations:

$$\hat{f}(x_2, \boldsymbol{\kappa}, \omega) = \int \int_{-\infty}^{\infty} f(\mathbf{x}, t) e^{-i\boldsymbol{\kappa} \cdot \mathbf{x} + i\omega t} dx_1 dx_3 dt, \quad (3.12a)$$

$$f(\mathbf{x}, t) = \frac{1}{(2\pi)^3} \int \int_{-\infty}^{\infty} \hat{f}(x_2, \boldsymbol{\kappa}, \omega) e^{i\boldsymbol{\kappa} \cdot \mathbf{x} - i\omega t} d^2\boldsymbol{\kappa} d\omega, \quad (3.12b)$$

$$\boldsymbol{\kappa} = (\kappa_1, 0, \kappa_3). \quad (3.12c)$$

This ensures that the Fourier transform (3.12) is consistent with that of the wall pressure spectrum models [63], and Howe's derivation should be modified accordingly.

In the far field the acoustic power radiated from unit area of the rough wall is equal to the mean acoustic intensity flow,  $\langle pv \rangle$ , where the angle bracket denotes an ensemble average near the wall where  $Q = 0$ . The  $x_2$ -component of the perturbation velocity,  $v$ , is determined from Equation (3.11) by making use of the low Mach number approximation to the linearized momentum equation:

$$\rho_0 \frac{\partial v}{\partial t} = -\frac{\partial p}{\partial x_2}. \quad (3.13)$$

The rough-wall acoustic power spectrum  $\Pi(\omega)$  is defined as the Fourier transform of  $\langle pv \rangle$  with respect to  $t$ ,

$$\Pi(\omega) = \int_{-\infty}^{\infty} \langle p(\mathbf{x}, \tau) v(\mathbf{x}, \tau + t) \rangle e^{i\omega t} dt, \quad (3.14)$$

which expresses the frequency spectrum of the total radiated sound power per unit area of the rough wall.

Following Howe [77], from Equations (3.5–3.11), (3.13) and (3.14),  $\Pi(\omega)$  can be expressed as

$$\begin{aligned} \Pi(\omega) &= \frac{N\pi^2\mu^2 R^6\omega^2}{6\rho_0 c^3} \int_{-\infty}^{\infty} \Psi(\boldsymbol{\kappa}) e^{-2\kappa R} \\ &\times \int_0^{\infty} S(y_2, y'_2; \boldsymbol{\kappa}, \omega) e^{i(\gamma y_2 - \gamma^* y'_2)} dy_2 dy'_2 d^2\boldsymbol{\kappa}, \end{aligned} \quad (3.15)$$

where the asterisk denotes the complex conjugate. The term  $\gamma$  is defined by

$$\gamma(\kappa) = (k_0^2 - \kappa^2)^{\frac{1}{2}} \quad (3.16)$$

with the acoustic wavenumber  $k_0 = \omega/c$ , and the branch cuts are chosen such that  $\text{sgn}(\gamma) = \text{sgn}(k_0)$  when  $\gamma$  is real and  $\gamma \rightarrow +i\kappa$  as  $|\kappa| = \kappa \rightarrow \infty$  on the real axis.  $S$  is the cross-spectral density of the turbulence Reynolds stress according to the definition:

$$S(y_2, y_2'; \boldsymbol{\kappa}, \omega) = \frac{1}{(2\pi)^3} \iint_{-\infty}^{\infty} \langle \hat{Q}(y_2, \boldsymbol{\kappa}, \omega) \hat{Q}^*(y_2', \boldsymbol{\kappa}', \omega') \rangle d^2\boldsymbol{\kappa}' d\omega', \quad (3.17)$$

where  $\hat{Q}(y_2, \boldsymbol{\kappa}, \omega)$  is the Fourier transform of the Reynolds stress source  $Q(\mathbf{y}, \tau)$ . Note that  $\hat{Q}(y_2, \boldsymbol{\kappa}, \omega)$  is well defined only for  $y_2 > R$ , and it vanishes in the region occupied by the roughness bosses.

In addition, the term  $\Psi(\kappa)$  is determined by the average number of roughness bosses in unit area of the plane. The precise value of  $\Psi(\kappa)$  is unknown, but for practical purposes use may be made of an interpolation formula given by Howe [77, 79], namely

$$\Psi(\kappa) = \frac{[1 - \sigma J_1(2\kappa R)/\kappa R]^3}{[1 + \sigma J_1(2\kappa R)/\kappa R]}, \quad (3.18)$$

where  $J_1$  is the Bessel function of order unity. This result is exact for  $\kappa R = 0$ , and varies significantly only when  $\kappa R$  exceeds unity. Possible discrepancies between interpolated and exact values for large values of  $\kappa R$  are of no practical importance because of the accompanying exponential factor  $e^{-2\kappa R}$  in Equation (3.15).

Let  $P_R(\mathbf{x}, \omega)$  denote the frequency spectrum of the acoustic pressure fluctuations produced by diffraction by a finite area  $A$  of the rough wall, defined such that

$$\langle p^2(\mathbf{x}, t) \rangle = \frac{1}{2\pi} \int_{-\infty}^{\infty} P_R(\mathbf{x}, \omega) d\omega. \quad (3.19)$$

If the origin of coordinates is taken at the centre of the region  $A$ , and the observer  $\mathbf{x}$  is in the acoustic far field from  $A$  in a direction specified by the polar angles  $(\theta, \phi)$ , as illustrated in Figure 3.2, it follows from Equations (3.14), (3.15) and (3.19) that [77]

$$\begin{aligned} P_R(\mathbf{x}, \omega) &= \frac{AN\pi\mu^2 R^6 k_0^2}{4|\mathbf{x}|^2} \int_{-\infty}^{\infty} \frac{(\boldsymbol{\kappa} \cdot \tilde{\mathbf{n}})^2 \Psi(\kappa) e^{-2\kappa R}}{\kappa^2} \\ &\times \int_0^{\infty} S(y_2, y_2'; \boldsymbol{\kappa}, \omega) e^{i(\gamma y_2 - \gamma^* y_2')} dy_2 dy_2' d^2\boldsymbol{\kappa}. \end{aligned} \quad (3.20)$$

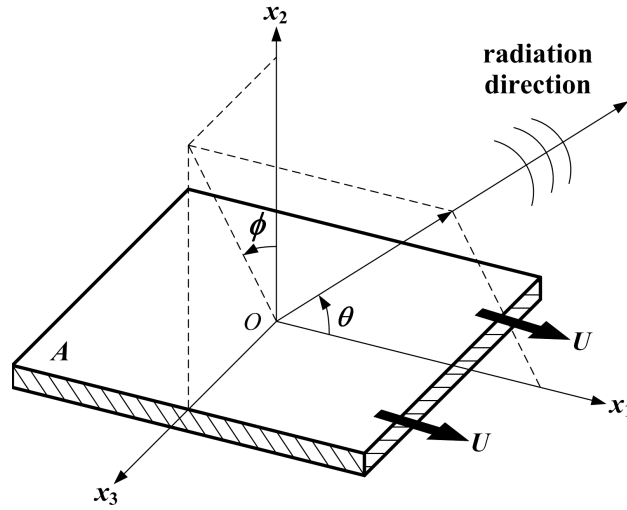


Figure 3.2: Sound radiation from a region of area  $A$  of the rough wall.

where  $\tilde{\mathbf{n}} = \mathbf{x}/|\mathbf{x}|$ , and

$$\begin{aligned} \mathbf{x} &= |\mathbf{x}|(\cos \theta, \sin \theta \cos \phi, \sin \theta \sin \phi), \\ (0 \leq \theta \leq \pi, \quad |\phi| \leq \pi/2) \end{aligned} \quad (3.21)$$

is the polar representation of the far-field observer  $\mathbf{x}$ . In this formula,  $P_R(\mathbf{x}, \omega)$  expresses the frequency spectrum of the acoustic pressure at the observer  $\mathbf{x}$  which is radiated within the solid angle element  $\sin \theta d\theta d\phi$ .

### 3.3 Rough-Wall Turbulent Boundary-Layer Pressures

#### 3.3.1 Modelling turbulence Reynolds stress sources

To complete the determination of the acoustic frequency spectrum  $P_R(\mathbf{x}, \omega)$ , it is necessary to model the turbulence Reynolds stress source term  $Q(\mathbf{y}, \tau)$ . The experimental data of Blake [17] and Schultz and Flack [131] have shown  $v_{\text{rms}}/u_\tau$  as the same function of  $y/\delta$  for different surface roughness and smooth walls, where  $v_{\text{rms}}$  is the root mean square of the perturbation velocity.

We therefore assume that the source  $Q(\mathbf{y}, \tau)$  scales as  $u_\tau^2$  when expressed as a function of  $y_2/\delta$ . To implement this scaling it is convenient to introduce a hypothetical smooth-wall pressure fluctuation  $p_s(\mathbf{x}, t)$  which would be generated on a smooth wall by the same Reynolds stress source. It is determined by solving

Equation (3.1) with the boundary condition

$$\frac{\partial p_s}{\partial x_2} = 0 \quad \text{on} \quad x_2 = 0, \quad (3.22)$$

and its Fourier transform is given by [34]

$$\hat{p}_s(0, \boldsymbol{\kappa}, \omega) = -\frac{1}{i\gamma(\boldsymbol{\kappa})} \int_0^\infty \hat{Q}(y_2, \boldsymbol{\kappa}, \omega) e^{i\gamma y_2} dy_2. \quad (3.23)$$

The conventional wavenumber-frequency spectrum  $P_s(\boldsymbol{\kappa}, \omega)$  of a smooth wall is the Fourier transform of the cross correlation of the pressure in the plane of the wall,

$$\langle \hat{p}_s(0, \boldsymbol{\kappa}, \omega) \hat{p}_s^*(0, \boldsymbol{\kappa}', \omega') \rangle = (2\pi)^3 P_s(\boldsymbol{\kappa}, \omega) \delta(\boldsymbol{\kappa} - \boldsymbol{\kappa}') \delta(\omega - \omega'). \quad (3.24)$$

For a rough wall it is necessary to relocate the plane of definition to be  $x_2 = R+0$ , just above the roughness bosses. By hypothesis,  $Q$  vanishes for  $y_2 < R$ , *i.e.*, the principal Reynolds stress noise sources are assumed to be confined to the region  $y_2 > R$ . The substitution of Equation (3.23) into (3.24) gives

$$P_s(\boldsymbol{\kappa}, \omega) = \frac{1}{|\gamma(\boldsymbol{\kappa})|^2} \int_0^\infty S(y_2, y'_2; \boldsymbol{\kappa}, \omega) e^{i(\gamma y_2 - \gamma^* y'_2)} dy_2 dy'_2, \quad (3.25)$$

where the Reynolds stress cross-spectral density  $S(y_2, y'_2; \boldsymbol{\kappa}, \omega)$ , as defined in Equation (3.17), is highly peaked in the neighbourhood of the convective ridge of wavenumber-frequency space. Substituting Equation (3.25) into (3.20), we obtain the acoustic frequency spectrum  $P_R(\boldsymbol{x}, \omega)$  in the reduced form:

$$P_R(\boldsymbol{x}, \omega) = \frac{AN\pi\mu^2 R^6 k_0^2}{4|\boldsymbol{x}|^2} \int_{-\infty}^\infty \frac{(\boldsymbol{\kappa} \cdot \tilde{\boldsymbol{n}})^2 |\gamma(\boldsymbol{\kappa})|^2 P_s(\boldsymbol{\kappa}, \omega) \Psi(\boldsymbol{\kappa}) e^{-2\kappa R} d^2\boldsymbol{\kappa}}{\kappa^2}, \quad (3.26)$$

which is equivalent to Equation (3.16) in Howe's model [77].

### 3.3.2 Wall pressure wavenumber-frequency spectrum

In Equation (3.26) the wall pressure spectrum  $P_s(\boldsymbol{\kappa}, \omega)$  which would be induced on a fictitious smooth wall by the rough-wall turbulence Reynolds stresses needs to be specified to evaluate  $P_R(\boldsymbol{x}, \omega)$ . This can be achieved by making use of the available models for the pressure spectrum on a smooth wall and scaling the Reynolds stresses through their dependence on  $u_\tau^2$  and  $\delta$ .

Graham [63] has drawn a comparison of different models<sup>†</sup> for the smooth-wall wavenumber-frequency spectrum of turbulent boundary-layer pressures. In his paper the nondimensional wavenumber-frequency spectrum  $\tilde{\Phi}_p(\boldsymbol{\kappa}, \omega)$  was defined on  $x_2 = 0$  in the form:

$$\begin{aligned} & 2\pi\delta(\omega - \omega')\tilde{\Phi}_p(\kappa_1, \kappa_3, \omega) \\ &= \frac{\omega^2}{U_c^2\Phi(\omega)} \int_{-\infty}^{\infty} \langle p(\mathbf{x} + \boldsymbol{\Delta}, \omega)p^*(\mathbf{x}, \omega') \rangle e^{-i\boldsymbol{\kappa}\cdot\boldsymbol{\Delta}} d\Delta_1 d\Delta_3, \end{aligned} \quad (3.27)$$

where the tilde on  $\tilde{\Phi}_p$  indicates that it is normalized by  $\Phi(\omega)U_c^2/\omega^2$ . The typical eddy convection velocity  $U_c$  is assumed to be a fixed fraction of the free-stream velocity  $U$ . Both experiments and numerical simulations indicate that  $U_c \approx 0.5\text{--}0.7U$  with only a weak dependence on the frequency [25].  $\Phi(\omega)$  is the point pressure frequency spectrum whose curve-fitted formulation will be discussed in Section 3.4. Similar to Equation (3.24), Equation (3.27) may be rearranged by integrating on both sides, yielding

$$\tilde{\Phi}_p(\boldsymbol{\kappa}, \omega) = \frac{\omega^2}{U_c^2\Phi(\omega)} \frac{1}{|\gamma(\boldsymbol{\kappa})|^2} \int_0^\infty S(y_2, y'_2; \boldsymbol{\kappa}, \omega) e^{i(\gamma y_2 - \gamma^* y'_2)} dy_2 dy'_2. \quad (3.28)$$

For moderately rough surfaces, we assume that the principal features of the wall-pressure spectrum would not differ substantially from those of the pressure spectrum on a smooth wall, especially in the vicinity of the convective ridge [26]. Note that it is now essential to increase  $u_\tau$  and  $\delta$  in the definition of  $\tilde{\Phi}_p(\boldsymbol{\kappa}, \omega)$  to the rough-wall values in order to compensate for the enhanced surface drag and turbulence production [18, 130]. In this case, by comparing the definitions (3.25) and (3.28) we can directly relate  $\tilde{\Phi}_p(\boldsymbol{\kappa}, \omega)$  with  $P_s(\boldsymbol{\kappa}, \omega)$ ,

$$P_s(\boldsymbol{\kappa}, \omega) = \frac{U_c^2}{\omega^2} \Phi(\omega) \tilde{\Phi}_p(\boldsymbol{\kappa}, \omega), \quad (3.29)$$

provided that the principal contributions to the integral in Equation (3.28) are from the region  $y_2, y'_2 > R$ . Therefore by substituting Equation (3.29) into (3.26) and rearranging, the far-field acoustic frequency spectrum  $P_R(\mathbf{x}, \omega)$  may be expressed

<sup>†</sup>These models are the Corcos model [31], the Efimtsov model [43], the Smol'yakov and Tkachenko model [140], the Ffowcs Williams model [52], the Chase I model [25], and the Chase II model [26], respectively (see Appendix A for details).

in terms of the smooth-wall wavenumber-frequency spectrum  $\tilde{\Phi}_p(\boldsymbol{\kappa}, \omega)$ ,

$$P_R(\mathbf{x}, \omega) = \frac{AN\pi\mu^2 R^6 U_c^2}{4|\mathbf{x}|^2 c^2} \Phi(\omega) \times \int_{-\infty}^{\infty} \frac{(\boldsymbol{\kappa} \cdot \tilde{\mathbf{n}})^2 |\gamma(\kappa)|^2 \tilde{\Phi}_p(\boldsymbol{\kappa}, \omega) \Psi(\kappa) e^{-2\kappa R} d^2\boldsymbol{\kappa}}{\kappa^2}. \quad (3.30)$$

### 3.3.3 Determinations of $u_\tau$ and $\delta$

The evaluation of  $\tilde{\Phi}_p(\boldsymbol{\kappa}, \omega)$  in Equation (3.30) depends on two boundary-layer parameters: the friction velocity  $u_\tau$  and the boundary-layer thickness  $\delta$ , both of which are enhanced by surface roughness. The principal effect of a rough surface is to alter the structure of the boundary layer near the wall thereby increasing the surface skin friction. Hence it is critical to first review the skin friction formula for a rough wall.

Prandtl and Schlichting [124] derived an interpolation formula for skin friction based on the sand grain roughness experiments of Nikuradse [115]. For fully developed roughness flows (*i.e.*  $Re_\tau > 70$ ) over the whole plate, they recommended a simple formula as:

$$\begin{cases} c_f = \left( 2.87 + 1.58 \log_{10} \frac{x_1}{k_s} \right)^{-2.5} \\ C_F = \left( 1.89 + 1.62 \log_{10} \frac{L}{k_s} \right)^{-2.5} \end{cases}, \quad (3.31)$$

which was claimed to be valid for  $10^2 < L/k_s < 10^6$ . In this formula (3.31),  $c_f$  and  $C_F$  are the local and overall skin friction coefficients, respectively;  $C_F$  is also known as the drag coefficient for a plate of length  $L$  [42],

$$C_F = \frac{1}{L} \int_0^L c_f(x_1) dx_1. \quad (3.32)$$

For the fully developed roughness flow over a flat plate, the effective equivalent height of the roughness particles  $k_s$  is very much larger than the thickness of the viscous sublayer. In this case  $C_F$  is independent of  $Re_L$  and is a function of  $L/k_s$  only [44], where  $Re_L = UL/\nu$  is a Reynolds number based on the whole plate.

Mills and Hang [106] compared the formulation of Prandtl and Schlichting [124] with some experimental data sets for fully rough flow over sand grain roughness



(Pimenta *et al.* [122]) and found that it gave an average error of 17.5 percent. They attributed the discrepancy to the failure of the formulation to account for the wake component of the mean velocity profile, and proposed a skin friction formula in the form:

$$\begin{cases} c_f = \left( 3.476 + 0.707 \ln \frac{x_1}{k_s} \right)^{-2.46} \\ C_F = \left( 2.635 + 0.618 \ln \frac{L}{k_s} \right)^{-2.57} \end{cases}, \quad (3.33)$$

where  $c_f$  and  $C_F$  were curve-fitted from the experimental data of Pimenta *et al.* [122]. This formula gives an average error of 2.7 percent only when compared to the same data and is valid over a wide parameter range ( $150 < x_1/k_s < 1.5 \times 10^7$ ).

The two different formulae of skin friction in (3.31) and (3.33) will be compared in Section 4.4 with experimental data collected by hot-wire measurement. The accuracy of Mills and Hang's formula [106] is verified and we hence employ the skin friction formula (3.33) in this research. With the skin friction determined for a rough wall, the friction velocity  $u_\tau$  can be obtained through the definition,

$$u_\tau = U \sqrt{c_f/2}. \quad (3.34)$$

Building on the work of von Kármán [152], Krogstad *et al.* [93] suggested a composite relationship to match the mean velocity profile in the logarithmic and outer regions of a turbulent boundary layer over a rough wall,

$$\frac{u}{u_\tau} = \frac{1}{\kappa_0} \ln \left( \frac{y}{k_s} \right) + B + \frac{2\Pi_0}{\kappa_0} w \left( \frac{y}{\delta} \right), \quad (3.35)$$

where  $\kappa_0 \approx 0.41$  and  $B = 8.5$  are empirical constants. The wake function  $w(y/\delta)$  is expressed as follows

$$w \left( \frac{y}{\delta} \right) = \frac{1}{2\Pi_0} \left[ (1 + 6\Pi_0) - (1 + 4\Pi_0) \left( \frac{y}{\delta} \right) \right] \left( \frac{y}{\delta} \right)^2, \quad (3.36)$$

where  $\Pi_0$  represents the strength of the wake. The value of  $\Pi_0$  for a rough surface is typically larger than for a smooth surface, and it varies with different types of surface roughness. In the present study,  $\Pi_0 \approx 0.45$  has been tentatively applied to the rough surface formed by hemispherical bosses because this value gives the best fit to the boundary-layer thickness measured by hot-wire anemometry (see Figure 4.19 in Section 4.4.2).

The boundary-layer thickness  $\delta$  on a rough wall is therefore determined from Equations (3.33–3.36). If we take  $y = \delta$  in Equation (3.35), then at this location

$$u \approx U \quad \text{and} \quad w(1) = 1. \quad (3.37)$$

In this case Equation (3.35) is simplified as

$$\frac{U}{u_\tau} = \frac{1}{\kappa_0} \ln \left( \frac{\delta}{k_s} \right) + B + \frac{2\Pi_0}{\kappa_0}. \quad (3.38)$$

The only unknown in Equation (3.38) is  $\delta$  and it can also be expressed in terms of the skin friction coefficient  $c_f$ ,

$$\delta = k_s \exp \left( \kappa_0 \sqrt{2/c_f} - \kappa_0 B - 2\Pi_0 \right). \quad (3.39)$$

This expression gives the local boundary-layer thickness developing on a rough plate. The average value of  $\delta$  suitable for crude calculations for the whole plate,  $\bar{\delta}$ , can be obtained by substituting  $C_F$  for  $c_f$  in Equation (3.39).

## 3.4 Evaluation of the Rough-Wall Acoustic Spectrum

### 3.4.1 Asymptotic approximation and empirical model

Howe [77, 79] evaluated the integral in Equation (3.30) approximately to obtain an estimate of the radiated roughness noise in the far field. As mentioned before the principal components of the boundary-layer Reynolds stress occur in the hydrodynamic domain wherein

$$\kappa = |\boldsymbol{\kappa}| \sim |\omega|/U_c. \quad (3.40)$$

The wall pressure wavenumber-frequency spectrum  $\tilde{\Phi}_p(\boldsymbol{\kappa}, \omega)$  is expected to be sharply peaked in the neighbourhood of a “convective ridge” centred on  $\kappa_1 \sim \omega/U_c$ ,  $\kappa_3 = 0$ , and the main contribution to the integral will therefore be from this vicinity of the convective ridge. The way Howe evaluated the integral in Equation (3.30) was to expand the remaining terms in the integrand about the convective ridge and integrate term by term. It is essentially a representation of asymptotic approximation, and may be unable to evaluate the integral with sufficient accuracy.

Howe [79, 81, 82] also proposed empirical models for the rough-wall acoustic frequency spectrum aimed at larger values of  $R$  where there may be interstitial flows and wake formation. In the most recent work [82], he assumes the empirical model to be in the form:

$$\frac{\Phi_R(\mathbf{x}, \omega)}{\rho_0^2 u_\tau^3 \delta} \approx \tau_0 \frac{A \cos^2 \theta R u_\tau^2}{|\mathbf{x}|^2 \delta c_0^2} \frac{(\omega R / u_\tau)^3}{[1 + \beta (\omega R / u_\tau)^2]^{n/2}}, \quad (3.41)$$

where the empirical coefficients,  $\tau_0$ ,  $\beta$  and  $n$ , are partially estimated by the experimental data of Hersh [71] on sound radiation by sand-roughened pipes of various grit sizes. The best fit to Hersh's data can be achieved by taking

$$\beta = 0.0025 \quad \text{and} \quad n = 11. \quad (3.42)$$

Following Howe [82], the "roughness parameter"  $\tau_0$  depends primarily on the spacing of the roughness elements, determined by  $\sigma$ :

$$\tau_0 \approx (u_\tau / U_c)^2 (\sigma / \pi) \quad \text{when} \quad \sigma \ll 1. \quad (3.43)$$

However, these values of adjustable coefficients should be regarded as tentative because no directivity information is available from the Hersh data [71]. For this reason, although  $\beta$  and  $n$  are capable of fixing the shape of the spectrum (see Figure 3.4), it is not possible to derive the absolute levels from Hersh's data.

### 3.4.2 Direct numerical integration

The direct numerical integration is therefore considered instead to evaluate the integral in Equation (3.30). It is convenient to introduce the polar representation  $(\kappa, \alpha)$  in the wavenumber plane, so that

$$\kappa_1 = \kappa \cos \alpha, \quad \kappa_3 = \kappa \sin \alpha. \quad (3.44)$$

Combining Equation (3.44) with the definition of the unit vector in the far field

$$\tilde{\mathbf{n}} = \frac{\mathbf{x}}{|\mathbf{x}|} = (\cos \theta, \sin \theta \cos \phi, \sin \theta \sin \phi) \quad (3.45)$$

yields  $\kappa \cdot \tilde{\mathbf{n}}$  in the polar coordinates,

$$\kappa \cdot \tilde{\mathbf{n}} = \kappa (\cos \alpha \cos \theta + \sin \alpha \sin \theta \sin \phi). \quad (3.46)$$

Therefore the acoustic pressure frequency spectrum  $P_R(\mathbf{x}, \omega)$  becomes

$$P_R(\mathbf{x}, \omega) = \frac{A\sigma\mu^2 R^4 U_c^2}{4|\mathbf{x}|^2 \delta^{*4} c^2} \Phi(\omega) D(\theta, \phi), \quad (3.47)$$

where the non-dimensional term  $D(\theta, \phi)$  gives the directivity information:

$$D(\theta, \phi) = I_1 \cos^2 \theta + I_2 \sin^2 \theta \sin^2 \phi + 2I_3 \cos \theta \sin \theta \sin \phi. \quad (3.48)$$

In the above expression,  $I_1$ – $I_3$  are integrals with respect to the nondimensional polar coordinates  $\kappa\delta^*$  and  $\alpha$ ,

$$I_1 = \int_0^{2\pi} \int_0^\infty \chi \cos^2 \alpha \, d\kappa\delta^* \, d\alpha, \quad (3.49a)$$

$$I_2 = \int_0^{2\pi} \int_0^\infty \chi \sin^2 \alpha \, d\kappa\delta^* \, d\alpha, \quad (3.49b)$$

$$I_3 = \int_0^{2\pi} \int_0^\infty \chi \cos \alpha \sin \alpha \, d\kappa\delta^* \, d\alpha, \quad (3.49c)$$

where  $\chi$  is a non-dimensionalized term,

$$\chi = [|\gamma(\kappa)|\delta^*]^2 \tilde{\Phi}_p(\boldsymbol{\kappa}, \omega) \Psi(\kappa) e^{-2\kappa R \kappa\delta^*}. \quad (3.50)$$

As is evident from Equations (3.48–3.50), the term  $I_1 \cos^2 \theta$  describes the effect of a dipole in the flow direction, and the term  $I_2 \sin^2 \theta \sin^2 \phi$  accounts for the sound from a dipole in the plate plane but normal to the flow direction. The integrand in  $I_3$  shows the features of a periodic odd function of  $\sin \alpha$ , and so its integration with respect to  $\alpha \in [0, 2\pi]$  is identically zero. This term will therefore be discarded in the numerical integration.

It should be noted that the original infinite double integral over rectangular coordinates in Equation (3.30) is now reduced to a series of mixed double integral over polar coordinates with directivity information excluded from the integrals, which greatly improves the computation efficiency. The numerical integrations of  $I_1$  and  $I_2$  are then carried out by using the five-point Gauss-Legendre quadrature with adjustable integration subintervals. Moreover, the infinite  $\kappa\delta^*$ -integral can be reduced to a finite integral with sufficient accuracy thanks to the existence of a weighting function  $e^{-2\kappa R}$  in  $\chi$ . Hence the infinite upper bound in the  $\kappa\delta^*$ -integral may be substituted by a positive real number,  $\kappa\delta^* \leq 25\delta^*/R$ , to make the numerical integration practical.

It remains to find a suitable form of the point pressure frequency spectrum  $\Phi(\omega)$  in Equation (3.47). Blake [18] has discussed features of the frequency spectrum of wall pressures and categorized it into three different frequency regions as below:

$$\Phi(\omega) \sim \rho^2 u_\tau^4 (\delta/U_c) (\omega\delta/U_c)^2 \quad \omega\delta/U_c \ll 1, \quad (3.51a)$$

$$\Phi(\omega) \sim \rho^2 u_\tau^4 \omega^{-1} \quad 1 < \omega\delta/U_c < \frac{1}{30} u_\tau \delta/\nu, \quad (3.51b)$$

$$\Phi(\omega) \sim \rho^2 u_\tau^4 \omega^{-1} (\omega\delta/U_c)^{-4} \quad \omega\delta/U_c > \frac{1}{30} u_\tau \delta/\nu. \quad (3.51c)$$

However, these regions are not unambiguously identifiable in experimental data, and hence Ahn [4] approximated a curve fit for the frequency spectrum data in Blake [17] as:

$$\begin{aligned} \Phi_B(\omega) &= \left( \frac{\tau_w^2 \delta^*}{U} \right) \frac{2\pi 8.28 Sh^{*0.8}}{[1 + 4.1 Sh^{*1.7} + 4.4 \times 10^{-4} Sh^{*5.9}]} \\ &= \left( \frac{\tau_w^2 \delta^*}{U} \right) g(Sh^*), \end{aligned} \quad (3.52)$$

wherein  $\tau_w = \rho_0 u_\tau^2$  is the mean wall shear stress, and  $Sh^* = \omega\delta^*/U$  is the Strouhal number based on the displacement boundary-layer thickness  $\delta^*$ . It may be assumed that  $\delta^* \approx \delta/8$  for practical purposes [82].

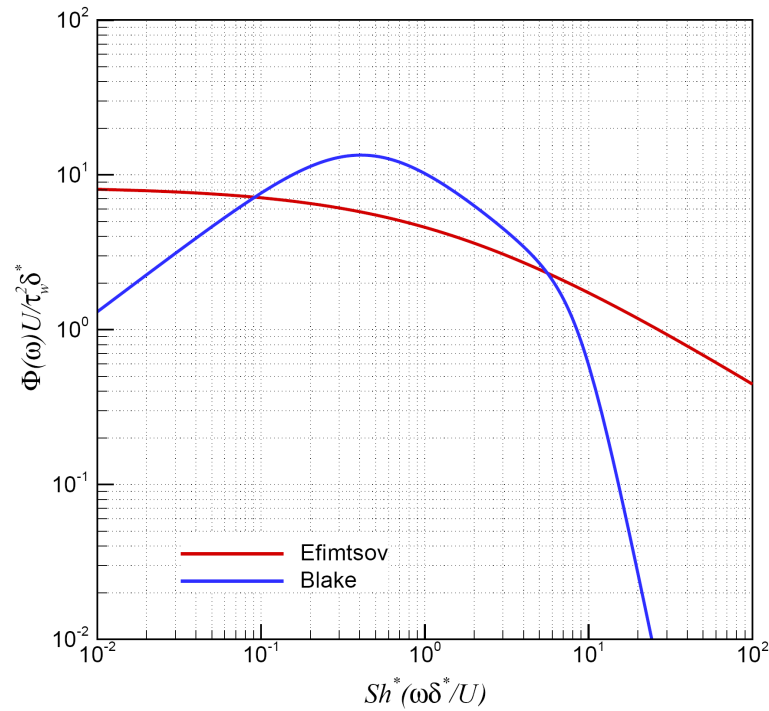


Figure 3.3: Curve fits of the frequency spectrum of wall pressure fluctuations (Ahn [4]).

In fact there are other forms of  $\Phi(\omega)$ , *e.g.* the Efimtsov curve fit [43] for the frequency spectrum of high flight-test data based on the Strouhal number  $Sh = \omega\delta/u_\tau$ ,

$$\Phi_E(\omega) = \left( \frac{\tau_w^2 \delta}{u_\tau} \right) \frac{0.01\pi}{[1 + 0.02Sh^{2/3}]}. \quad (3.53)$$

The frequency spectra of  $\Phi_B(\omega)$  and  $\Phi_E(\omega)$  are shown in Figure 3.3. The reason for choosing the curve fit  $\Phi_B(\omega)$  in this work is because it is capable of reproducing the features in the three different frequency regions as Blake suggested [18], whereas the Efimsov curve fit  $\Phi_E(\omega)$  fails to give these features, notably in the low- and high-frequency regions.

The main parametric dependency of surface roughness noise can then be discovered from Equations (3.47–3.50) and (3.52). By substituting Equation (3.52) into (3.47) and integrating  $P_R(\mathbf{x}, \omega)$  with respect to  $\omega$ , we obtain the mean square pressure in the form:

$$\langle p^2(\mathbf{x}, t) \rangle = \frac{A\sigma\mu^2\rho_0^2}{8\pi|\mathbf{x}|^2c^2} \left( \frac{R}{\delta^*} \right)^4 \left( \frac{U_c}{u_\tau} \right)^2 u_\tau^6 D(\theta, \phi) \int_{-\infty}^{\infty} g(Sh^*) dSh^*. \quad (3.54)$$

This indicates that  $\langle p^2(\mathbf{x}, t) \rangle$  scales on the 6<sup>th</sup> power of Mach number, *i.e.*  $\langle p^2(\mathbf{x}, t) \rangle \sim M^6$ , suggesting that surface roughness noise is a distribution of dipole sources in nature. In addition, the mean square pressure is proportional to the rough area  $A$  and there is an explicit dependence of  $\langle p^2(\mathbf{x}, t) \rangle$  on  $R^4$ . However,  $R$  also influences the turbulent boundary-layer properties  $\delta^*$  and  $u_\tau$  and the wavenumber contribution to  $D(\theta, \phi)$  through the weighting function  $e^{-2\kappa R}$  in the integrals  $I_1$ – $I_3$ . The actual dependence on  $R$  is therefore more complicated and a full parametric study is carried out in Section 5.2.3.

### 3.4.3 Comparison of empirical model with numerical method

A comparison between the empirical model of Equation (3.41) and the results of the numerical integration of Equations (3.47–3.50) and (3.52), which will be referred to as the “numerical method”, is illustrated in Figure 3.4 for the following nondimensional parameters:

$$\begin{aligned} \sigma = 0.2, \quad R/\delta = 0.01, \quad U_c/U = 0.6, \\ u_\tau/U = 0.05, \quad M = 0.005. \end{aligned} \quad (3.55)$$

These values have been selected to enable the comparison with Howe's empirical model  $\Phi_R(\mathbf{x}, \omega)$ , and might be encountered in underwater applications. In these plots the far-field observer is chosen as on the positive  $x_1$ -axis, *i.e.*,  $\theta = 0$  and  $\phi = 0$ , leading  $D(\theta, \phi)$  to be reduced to  $I_1$ .

The numerical integration of  $P_R(\mathbf{x}, \omega)$  is repeated with different wall pressure spectrum models by Corcos [31], Efimtsov [43], Smol'yakov and Tkachenko [140], and Chase [25, 26]. The Ffowcs Williams model [52] is rejected, as suggested by Graham [63], because its divergent behavior in the high-wavenumber region does not satisfy the integral requirement:

$$\frac{1}{(2\pi)^2} \int_{-\infty}^{\infty} \tilde{\Phi}_p(\kappa_1, \kappa_3, \omega) \left( \frac{U_c}{\omega} \right)^2 d\kappa_1 d\kappa_3 = 1. \quad (3.56)$$

The curves in Figure 3.4 represent the variations of  $\Phi_R(\mathbf{x}, \omega)$  and  $P_R(\mathbf{x}, \omega)$  as functions of the nondimensional frequency  $\Omega = \omega R/u_\tau$ . Hersh's experimental data [71] for sand-roughened pipes of various grit sizes are also shown as scatter points. No comparison of the absolute levels of the predicted and measured noise is possible due to the unknown effects of acoustic refraction by the free-jet shear layers downstream of the nozzle exit [79]. Accordingly, the heights of the curves have been

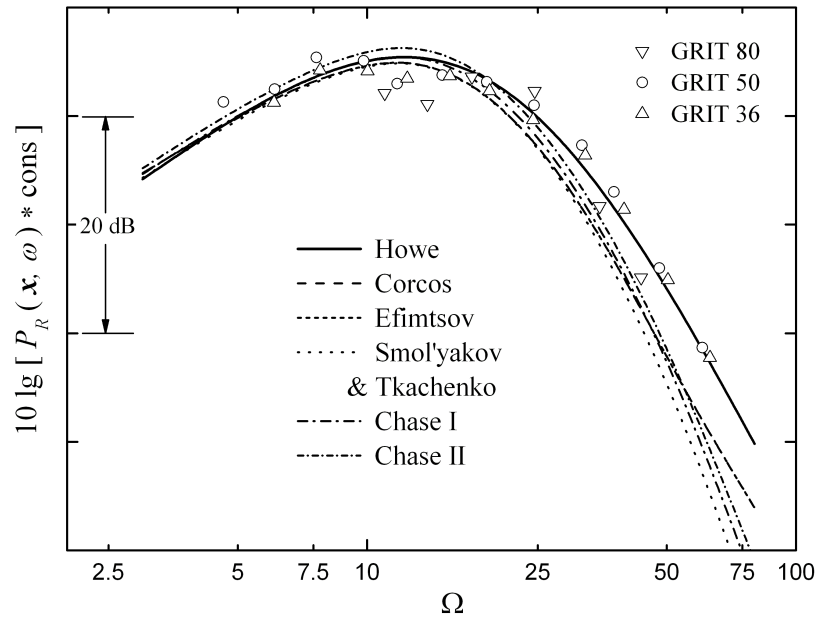


Figure 3.4: Comparison of roughness noise spectra predicted by the empirical model [82] and the present numerical method.  $\nabla \circ \triangle$  Previous experimental data obtained by Hersh [71].

adjusted to yield the best fit to the data points.

As shown in Figure 3.4, the shape of the empirical spectrum  $\Phi_R(\mathbf{x}, \omega)$  fits the experimental data very well by using the coefficients in Equation (3.42). Moreover, the comparison between the empirically and numerically predicted roughness noise spectra exhibits encouraging agreement. Both  $\Phi_R(\mathbf{x}, \omega)$  and  $P_R(\mathbf{x}, \omega)$  peak around  $\Omega \approx 13$  and decay rapidly at higher frequencies. The relatively abrupt fall-off of  $P_R(\mathbf{x}, \omega)$  is due to the features of  $\Phi(\omega)$  specified in Equation (3.52). In addition, the numerically predicted spectra obtained from different models of  $\tilde{\Phi}_p(\boldsymbol{\kappa}, \omega)$  agree with one another very well. In this frequency range  $3 \leq \Omega \leq 80$ , the Efimtsov model reduces to the Corcos model and thus their curves coincide, predicting levels comparable to other models except when  $\Omega > 60$ .

### 3.5 Summary

Howe [77] has developed a theory of sound generation by turbulent boundary-layer flow over a rough wall in which the surface roughness is modelled by a distribution of rigid, hemispherical bosses on a rigid plane. The roughness noise is attributed to the diffraction of the turbulence near field by the bosses, and calculated by means of conventional asymptotic approximation. An empirical model was also proposed by Howe [82] by curve-fitting Hersh's experimental data [71].

In this chapter, the diffraction theory has been extended to numerically quantify the radiated roughness noise from a finite surface area to the far field using available empirical models of smooth-wall wavenumber-frequency spectrum scaled by the enhanced friction velocity and boundary-layer thickness for a rough surface. The objective has been to ascertain the reliability of this solution scheme. Comparison of numerically predicted roughness noise spectra with Howe's empirical model [82] and previous data measured by Hersh [82] has provided preliminary confirmation of the validity of the diffraction theory and the solution scheme.



# Chapter 4

## Experimental Validation

### 4.1 Introduction

THE objective of this chapter is to validate the theoretical model derived in Chapter 3 through a series of experiments, so that it can be applied to the numerical prediction of surface roughness effects to airframe noise. In Section 4.2, acoustic measurements are conducted by making use of an open-jet wind tunnel and individual microphones to enable the comparison between the measured and predicted roughness noise spectra. We make modifications to the prediction model to take into account the effects of noncompact surface roughness, cross-spectra data and a partially roughened plate.

Following the preliminary validation of roughness noise in spectral level, we apply phased microphone arrays to the experimental study in Section 4.3. The source locations and source strengths of the roughness dipoles distributed on a rigid plate are identified and discussed. Measurements are performed at three streamwise locations to explore the dipole directivity features. The array measurements can be misinterpreted if applied directly to reconstruct dipole sources due to the monopole assumption in the standard beamforming algorithm [16, 38, 87]. Instead, we process the theoretical simulation through the same algorithm as the experimental data and compare the resulting predicted and measured source maps. This is equivalent to comparing theory and experiment after applying a filter which suppresses much of the extraneous noise in the experiments. A distribution of incoherent dipoles

is simulated over the rigid plate with the source strengths determined using the prediction model. Comparison of the beamforming results between measurement and simulation provides indirect validation of the predicted source type, magnitude and distribution.

Section 4.4 presents some data from hot-wire measurement to confirm the wake strength and skin friction coefficient used in the prediction model. We determine the suitable value of wake strength by comparing with the measured rough-wall boundary-layer thickness. The accuracy of the skin friction formula (3.33) presented in Chapter 3 is verified by the experimental data of skin friction coefficient. The results of the acoustic spectrum measurement, phased array measurement and hot-wire measurement are then summarized in Section 4.5.

## 4.2 Acoustic Spectrum Measurement

### 4.2.1 Experimental setup

The acoustic experiments were conducted in the open jet of a low-speed wind tunnel in the Whittle Laboratory of Cambridge University Engineering Department (CUED) to measure the radiated sound from a rough plate. Individual microphones were first utilized to obtain the acoustic spectrum of radiated roughness noise. A schematic of the experimental setup is shown in Figure 4.1. The wind tunnel has an inner cross-section of  $0.586 \times 0.350 \text{ m}^2$  at the outlet and a velocity range of 0–31 m/s. Plastic foam lining on the inner walls and a splitter silencer were installed to reduce the wind noise and motor noise travelling inside the tunnel.

#### 4.2.1.1 Test flat plate

A large flat plate made of aluminium alloy is placed nominally in the vertical meridian plane of the open jet, as shown in Figure 4.1. It is secured to a vertical frame of aluminium rods adjacent to the tunnel outlet (see Figure 4.5(a)). On the test flat plate, the boundary layer was tripped using four layers of tape<sup>†</sup> cut in sawtooth

---

<sup>†</sup>The number of trip tape layers is determined by the height of trip strip recommended by Barlow *et al.* [10] for free-stream velocity  $U = 30 \text{ m/s}$ .

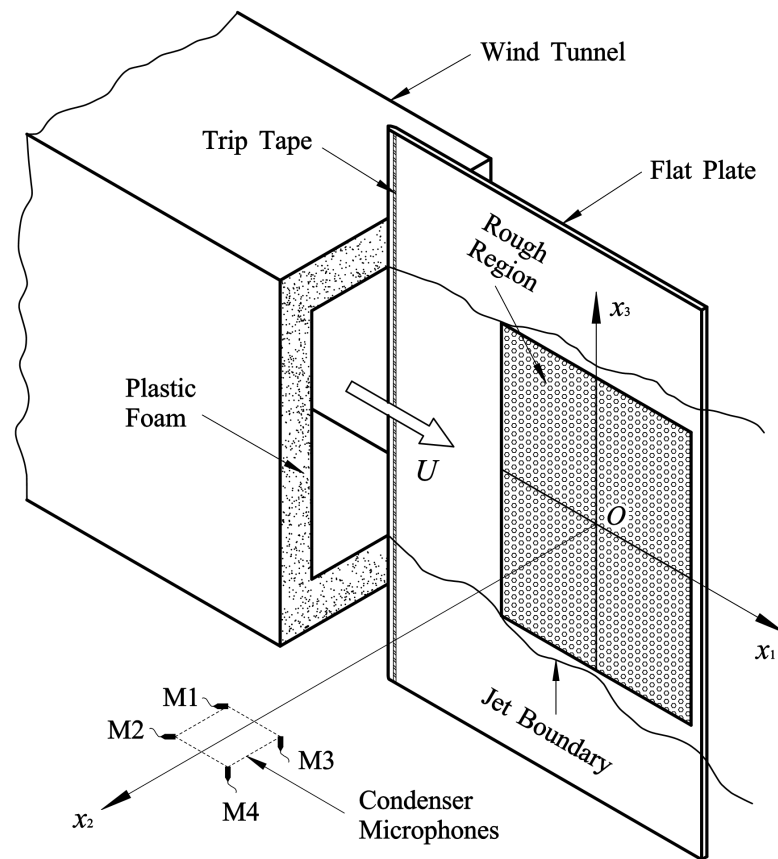


Figure 4.1: Schematic of the experimental setup for acoustic spectrum measurement. The rectangular region on the test plate is the effective rough region.

form with 0.13 mm in thickness and 1.5 mm in width. The tape was placed 4 cm from the leading edge over the entire span of the plate. This encourages a fully developed turbulent boundary layer close to the leading edge. A stethoscope was employed to verify whether or not the trips induced the desired boundary layer transition. The stethoscope was attached to an L-shaped total pressure tube, which was traversed manually over the surface of the flat plate. Transition from a turbulent boundary layer was observed by listening.

The leading edge of the flat plate was carefully streamlined to reduce sound scattering effects due to flow separation at a bluff-headed nose. The rough region was located at 0.34 m from the leading edge of the plate to satisfy the assumption that the roughness elements are contained entirely within the boundary layer, and to avoid the interference of sound scattering at the leading edge in subsequent noise source localization of phased array measurements (see Section 4.3).

### 4.2.1.2 Test rough panels

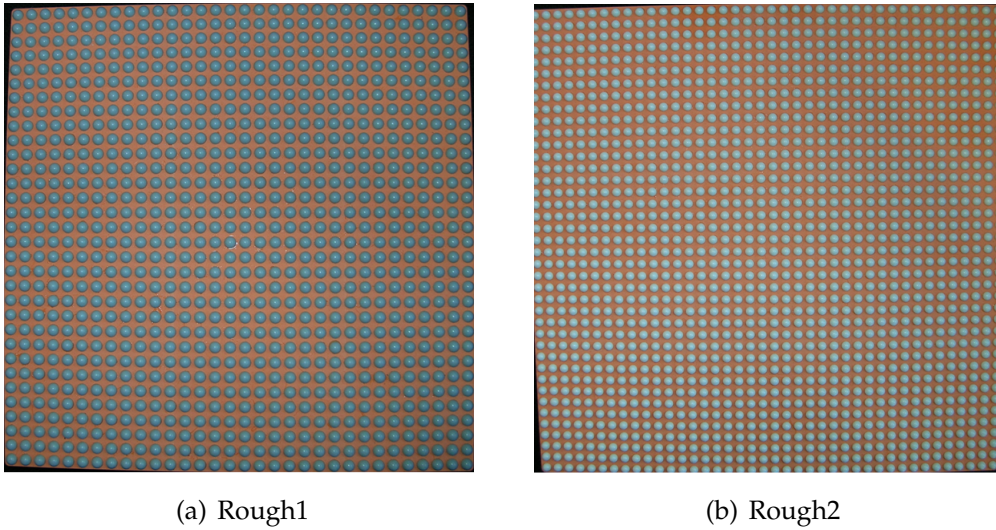


Figure 4.2: Test rough panels of Rough1 and Rough2 with rigid hemispherical roughness elements formed by plastic beads.

Figure 4.1 shows that the plate surface is partially roughened in an effective rectangular region by hemispherical roughness elements which are assumed by the theoretical model in Chapter 3. To form the rough region, four panels each of  $0.32 \times 0.32 \text{ m}^2$  were roughened with rigid hemispherical bosses (see Figure 4.2) flush mounted in a recess of  $0.64 \times 0.64 \text{ m}^2$  machined into the plate surface. The use of four small panels instead of one large board is because a whole board of such breadth is more likely to be cracked by structural vibration in a high-speed flow. To reduce the flow-induced vibration, each rough panel is fastened to the recess by 5 screws, 4 at the corners and 1 in the centre.

The rigid hemispherical roughness elements were achieved by drilling a number of hemispherical holes in parallel columns into a modelling panel and then adhering spherical plastic beads to the hole surfaces. Each column spans the entire height

Table 4.1: Surface conditions to be tested in the experiment.

Surface	$R$ (mm)	$\sigma$	$N_{\text{tot}}$
<b>Rough1</b>	4	0.50	1024
<b>Rough2</b>	3	0.44	1600
<b>Smooth</b>	0	0.00	0

of the rough region. Four smooth panels were also fabricated to enable the measurement of a smooth plate or a rough plate with a smaller roughened region. Three different surface conditions were examined, as shown in Table 4.1. The values of both  $R$  and  $\sigma$  for Rough1 and Rough2 were chosen to be comparatively high to ensure that noise radiated from the two rough plates could be detected from background noise and other sources.  $N_{\text{tot}}$  is the total number of roughness elements per panel. Figure 4.2 shows the test rough panels of Rough1 and Rough2.

### 4.2.1.3 Microphones

As marked in Figure 4.1, the radiated sound from the rough plate was detected by four 1/2" free-field condenser microphones of Brüel & Kjær (B&K) with a usable frequency range 7 Hz – 25.6 kHz. The acoustic signals were acquired for a duration of 60 s at a sampling frequency of 65.536 kHz. The Cartesian coordinate system is also indicated in the schematic Figure 4.1 and the origin is chosen to be at the centre of the rough region. The four B&K microphones were arranged in a 0.16 m × 0.16 m square array on the horizontal plane  $x_3 = 0$  and axisymmetric to the vertical plane  $x_1 = 0$  with microphones M1 & M2 upstream and M3 & M4 downstream. To reduce unwanted turbulence fluctuations around the microphones (wind noise), it is important to put the microphones out of the jet boundary, and hence the distance between the plate plane and front microphones M1 & M3 was set as 0.6 m.

Considering the dipole directivity, one may cast doubts on the validity of the microphone positions in Figure 4.1 as they are very close to the  $x_2$ -axis. It is true that the roughness dipole sources radiate no sound at  $90^\circ$  to the plate plane. However, the test plate is large compared to propagation distance  $|x|$ , and thus the microphones M1–M4 were located in the far field of each roughness dipole but not in the far field of the entire rough region. As will be discussed in Section 4.2.2, the angle from different portions of the plate to the microphones varies significantly, and so it is possible to measure considerable roughness noise at this location. In addition, constraints imposed by the experimental setup (*e.g.* scattering at the duct exit and reflection from the downstream wall) meant that it was difficult to alter the microphone positions.

## 4.2.2 Modifications of the numerical method

For the particular experimental setup illustrated in Figure 4.1, the numerical method (3.47) should be accordingly modified to enable the comparison of the numerical prediction with experimental results.

Firstly, the nonuniform directivity function  $D(\theta, \phi)$  for sound radiated from different portions of the rough region should be reconsidered as the far-field distance  $|\mathbf{x}|$  and the dimensions of the rough area  $A$  are now comparable. In this case the rough area  $A$  should be divided into a number of equal subareas  $A_j$ ,  $j = 1, \dots, N_A$ ; then one can apply the numerical integration to determine the roughness noise radiated from each subarea, and sum their mean square pressures to obtain the total radiation from the whole rough region. In the present setup, the effective rough region is about  $0.640 \text{ m} \times 0.586 \text{ m}$ , and thus the far-field condition  $|\mathbf{x}| \gg \sqrt{A_j}$  can be satisfied if the number of subareas  $N_A > 12 \times 10$  is taken. The growing boundary-layer thickness along the plate chord is also taken into account.

Secondly, cross-spectra data were used for the measured noise spectra to discard the interference of uncorrelated noise signals. The microphones were located outside the flow region, but some unwanted noise (*e.g.* noise from the air supply) still exists as the measurements were not performed in an anechoic chamber. The cross-correlation technique was therefore applied to pick out radiated sound from the rough plates. Accordingly the numerical prediction should also consider the cross correlation between two close microphones.

We assume that the noise signals obtained by the two microphones, *i.e.*  $p(\mathbf{x}_1, t_1)$  and  $p(\mathbf{x}_2, t_2)$  for each subarea, are well correlated, so that

$$p(\mathbf{x}_2, t_2)|_{\mathbf{x}_2} = p(\mathbf{x}_1, t_1 + \Delta t)|_{\mathbf{x}_1}, \quad (4.1)$$

where  $\Delta t$  is the difference in observer time of two microphones,

$$\Delta t = t_2 - t_1 = \frac{|\mathbf{x}_2| - |\mathbf{x}_1|}{c}. \quad (4.2)$$

Hence the Fourier transform of  $p(\mathbf{x}_1, t_1)$  and  $p(\mathbf{x}_2, t_2)$  can be related,

$$\hat{p}(\mathbf{x}_2, \omega) = \hat{p}(\mathbf{x}_1, \omega) \frac{|\mathbf{x}_1|}{|\mathbf{x}_2|} e^{-i\omega\Delta t} \quad (4.3)$$

and the power spectral density becomes

$$\langle \hat{p}(\mathbf{x}_1, \omega) \hat{p}^*(\mathbf{x}_2, \omega) \rangle = |\hat{p}(\mathbf{x}_1, \omega)|^2 \frac{|\mathbf{x}_1|}{|\mathbf{x}_2|} e^{i\omega\Delta t}, \quad (4.4)$$

where  $e^{i\omega\Delta t}$  describes the difference in phase between the two microphones. Similarly, the cross spectrum of predicted roughness noise for two microphones can be approximated by taking the average far-field distance

$$|\bar{\mathbf{x}}| = \sqrt{|\mathbf{x}_1||\mathbf{x}_2|} \quad (4.5)$$

and average directivity angles  $(\bar{\theta}, \bar{\phi})$  in Equation (3.47).

Incorporating these two factors, the numerical method (3.47) becomes

$$P_R(\bar{\mathbf{x}}, \omega) = \sum_{j=1}^{N_A} \frac{A_j \sigma \mu^2 R^4 U_c^2}{4|\bar{\mathbf{x}}|^2 \delta_j^{*4} c^2} \Phi(\omega) D(\bar{\theta}_j, \bar{\phi}_j) e^{i\omega\Delta t}, \quad (4.6)$$

which expresses the cross spectrum of surface roughness noise radiated from a total of  $N_A$  subareas. The effects of shear-layer refraction at the jet boundary is not considered in the modification, which will be explained in Section 4.3.2.

It should also be noted that in Figure 4.1 the rough region starts at 0.34 m from the leading edge, whereas it is assumed in the skin friction formula (3.33) that the surface is roughened over the whole plate. This contradiction can be removed by a correction to the length of the rough region. As shown in Figure 4.3, the boundary-layer thickness after the trip tape can be approximated as the turbulent boundary layer starts from the leading edge. This boundary layer grows along the smooth surface until it achieves a thickness  $\delta_0$  at the front edge of the rough region.  $\delta_0$  can be calculated by means of the 1/9 power law for smooth walls [42],

$$\delta_0 = \frac{0.36 x_{le}}{Re_{le}^{1/6}}, \quad (4.7)$$

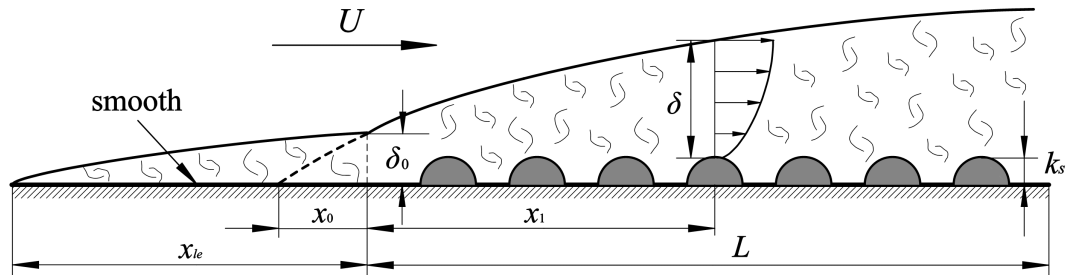


Figure 4.3: Schematic of the rough region at a distance from the leading edge.

where  $Re_{le} = Ux_{le}/\nu$  is a Reynolds number based on the distance  $x_{le}$  from the leading edge. Another way of viewing this is that  $\delta_0$  can be assumed as produced by a hypothetical extension  $x_0$  of the rough region.

Substituting this value of  $\delta_0$  into Equation (3.39) and combining Equation (3.33) gives the correction term

$$x_0 = k_s \exp \left[ \frac{1}{0.707} (c_{f0}^{-1/2.46} - 3.476) \right], \quad (4.8)$$

where  $c_{f0}$  is the local skin friction coefficient at  $x_{le}$ ,

$$c_{f0} = 2 \left[ \frac{1}{\kappa_0} \ln(\delta_0/k_s) + B + \frac{2\Pi_0}{\kappa_0} \right]^{-2}. \quad (4.9)$$

Therefore the length scales in the skin friction formula (3.33), *i.e.*  $x_1$  and  $L$ , are corrected to  $x_1 + x_0$  and  $L + x_0$ , respectively, for the rough region not starting from the leading edge of the plate.

### 4.2.3 Results and discussion

The sound pressure spectra for the rough and smooth plates measured by the B&K microphones are shown in Figure 4.4 and compared with the numerically predicted roughness noise spectra using different wavenumber-frequency spectrum models. The cross-spectra results are presented for the microphone pair, M3 & M4, because it showed the greatest signal to noise. The experimental data were processed in narrow band and divided by the bandwidth  $\Delta f = 8$  Hz. For the B&K microphone system in use, the sampling frequency is  $65.536$  kHz =  $2^{16}$  Hz, the data length is 60 s and the overlap value is 2. Therefore the length of fast Fourier transform (FFT) is  $2^{16}/8 = 8192$  samples, and the number of average for cross-spectra is  $(60 \times 2^{16} \times 2/8192) - 1 = 959$ .

The acoustic measurements were performed for a series of flow velocities,  $U = 10, 15, \dots, 30$  m/s. The free-stream velocities were measured using a Pitot tube and a differential transducer with a resolution of 0.01 mm H<sub>2</sub>O. The surface roughness noise scales as  $U^6$  and so it is too quiet at lower flow velocities and more evident above the TE noise which scales as  $U^5$  at the higher velocity. Therefore the



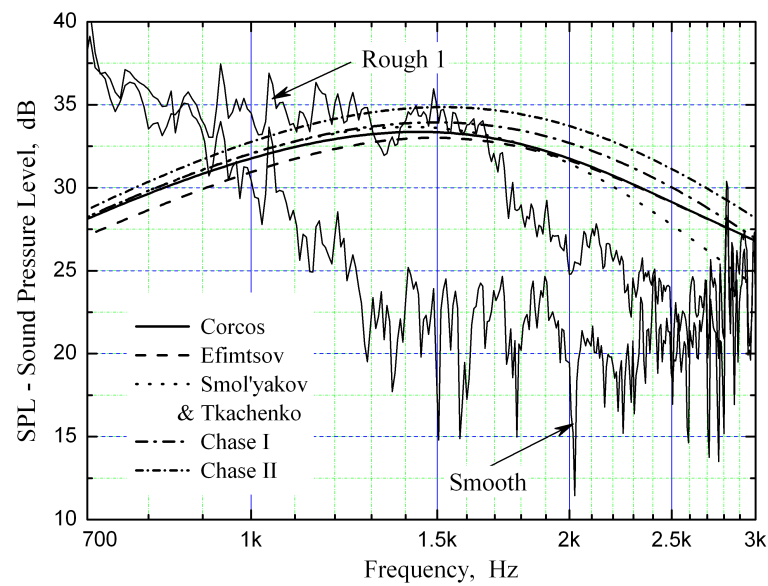
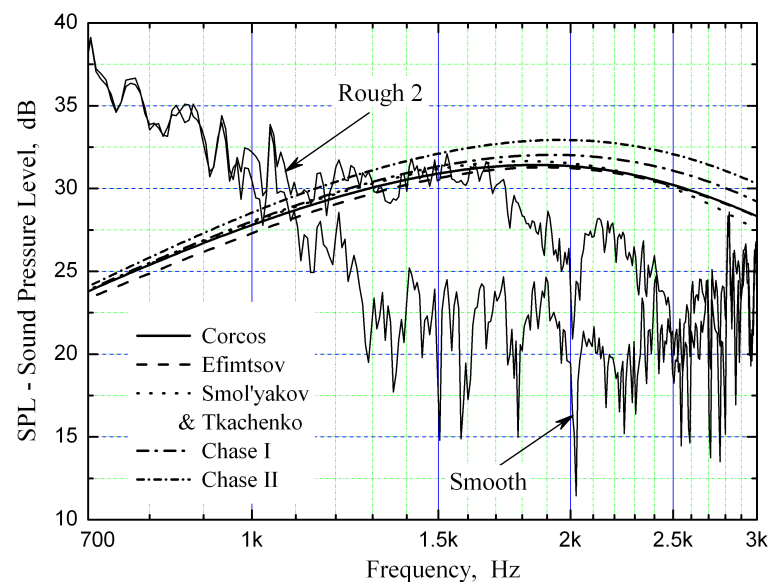
(a) Rough 1,  $R = 4$  mm,  $\sigma = 0.50$ (b) Rough 2,  $R = 3$  mm,  $\sigma = 0.44$ 

Figure 4.4: Comparison between experimental and predicted roughness noise spectra. Smooth-wall experimental results are shown for comparison.  $U = 30$  m/s.

experimental results discussed in this section (and Sections 4.3.3–4.3.5) are for the velocity  $U = 30$  m/s when differences between the acoustic data of the rough and smooth plates are most evident.

As shown in Figure 4.4, the measured noise spectra are significantly contaminated by facility noise. The background noise dominates at most of the frequencies including noticeable peaks at 3 kHz which are from the driving motor

and fan of the wind tunnel. At the low frequencies ( $f < 800$  Hz) the dominating noise is probably from the air supply. The predicted TE noise spectrum peaks around 100 Hz with very low spectral levels. Since there is no difference between the measured background noise spectra with a smooth plate and without any plate, it is assumed that the contribution of the TE noise to the total noise spectrum is negligible.

However, the measured noise spectra of the rough plates are still above that of the smooth plate between 1–2.5 kHz, making the roughness noise detectable from the noise of the smooth plate. This appears to be confirmed by the fact that the rough-plate spectra are less fluctuating than that of the smooth plate in this frequency range, which suggests that they contain statistically steady sources actively radiating sound. Comparing results for the two roughness elements, one notices that the sound from the smaller roughness element displays a lower spectral peak, though not very distinct, by about 5 dB at a slightly higher frequency. Beamforming source maps in Section 4.3 also confirm that the rough plates have remarkably higher acoustic source strengths than the smooth plate in this frequency range. Moreover, it is shown that different wavenumber-frequency spectrum models produce approximately the same roughness noise spectra.

The measured and predicted roughness noise spectra show a reasonable amount of agreement. The numerical method is capable of predicting radiated roughness noise at approximately the same absolute levels as the experimental results in the frequency range 1–1.7 kHz, although the difference becomes notable at higher frequencies. One possible reason for the discrepancy in  $f > 1.7$  kHz frequency is that the approximate Green's function in Equation (3.5) is based on the assumption,  $k_0\delta \ll 1$ . Take Rough1 for example, the average boundary-layer thickness over the rough region  $\bar{\delta} \sim 2.9$  cm, and thus the above assumption is not met when  $f = c/2\pi\bar{\delta} \sim 1.8$  kHz. Another reason could be the inaccuracy in the empirical models of smooth-wall wavenumber-frequency spectrum. The adjustable coefficients in these models were fixed by the authors [25, 26, 31, 43, 140] in comparison with their experimental data. However, there is no completely satisfactory theoretical understanding of the characteristics of the smooth-wall pressure spectrum so far.

## 4.3 Phased Array Measurement

### 4.3.1 Introduction and survey

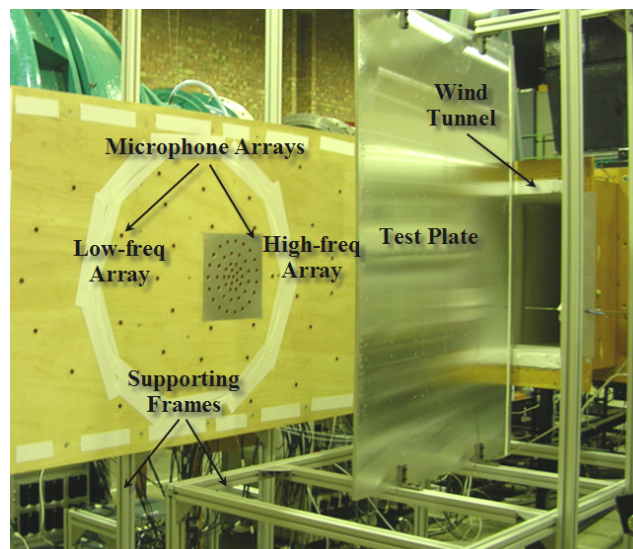
With the prediction model preliminarily validated through the acoustic spectrum measurement, we apply phased microphone arrays to the experimental study to localize the possible dipole sources in the rough region and to provide another form of validation for the prediction model. The advantage of phased microphone arrays lies in the improved signal-to-noise ratio, and hence noise sources below the background tunnel noise can be identified.

Over the past decade, an increasing need has emerged for noise source localization in acoustic measurement. Phased microphone arrays, based on the technique of acoustic beamforming [38, 87], have been widely applied to experimental acoustics and numerous engineering fields. The theoretical foundation of microphone array was established by Billingsley and Kinns [16] who constructed a one-dimensional linear microphone array for real-time jet-noise source location on full-size jet engines. Fisher *et al.* [55] also measured jet noise with two microphones using a polar correlation technique. Recent applications of microphone arrays to jet noise were reported by Ahuja *et al.* [5], Narayanan *et al.* [113], Hileman *et al.* [74], *etc.*

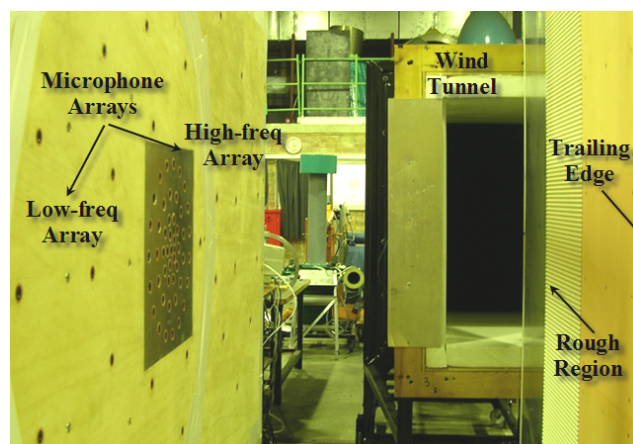
Siller *et al.* [134] discussed the advantages and disadvantages of a phased array for monitoring engine core noise. More recently, Quayle *et al.* [125] examined the effect of overall layout changes on landing-gear noise production at low frequencies with two nested 48-microphone arrays. Martinez [102] used a polar-arc phased array to locate turbofan-engine noise source components. Lan *et al.* [94] reported the measurement of engine inlet noise using several advanced array systems with different elements and testing locations. Other applications of microphone arrays in aeroacoustics include airframe noise [68, 70, 120], aircraft flyover noise [104, 105, 121], and ground vehicle noise [11, 92].

The principle idea for microphone array processing techniques is to sum the signals coherently at different microphones to enhance the signal emanating from

a focal position while minimizing the contribution from out-of-focus locations [87]. A crucial step for this technique is to specify a rule, referred to as *beamforming*, for appropriate summation of the microphone signals to reconstruct the spatial distribution of noise sources [151]. For the simplest delay-and-sum beamformer, the outputs of time-delayed signals are summed, with the delays as a function of focus position and microphone location, to estimate the source distribution [87]. When a source is at the focus position, the signals add to produce an enhanced signal, whereas for out-of-focus positions the signals cancel.



(a) Overview



(b) Closeup

Figure 4.5: Schematic of the experimental setup for phased array measurement.

### 4.3.2 Experimental setup

The phased array measurement utilizes the same open-jet wind tunnel facility and the test rough plates as the acoustic spectrum measurement. These facilities have been described in Section 4.2.1 and this section will be focused on the phased microphone array system. This array system is the same as the nested microphone arrays installed in the CUED Markham wind tunnel, and its design and implementation can be found in Shin *et al.* [132].

Figure 4.5 illustrates the experimental setup for the phased array measurement. In the present study, a two-dimensional (2D) phased microphone array system consisting of a high-frequency (HF) array and a low-frequency (LF) array was used. Both arrays contain 48 microphones located on optimized concentric circles or ellipses and flush mounted in a rigid board. As shown in Figure 4.5(a), the array board is supported by an aluminium frame with wheels. The board plane is aligned parallel to the test plate and the distance between them is adjustable. As the B&K microphones in Figure 4.1, the microphone arrays were located in the far field of each roughness element, but not in the far field of the entire rough region.

For both arrays, the 48 microphones are positioned irregularly with nonuniform spacing. As shown in Figure 4.6, the microphones are packed more closely near the centre of the array and are wider spaced towards the boundary. For each microphone,  $d$  is defined as the distance to its nearest neighbour. Table 4.2 gives the overall array dimensions and the maximum and minimum values of  $d$  for each array. The LF array employs a wider distribution of microphones and hence has a better resolution of source localization than the HF array at low frequencies.

Figure 4.7 illustrates the schematic of the acoustic measurement by a phased microphone array. During a measurement the acoustic pressures were synchronously acquired by array microphones at a sampling frequency of 120 kHz (HF array) or 30 kHz (LF array) and a duration time of 60 s. The raw data were transferred to the computer through the 48-channel data acquisition system and post-processed by analysis software. Then in the beamforming of the post-processed data, narrow-band acoustic scans were performed to determine the

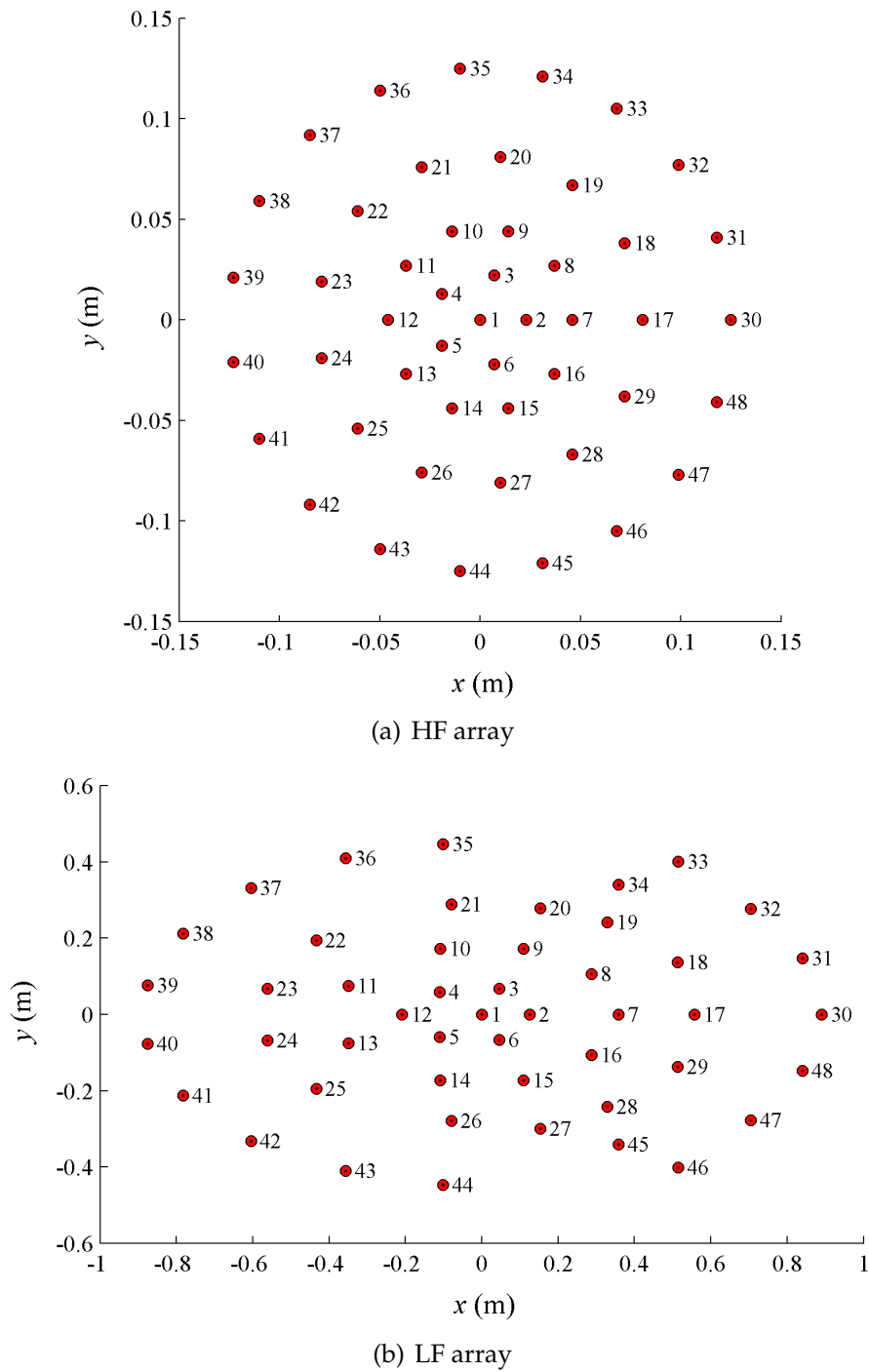


Figure 4.6: Microphone positions of the HF and LF arrays.

Table 4.2: Overall dimensions and the maximum and minimum values of  $d$  for each array.

Microphone array	Length (m)	Width (m)	$d_{\min}$ (m)	$d_{\max}$ (m)
HF array	0.25	0.25	0.023	0.044
LF array	1.77	0.89	0.081	0.238

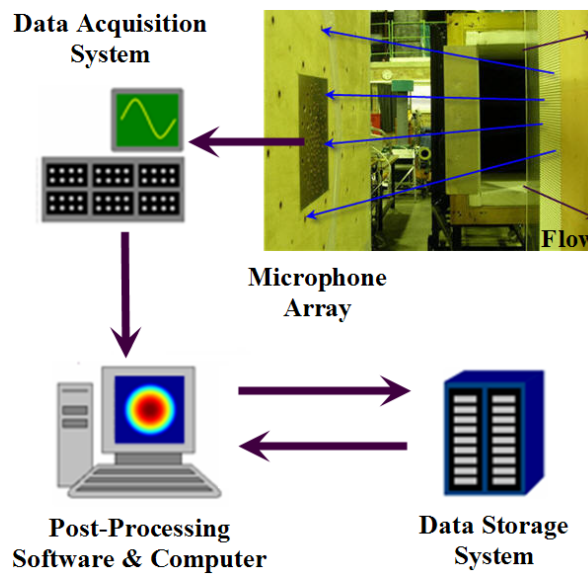


Figure 4.7: Schematic of the acoustic measurement by a phased microphone array.

source powers (see Section 7.3.1) in a given scanning grid. Finally, source maps with sound pressure level (SPL) data were generated by summing the narrow-band data to 1/3 octave-band data. The final data were sent to the 1.2 TB data storage system for future reference.

In the present beamformer, the measured signals in the time domain are transformed to complex pressures in the frequency domain by the FFT. The matrix of cross-power spectral densities between all microphone combinations is formulated in the frequency domain. The open-jet tunnel has some background noise and so we remove the diagonal elements of the matrix (*i.e.* the auto-power) and determine the monopole source strength at each element of the source grid that gives a best least-square fit to the measured cross-powers. First, a scanning grid containing the test plate is defined. The monopole source strength at each grid point is estimated by finding the value which gives the best match between measured cross-powers and the sound field of a simulated, unit strength monopole located at that grid point. The beamformer uses the true distance from each source element to each microphone.

It is also possible to obtain an estimate of source powers at each location by using matrix inversion techniques to solve for all sources in the scanning plane simultaneously. This approach was pioneered for phased array measurements

by Brooks and Humphreys [20] and is referred to as a “Deconvolution Approach for the Mapping of Acoustic Sources” (DAMAS) that gives very good solutions for simulated, incoherent monopole sources. However, the DAMAS approach is very computationally intensive, the computation time scaling with the square of the number of grid points, and so its implementation is significantly beyond the facilities available in this study.

Obviously, the advantage of an open jet is to eliminate the reverberation noise of a closed-return wind tunnel. However, the uniform flow assumption of analysis software is not valid in the case of out-of-flow measurements in the test section of an open jet [133]. In this case, the effect of shear-layer refraction must be incorporated in the source description of beamforming analysis. In fact for the low-speed wind tunnel in use ( $M < 0.1$ ), although the propagating acoustic wave is somewhat refracted during transmission through the shear layer, the amplitude of received acoustic pressure by array microphones is almost unaltered [38], and hence the effect of shear-layer refraction on the predicted source strengths is negligible. However, even a minor error in the signal phase will be amplified into a considerable distortion of source locations. In this study, the Amiet correction [6] for an infinitely thin shear layer was applied in the beamforming analysis for the shear-layer correction.

### 4.3.3 Results and discussion

#### 4.3.3.1 Beamforming source maps

The comparison of measured noise spectra in Figure 4.4 suggests that it would be beneficial to focus the microphone array measurements within 1000–2500 Hz frequency range. Figures 4.8 and 4.9 illustrate the beamforming source maps for the rough and smooth plates obtained by the HF and LF arrays at Location 2 (see Table 4.3). Three 1/3 octave-band frequencies are selected with centre frequencies 1250 Hz, 1600 Hz and 2000 Hz, respectively.

In the beamforming analysis, the origin of the  $x$ - $y$  coordinates in all source maps is fixed at the array centre. The flow direction is from the left to the right. The inner



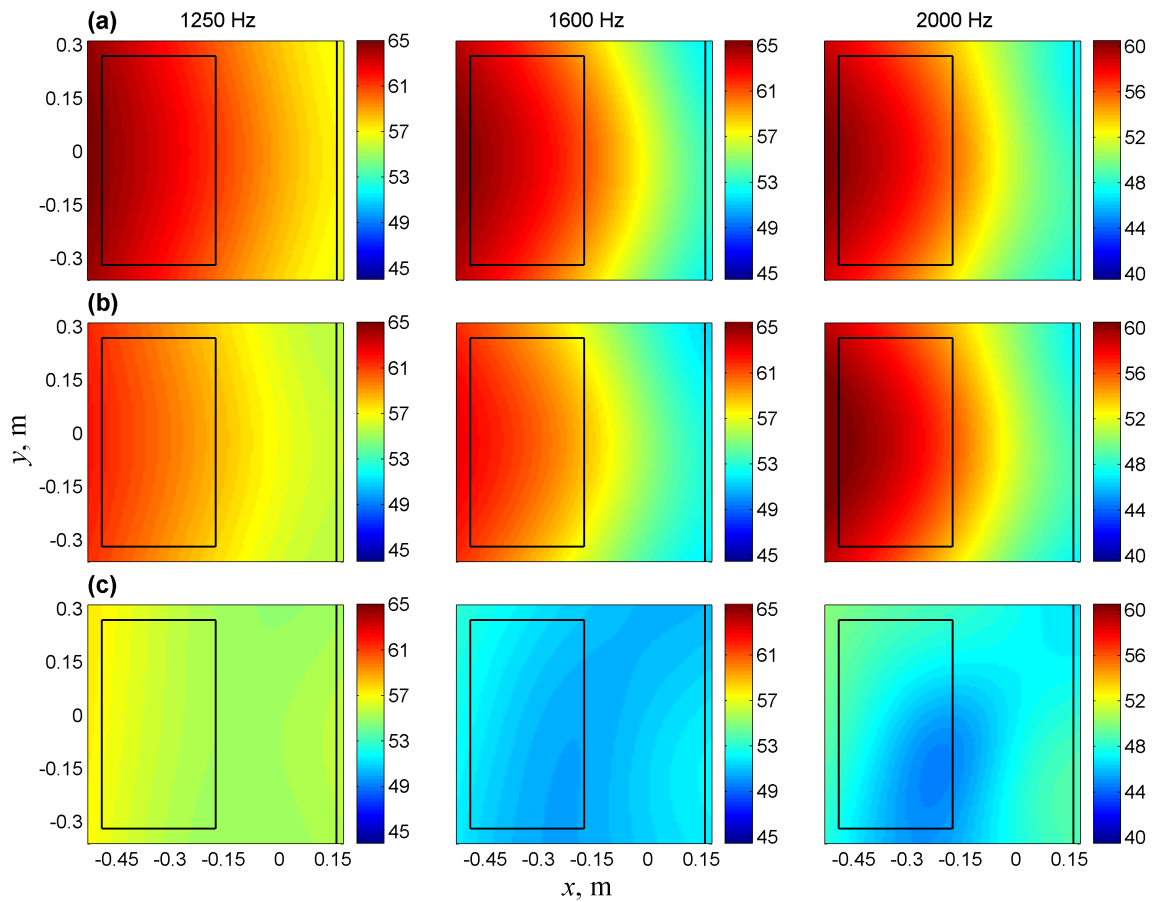


Figure 4.8: Measured source maps by the HF array: (a) Rough1, (b) Rough2, (c) Smooth.  $U = 30$  m/s.

frame outlines the boundary of the rough region and the dark line downstream denotes the trailing edge. Note that in the current setup, only two rough panels were mounted into the  $0.64 \times 0.64$  m<sup>2</sup> recess to form a smaller rough region upstream, which helps reduce the interference of sound scattering from the trailing edge. In addition, the source powers have been converted to SPL data at a reference distance of  $1/\sqrt{4\pi}$  m from the source [133]. The colour bar gives the SPL in dB, and the colour bars for the rough and smooth plates at the same frequency are shown on identical scales for easy comparison. The dynamic ranges of the source maps obtained by the HF and LF arrays are about 12 dB and 16 dB, respectively.

As shown in Figures 4.8 and 4.9, the source strengths on the rough plates exceed those on the smooth plate by about 10–15 dB. The source patterns of the two rough plates appear very similar with higher SPL for Rough1 at frequencies of 1250 and 1600 Hz. However at  $f = 2000$  Hz, the source strengths of Rough2 exceed those of

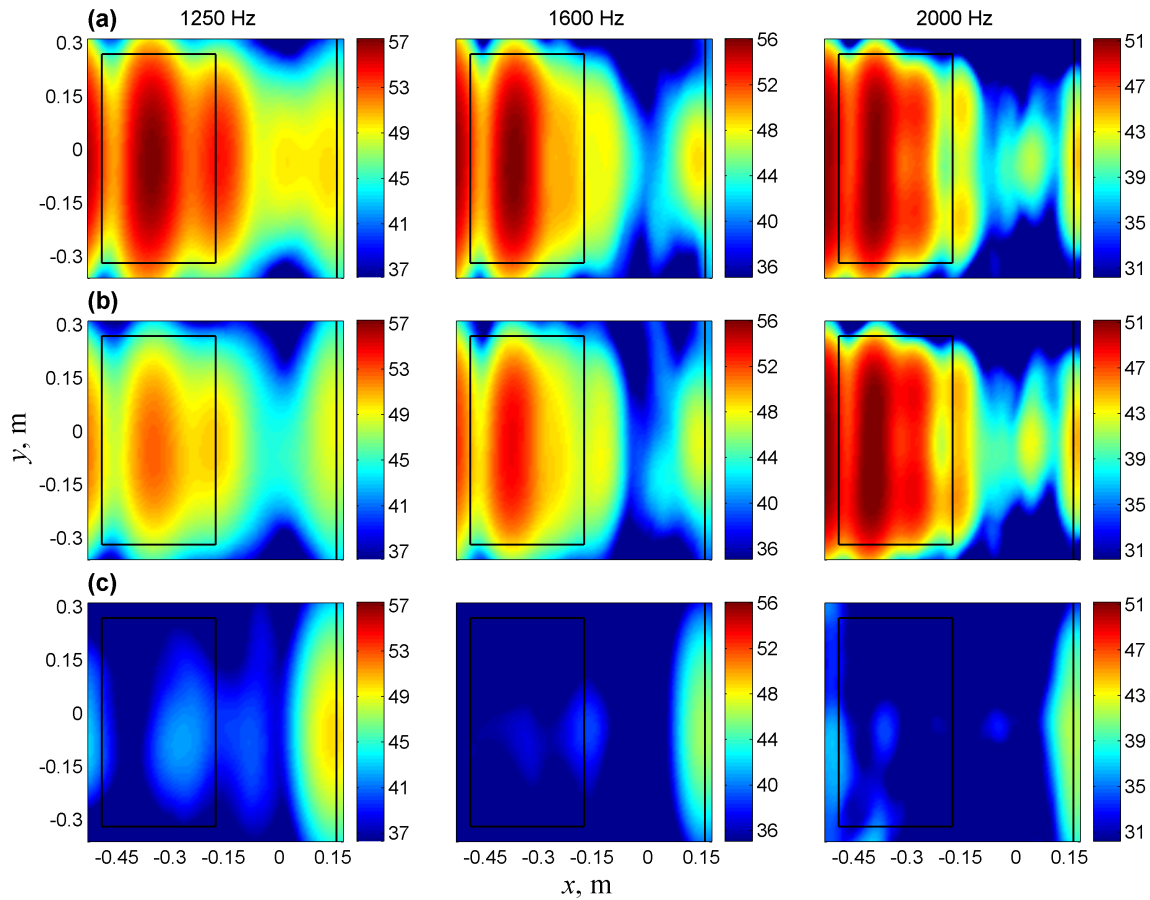


Figure 4.9: Measured source maps by the LF array: (a) Rough1, (b) Rough2, (c) Smooth.  $U = 30$  m/s.

Rough1, which is consistent with the noise spectra data in Figure 4.4. The major lobe of maximum source strengths occurs in the upstream portion of the rough region. This is because the ratio of roughness height to boundary-layer thickness,  $R/\delta$ , decreases as the boundary layer grows along the plate chord, which makes the downstream roughness elements less significant as sound scatterers.

Comparing the source maps in Figures 4.8 and 4.9, we find that the LF array gives better resolution than the HF array due to the selected low frequencies and the widely distributed sources in this case. The LF array is able to detect a secondary lobe around the dark line, as can be seen in Figure 4.9, which is principally produced by the trailing edge. The rough plates also generate stronger TE noise than the smooth plate because on a rough plate the friction velocity  $u_\tau$  and boundary-layer thickness  $\delta$  are increased due to the enhanced surface drag and turbulence production [130].

However, we notice that the HF array measures 8–9 dB higher maximum SPL than the LF array at all frequencies. A possible explanation is that the beamforming algorithm assumes a monopole source with uniform directivity, and that the locations of the array microphones are different. The microphones of the HF array are confined in a relatively small region where considerable sound radiation can be received from the rough region upstream, while the microphones of the LF array are distributed in a much wider area and thus some of them are located close to the  $z$ -axis where the roughness dipoles radiate little sound. The other and perhaps more important reason is based on the combination of the distributed nature of roughness sources and the difference in the resolution of both arrays. The HF array has poorer resolution than the LF array at the chosen frequencies, and hence tends to capture more roughness sources and add up their source levels.

#### 4.3.3.2 Effect of array locations

Table 4.3: Locations of the array centre.

Location no.	$x$ (m)	$y$ (m)	$z$ (m)
1	0.04	0.025	0.47
2	0.18	0.025	0.64
3	0.36	0.025	0.60

The sound radiation from the two rough plates, Rough1 and Rough2, was measured at three streamwise locations to detect some directivity features of the dipole sources. The coordinates of the array centre for Locations 1–3 are listed in Table 4.3 with the origin  $O$  at the centre of the rough region (see Figure 4.12). In the  $x$ -direction, Location 1 is very close to the origin  $O$ , Location 2 is a bit downstream, and Location 3 is further downstream and behind the rear edge of the rough region. Location 1 is also closest to the origin  $O$  in the  $z$ -direction. In these measurements, four rough panels were used and so the rough region is doubled in area compared with that in Figures 4.8 and 4.9.

Figure 4.10 shows the beamforming source maps of Rough1 and Rough2 obtained by the HF array at Locations 1–3, respectively. As can be seen from

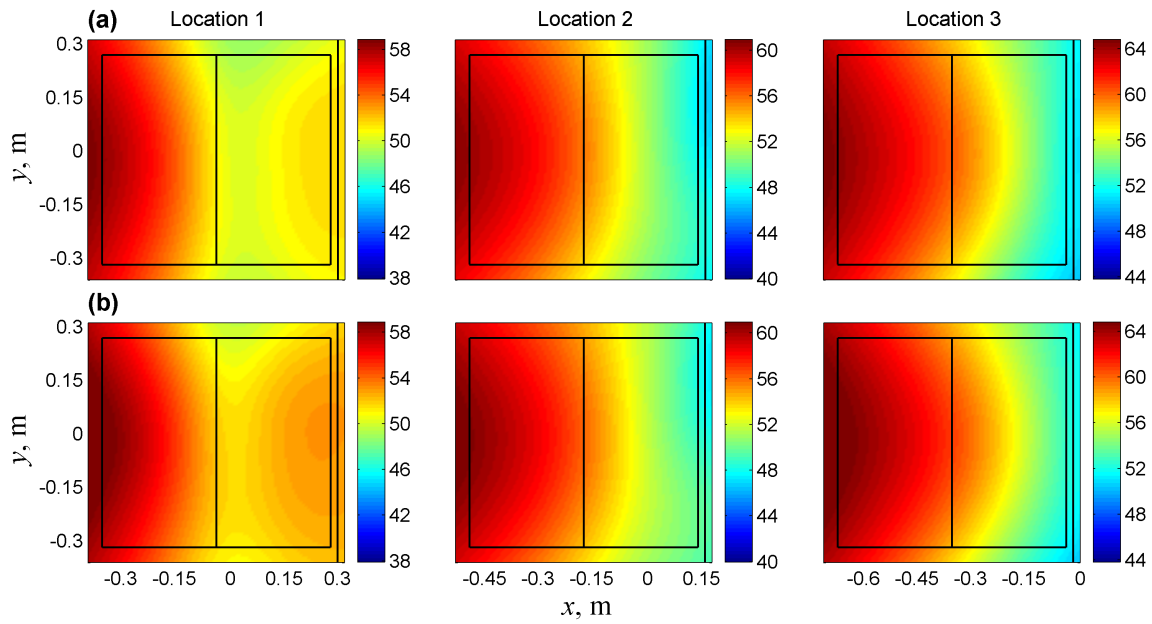


Figure 4.10: Measured source maps at Locations 1–3: (a) Rough1, (b) Rough2. HF array,  $f = 2000$  Hz,  $U = 30$  m/s.

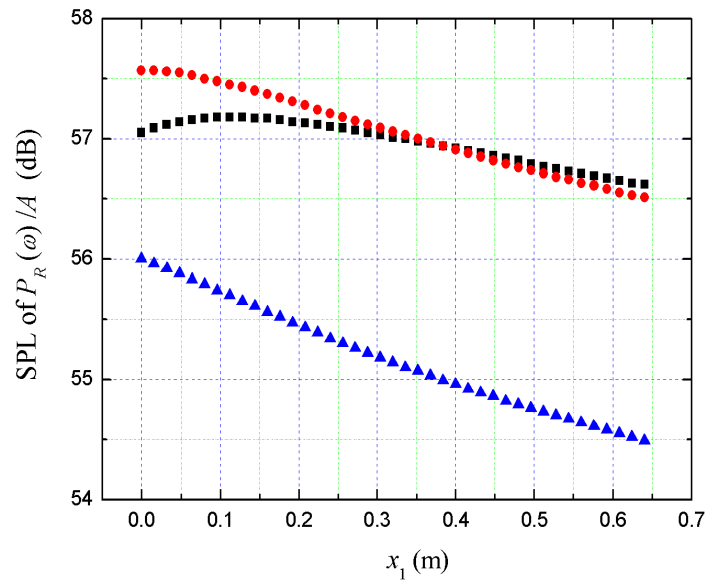
Figure 4.10, Location 1 produces a major lobe upstream with a secondary lobe downstream. The minimum source strength lies in the middle of the rough region. This is very close to the centre of the array and occurs because the dipoles do not radiate sound in their normal plane. At the chosen frequency  $f = 2000$  Hz, the secondary lobe of Rough2 is stronger than that of Rough1 and covers a larger area, which has been predicted by the noise spectra comparison in Figure 4.4. In contrast, only the distributed major lobe exists in the source maps at downstream Locations 2 and 3. Higher maximum strengths can be observed as the array shifts downstream from Location 1 to Locations 2 and 3. All these features agree with the directivity characteristics of a distribution of dipole sources in the flow direction.

Comparing the distributed area of the major lobe at Locations 1–3, we notice that the beamforming resolution becomes gradually worse as the array moves farther from the origin  $O$ . However at the nearest location, least radiated roughness noise is received by the microphone array due to the dipole directivity. Therefore, the compromise solution is to choose an array location a bit downstream from the central rough region, and this explains why Location 2 was used for the measurements in Section 4.3.3.1.

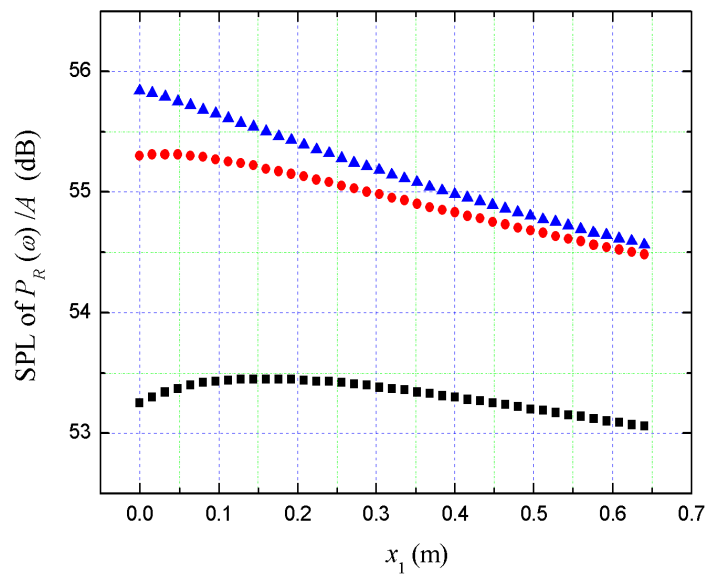
### 4.3.4 Theoretical simulation

#### 4.3.4.1 Theory

In this section, the theoretical prediction model described in Equation (3.47) of Chapter 3 is applied to calculate sound radiation from different streamwise portions of the two rough plates in the experiments. The theoretical results are for the power



(a) Rough1



(b) Rough2

Figure 4.11: Predicted SPL of  $P_R(\omega)/A$  with streamwise distance  $x_1$  for chosen frequencies: ■ 1250 Hz, ● 1600 Hz, ▲ 2000 Hz.  $U = 30$  m/s.

spectral density  $P_R(\omega)$  from a unit rough area to an observer at  $\theta = \pi/4$ ,  $\phi = 0$  and  $|\mathbf{x}| = 1/\sqrt{4\pi}$  m. Figure 4.11 shows the predicted SPL of  $P_R(\omega)/A$  distributed over the two rough plates at 1250 Hz, 1600 Hz and 2000 Hz frequencies. At the two higher frequencies,  $P_R(\omega)/A$  decreases with streamwise distance  $x_1$  from the front edge of rough region. At 1250 Hz, there is a maximum at  $x_1 = 0.11$  m for the plate Rough1 and 0.16 m for Rough2.

On a rough plate, as the boundary layer grows along the chord ( $x$ -axis), the local boundary-layer properties  $\delta^*$  and  $u_\tau$  are increasing and decreasing, respectively, both of which are determined by  $x_1$ . The overall dependence of  $P_R(\omega)/A$  on  $x_1$  at a particular frequency is principally due to the variation of  $\Phi(\omega)$  as shown in Figure 3.3. More detailed investigation of the terms shows that the variation of  $\Phi(\omega)$  accounts for the maximum of  $P_R(\omega)/A$ . At a frequency of 1250 Hz,  $\Phi(\omega)$  has a maximum at  $x_1 = 0.11$  m for Rough1 and at  $x_1 = 0.16$  m for Rough2. At the higher frequencies  $\Phi(\omega)$  decreases across the entire rough regions.

#### 4.3.4.2 Motivation

The comparison of beamforming source maps in Section 4.3.3.1 demonstrates that the rough plates produce distinctly stronger noise sources than the smooth plate and enhance the TE noise somewhat. However, these “source” maps are not a true representation of the locations and relative strengths of the roughness dipoles because the beamforming algorithm assumes a distribution of monopole sources, and hence can not be used directly to validate the theoretical prediction.

Jordan *et al.* [89] have shown that the standard beamforming technique is inadequate for both the source location and the measurement of a simple dipole, and that this is due to the assumption of monopole propagation in the calculation of the phase weights used to steer the focus of the array. They developed a correction to the beamforming algorithm to account for the dipole propagation characteristics, and applied it to array measurements for an aeroacoustic dipole produced by a cylinder in a cross flow. The true source location and source energy of the dipole was then retrieved in the resulting source map after applying this correction.

The technique of Jordan *et al.* [89], however, is not applicable in the case of a distribution of dipoles because their directivities and hence the required corrections vary over the source region, unlike the case of a single dipole. Moreover, in practice the source mechanisms of a general aeroacoustic system could be very complex. There might be a combination of both monopole and dipole sources, and the dipoles may have axial and spanwise components. Therefore it would be difficult to implement a beamformer consistent with the hypothesized type of sources.

Instead of altering the beamformer, an indirect approach is to theoretically simulate a distribution of incoherent dipoles over a rigid plate using the prediction model developed in this thesis, to process the predicted sound field through the same algorithm as the experiment, and to generate predicted source maps that can be directly compared with the experimental results. This is equivalent to comparing theory and experiment after applying a filter which suppresses much the extraneous noise in the experiments. It provides an indirect way of comparing all the theoretical and experimental cross-powers between microphone pairs. For each grid point on the source-scanning plane, we determine the monopole source strength that gives the best fit to all the cross-powers. The quantitative agreement between the best-fit monopoles over the source plane for the theoretical and experimental cross-powers validates the prediction model.

#### 4.3.4.3 Simulation overview

The theoretical simulation for an experiment using phased microphone arrays is illustrated in Figure 4.12. A program SIMSRC was utilized to describe a distribution of incoherent dipoles over the rigid plate and simulate the sound detected by the microphone array, as exactly in the experimental setup. This program requires the original source locations and source strengths as input parameters. The post-processing and beamforming analysis of the simulation are based on a monopole source assumption as previously mentioned, and thus are not directly applicable to the dipole case of roughness noise. Nevertheless, SIMSRC is able to generate cross-power data for incoherent groups of coherent monopole sources [133]. In this case, each dipole source can be modelled by coherent pairs of

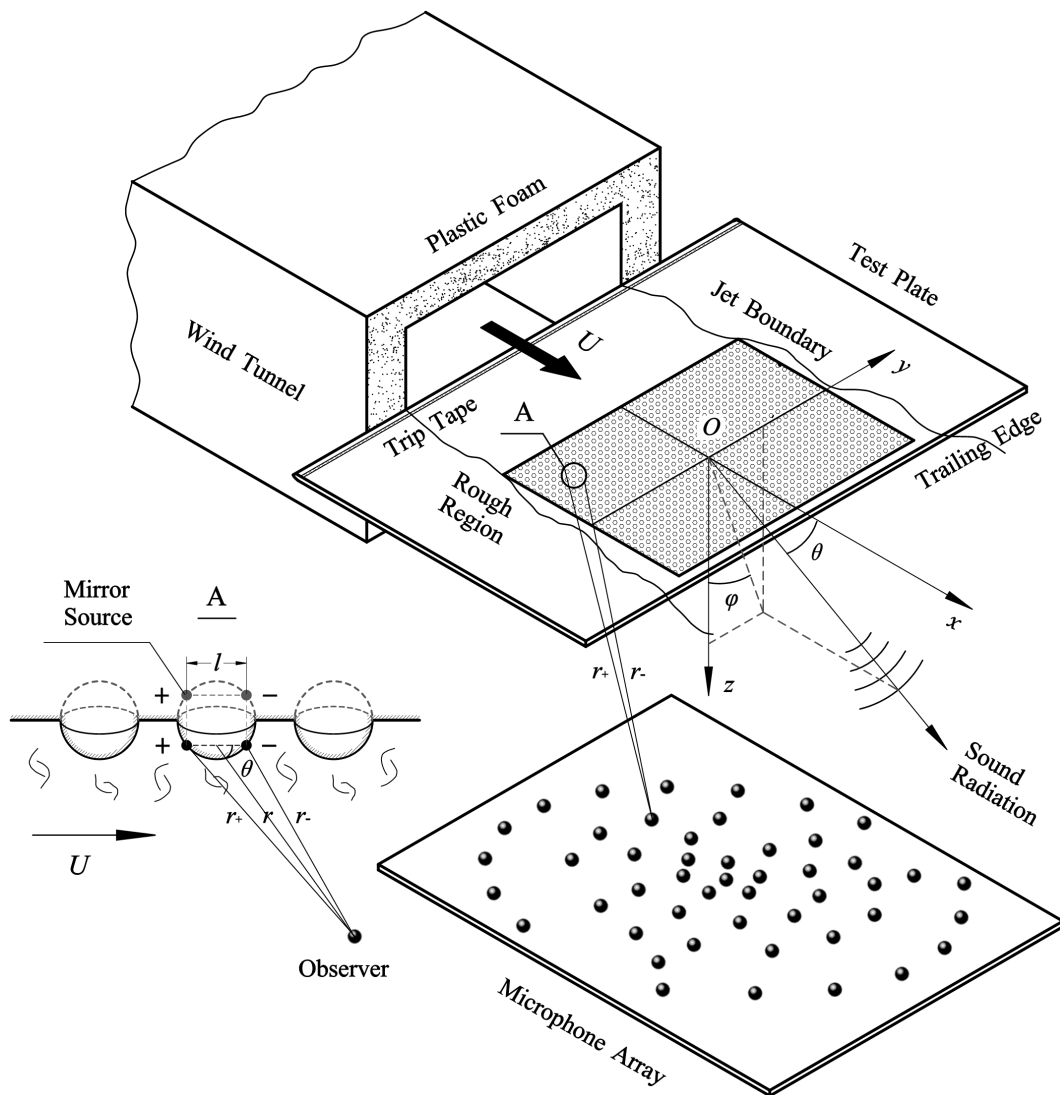


Figure 4.12: Schematic of the theoretical simulation.

closely spaced monopoles with opposite phase. Because the rigid plate behaves as a passive reflector, the mirror sources were also taken into account as coherent with the original sources. The distribution of incoherent dipoles was therefore modelled by incoherent groups of the four coherent monopole sets.

The phased microphone array is generally used to detect the source locations and source patterns, and the SPL data shown in source maps are usually obtained as relative and just for reference. In this study, however, we attempted to simulate the real source strengths in magnitude as well as the source locations. The simulated dipole sources were located at each hemispherical boss and the equivalent source strengths were determined from the prediction model as described below. The



simulated acoustic field was then processed in the same way as in the experiments to obtain predicted beamforming source maps.

We now commence the determination of equivalent source strengths with the derivation of the acoustic field of a dipole source. The mean flow effects have been neglected since the prediction model is based on an assumption of low Mach number which is also satisfied in the experimental setup ( $M < 0.1$ ). The shear-layer refraction has therefore not been considered in the derivation either.

#### 4.3.4.4 Acoustic field of a dipole

The acoustic frequency spectrum for an ideal monopole in a medium without flow can be expressed as [39]:

$$\hat{p}(\omega) = \frac{-a(\omega)}{4\pi r} e^{-ikr}, \quad (4.10)$$

where  $a(\omega)$  is the monopole strength in frequency domain,  $k = \omega/c$  is the acoustic wavenumber, and  $r$  is the propagation distance from source to observer.

A dipole source can be modelled as a coherent pair of closely placed monopoles with opposite phase at a distance  $l$  apart, as shown in Figure 4.12. The acoustic field of a dipole is obtained by combining the radiated sound of these two monopoles:

$$\hat{p}(\omega) = \frac{-a(\omega)}{4\pi r_+} e^{-ikr_+} - \frac{-a(\omega)}{4\pi r_-} e^{-ikr_-}, \quad (4.11)$$

where  $r_+$  and  $r_-$  are the propagation distances for the two monopoles with opposite phase,

$$\begin{cases} r_+ \approx r + \frac{l}{2} \cos \theta, \\ r_- \approx r - \frac{l}{2} \cos \theta. \end{cases} \quad (4.12)$$

In the far field,  $r \gg l$ , the amplitude difference between the radiated sound of two monopoles is small, and thus in Equation (4.11)  $r_+$  and  $r_-$  can be approximated by  $r$  in the amplitude part. However, the phase difference can not be ignored. Substituting Equation (4.12) into Equation (4.11), we obtain

$$\begin{aligned} \hat{p}(\omega) &\approx \frac{-a(\omega)}{4\pi r} e^{-ikr} \left( e^{-i\frac{kl \cos \theta}{2}} - e^{i\frac{kl \cos \theta}{2}} \right) \\ &= \frac{-a(\omega)}{4\pi r} e^{-ikr} \left( -2i \sin \frac{kl \cos \theta}{2} \right). \end{aligned}$$

If the dipole is compact (*i.e.*  $kl \ll 1$ ), Equation (4.13) can be simplified as:

$$\hat{p}(\omega) = \frac{a(\omega)}{4\pi r} e^{-ikr} \cdot ikl \cos \theta. \quad (4.13)$$

In the presence of a reflecting rigid plate, the mirror source of the dipole need to be included, and hence the aggregate acoustic field can be obtained by multiplying Equation (4.13) by a factor of 2. The power spectral density of the acoustic frequency spectrum  $\hat{p}(\omega)$  is

$$P(\omega) = \Lambda(\omega) \left| \frac{ikl \cos \theta}{2\pi r} e^{-ikr} \right|^2, \quad (4.14)$$

where  $\Lambda(\omega)$  is the power spectral density of  $a(\omega)$ ,

$$\langle a(\omega)a(\omega') \rangle = 2\pi\Lambda(\omega)\delta(\omega + \omega'). \quad (4.15)$$

#### 4.3.4.5 Equivalent source strengths

As has been discussed in Section 3.4.2, the first term of the directivity function (3.48),  $I_1 \cos^2 \theta$ , describes the sound field due to a dipole in the flow direction, while the second term  $I_2 \sin^2 \theta \sin^2 \phi$  accounts for a dipole in the plate plane but normal to the flow direction. To link this to the beamforming simulation, we consider a distribution of dipoles with two dipoles  $DPL_1$  and  $DPL_2$  at each hemispherical boss and determine the equivalent source strengths  $a_1(\omega)$  and  $a_2(\omega)$ . Herein  $DPL_1$  is orientated in the flow direction and  $DPL_2$  is normal to the flow direction.

Now we consider a rough region of unit area which contains  $N$  roughness elements. The acoustic field of  $DPL_1$  can be described by Equation (4.14), and hence the aggregate power spectral density of  $N$  incoherent dipoles is

$$P_1(\omega) = \sum_{j=1}^N P_{1j}(\omega) = \frac{N\Lambda_1(\omega)k^2 l^2 \cos^2 \theta}{4\pi^2 r^2}. \quad (4.16)$$

From the prediction model (3.47), the contribution of the dipole  $DPL_1$  to  $P_R(\omega)$  for a unit rough area  $A = 1$  is

$$P_{R1}(\mathbf{x}, \omega) = \frac{\sigma\mu^2 R^4 U_c^2}{4|\mathbf{x}|^2 \delta^{*4} c^2} \Phi(\omega) I_1 \cos^2 \theta. \quad (4.17)$$

Combining Equations (4.16) and (4.17) and taking  $r = |\mathbf{x}|$ , we obtain the theoretical prediction for  $\Lambda_1(\omega)$ :

$$\Lambda_1(\omega) = \frac{\pi^2 \sigma \mu^2 R^4 U_c^2}{N l^2 \delta^{*4} \omega^2} \Phi(\omega) I_1. \quad (4.18)$$

The above derivation is based on the continuous Fourier transform (CFT) and  $\Lambda_1(\omega)$  denotes the power spectral density of  $a_1(\omega)$ . However in the theoretical simulation for acoustic measurements, the discrete Fourier transform (DFT) is applied and thus  $\Lambda_1(\omega)$  actually means the frequency-dependent source power [39]. In this case, the equivalent source strength  $a_1(\omega)$  required by the simulation program SIMSRC can not be derived directly from  $\Lambda_1(\omega)$ . Instead, it is necessary to compare the total source power in a frequency band between the CFT and DFT.

The predicted total power of  $\Lambda_1(\omega)$  in the frequency band  $[\omega_1, \omega_n]$  is

$$\langle a_1^2(t) \rangle = \frac{1}{2\pi} \int_{\omega_1}^{\omega_n} \Lambda_1(\omega) d\omega. \quad (4.19)$$

In the simulation, the total power of  $\Lambda_1(\omega)$  in  $[\omega_1, \omega_n]$  can be expressed as (see Appendix B or [58]):

$$\Lambda_{1\text{tot}} = \sum_{i=1}^n |a_1(\omega_i)|^2 = n |\bar{a}_1(\omega)|^2, \quad (4.20)$$

where  $n$  is the number of frequency intervals;  $a_1(\omega_i)$  is the equivalent source strength in the  $i$ th frequency interval;  $\bar{a}_1(\omega)$  is the average source strength of  $n$  intervals,  $\omega_1, \omega_2, \dots, \omega_n$ , and is used as the input source strength for the frequency band  $[\omega_1, \omega_n]$  in SIMSRC. By equating the total source powers in the prediction (4.19) and simulation (4.20), the predicted equivalent source strength for the two coherent monopoles of  $\text{DPL}_1$  is given by

$$|\bar{a}_1(\omega)| = \frac{\mu U_c R^2}{l \delta^{*2}} \left[ \frac{\pi \sigma I_1}{2Nn} \int_{\omega_1}^{\omega_n} \frac{\Phi(\omega)}{\omega^2} d\omega \right]^{1/2}. \quad (4.21)$$

Just as the power spectral density  $P_R(\omega)$ , the equivalent source strength  $\bar{a}_1(\omega)$  decreases with increasing streamwise position along the rough region, except at the lowest frequency  $f = 1250$  Hz where it has a maximum near  $x_1 = 0.11$  m for the plate Rough1 and 0.16 m for Rough2. Equation (4.21) describes the variation of the roughness dipole strength with streamwise locations. The value of the dipole size  $l$  is unimportant because  $\Lambda_1(\omega) \sim l^{-2}$  from Equation (4.18) and hence the predicted power spectral density  $P_1(\omega)$  is independent of  $l$ . The only constraint is that  $l$  should satisfy the compact dipole assumption  $kl \ll 1$ . In the present study  $l = R$  is used for convenience.

Similarly, the theoretical prediction for  $|\bar{a}_2(\omega)|$  can be obtained as:

$$|\bar{a}_2(\omega)| = \frac{\mu U_c R^2}{l \delta^{*2}} \left[ \frac{\pi \sigma I_2}{2Nn} \int_{\omega_1}^{\omega_n} \frac{\Phi(\omega)}{\omega^2} d\omega \right]^{1/2}. \quad (4.22)$$

Nevertheless, the contribution of  $I_1$  to  $P_R(\omega)$  is more important than that of  $I_2$  for sufficiently large roughness elements, *i.e.* the roughness Reynolds number  $Ru_\tau/\nu > 1000$ . In addition, in Figure 4.12 the centre of the microphone array is located very close to the centre of the rough region in the  $y$ -direction which is the direction of the dipole  $DPL_2$ . This results in a nearly negligible contribution of  $DPL_2$  to the SPL of the source maps as there is no sound radiation in the normal plane of the  $DPL_2$  orientation. The predicted  $|\bar{a}_1(\omega)|$  and  $|\bar{a}_2(\omega)|$  from Equations (4.21) and (4.22) were then used in the theoretical simulation as the equivalent source strengths for  $DPL_1$  and  $DPL_2$ , respectively.

### 4.3.5 Comparison of measurement and simulation

To compare the source maps of measured roughness noise and simulated dipole sources, “clean” source maps of Rough1 and Rough2 need to be obtained. Although the reverberation noise of a closed-return wind tunnel is avoided in the case of out-of-flow measurements in an open jet, Figures 4.8 and 4.9 still indicate considerable contamination from other sound sources, *e.g.* trailing edge, leading edge, seams. A straightforward but effective method to eliminate the contamination is to subtract the source powers of the smooth plate from those of the rough plates. This method was applied to the raw source maps in Figures 4.8 and 4.9, and corrected “clean” source maps were obtained for comparison with simulation.

Figures 4.13–4.16 illustrate the comparison of measured and simulated source maps for Rough1 and Rough2, and both the HF and LF array data are shown. Unlike the identical colour bars for Rough1, Rough2 and Smooth in Figures 4.8 and 4.9, the colour bars in Figures 4.13–4.16 give the unaltered maximum source strengths for a better comparison of measurement and simulation. The simulated equivalent source strengths at each 1/3 octave-band frequency have been averaged over the whole bandwidth, as in the beamforming analysis of the experimental data.

In all these figures, the top row shows the “clean” source maps with the Smooth

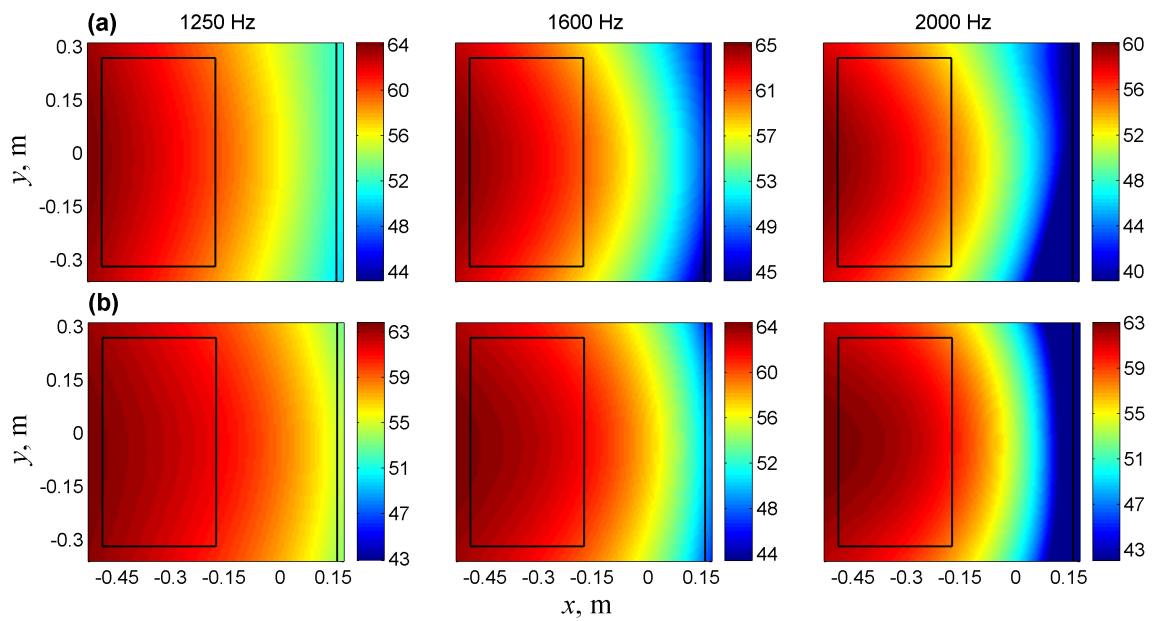


Figure 4.13: Comparison of source maps between measurement and simulation: (a) measurement, (b) simulation. Rough1, HF array,  $U = 30$  m/s.

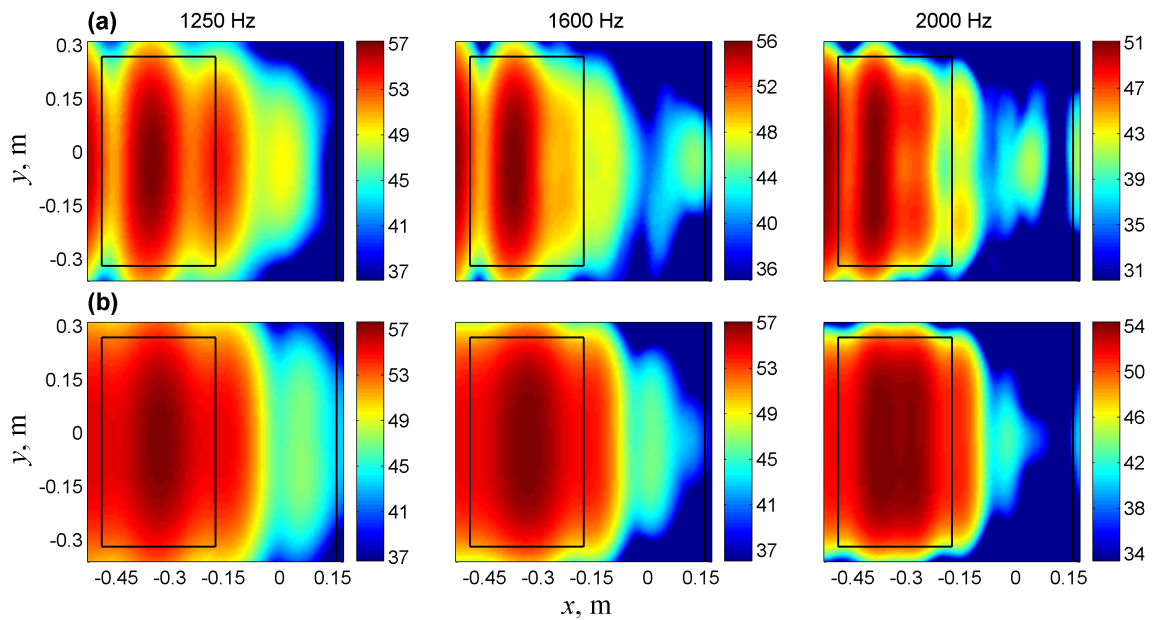


Figure 4.14: Comparison of source maps between measurement and simulation: (a) measurement, (b) simulation. Rough1, LF array,  $U = 30$  m/s.

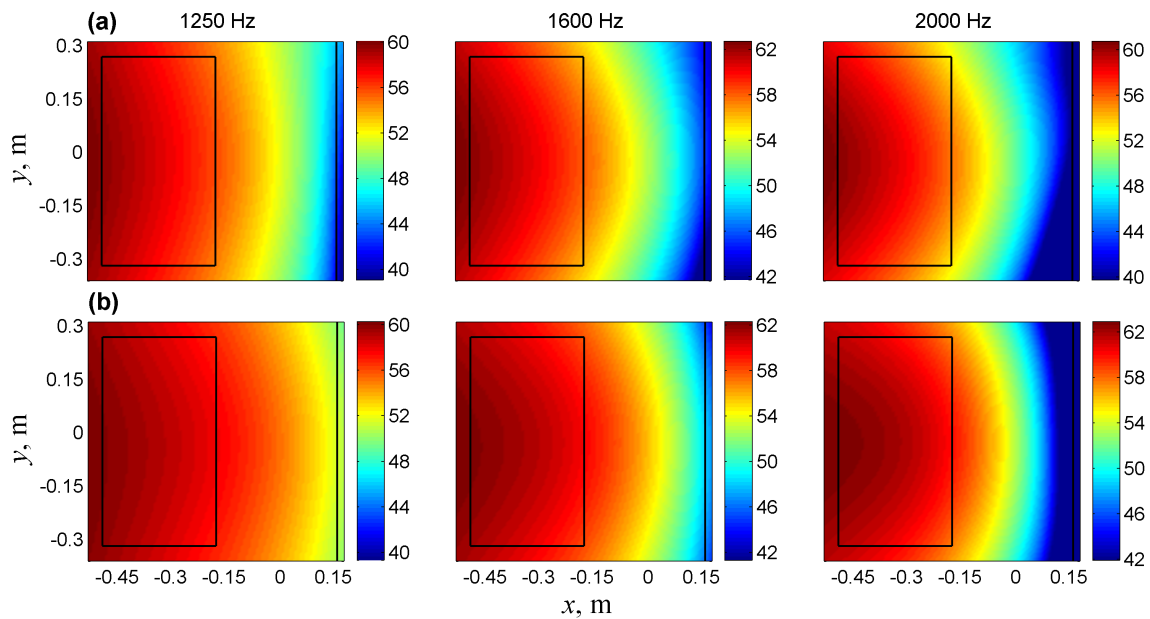


Figure 4.15: Comparison of source maps between measurement and simulation: (a) measurement, (b) simulation. Rough2, HF array,  $U = 30$  m/s.

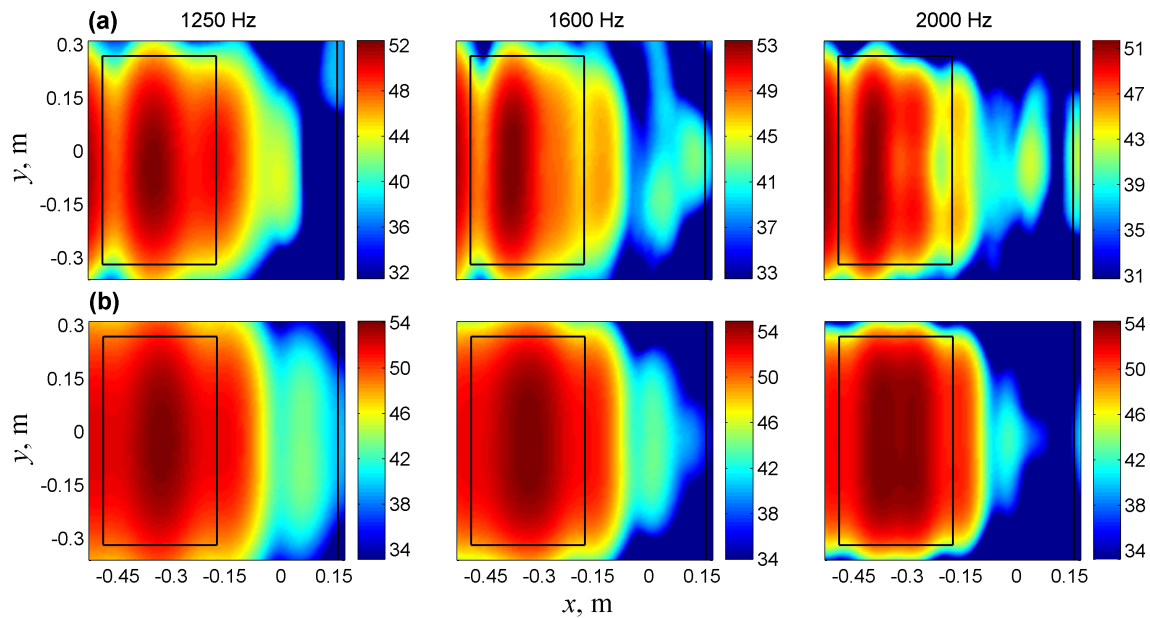


Figure 4.16: Comparison of source maps between measurement and simulation: (a) measurement, (b) simulation. Rough2, LF array,  $U = 30$  m/s.

source powers subtracted. As can be seen from the HF array data in Figures 4.13 and 4.15, the SPL of the “clean” source maps has been diminished a bit and the major lobe is concentrated more in the upstream rough region compared with the raw source maps in Figure 4.8. This correction is shown more evidently for the LF array data in Figures 4.14 and 4.16 in which the interference from the TE noise seen originally in Figure 4.9 has been greatly reduced.

The bottom row of Figures 4.13–4.16 shows the corresponding source maps by simulating a distribution of incoherent dipoles over the rigid plate with strengths derived from the prediction model in Chapter 3. The beamforming predictions of the source patterns of measurement and simulation exhibit satisfactory similarities, which confirms the dipole nature of surface roughness noise. The major lobe in the top row gradually reduces in the spanwise direction ( $y$ -axis) along the plate chord ( $x$ -axis), whereas in the bottom row the major lobe almost fills the entire dark frame. This is because in the experiment the boundary of the open jet expands along the flow direction as the jet mixes with the still air in free space. The expansion effect results in a decrease of flow velocity around the jet boundary. In the simulation, however, this effect is too complicated to be considered for the correction of the predicted equivalent source strengths around the jet boundary.

Furthermore, as indicated by the colour bars of Figures 4.13–4.16, the simulation program SIMSRC is capable of approximately predicting the equivalent source strengths of roughness noise in magnitude at 1250 Hz and 1600 Hz frequencies, which provides further form of validation for the prediction model developed in this thesis from the perspective of microphone array measurements. However, a discrepancy of about 3 dB can be observed for the comparison at 2000 Hz, and this should be ascribed to the limitation of the theoretical model which predicted spectral levels a few dB higher than the measured roughness noise in  $f > 1.7$  kHz frequency, as has been discussed in Section 4.2.3. In addition, SIMSRC predicts somewhat higher source strengths in the downstream portion of the rough region, namely, the streamwise gradient of simulated source strengths are a bit lower than that of the measured source strengths. Hence there is scope to improve the theoretical model to capture these aspects of surface roughness generated noise.

## 4.4 Hot-Wire Measurement

### 4.4.1 Experimental setup

A short experimental study using hot-wire anemometer was carried out to measure the mean velocity profile and hence the boundary-layer thickness of turbulent boundary-layer flow over a flat plate roughened by hemispherical bosses. The objectives are in two counts: (i) to determine the wake strength  $\Pi_0$  for the boundary-layer thickness formula (3.39); and (ii) to verify the skin friction formula (3.33) proposed by Mills and Hang [106]. Both formulae have been described in Section 3.3.3 and applied to the roughness noise predictions in Sections 4.2.3 and 4.3.4.

A schematic of the hot-wire experimental setup is shown in Figure 4.17. The hot-wire measurement was performed in an open throat wind tunnel, the No. 1B

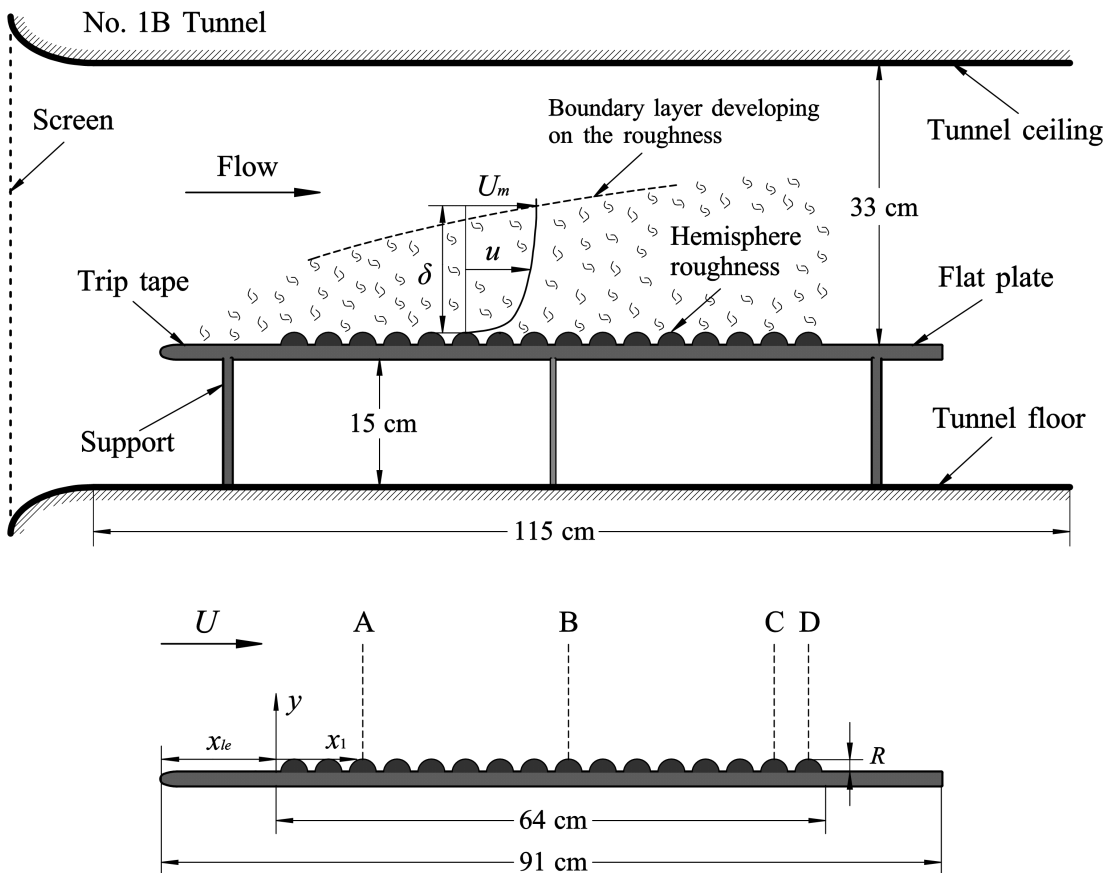


Figure 4.17: Schematic of the hot-wire experimental setup and measurement stations A–D.



Tunnel, at the CUED main site. A contraction with a turbulence reduction screen precedes the wind tunnel with a  $0.72 \times 0.50 \text{ m}^2$  test section. In the approach flow close to the tunnel floor, the mean velocity distribution resembles a typical smooth-wall boundary-layer profile. A flat plate spanning the width of the tunnel is placed parallel to the tunnel floor at a distance of 15 cm. The flow is tripped at 2 cm from the leading edge of the plate, and is free to pass over and under the flat plate. The plate surface is partially roughened in a square region of  $0.64 \times 0.64 \text{ m}^2$  using four rough panels with hemispherical bosses. These rough panels have been described in Section 4.2.1.2 and both Rough1 and Rough2 are tested in this study. The nominal depth ( $d_n$ ) of flow above the roughness elements is 33 cm, yielding a low ratio of the roughness height ( $R = 3$  or 4 mm) to the flow depth,  $R/d_n \sim 0.01$ .

A simple representation of the streamwise mean velocity ( $u$ ) profile above the plate is shown in Figure 4.17. For convenience, the boundary-layer thickness  $\delta$  is defined as the wall normal location where the streamwise mean velocity achieves a maximum [8], *i.e.*  $u = U_m$ . There is no region of constant mean velocity beyond  $y = \delta$ . In fact, the mean velocity decreases slightly towards the tunnel ceiling. Mean and fluctuating velocities were measured using hot-wire anemometry with a single probe as shown in Figure 4.18. The hot-wire probe has a tungsten sensor wire that is  $3.8 \mu\text{m}$  in diameter and 1.25 mm in length. It was operated with a DANTEC 56C Constant Temperature Anemometer (CTA) unit. Data acquisition was done by a PC with a National Instruments Lab PC1200 Data Acquisition board running LabView software. The sampling frequency used is 48 kHz. The hot-wire probe was always calibrated before each set of experiments within the free stream of the wind tunnel

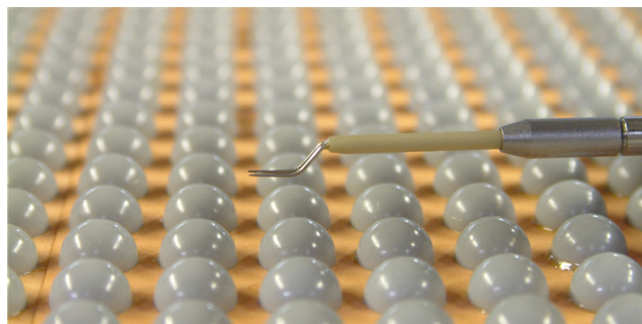


Figure 4.18: The hot-wire probe above hemispherical roughness elements.

with a compensating temperature system.

The wind tunnel was run at two different free-stream velocities of 10 and 20 m/s measured by a Pitot tube, but only the velocity  $U = 20$  m/s was analyzed yielding a Reynolds number  $Re_L = 1.25 \times 10^6$ . Measurements were made in the plate boundary layer from the top of the roughness elements at four stations denoted A–D respectively. As shown in Figure 4.17, the distance from the leading edge of the plate to the front edge of the rough region is  $x_{le} = 135$  mm, and the streamwise distances  $x_1$  along the rough region of the four measurement stations are listed in Table 4.4 for the two types of surface roughness. Note that in the present experimental setup  $x_{le} > 0$  and so the length correction  $x_0$  given in Equation (4.8) needs to be taken into account in the predictions of boundary-layer thickness and skin friction coefficient as discussed below.

Table 4.4: Streamwise locations of measurement stations A–D.

$x_1$ (mm)	Station			
	A	B	C	D
Roughness				
Rough1	90	340	590	620
Rough2	96	344	592	624

## 4.4.2 Results and discussion

### 4.4.2.1 Wake strength

Figure 4.19 shows the predicted local boundary-layer thickness  $\delta$  based on Equation (3.39) for Rough1 ( $R = 4$  mm) and Rough2 ( $R = 3$  mm), respectively. Three tentative values of the wake strength  $\Pi_0$ , *i.e.* 0.40, 0.45 and 0.50, have been tested to find the one suitable for the surface roughened by hemispherical bosses. The experimental results through the hot-wire measurement at the four stations along the flat plate are also shown for comparison.

As can be observed in Figure 4.19, the formula (3.39) with the wake strength  $\Pi_0 = 0.45$  is able to give very close predictions of rough-wall boundary-layer thickness to the measured values of  $\delta$  especially at the downstream stations C and

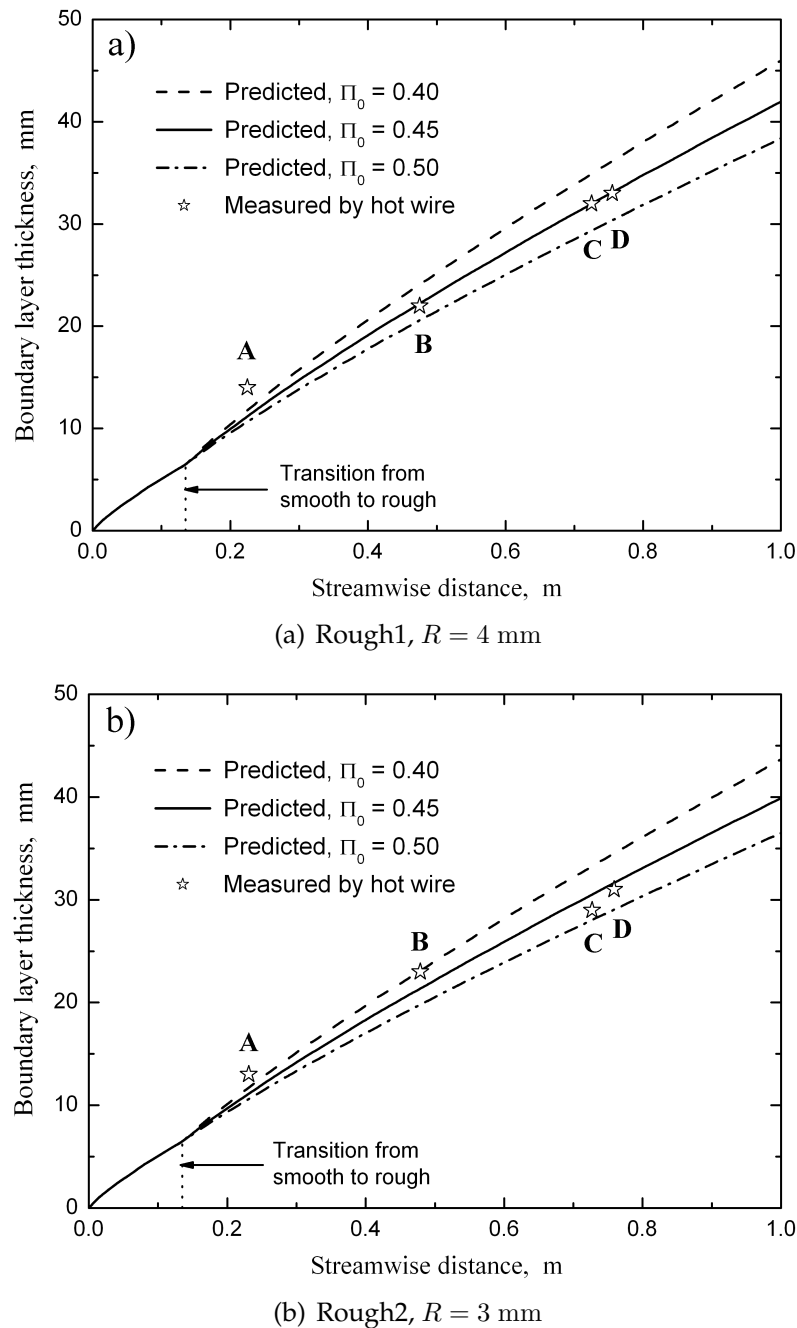


Figure 4.19: Comparison of the predicted and measured boundary-layer thickness  $\delta$  on a rough plate with streamwise distance  $x_{le} + x_1$ .  $U = 20$  m/s.

D. Noticeable errors occur at upstream stations particularly Station A where the measured data are above the predicted curve and this could be due to the effect of the trip tape or to turbulence in the oncoming flow. Nevertheless, the mean error should be sufficiently small to give an approximate prediction for the average boundary-layer thickness  $\bar{\delta}$  on a rough flat plate.

#### 4.4.2.2 Skin friction

From the mean velocity profiles measured at two stations along the flat plate, the average skin friction coefficient  $\bar{c}_f$  between the two stations can be calculated. The derivation of  $\bar{c}_f$  from the hot-wire measurement is described in Appendix C. On the other hand,  $\bar{c}_f$  can be predicted through the skin friction formulae (3.31) and (3.33). Here we verify the accuracy of the two different formulae proposed by Prandtl and Schlichting [124] and Mills and Hang [106] by comparing with the  $\bar{c}_f$  derived from the measured mean velocity profiles. The predicted average skin friction coefficient is obtained by a numerical integration of the local skin friction coefficient  $c_f$  over the streamwise distance between two measurement stations.

Table 4.5 compares the experimental data of  $\bar{c}_f$  with the predictions using Formulae (3.31) and (3.33). The average skin friction coefficient is examined for three station pairs, *i.e.* AB, BC and AC (see Figure 4.17 and Table 4.4), and the two types of surface roughness, Rough1 and Rough2. As can be seen in Table 4.5, the skin

Table 4.5: Comparison of the average skin friction coefficient  $\bar{c}_f$  between measurement and predictions by Formula (3.31) (Prandtl and Schlichting [124]) and Formula (3.33) (Mills and Hang [106]). Rough surfaces: (a) Rough1 and (b) Rough2.

(a)		Prediction			
	Measurement	Formula (3.31)		Formula (3.33)	
Station pair	$\bar{c}_f$	$\bar{c}_f$	Error (%)	$\bar{c}_f$	Error (%)
AB	0.01095	0.01111	1.45	0.01384	20.90
BC	0.00865	0.00887	2.51	0.01079	19.84
AC	0.00980	0.00999	1.92	0.01232	20.44
(b)		Prediction			
	Measurement	Formula (3.31)		Formula (3.33)	
Station pair	$\bar{c}_f$	$\bar{c}_f$	Error (%)	$\bar{c}_f$	Error (%)
AB	0.01069	0.01018	-4.99	0.01257	14.93
BC	0.00871	0.00824	-5.76	0.00994	12.40
AC	0.00970	0.00921	-5.33	0.01126	13.81

friction is stronger close to the leading edge of the rough region (station pair AB). When compared to the measured values of  $\bar{c}_f$ , the average absolute deviations for Formula (3.31) are 20.44% (Rough1) and 13.81% (Rough2), while for Formula (3.33) they are only 1.92% (Rough1) and 5.33% (Rough2), respectively. This confirms that the theory underlying Formula (3.33) is in good accord with experiment. Therefore the skin friction formula of Mills and Hang [106] is verified in accuracy and it is reliable to apply this formula to the prediction model of surface roughness noise developed in this thesis.

## 4.5 Summary

The prediction model developed in the previous chapter have been validated experimentally in this chapter. Acoustic spectrum measurement was firstly carried out for two rough plates in an open jet. The measured noise spectra were significantly contaminated by background noise, but the roughness noise was detected in 1–2.5 kHz frequency. The prediction model has been modified to be in accordance with the experimental setup. The reasonable agreement between measurement and prediction provides validation of the theoretical model.

Secondly, phased microphone arrays have been applied to the measurement and simulation of surface roughness noise. From the resulting beamforming source maps, the rough plates exhibited higher source strengths than the smooth plate, and the TE noise was somewhat enhanced by surface roughness. Measurements at three streamwise locations demonstrated some features of the dipole directivity. Theoretical simulations have been performed for a distribution of incoherent dipoles over the rough plates with the equivalent source strengths determined by the prediction model. The same beamforming algorithm was applied to measurement and simulation and the source maps exhibited satisfactory similarities in source pattern with approximate source strengths. This has confirmed the dipole nature of roughness noise and validated the source amplitude predicted by the theory. However, the streamwise gradient of the source strengths was a bit underestimated in the simulations, and at the highest frequency the source

strengths were overestimated by about 3 dB, which indicates that there is scope for an improved theoretical prediction which captures these aspects.

Finally, we performed hot-wire measurement to determine two important parameters, wake strength and skin friction coefficient, that account for the roughness effects of turbulence enhancement in the prediction model. The wake strength  $\Pi_0 = 0.45$  has been found to enable Formula (3.39) to give the best fit to the measured  $\delta$ . The skin friction formula by Mills and Hang [106] has been verified through comparison with the experimental data, and this formula predicts more accurate skin friction coefficient than the formula of Prandtl and Schlichting [124].

# Chapter 5

## Numerical Prediction and Analysis

### 5.1 Introduction

CHAPTERS 3 and 4 have provided reasonable validation of the theoretical model of surface roughness noise through comparisons of the predicted roughness noise with the empirical model [82] and experimental results in spectral shape, absolute spectral level, and source location and strength. On this basis, the prediction model is employed in this chapter to investigate the effects of surface roughness on airframe noise.

We first apply the validated prediction model in Section 5.2 to estimate the far-field radiated roughness noise from a Boeing-757 sized aircraft wing with three idealized levels of surface roughness. It is shown that in the high-frequency region the sound radiated from surface roughness may exceed that from the trailing edge, and higher OASPL is observed for the roughness noise, too. The TE noise is also enhanced by surface roughness somewhat. A parametric study indicates that roughness height  $R$  and roughness density  $\sigma$  significantly affect surface roughness noise with roughness height having the dominant effect. The directivity pattern of roughness noise varies with different levels of surface roughness.

In Section 5.3, we provide approximate assessment of surface roughness noise for the full-size SAI design SAX-40 during approach. The prediction model is utilized to estimate the radiated roughness noise from the complicated configuration of the entire BWB surface of SAX-40. Similarly, noise assessments

are performed for the three idealized test cases. A parametric study is carried out and the effects of the two most significant parameters,  $R$  and  $\sigma$ , are discussed. The enhancement of TE noise due to surface roughness is also investigated. We finally present two candidate rough surfaces for SAX-40 to keep its roughness noise at a negligible level and thus meet an aggressive noise target.

## 5.2 Boeing-757 Sized Aircraft Wing

### 5.2.1 Roughness noise from an aircraft wing

In this section, the far-field roughness noise generated by an aircraft wing will be numerically predicted and compared with the corresponding TE noise. The noise prediction is based on the approximate dimensions of the wing of a Boeing-757 sized aircraft (see Figure 5.1), and only the underside of the aircraft wing is considered. The evolution of the approximation of a Boeing-757 sized aircraft wing to the model as a flat plate is illustrated in Figure 5.2. The flat plate model has been estimated with the following dimensional parameters:

$$L_c \approx 5 \text{ m}, \quad L_s \approx 16.5 \text{ m}, \quad (5.1a)$$

$$A = L_c \cdot L_s \approx 82.5 \text{ m}^2, \quad (5.1b)$$

where  $L_c$  and  $L_s$  are the equivalent chord and span, respectively, and  $A$  is the equivalent area of the wing.

Aircraft noise is most annoying to the residents outside the airport perimeter in a typical built-up area when the airplane is approaching or taking off from the airport. In this case the typical Mach number  $M$  of the free stream velocity and far-field observer may be taken as

$$\begin{aligned} M = U/c = 0.2, \quad |\mathbf{x}| = 500 \text{ m}, \\ \theta = \pi/4, \quad \phi = 0. \end{aligned} \quad (5.2)$$

Note that in this direction the directivity function  $D(\theta, \phi)$  in Equation (3.48) is reduced to  $I_1/2$ .

Furthermore, it is necessary to evaluate the ensemble average  $\langle p^2(\mathbf{x}, t) \rangle$  of the far-field acoustic pressure by integrating the frequency spectrum  $P_R(\mathbf{x}, \omega)$  over the



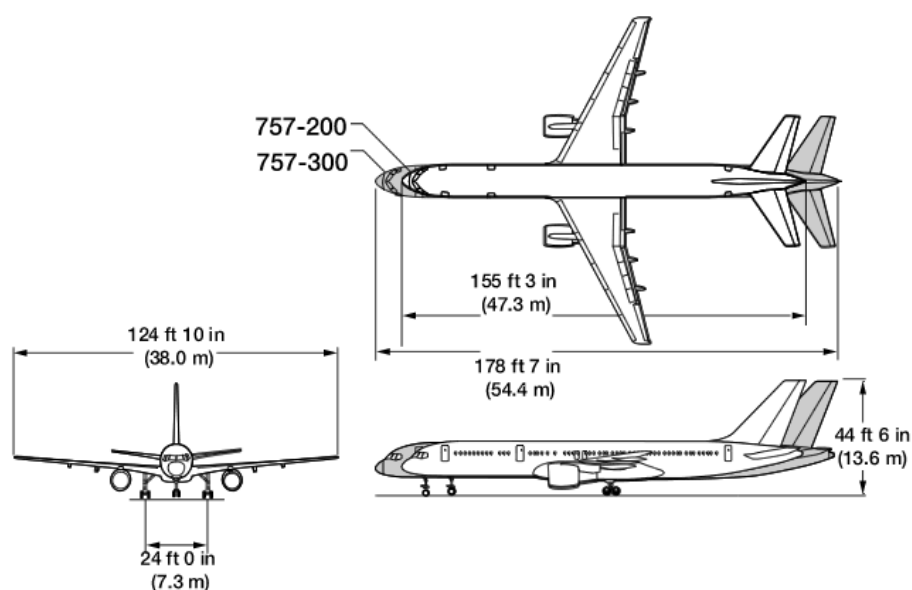


Figure 5.1: 3-view drawing of a commercial airplane type, the Boeing 757 family [19].

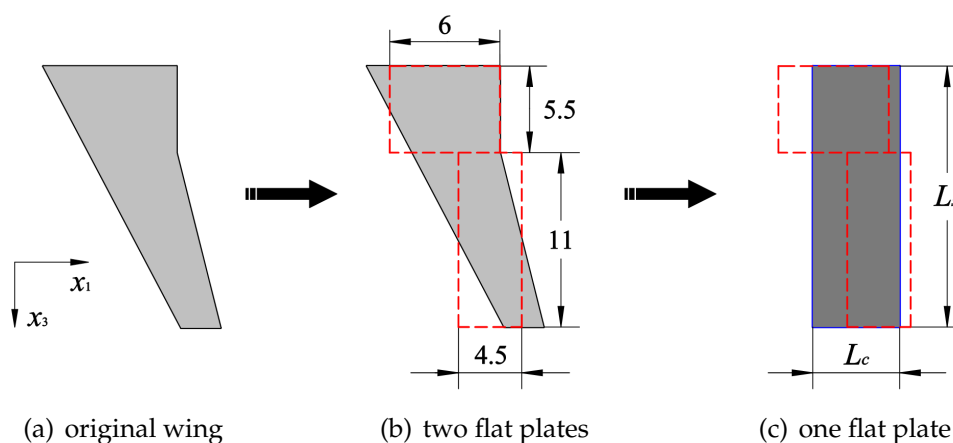


Figure 5.2: Evolution of the approximation of a Boeing-757 sized aircraft wing to a flat plate model. Dimensions are in metres and are estimated from Figure 5.1.

audible frequency range,  $f \in [20 \text{ Hz}, 20 \text{ kHz}]$ . A-weighting [39] is also taken into account in the integration to yield a more accurate noise prediction. Provided that  $P_R(\mathbf{x}, \omega)$  is an even function and  $\omega = 2\pi f$ , the representation of  $\langle p^2(\mathbf{x}, t) \rangle$  in Equation (3.19) becomes

$$\langle p^2(\mathbf{x}, t) \rangle = \frac{1}{\pi} \int_{40\pi}^{4 \times 10^4 \pi} 10^{C_A/10} P_R(\mathbf{x}, \omega) d\omega, \quad (5.3)$$

where  $C_A$  is the A-weighting factor (dBA) dependent on frequency. The curve in Figure 5.3 shows a defined roll-off above and below the centre frequency. The reference point is at 1 kHz, where the gain is 0 dB. However, exact values of  $C_A$

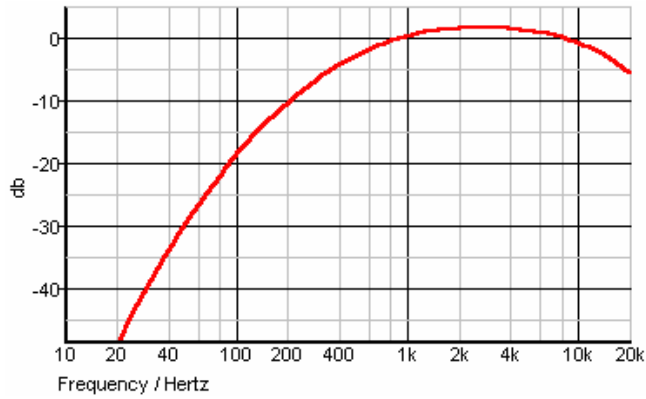


Figure 5.3: Frequency response of the A-weighting filter for the dBA scale.

are not available for all definite frequencies; hence interpolation is used if necessary.

Finally, the SPL of the rough noise spectrum is obtained by comparing  $P_R(\mathbf{x}, \omega)$  with the reference SPL ( $4 \times 10^{-10} \text{ Pa}^2$ ):

$$\text{SPL} = 10 \log_{10} \left[ \frac{P_R(\mathbf{x}, \omega)}{4 \times 10^{-10} \text{ Pa}^2} \right], \quad \text{dB.} \quad (5.4)$$

Similarly, the OASPL is given by

$$\text{OASPL} = 10 \log_{10} \left[ \frac{\langle p^2(\mathbf{x}, t) \rangle}{4 \times 10^{-10} \text{ Pa}^2} \right], \quad \text{dBA,} \quad (5.5)$$

$$f \in [20 \text{ Hz}, 20 \text{ kHz}].$$

For comparison, the corresponding TE noise was calculated based on the same dimensions of the aircraft wing for both rough and smooth surfaces. The surface roughness increases the friction velocity  $u_\tau$  and boundary layer thickness  $\delta$ , as mentioned before, and hence similar increases will be expected for the TE noise of a rough surface. However, the smooth-wall TE noise was chosen as the comparison reference because the surface roughness was generally not taken into account in the traditional estimate of airframe noise, and hence its effects will be more explicit if the roughness noise is compared with the traditionally predicted TE noise. Moreover, to be consistent with the roughness noise prediction, the TE noise is also predicted on the basis of an empirical model by Howe [82] using Chase's formula [25] of wall pressure spectrum. The directivity function in this model has been taken as 1 to obtain the maximum sound radiation.

### 5.2.2 Idealized test cases

Three idealized test cases were considered to approximately quantify the possible roughness noise from the wing of a Boeing-757 sized aircraft:

**Case 1** Rough surfaces formed by rivets, ribs, joints, *etc.*;

**Case 2** Rough surfaces formed by environmental contamination;

**Case 3** Dip-galvanized metal surfaces.

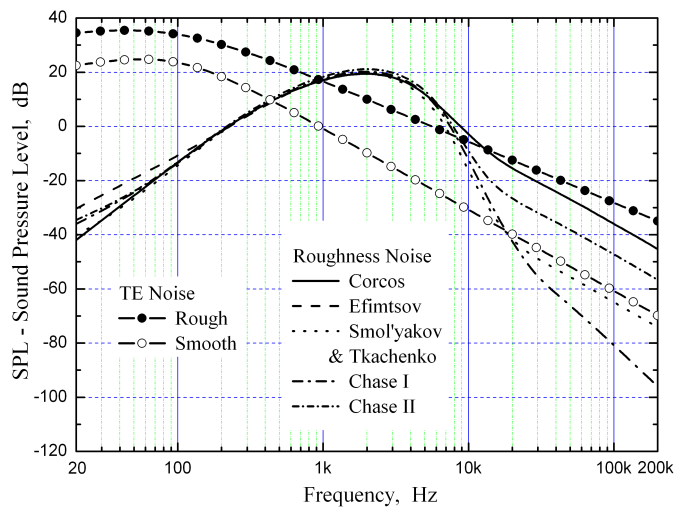
Table 5.1: Test case parameters.

Case no.	$R$ , mm	$\sigma$	$C_F$	$u_\tau$ , m/s	$u_\tau/U$	$\bar{\delta}$ , cm	$R/\bar{\delta}$	$Re_\tau$
1	5.0	0.05	0.0060	3.72	0.055	11.28	0.0443	1272.86
2	0.5	0.85	0.0036	2.90	0.043	9.38	0.0053	99.26
3	0.152	0.85	0.0029	2.59	0.038	8.91	0.0017	26.98
4 <sup>†</sup>	/	/	0.0027	2.52	0.037	6.07	/	/

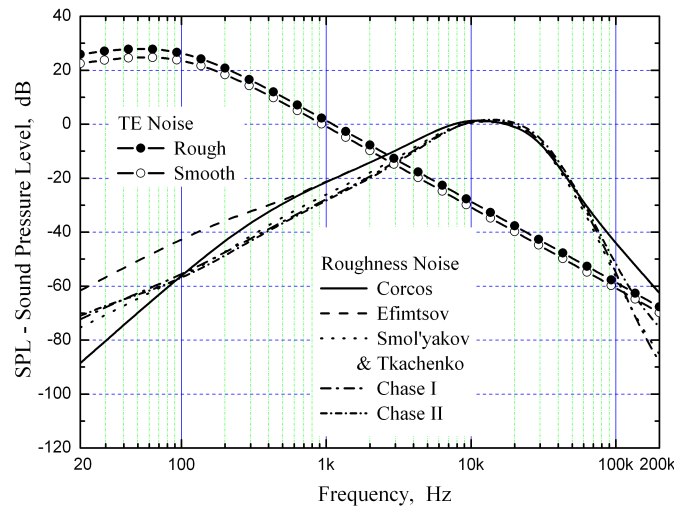
<sup>†</sup> Aerodynamically smooth surfaces;  $u_\tau/U$  is characterized by Howe [79].

The relative parameters of test cases 1–3 are listed in Table 5.1 with the corresponding values of aerodynamically smooth surfaces for comparison. As shown in Table 5.1, Cases 1 and 2 can be categorized as fully developed roughness ( $Re_\tau > 70$ ) and hence the skin friction formula (3.33) is applicable, while Case 3 is in fact transitional roughness ( $5 < Re_\tau < 70$ ) in which the overall skin friction coefficient  $C_F$  is dependent on both  $Re_L$  and  $L/k_s$ . For convenience Equation (3.33) is still applied to Case 3 in the calculation but it should be noted that the actual skin friction is a bit smaller. As previously mentioned, the values of  $u_\tau$  and  $\delta$  for Cases 1 and 2 have been increased substantially due to the enhanced surface drag and turbulence production. However, because of the very small roughness height, the surface of Case 3 appears more like a smooth wall with similar parameter values.

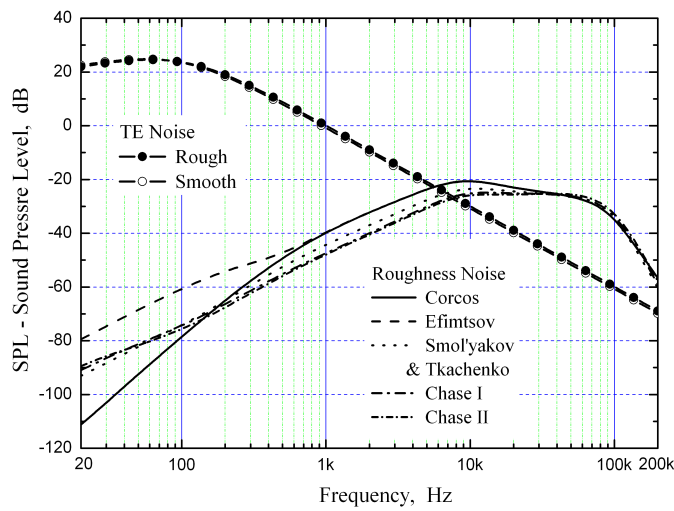
Note that the roughness elements in these test cases are generally not perfect hemispheres, and  $R$  herein corresponds to the equivalent roughness height. The value of  $\sigma$  varies with the different rough surfaces. It is reasonable to take  $\sigma$  as small as 0.05 for an aerofoil surface with a sparse distribution of rivets, ribs, joints,



(a) Case 1,  $R = 5 \text{ mm}$ ,  $\sigma = 0.05$



(b) Case 2,  $R = 0.5 \text{ mm}$ ,  $\sigma = 0.85$



(c) Case 3,  $R = 0.152 \text{ mm}$ ,  $\sigma = 0.85$

Figure 5.4: Predicted spectra of roughness noise and TE noise for Cases 1–3.

*etc.*, whereas for the other cases the roughness elements are assumed distributed very densely over the aerofoil surface. Following Howe [77], the maximum value of roughness density,  $\sigma_{\max} \sim 0.91$ , occurs for a hexagonal close packing, but this would not be representative for a purely random distribution. The value of  $\sigma$  for a square close packing is  $\sigma_{\text{sq}} \sim 0.78$ . Hence the mean value of  $\sigma_{\max}$  and  $\sigma_{\text{sq}}$ , *ca.* 0.85, is tentatively used as the practical maximum  $\sigma$  in Cases 2 and 3.

The predicted roughness noise spectra in dB for the three test cases are depicted in Figure 5.4, and compared with corresponding TE noise spectra for both rough and smooth surfaces. Similar to Figure 3.4, different models of wavenumber-frequency spectrum produce similar roughness noise spectra, especially around the peaks where all these curves almost coincide with one another. As can be seen in Figure 5.4, the smooth-wall TE noise spectra are significant only in the low-frequency region. They always peak around very low frequencies, *ca.* 65 Hz, then decay monotonically with increasing frequencies. The roughness noise spectra, however, can be nearly ignored in the low-frequency region but achieve their peaks at very high frequencies. This tends to confirm that surface roughness noise can be comparable to or even more significant than the corresponding TE noise at sufficiently high frequencies.

For Case 1, a distinct spectral peak of roughness noise occurs around 2 kHz and is at the same approximate level as the peak of the smooth-wall TE noise. However for Cases 2 and 3, the former becomes obviously lower than the latter due to the diminishing size of roughness elements. Nevertheless, the roughness noise spectra of Case 2 are still significantly above that of the TE noise spectrum in the frequency range 3–100 kHz. In contrast, Case 3 shows significantly lower roughness noise spectra with the maximum SPL  $< -20$  dB. This is because the very small roughness elements in Case 3, *i.e.*  $R = 0.152$  mm, give the dip-galvanized metal surface similar features of a smooth wall. Other possible surface finishes of an aerofoil, *e.g.*, camouflage paint in mass production spraying ( $R = 0.0305$  mm) and smooth matt paint ( $R = 0.0064$  mm) as listed in Table 5.2, generate even quieter roughness noise and are therefore not considered further.

Table 5.2: Equivalent roughness heights  $k_s$  for common surfaces [44].

Surface Type	$k_s, \text{ m} \times 10^5$	$k_s, \text{ in} \times 10^3$
Aerodynamically smooth	0	0
Polished wood or metal	0.05–0.20	0.02–0.08
Natural sheet metal	0.41	0.16
Smooth matt paint, careful application	0.64	0.25
Standard camouflage paint, average application	1.02	0.40
Camouflage paint, mass production spray	3.05	1.20
Dip-galvanized metal surface	15.2	6.0
Cast iron, natural surface	25.4	10.0

Surface roughness also has important effects on the TE noise through enhanced friction velocity  $u_\tau$  and boundary layer thickness  $\delta$ . As observed in Figure 5.4(a), the rough-wall TE noise is considerably increased for Case 1 with a 10.7 dB higher spectral peak at an even lower frequency, *ca.* 35 Hz, than that of the smooth-wall TE noise. However, the effects of surface roughness are not so evident in Figures 5.4(b) and 5.4(c). The differences between the rough- and smooth-wall TE noise SPL are only 1.0–3.4 dB for Case 2 and 0.9 dB at most for Case 3 in the whole frequency range, 20 Hz – 200 kHz.

Attention is then confined to the audible frequency range,  $f \in [20 \text{ Hz}, 20 \text{ kHz}]$ . Table 5.3 presents the predicted roughness noise OASPL in this frequency range and it suggests the same comparative relationship between the roughness noise and TE noise. For Case 1, the roughness noise OASPL is higher than the smooth-wall

Table 5.3: Predicted roughness noise and TE noise OASPL for test cases 1–3.

Case no.	Roughness Noise <sup>†</sup> dBA					TE Noise, dBA	
	1	2	3	4	5	Smooth	Rough
1	50	50	49	50	51	30	36
2	34	34	33	33	33	30	32
3	13	13	10	8	7	30	31

<sup>†</sup> Empirical models for smooth-wall pressure spectrum: 1 – Corcos, 2 – Efimtsov, 3 – Smol'yakov and Tkachenko, 4 – Chase I, 5 – Chase II.

TE noise OASPL by 20 dBA in average; the rough-wall TE noise OASPL is also enhanced by 6 dBA. Similarly, the predicted OASPL of Case 2 shows a much smaller difference of 3–4 dBA between the roughness noise and smooth-wall TE noise, and the surface roughness increases the TE noise OASPL by only 2 dBA. In Case 3, however, the OASPL of roughness noise decreases greatly due to the very small roughness height, and becomes 17–23 dBA lower than that of the TE noise. For the same reason the difference between the rough- and smooth-wall TE noise OASPL is merely 1 dBA. These features tend to support the speculation that surface roughness generated noise would contribute substantially to the airframe noise of a “clean” configuration and the TE noise would be enhanced by surface roughness to some extent provided that the roughness elements are not too small in size.

### 5.2.3 Parametric study

A parametric study was carried out to investigate the effects of two important parameters, roughness height  $R$  and roughness density  $\sigma$ , on the roughness noise from a Boeing-757 sized aircraft wing<sup>†</sup>. In Figure 5.5(a), the roughness noise spectra for different values of  $R$  are compared in a wide frequency range, 20 Hz – 200 kHz, with the value of  $\sigma$  fixed to 0.85. As  $R$  decreases from 5.0 mm the spectral peak decreases and shifts to progressively higher frequencies until  $R = 0.1$  mm, where there is no evident peak for  $R \leq 0.1$  mm. In addition, Figure 5.5(a) implies that the peak frequency of the roughness noise spectrum is approximately proportional to  $R^{-1}$ . Below the peak frequency, the approximate parametric dependency  $\text{SPL} \sim (\omega R)^4$  can be observed.

The dependence of roughness noise OASPL on roughness height  $R$  for various values of  $\sigma$  is depicted in Figure 5.6(a). It is shown that the parameter  $R$  has significant effects on the roughness noise OASPL. For  $R < 1$  mm, the OASPL varies as  $R^\varepsilon$ , where  $3.2 < \varepsilon < 4.3$  dependent on the value of  $\sigma$ ; while for larger values of  $R$ , the OASPL increases less rapidly with increasing roughness height.

Roughness density  $\sigma$  is another important parameter for the roughness noise.

<sup>†</sup>Hereafter for simplicity the numerical integration is based on the Smol’yakov and Tkachenko model only as all wall pressure models give very similar plots.

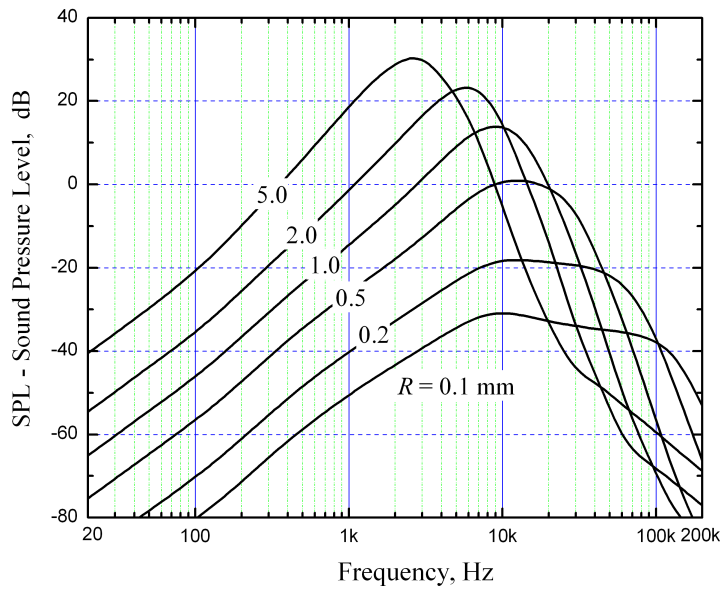
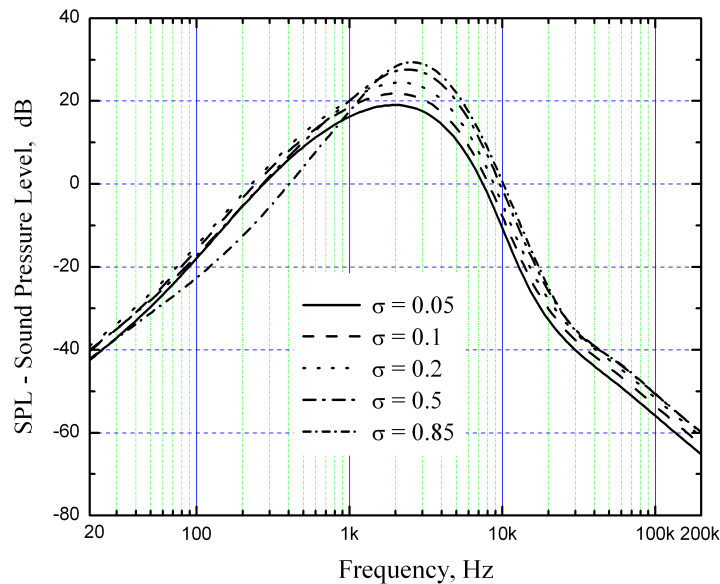
(a) Effect of  $R$ ,  $\sigma = 0.85$ (b) Effect of  $\sigma$ ,  $R = 5.0$  mm

Figure 5.5: Effects of roughness height  $R$  and roughness density  $\sigma$  on predicted roughness noise spectra.

The roughness noise spectra for  $R = 5.0$  mm and different values of  $\sigma$  are compared in Figure 5.5(b). As  $\sigma$  increases from 0.05 the spectral peak shifts to progressively higher frequencies with increasing SPL, though not as obviously as the variation with  $R$  in Figure 5.5(a). This implies that the spectral peak of roughness noise is also related to the distribution of roughness elements. A denser distribution results in the higher peak SPL and peak frequency because there are more roughness elements



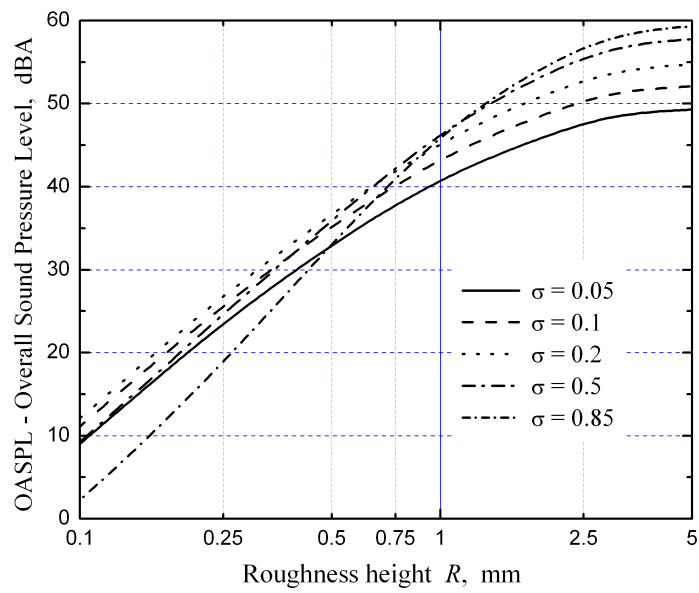
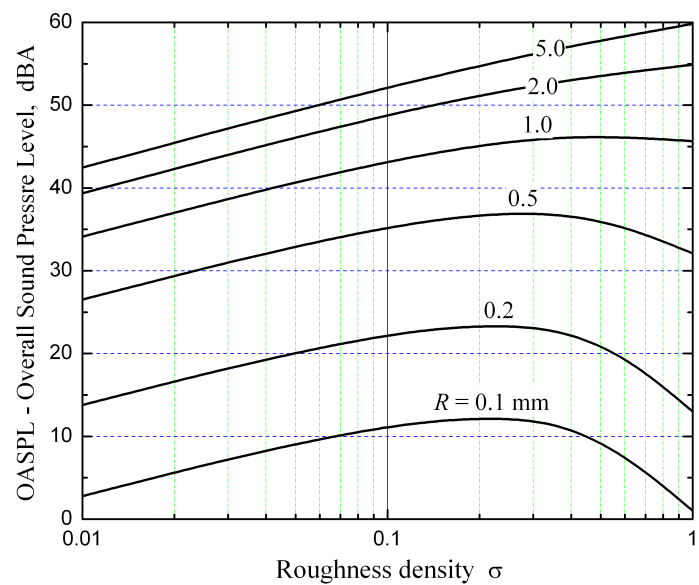
(a) OASPL vs.  $R$ (b) OASPL vs.  $\sigma$ 

Figure 5.6: Effects of roughness height  $R$  and roughness density  $\sigma$  on predicted roughness noise OASPL.

interacting with turbulence near field and scattering sound.

Figure 5.6 shows the dependence of roughness noise OASPL on roughness density  $\sigma$ . As observed in Figure 5.6(a), larger values of  $\sigma$  usually generate louder roughness noise for large roughness elements ( $R > 2.0$  mm). The OASPL variation in Figure 5.6(b) also shows that at low values of  $\sigma$  the mean square pressure scales approximately on  $\sigma$ . However, it is not always the case. In Figure 5.6(b) for  $R \leq$

1.0 mm, the roughness noise OASPL increases slowly with  $\sigma$ , attains a maximum at  $\sigma_p$ , and then decreases. The peak value  $\sigma_p$  shifts, as  $R$  increases, to a larger value of  $\sigma$  with higher OASPL. This is because for larger values of  $\sigma$  than  $\sigma_p$  the wall appears gradually “smoother” as roughness elements become progressively compacter. But this effect will be counteracted to some extent by larger roughness height ( $R \geq 2.0$  mm) because the absolute space among the roughness elements increases with  $R$  even for a very dense distribution.

Nevertheless, the effect of roughness density  $\sigma$  on roughness noise prediction is not as significant as that of roughness height  $R$  due to the different OASPL dependencies on  $R$  and  $\sigma$ . For instance, the OASPL variation in Figure 5.6(b) is at most 17.4 dBA from  $\sigma = 0.01$  to 1.0 for the case  $R = 5.0$  mm, although such a large roughness density of 1.0 is not achievable in practice, which is greatly less than the OASPL increase of at least 40 dBA ( $\sigma = 0.05$ ) from  $R = 0.1$  mm to 5.0 mm in Figure 5.6(a).

## 5.2.4 Directivity

In previous roughness noise predictions the far-field observer is fixed at  $|x| = 500$  m,  $\theta = \pi/4$ ,  $\phi = 0$ , and the directivity function  $D(\theta, \phi)$  is therefore reduced to  $I_1/2$ . However, the roughness noise radiation will vary in different directions as described in Equation (3.48). The first term  $I_1 \cos^2 \theta$  describes the effect of a dipole in the flow direction. The contribution of the term  $I_2 \sin^2 \theta \sin^2 \phi$  to  $D(\theta, \phi)$  should be taken into account when  $\phi \neq 0$ , and it accounts for the sound from a dipole in the plane of the wing but normal to the flow direction.

The directivities of roughness noise OASPL in the plane of a Boeing-757 sized aircraft wing (*i.e.*  $\theta \in [0, \pi]$  and  $|\phi| = \pi/2$ ) were predicted for the three idealized test cases, as shown in Figure 5.7. It can be seen from Equation (3.48) that the roughness noise OASPL is symmetrical to  $\theta = \pi/2$  ( $I_3 \equiv 0$ ). In addition, Case 1 indicates that the radiated roughness noise is 7 dBA higher in  $\theta = 0, \pi$  than in  $\theta = \pi/2$  ( $I_1 > I_2$ ), while for Cases 2 and 3 the maximum sound occurs in the direction  $\theta = \pi/2$  ( $I_1 < I_2$ ).

We can understand this by looking at the variation of the integrands in Equation

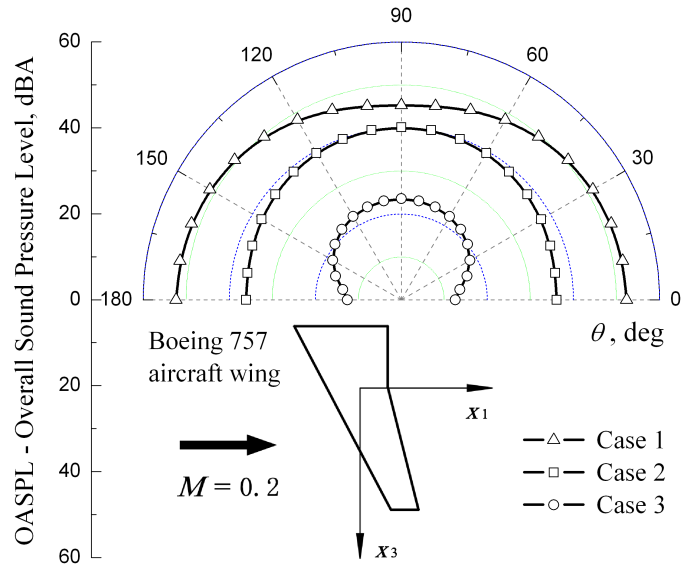


Figure 5.7: Predicted directivities of roughness noise OASPL for Cases 1–3,  $|\mathbf{x}| = 500$  m,  $\phi = -\pi/2$ .

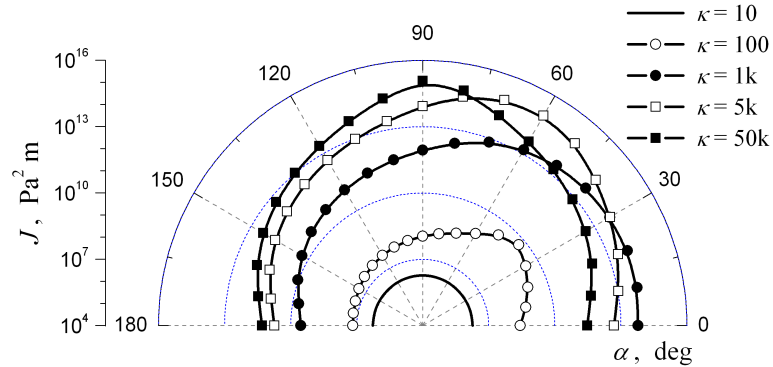


Figure 5.8:  $J$ , as defined in Equation (5.6), as a function of  $\kappa$  and  $\alpha$ .

(3.49) with  $\kappa$  and  $\alpha$ . Figure 5.8 is a plot of the integral,

$$J = \int_{40\pi}^{4 \times 10^4 \pi} 10^{C_A/10} |\gamma(\kappa)|^2 \tilde{\Phi}_p(\boldsymbol{\kappa}, \omega) \kappa \, d\omega, \quad (5.6)$$

as a function of  $\alpha$  for different values of  $\kappa$ .  $J$  is a component of Equation (5.3) and needs to be multiplied by

$$(\cos^2 \alpha, \sin^2 \alpha) \Psi(\kappa) e^{-2\kappa R} \delta^{*3} \quad (5.7)$$

and integrated over  $\kappa \delta^*$  and  $\alpha$  to give  $\int 10^{C_A/10} (I_1, I_2) \, d\omega$  which leads to the roughness noise OASPL. As shown in Figure 5.8, the variation of  $J$  with the wavenumber direction  $\alpha$  changes as  $\kappa$  increases with the maximum strength moving towards  $\alpha = \pi/2$ . The exponential factor  $e^{-2\kappa R}$  means that the OASPL directivity

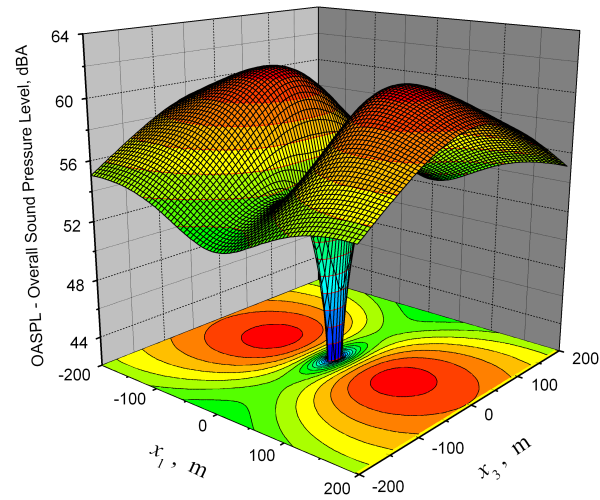
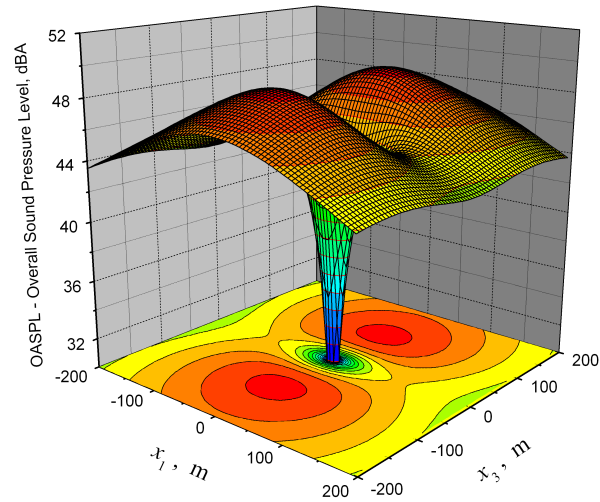
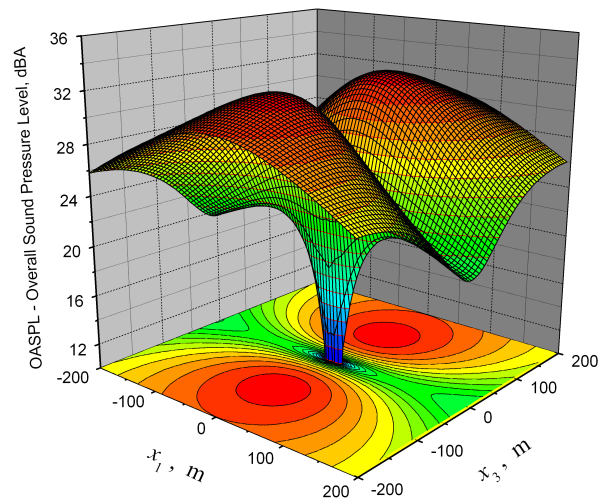
(a) Case 1,  $R = 5 \text{ mm}$ ,  $\sigma = 0.05$ (b) Case 2,  $R = 0.5 \text{ mm}$ ,  $\sigma = 0.85$ (c) Case 3,  $R = 0.152 \text{ mm}$ ,  $\sigma = 0.85$ 

Figure 5.9: Predicted ground contours of roughness noise OASPL for Cases 1–3.

is predominantly influenced by small  $\kappa$  for large roughness height, while a wider range of  $\kappa$  is important for small  $R$ . This explains the observed difference in the predicted directivities for different roughness levels of surface roughness in Figures 5.7 and 5.9.

In Figure 5.9 the predicted contours of roughness noise OASPL on the ground are depicted in the  $x_1$ - $x_3$  coordinates for test cases 1–3 to investigate the radiated roughness noise which can be heard by the people outside the airport perimeter in a typical built-up area. Suppose that an aircraft right above the origin  $(0, 0)$  at a height  $H = 100$  m is approaching or taking off from the airport in the positive  $x_1$ -direction with a Mach number  $M = 0.2$ . In this case the roughness noise radiated from the aircraft wing to the ground should vary with the observer direction  $(\theta, \phi)$ , and the far-field distance  $|\mathbf{x}|$  of an observer on the ground is also a function of  $(\theta, \phi)$ , *i.e.*,  $|\mathbf{x}| = H / \sin \theta \cos \phi$ .

As can be seen in Figure 5.9, the predicted ground contours are illustrated in a  $400 \times 400$  m<sup>2</sup> square region, and exhibit symmetries to both  $x_1$ - and  $x_3$ -axes as explained above. The contours are not shown in a central circular region of radius 5 m because for an observer at  $(0, 0)$  the observer vector  $\mathbf{x}$  is in the direction perpendicular to both dipoles described by  $I_1$  and  $I_2$ , namely,  $\langle p^2(\mathbf{x}, t) \rangle \rightarrow 0$ ,  $\text{OASPL} \rightarrow -\infty$  when  $\theta \rightarrow \pi/2$ ,  $\phi \rightarrow 0$ . Therefore the roughness noise OASPL drops abruptly as the observer approaches the origin and the lowest OASPL is observed at positions right underneath the aircraft for all test cases.

However, the highest OASPL occurs on the  $x_1$ -axis for Case 1 ( $I_1 > I_2$ ) and on the  $x_3$ -axis for Cases 2 and 3 ( $I_1 < I_2$ ), which is consistent with the features of the predicted directivities in Figure 5.7. Note that the highest OASPL is always positioned at a distance  $H$  from the origin  $(0, 0)$ . This is because on these axes the far-field distance  $|\mathbf{x}|$  and directivity function  $D(\theta, \phi)$  are reduced and the acoustic

Table 5.4: Reduced forms of expressions for observers on the  $x_1$ - and  $x_3$ -axis.

Observer	$\theta$	$ \phi $	$ \mathbf{x} $	$D(\theta, \phi)$	$P_R(\mathbf{x}, \omega)$	$\text{OASPL}_{\max}$
on $x_1$ -axis	$(0, \pi)$	0	$H / \sin \theta$	$I_1 \cos^2 \theta$	$\propto \sin^2 2\theta$	$\theta = \pi/4, 3\pi/4$
on $x_3$ -axis	$\pi/2$	$[0, \pi/2)$	$H / \cos \phi$	$I_2 \sin^2 \phi$	$\propto \sin^2 2\phi$	$\phi = \pi/4, -\pi/4$

frequency spectrum  $P_R(\mathbf{x}, \omega)$  becomes proportional to  $\sin^2 2\theta$  or  $\sin^2 2\phi$ , as shown in Table 5.4, which gives the maximum OASPL in  $\theta = \pi/4, 3\pi/4$  on the  $x_1$ -axis or in  $\phi = \pi/4, -\pi/4$  on the  $x_3$ -axis.

## 5.3 SAI Design SAX-40

### 5.3.1 Methodology

Following the roughness noise estimates for the Boeing-757 sized aircraft wing, we carry out similar assessment of surface roughness noise for the Silent Aircraft conceptual design SAX-40. In this work, the integral bounds  $[20 \text{ Hz}, 20 \text{ kHz}]$  in Equation (5.3) is replaced by the frequency band  $[50 \text{ Hz}, 10 \text{ kHz}]$  to be consistent

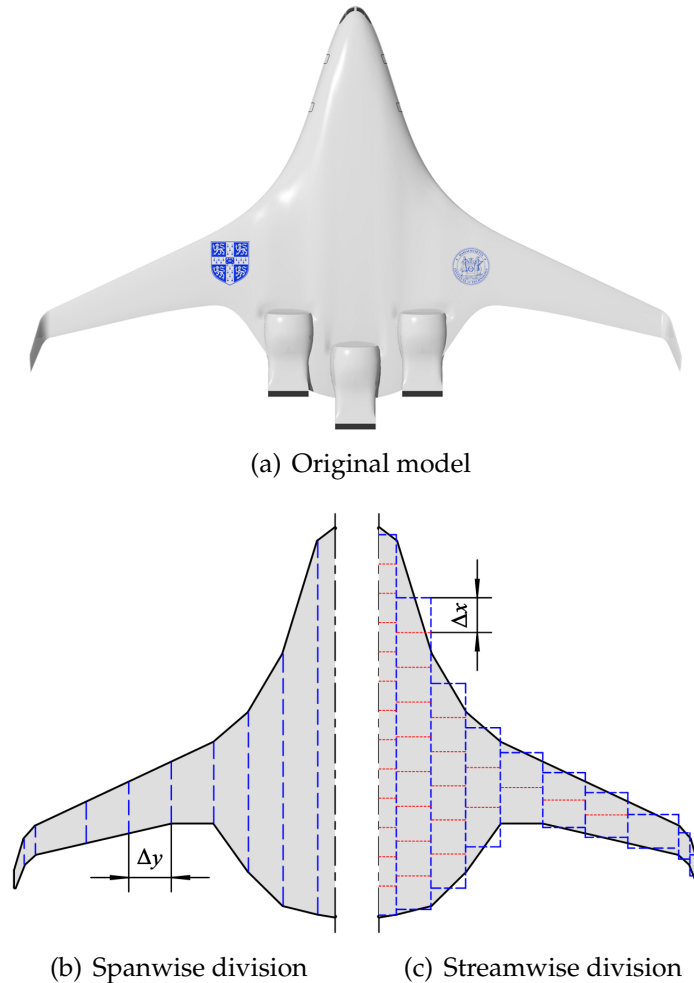


Figure 5.10: Evolution of the approximation of the SAX-40 planform.

with the estimation of other noise components of SAX-40 [32, 72]. This frequency band is typically used for noise analysis because frequencies below 50 Hz and above 10 kHz are barely perceived by humans and can be safely ignored when calculating A-weighted OASPL.

### 5.3.1.1 Approximation of SAX-40 planform

To apply the prediction model to the SAI conceptual design, the original BWB surface of SAX-40 as shown in Figure 5.10(a) is firstly approximated as a rigid flat plate and differences in the vertical  $z$ -direction are ignored in the planform. Roughness elements are assumed to be uniformly distributed over the whole plate. The planform is then divided spanwisely (increment  $\Delta y < 5.5$  m) into a series of subareas, as shown in Figure 5.10(b), which is able to reproduce the main characteristics of the original geometry of SAX-40. The coordinates of the approximated leading edge points and the chord are listed in Table 5.5.

Moreover, to consider the effect of the decreasing ratio  $R/\delta$  along the plate

Table 5.5: Approximate configuration of the SAX-40 planform.

	Leading edge points		Chord, m
	$y^\ddagger$ m	$x^\dagger$ m	
Centreline	0.0000	0.0000	41.0000
	1.8288	1.4000	39.3000
	5.4864	13.3000	26.5000
	9.1440	19.5000	16.7000
	12.8016	22.6468	8.4365
	17.2847	24.7541	6.3292
	21.7678	26.8613	5.2579
	26.2510	28.9686	4.1866
	31.6141	31.4896	2.9050
Wing tip	32.8000	32.8287	2.6451
Winglet tip	33.7736	36.1287	1.8000

<sup>†</sup>  $x$  is longitudinal, positive towards the back of the aircraft.

<sup>‡</sup>  $y$  is lateral, positive to the left.

chord ( $x$ -direction), the subareas in Figure 5.10(b) are approximated as rectangles and divided streamwisely (increment  $\Delta x < 3.5$  m) into a number of rectangular panels shown in Figure 5.10(c). The panel dimensions  $\Delta x \times \Delta y$  are sufficiently small to ensure that the far-field condition  $|\mathbf{x}| \gg \Delta x, \Delta y$  is satisfied. For each panel, streamwisely averaged values of the local boundary-layer properties  $\delta$  and  $u_\tau$  on a rough plate are determined through the empirical formulae (3.33) and (3.39) in Section 3.3.3. The total roughness noise radiation from the whole SAX-40 surface is therefore obtained by adding up the sound power radiated from each panel.

### 5.3.1.2 Approach configuration

Because surface roughness noise is a dipole-type source [77–79, 81], the OASPL has an intensity proportional to the 6<sup>th</sup> power of flow velocity, *i.e.*  $\langle p^2(\mathbf{x}, t) \rangle \sim U^6$ . Therefore lower approach speeds and/or clean configurations can significantly reduce the noise of approaching aircraft. The Silent Aircraft design utilizes an all-lifting body with large surface area, which potentially leads to an estimated approach speed of 60.8 m/s, a 28% reduction as compared to current aircraft of similar size [72].

The OASPL of surface roughness noise is logarithmically proportional to  $1/|\mathbf{x}|^2$ . Steeper approach angles thereby reduce noise by keeping aircraft at higher altitudes at a given distance from touchdown. In addition, displacing the landing point further down the runway also increases the altitude of the aircraft when crossing the airport perimeter [72]. Therefore a slightly steeper approach path angle  $\alpha = 3.9^\circ$  and a threshold displacement of 1.2 km are utilized to increase the distance between

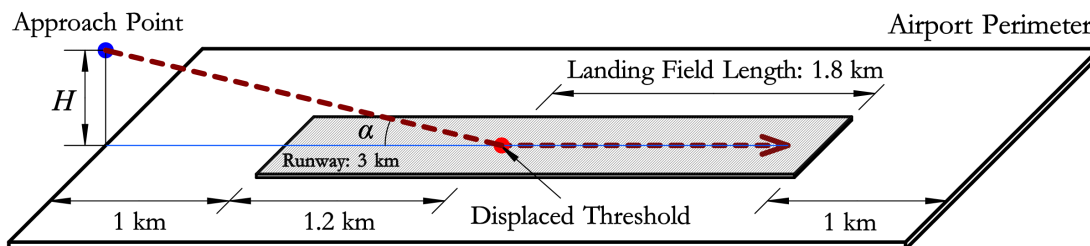


Figure 5.11: Hypothetical airport dimensions used for the noise assessment of SAX-40 during approach.



the aircraft and the ground during the approach phase of flight. As shown in Figure 5.11, the displaced landing point is then 2.2 km away from the airport perimeter for our hypothetical airport. These changes lead to an aircraft altitude  $H \approx 150$  m at the airport perimeter which is increased by 97.5 m compared to a conventional  $3^\circ$  non-displaced approach [72].

### 5.3.2 Noise assessment

#### 5.3.2.1 Idealized test cases

Following the test cases in Section 5.2.2, we consider three hypothetical rough surfaces with idealized roughness levels (see Table 5.1) to preliminarily estimate the noise impact due to surface roughness of an approaching SAX-40. Note that in these test cases, Case 1 is actually a sparse distribution of very large roughness elements with an overestimated value of roughness density  $\sigma = 0.05$ , while Cases 2 and 3 consist of small roughness elements densely distributed over the whole surface.

The predicted ground contours of roughness noise OASPL as the aircraft passes the airport perimeter are illustrated in Figure 5.12 for the three test cases. The dashed line in the ground noise footprint shows the airport perimeter, while the solid black line represents the aircraft flight path. As shown in Figure 5.12, Case 1 generates a loud noise level (maximum OASPL  $> 61$  dBA), whereas the noise level of Case 2 is acceptably quiet and the maximum OASPL is lower than that of Case 1 by about 12 dBA. For Case 3, the noise level is even quieter (maximum OASPL decreased by almost 28 dBA compared to Case 1) and the noise impact is negligible.

Moreover, the ground contours of Cases 1–3 are predicted symmetrical to both eastward (*i.e.* aligned with the runway) and northward (direction normal to the runway) axes. This is because the prediction model is based on low Mach number assumption [77] and thus the flow effects have been neglected in the acoustic intensity as the approach Mach number ( $M \sim 0.18$ ) is sufficiently low. In addition, the maximum OASPL occurs on the eastward axis for Case 1 but on the northward axis for Cases 2 and 3, and is always positioned at a distance of  $H$  from the origin  $(0, 0)$ . However, the minimum OASPL is observed right underneath the aircraft

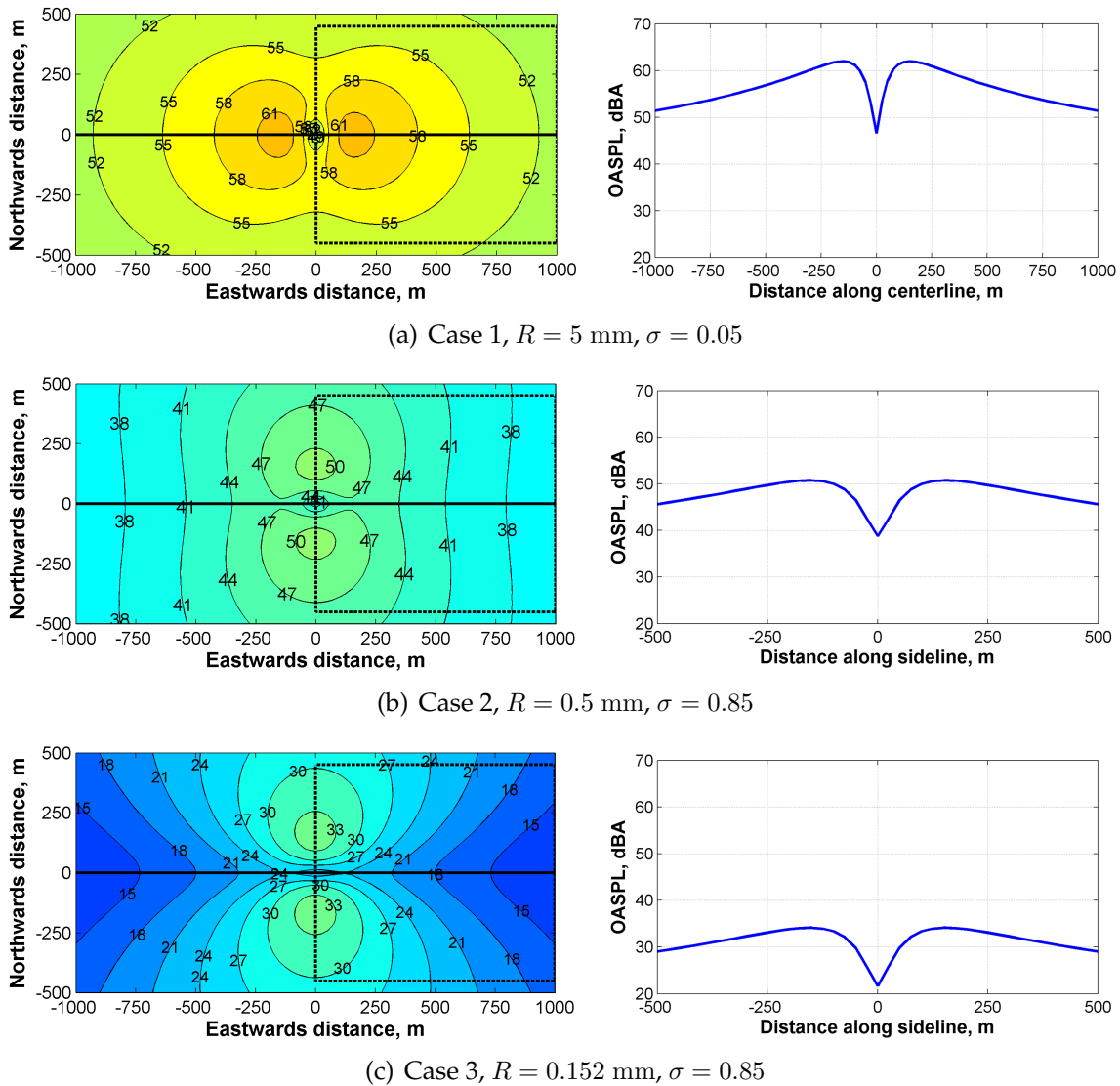


Figure 5.12: Predicted ground contours of roughness noise OASPL for Cases 1–3 of SAX-40.

for all test cases. These characteristics can be ascribed to the dipole directivity of surface roughness noise which have been discussed in Section 5.2.4. Because of the widely distributed SAX-40 planform compared to the aircraft height, the observer's directivity varies over the planform and so the minimum OASPL at the origin  $(0, 0)$  is not  $-\infty$  as expected for a "small" rough region.

### 5.3.2.2 Parametric study

The effects of two dominant parameters, roughness height  $R$  and roughness density  $\sigma$ , on the roughness noise estimate of SAX-40 during approach are illustrated in

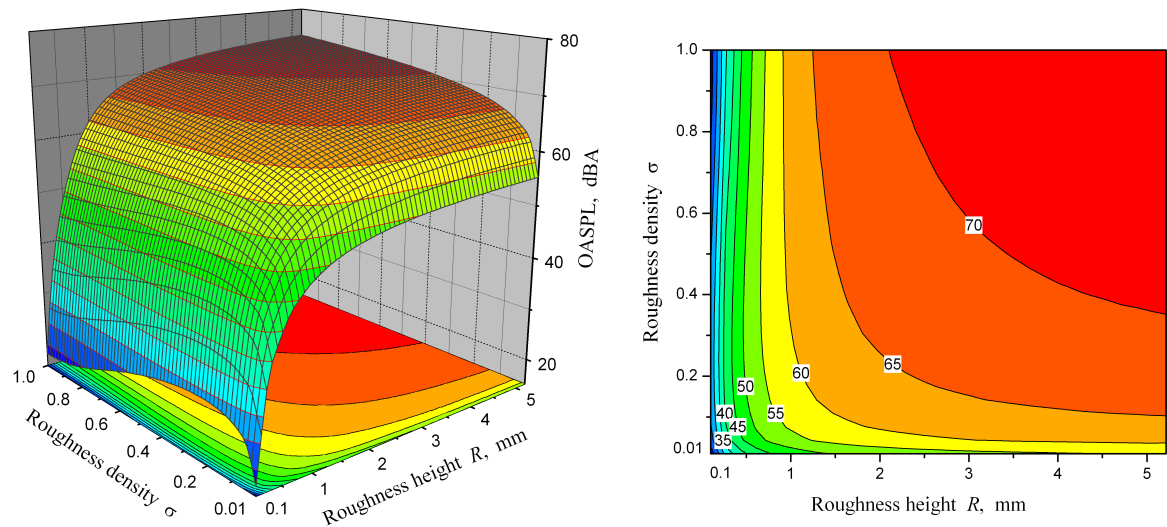


Figure 5.13: Effects of  $R$  and  $\sigma$  on roughness noise OASPL of SAX-40 during approach. Maximum OASPL on the eastward axis at  $(H, 0)$ .

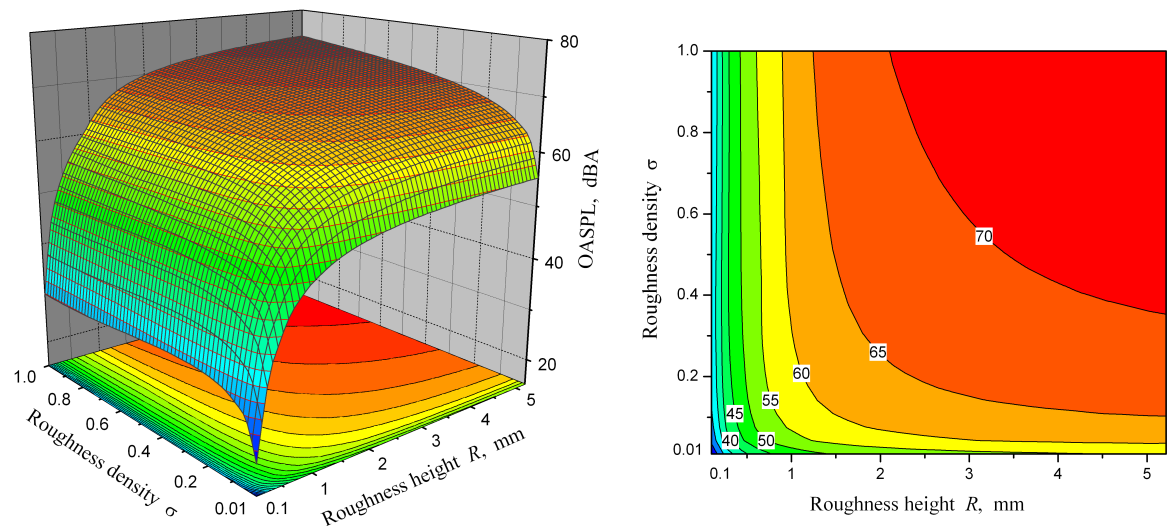


Figure 5.14: Effects of  $R$  and  $\sigma$  on roughness noise OASPL of SAX-40 during approach. Maximum OASPL on both northward and eastward axes at  $(H, 0)$  or  $(0, H)$ .

Figures 5.13 and 5.14. Figure 5.13 shows the variation of the maximum OASPL on the eastward axis fixed at  $(H, 0)$  with both  $R$  and  $\sigma$ , while Figure 5.14 is for the overall maximum OASPL on both northward and eastward axes located at  $(H, 0)$  or  $(0, H)$ . As can be observed in Figure 5.13, the roughness noise OASPL is significantly influenced by roughness height  $R$  and always increases monotonically with  $R$ . Take  $\sigma = 0.01$  for example, as  $R$  increases from 0.1 mm, the roughness noise OASPL increases rapidly from 16.7 dBA to 50.5 dBA at  $R = 1.5$  mm, and then begins to level off until it approaches 55.2 dBA for very large roughness heights ( $R > 5$  mm).

Roughness density  $\sigma$  is another important parameter but with different effects on roughness noise OASPL. For large values of  $R$ , the OASPL increases monotonically with  $\sigma$ , too, and a rapid increase occurs between  $\sigma = 0.01$  and  $0.15$ . However for  $R \leq 0.8$  mm, the variation of OASPL with  $\sigma$  achieves a maximum at a peak value of roughness density,  $\sigma_p$ , because when  $\sigma > \sigma_p$  the wall appears “smoother” as the distribution of roughness elements becomes gradually denser.

All these features of the dependence of the roughness noise OASPL at a fixed position on  $R$  and  $\sigma$  are consistent with those for a Boeing-757 sized wing in Section 5.2.3. Figure 5.14 shows similar characteristics for the overall maximum OASPL on both northward and eastward axes, but there is no evident peak in the variation of OASPL with  $\sigma$  for a fixed value of  $R$ . Furthermore, the OASPL surface, as shown in Figures 5.13 and 5.14 on the left, appears very flat at large values of  $R$  and  $\sigma$ , while it varies rapidly when either  $R$  or  $\sigma$  is small, and it is evident that roughness height  $R$  has more dominant effects than roughness density  $\sigma$  due to the much steeper OASPL surface at small roughness height ( $R < 1.5$  mm).

### 5.3.2.3 Source distribution

Calculation is performed for the distribution of roughness noise sources on the SAX-40 surface. Figure 5.15(a) depicts the  $42 \times 67$  grid for calculation. At each grid point, the sound radiation is calculated for a reference area of

$$A_{\text{ref}} = \frac{A_{\text{gro}}}{(42 - 1) \times (67 - 1)} \approx 0.31 \text{ m}^2, \quad (5.8)$$

where  $A_{\text{gro}}$  is the gross area of the SAX-40 planform ( $A_{\text{gro}} \approx 836.0 \text{ m}^2$ ) and the source powers are converted to OASPL data at a reference position  $(H, 0)$  on the ground. The three idealized test cases as described in Section 5.3.2.1 are investigated.

Figures 5.15(b)–5.15(d) illustrate the relative source distribution for these three cases. It is evident that the source strengths decrease along the chord ( $x$ -direction) for all cases with maximum source strengths at the leading edge. As described in Equation (3.47), in addition to the explicit dependence of  $P_R(\mathbf{x}, \omega)$  on  $\delta^{*-4}$ , the local boundary-layer properties  $u_\tau$  and  $\delta^*$  also influence  $\Phi(\omega)$  and  $D(\theta, \phi)$  implicitly. On a rough plate, the boundary layer is growing along the chord, and

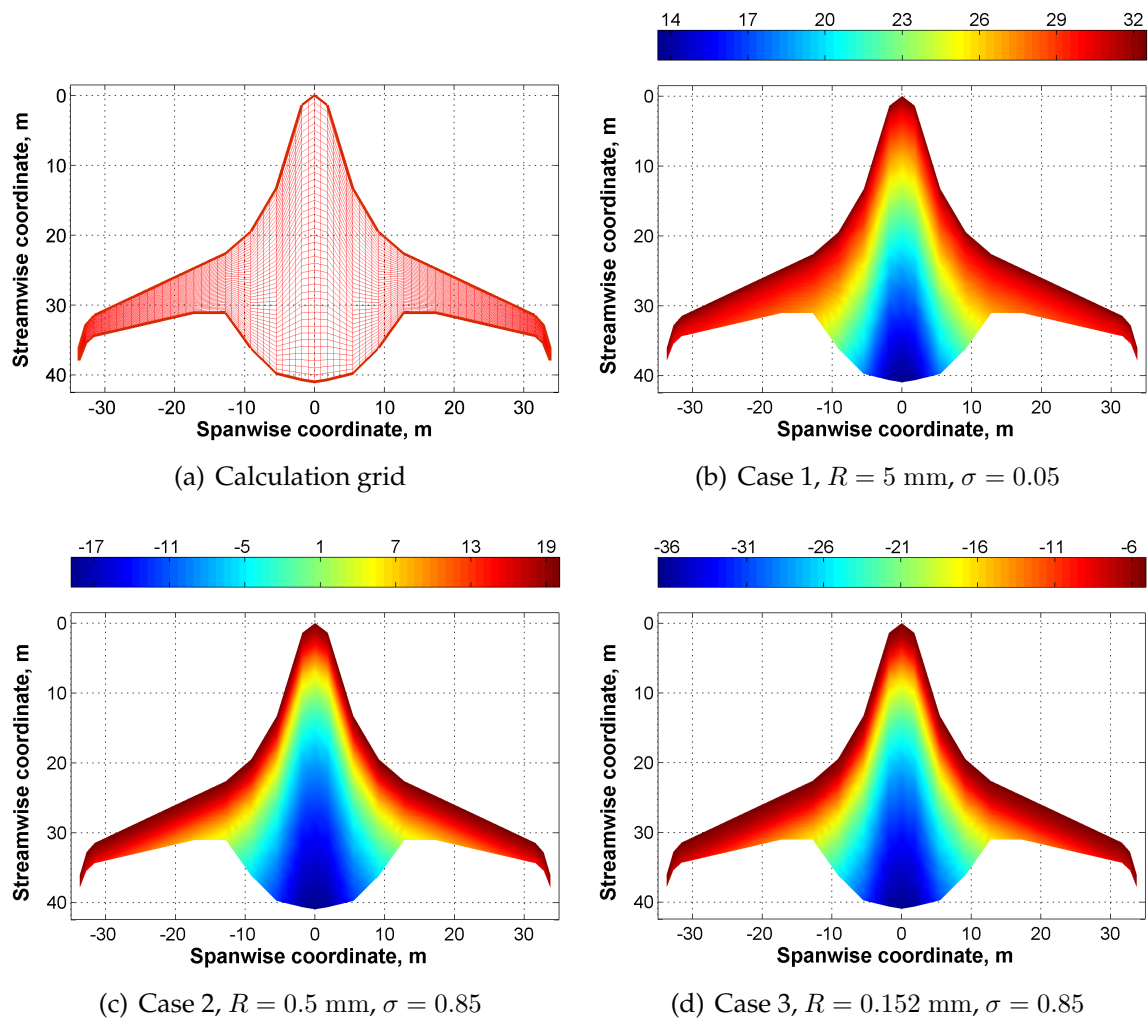


Figure 5.15: Distribution of roughness noise sources (dBA) on the SAX-40 surface.

the boundary-layer profile is determined by both  $x$  and  $R$ . The overall dependence of  $P_R(x, \omega)$  on  $x$  leads to a decreasing distribution of source strengths from upstream to downstream which has been observed in the beamforming source maps of phased array measurements (see Section 4.3). This also implies that the roughness elements on the SAX-40 surface, if possible, should be distributed in downstream region to achieve lower noise sources due to surface roughness.

Comparing Cases 1–3, we see that the source strengths vary gradually from 14 dBA to 32 dBA in Figure 5.15(b), while for Cases 2 and 3 the source distributions appear very similar. As shown in Figures 5.15(c) and 5.15(d), the source strengths are decreasing much more drastically over a range of 36 dBA and 30 dBA, respectively, and the strong sources (red region) are more concentrated around the

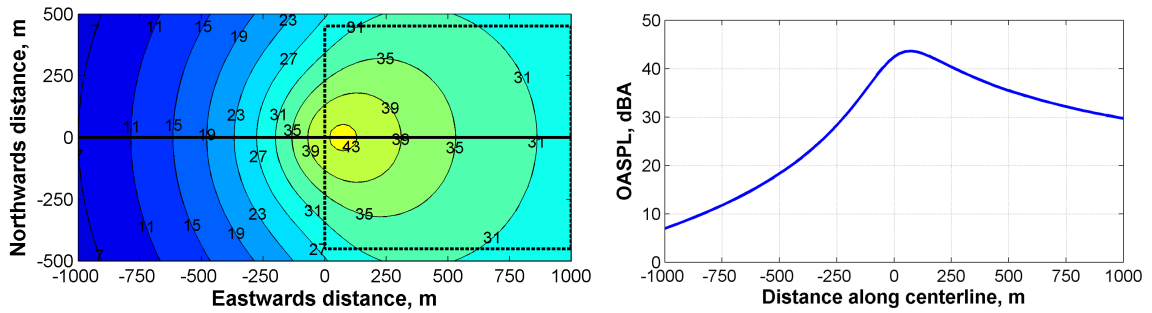
leading edge compared to those of Case 1. The maximum source strength drops rapidly as the size of roughness elements decreases from Case 1 to Cases 2 and 3 despite the increasing roughness density. This indicates that roughness height  $R$  has more effects on surface roughness noise than roughness density  $\sigma$ , which is consistent with the results discussed in Section 5.3.2.2.

#### 5.3.2.4 Effect on TE noise

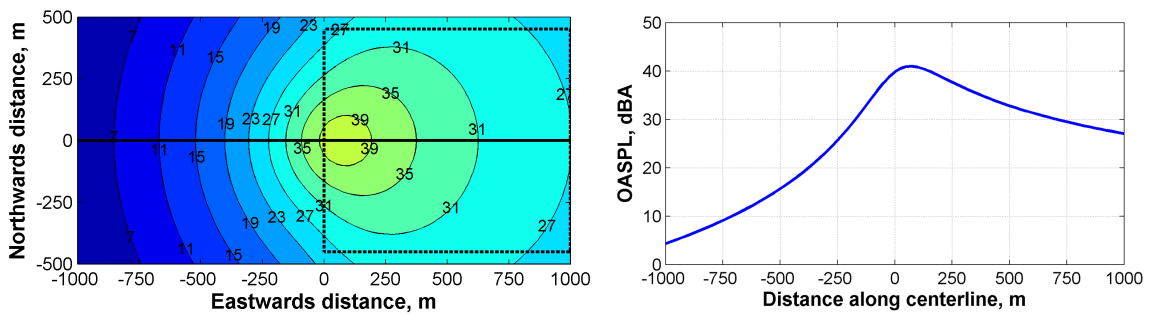
Surface roughness also affects the TE noise through changed boundary-layer properties due to enhanced surface drag and turbulence production [130]. In the numerical prediction for a Boeing-757 sized aircraft wing, the spectral level of TE noise was found to be increased to some extent by surface roughness. Stronger source strengths of TE noise have been observed on a rough plate than a smooth plate in the phased array measurements (see Section 4.3). In this section the effect of surface roughness on TE noise is studied with the same parameters as in Section 5.3.2.1. The empirical model presented by Howe [82] is used to predict the TE noise from SAX-40. The same three idealized roughness cases are studied together with a fourth case of an aerodynamically smooth surface for comparison (see Table 5.1).

Figure 5.16 illustrates the predicted ground contours of TE noise OASPL for test cases 1–4 and should be compared with the corresponding roughness noise estimates in Figure 5.12. As observed in Figure 5.16, the maximum TE noise OASPL in all cases occurs around (75, 0) m, and it shows the level of about 39 dBA for the smooth-wall TE noise in Figure 5.16(d). The maximum OASPL of the rough-wall TE noise is enhanced by 4.5 dBA for Case 1. Similarly in Figure 5.16(b), Case 2 surface roughness increases the maximum OASPL by almost 2 dBA. However for Case 3, the difference between the rough- and smooth-wall maximum OASPL is at most 0.5 dBA due to the very small roughness height which makes Case 3 demonstrate similar features to a smooth surface.

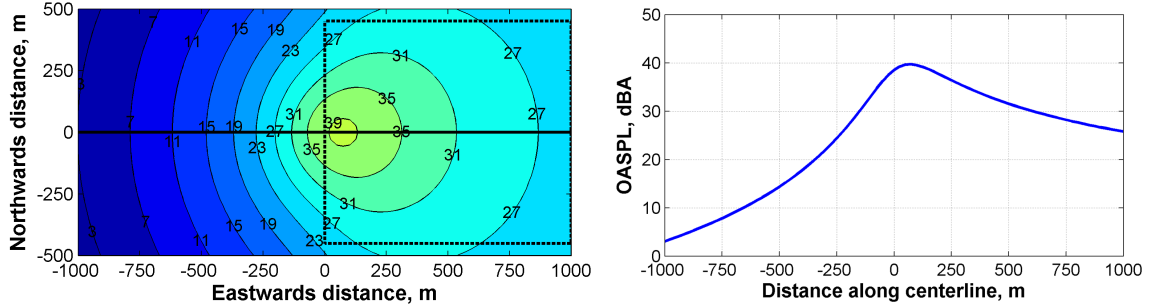
The enhanced TE noise on a rough surface is due to the increased boundary-layer properties as aforementioned. Figure 5.17 shows the comparison of displacement



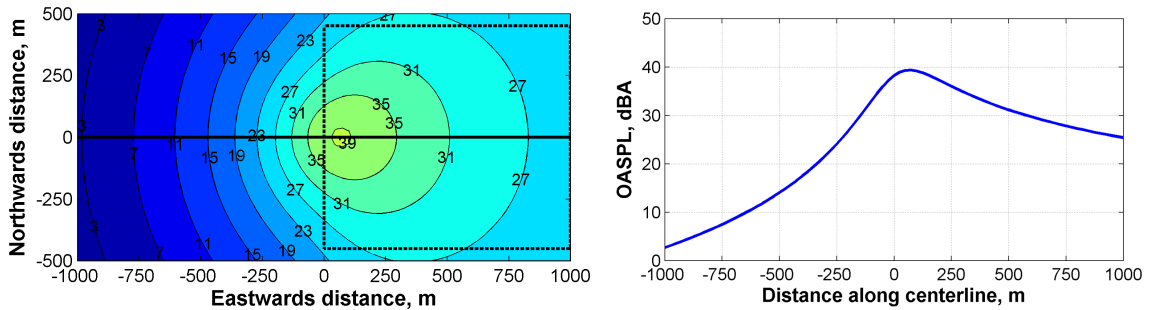
(a) Case 1,  $R = 5 \text{ mm}$ ,  $\sigma = 0.05$



(b) Case 2,  $R = 0.5 \text{ mm}$ ,  $\sigma = 0.85$



(c) Case 3,  $R = 0.152 \text{ mm}$ ,  $\sigma = 0.85$



(d) Case 4, aerodynamically smooth

Figure 5.16: Predicted ground contours of TE noise OASPL for Cases 1–4.

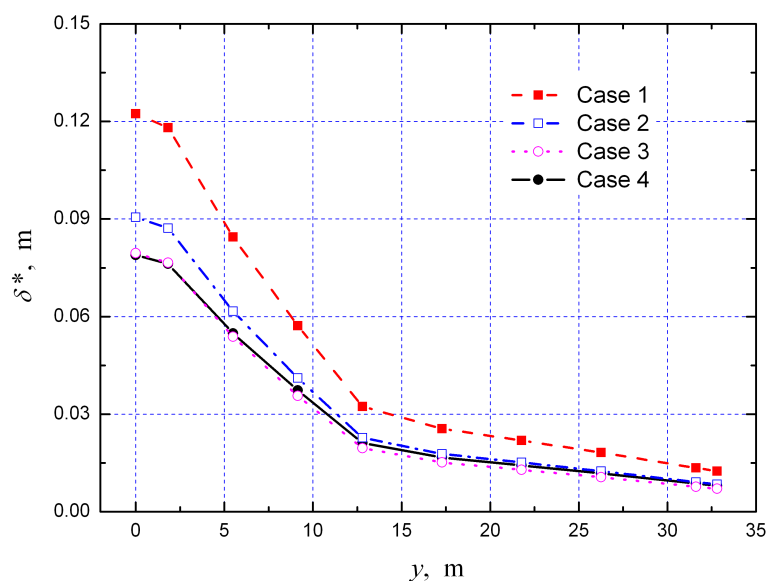


Figure 5.17: Comparison of displacement boundary-layer thickness  $\delta^*$  at the trailing edge of SAX-40 planform along lateral coordinate  $y$ .

boundary-layer thickness  $\delta^*$  at the trailing edge of SAX-40 planform along lateral coordinate  $y$  for Cases 1–4. The determination of boundary-layer thickness on a rough wall has been given in Equation (3.39), and  $\delta$  on a smooth surface is calculated by means of the 1/9 power law [42]. From Figure 5.17 we see that  $\delta^*$  decays along  $y$  due to the decreasing chord length as summarised in Table 5.5. At a fixed  $y$ ,  $\delta^*$  is considerably increased for Case 1, whereas for Case 2 the differences between the rough- and smooth-wall  $\delta^*$  are not so evident especially when  $y \geq 12.8$  m. For Case 3, the  $y$ - $\delta^*$  curve almost coincides with that of the smooth wall.

### 5.3.3 Candidate surface roughness

#### 5.3.3.1 Noise target

SAI has a maximum noise target of 63 dBA outside the airport perimeter for the sum of all noise components, such as the noise from fan, jet, airfoil, undercarriage, *etc.* As SAX-40 is a conceptual design, details of the material for the BWB surface are not available. Instead, we aim to find the maximum allowable roughness for the SAX-40 surface if it is to meet the given noise target. To keep surface roughness as a negligible contributor to the overall noise, a target of 50 dBA has been set for the roughness noise radiated from the SAX-40 surface to the ground.



Two categories of surface roughness which are common for current aircraft wings and fuselage are considered:

- **Category 1:**

Roughness due to large but sparsely distributed bosses, *e.g.* joints, seams, bugs, tentative roughness density  $\sigma = 0.01$ ;

- **Category 2:**

Roughness densely distributed over the entire BWB surface due to material or contamination, practical maximum density  $\sigma = 0.85$  [77];

and thus the unknowns become the maximum roughness heights for these two categories that meet the 50 dBA target.

### 5.3.3.2 Propagation effects

The parametric effects on surface roughness noise have been displayed in Figure 5.14 in which the overall maximum OASPL on the ground should be referred to regarding the 50 dBA noise target. As can be found in Figure 5.14, roughness densities of 0.01 and 0.85 correspond to the roughness heights of 1.4 mm and 0.4 mm along the 50 dBA contour line, which gives a preliminary estimate about the candidate roughness heights for the two categories of rough surfaces.

However in real cases, more effects need to be taken into account when acoustic energy is propagated from the source to the ground. In this work, we applied the techniques described by Evans [47] to propagate the resultant source noise to the ground. These techniques assume spherical spreading, atmospheric attenuation [45] and lateral attenuation [46] within a still, uniform medium, and attenuation/amplification of acoustic energy due to incidence onto a grassy surface. A +3 dB correction was made for ground reflection [72]. Therefore the maximum values of  $R$  could possibly be higher than 1.4 mm and 0.4 mm for Categories 1 and 2, respectively, when all propagation effects were included.

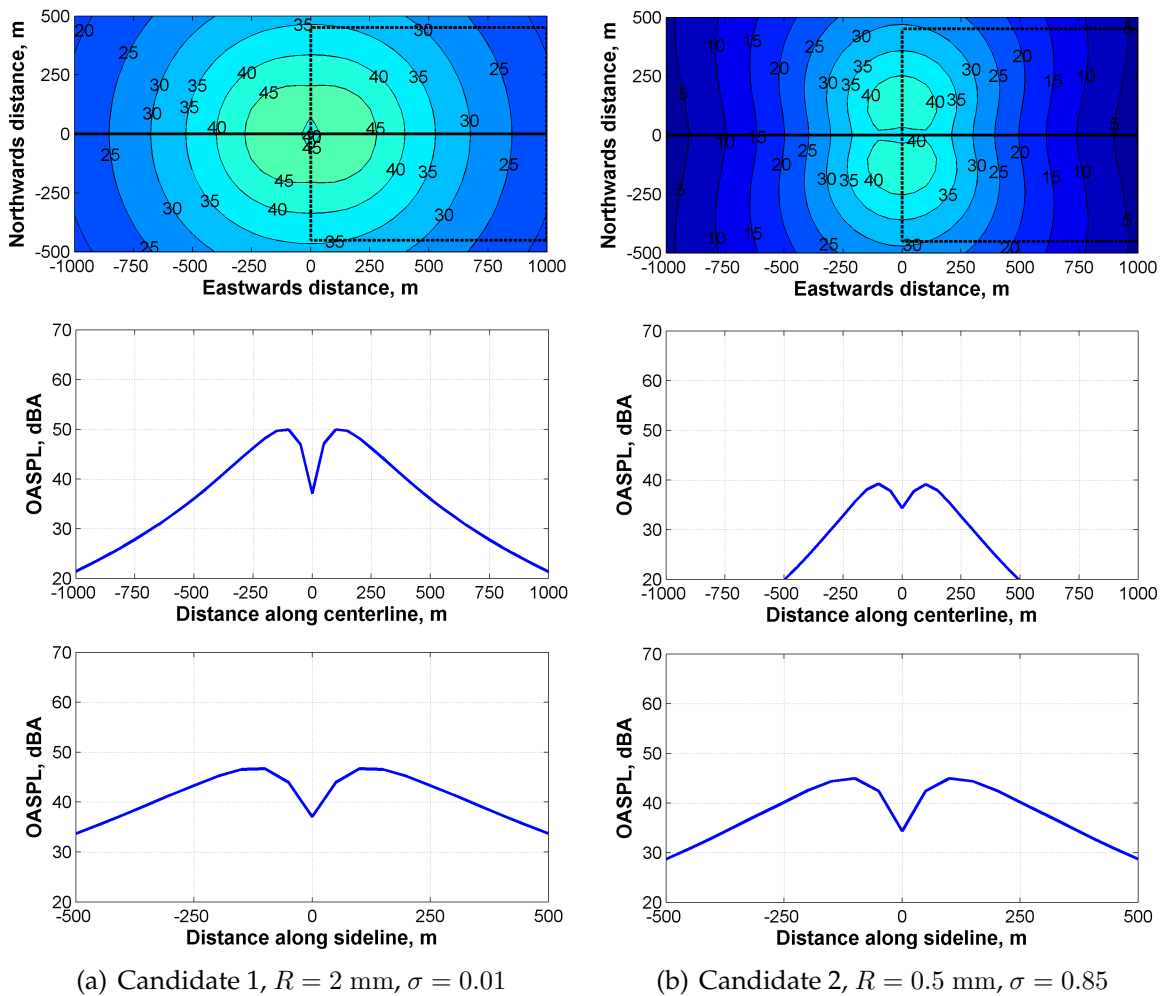


Figure 5.18: Ground noise footprints (dBA) for two candidate rough surfaces: top, ground contour; middle, noise level at flyover; bottom, noise level along sideline.

### 5.3.3.3 Results and discussion

Two candidate rough surfaces have been selected and the ground noise footprints as the aircraft passes the airport perimeter are shown in Figure 5.18. As evident from Figure 5.18, the maximum OASPL is below 50 dBA for both candidate rough surfaces. The ground contours around the aircraft are decaying much more rapidly than those in Figure 5.12, and this should be attributed to the propagation effects.

For Candidate 1, the maximum OASPL of 49 dBA in the centerline is close to the maximum allowable roughness noise OASPL. However, the tentative value  $\sigma = 0.01$  is a conservative estimate for the surface roughness of Category 1. The gross area of SAX-40 is  $836.0 \text{ m}^2$ , and thus a roughness density of 0.01 results in a fractional

area of  $8.36 \text{ m}^2$  fully covered by roughness elements, which is unlikely in practice. In fact, the large roughness bosses due to joints are distributed very sparsely over the aircraft surface, and the adhered bugs are even more sparse.

For Candidate 2, the maximum OASPL in the sideline is below 45 dBA, which makes roughness noise negligible to the aggregate aircraft noise. Furthermore,  $R = 0.5 \text{ mm}$  is also a conservative estimate for the surface roughness of Category 2. For current airliners, natural sheet metal ( $R = 0.0041 \text{ mm}$ ) [44], for example, is a commonly used material for the fuselage. Even for the worst case, smooth matt paint with careful application ( $R = 0.0064 \text{ mm}$ ) [44], the roughness height is still greatly less than  $0.5 \text{ mm}$ . Therefore the noise impacts due to the surface roughness of Category 2 can be ignored as the composite material (possibly forming SAX-40) should be even smoother.

## 5.4 Summary

In this chapter, the validated theoretical model of surface roughness noise has been applied to numerical prediction to assess the contribution of surface roughness to airframe noise. Approximate estimates of the far-field radiated roughness noise were obtained in sequence for a Boeing-757 sized aircraft wing and then the SAI conceptual design SAX-40.

In the first case of the aircraft wing, the absolute levels of roughness noise SPL and OASPL for three idealized test cases have been approximately quantified. It has been shown that TE noise is only significant at very low frequencies, while roughness noise turns out to be the dominant noise of a “clean” airframe in the high frequency region. The spectral level of roughness noise exceeds that of TE noise at sufficiently high frequencies, and corresponding differences in OASPL can be observed, too. Another indirect effect of surface roughness on airframe noise is accounted for by the somewhat enhanced TE noise.

The subsequent parametric study has indicated that both roughness height  $R$  and roughness density  $\sigma$  have significant effects on roughness noise in which roughness height affects the roughness noise more significantly. In addition the

directivity study has shown that the roughness noise OASPL is symmetrical to both  $x_1$ - and  $x_3$ -axes. The lowest OASPL has been observed right underneath the aircraft, and the highest OASPL occurs on the  $x_1$ -axis for Case 1 and on the  $x_3$ -axis for Cases 2 and 3 at the same distance from the origin as the aircraft height. In conclusion, the significant contribution of surface roughness to airframe noise needs to be carefully considered in the design of a low-noise airframe.

In the next application, surface roughness noise has been assessed for the Silent Aircraft conceptual design SAX-40. The three idealized test cases were estimated and the resulting ground contours demonstrated that significant levels of surface roughness noise could be produced from the SAX-40 surface. The parametric study indicated that both  $R$  and  $\sigma$  have significant effects on surface roughness noise with  $R$  a more dominant parameter. The roughness noise sources on the SAX-40 surface were found to be most significant at the leading edge and to decrease downstream due to the influence of the growing boundary layer along the chord. The TE noise was also somewhat enhanced by surface roughness. Candidate rough surfaces of two common categories have been selected for SAX-40 which are able to meet the 50 dBA noise target set for surface roughness noise. Therefore provided the surface finish meets these requirements surface roughness noise would not prevent SAX-40 from meeting the overall noise target.

# Chapter 6

## Drag Dipole Mechanism

### 6.1 Introduction and Survey

THE surface roughness noise due to near-field hydrodynamic pressure fluctuations in the turbulent boundary layer being scattered into sound has been theoretically formulated, experimentally validated and numerically predicted in Chapters 3–5. In this chapter we will focus on the alternative source mechanism, the drag dipole mechanism, and extend it to consider noise produced by fluctuating surface pressures on very large roughness elements. To determine the unsteady drag on the bluff-body-type hemispherical elements, we apply an analytical sphere model proposed by Howe *et al.* [83] (2001) and modify it to adapt to a wall-mounted hemisphere. We now commence with a brief survey on the relevant work of unsteady forces on a sphere and of hairpin vortices.

#### 6.1.1 Lift and drag fluctuations of a sphere

A non-spinning sphere in a high-Reynolds-number, incompressible and nominally steady flow is subject to unsteady lift<sup>†</sup> and drag. Willmarth and Enlow [159], Achenbach [3] and Taneda [144] have suggested that the fluctuating force is caused by the asymmetric shedding of large turbulent eddies into the wake which produces an unsteady bound vorticity vector. Numerous researchers have studied the

---

<sup>†</sup>The side component of the fluctuating force on a sphere has no preferred orientation in a plane normal to the free-stream direction, but nonetheless it is usually referred to as the unsteady *lift*.

vortex shedding characteristics due to uniform flow past spheres (Möller [110], Achenbach [2, 3], Sakamoto and Haniu [128], Taneda [143, 144], Willmarth and Enlow [159], *etc.*). It has been discovered that vortex shedding from a sphere at large Reynolds numbers occurs predominantly at a Strouhal number  $fD/U \approx 0.2$ , where  $D$  is the diameter of the sphere and  $U$  is the undisturbed stream velocity. The spectrum of the unsteady lift is generally very broadband. Willmarth and Enlow [159] reported measurements of the lift for a sphere in air, whose spectrum exhibits smoothly varying behaviour at Strouhal numbers  $\leq 0.3$  in the supercritical range  $4.84 \times 10^5 \leq Re \leq 1.67 \times 10^6$ .

There have been limited publications on measurements of the spectrum of the unsteady drag on a sphere and its magnitude relative to the lift. According to the numerical simulations at  $Re < 1000$  by Johnson and Patel [88], Mittal [107] and Tomboulides and Orszag [148], the wake becomes asymmetric when  $Re$  exceeds 350–450 and the drag at these Reynolds numbers is five or six times larger than the lift. However, Zierke [162] carried out a numerical study and showed that the time-dependent drag experienced by a freely falling sphere at  $Re = 1000$  is an order of magnitude smaller than the lift. The experiments by Howe *et al.* [83] indicate that this is also true at higher Reynolds numbers, at least for  $Re$  as large as about 17000. This is consistent with the corresponding results for a cylinder in a cross flow (Goldstein [62], Phillips [119]) where the root-mean-square lift is also an order of magnitude larger than that of the drag [156].

Willmarth and Enlow [159] have observed that the large fluctuating forces on the sphere are strongly correlated with fluctuations in the bound vorticity in the meridian plane normal to the force, and they conjectured that these fluctuations in bound vorticity arise from the shedding of large-scale coherent structures into the wake, even at supercritical Reynolds numbers ( $Re > 3.7 \times 10^5$ ). The general characteristics of the wake have been summarized by Sakamoto and Haniu [128] for subcritical, low and intermediate Reynolds number. In particular, hairpin-type vortices are found in the wake when  $300 < Re < 420$ . When  $Re$  exceeds 800 large-scale vortex loops were observed to move away from the sphere, rotating at random about an axis parallel to the flow through the centre of the sphere.

The Strouhal frequency of coherent shedding increases with Reynolds number and approaches the constant  $\sim 0.19$  at  $Re \sim 20000$ . Flow visualizations by Taneda [144] at  $Re = 3.5 \times 10^5$  revealed that the large-scale structure of the wake is asymmetric and contains a sequence of hairpin-shaped vortices which appear as quasi-regular spaced vortex loops in the region immediately downstream of separation.

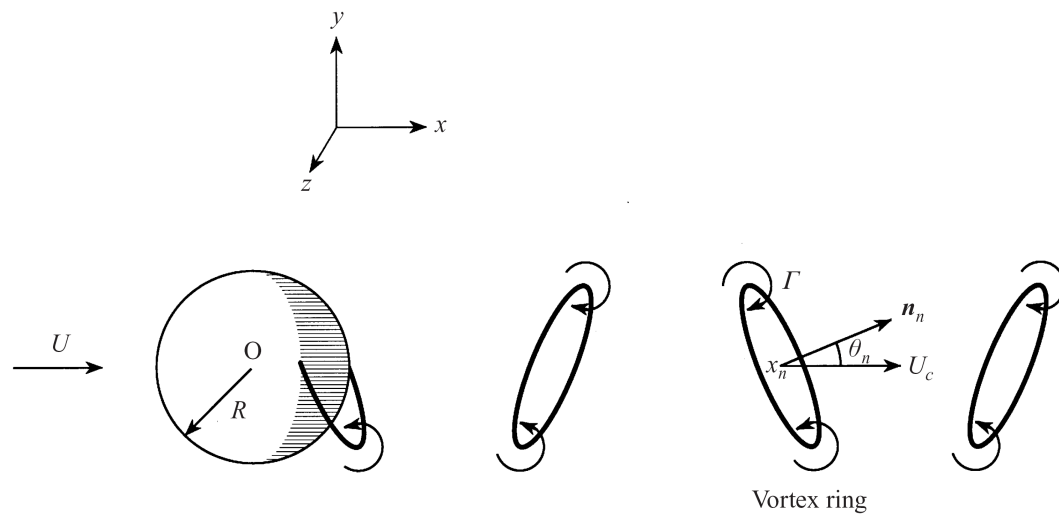


Figure 6.1: Vortex shedding from a sphere modelled by a sequence of randomly orientated vortex rings (Howe *et al.* [83]).

On the basis of these observations, Howe *et al.* [83] recently modelled the unsteady lift and drag on a sphere in high-Reynolds-number flow analytically in terms of a simplified model of vortex shedding that involves coherent eddies in the form of a succession of randomly orientated vortex rings, interconnected by pairs of oppositely rotating line vortices and shed quasi-periodically at a Strouhal number  $\sim 0.19$  (see Figure 6.1). The rings are rapidly dissipated at the higher Reynolds numbers by turbulence diffusion. However, significant fluctuations in the bound vorticity can occur only during the shedding of a vortex ring, and it is shown that the principal contribution to the surface force is supplied by the nascent vortex ring, and that the force spectrum at Strouhal numbers exceeding unity is effectively independent of the shape of the fully formed vortex. At these frequencies, Howe *et al.*'s predictions of the lift and drag spectra based on this model are in close agreement with their towing tank measurements.

### 6.1.2 Hairpin vortices

A hairpin (or horseshoe) vortex is a common vortical structure in the wake of a bluff body or in turbulent boundary layers. In addition to the work introduced in Section 6.1.1, it has long been known that spheres placed in either a uniform flow or a shear flow will shed hairpin-type vortices under certain flow conditions [1]. Since Theodorsen [146] proposed that the key element of the turbulent boundary layer structure is the hairpin vortex, there has been immense interest in the detection and characterisation of the vortical structures in turbulent boundary layers, and a systematic review has recently been given by Ahn [4] (2005). Here we will survey some of the representative studies related to hairpin vortices.

As the pioneer of this idea, Theodorsen [146] proposed a hairpin vortex model describing an instantaneous structure of the turbulent boundary layer. In his model, a hairpin-like vortex rises from the wall and grows outward with an angle of  $45^\circ$  to the wall, and the length between vortex legs is in inverse proportion to the distance from the wall. Head and Bandyopadhyay [69] investigated a turbulent boundary layer over a wider range of Reynolds numbers and observed a large number of hairpin vortices which are stretched out and thin at high Reynolds numbers, while at lower Reynolds numbers these vortices are thick (see Figure 6.2).

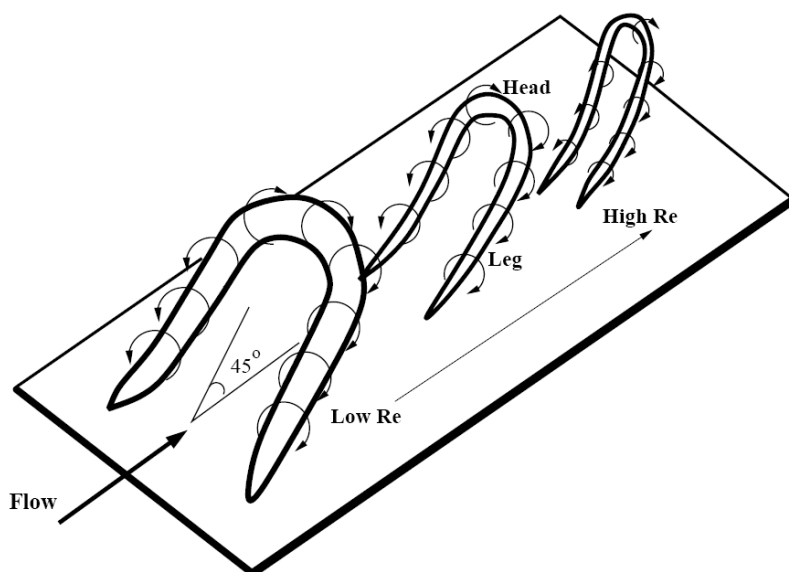


Figure 6.2: Hairpin vortex shapes at different Reynolds number ( $500 < Re_\theta < 17500$ ) flows (Head and Bandyopadhyay [69]).



They concluded that the turbulent boundary layer consists of a bunch of hairpin vortices inclined at  $45^\circ$  to the wall, and that these vortices maintain  $45^\circ$  for some distance while they are convected downstream. On the basis of flow visualization of the turbulent boundary layer, similar vortices of  $45^\circ$  inclination were detected by Bandyopadhyay [9], Perry *et al.* [118], Smith [137] and Acarlar and Smith [1]. However, there is no clear explanation for the  $45^\circ$  angle, other than the fact that the maximum mean rate of strain is acting at  $45^\circ$ .

Numerical simulations of turbulent flow also support the existence of hairpin vortices in wall turbulence. Moin and Kim [108] investigated turbulent channel flow with Large Eddy Simulation (LES) technique and found that the inclination angle of vorticity vectors attains its maximum at  $45^\circ$  to the wall. Kim and Moin [90] further investigated the same vorticity field to identify the vortical structures associated with the bursting process in wall turbulent flow, and showed that the ensemble averaged vorticity fields also provide strong evidence for the existence of hairpin vortices inclined at  $45^\circ$  to the wall during the bursting process. The numerical work of Singer and Joslin [135] showed the growth of a hairpin vortex in a flat plate boundary layer into a young turbulent spot, in which the legs of the vortex are stretched into a hairpin shape as it travels downstream.

Metzler [103] observed that under certain conditions symmetric, controlled hairpin vortices are generated in the separated laminar wake behind a hemisphere. Based on Metzler's observations, a comprehensive study was carried out by Acarlar and Smith [1] on the hairpin vortices generated by the interaction of a hemispherical protuberance within a developing low-Reynolds-number boundary layer, and it has been observed that many of the visual patterns in the near-wall region of the turbulent boundary layer can also be detected in the wake of the hairpin-shedding hemisphere. They summarised that once a hairpin vortex is formed, its transverse tip, head and counter-rotating legs begin to move away from the wall, and it aligns at  $45^\circ$  to the wall while moving downstream. As the hairpin rises the upper portions of the legs migrate across the boundary-layer velocity gradient, which results in a stretching of the legs. The portions of the legs that merge together begin to interact via viscous effects resulting in a mutual vorticity cancellation. The growth of the

hairpin head appears to continue as long as the head is in the boundary layer. Once the head passes out of the boundary layer, it is only under the influence of its own induced velocity and free-stream advection.

### 6.1.3 Motivation and structure of the chapter

Motivated by the analytical model of Howe *et al.* [83] and the observations of Acarlar and Smith [1], in this thesis we assume that the hairpin vortices in the wake of a hemispherical surface protuberance can be modelled by considering a succession of quasi-periodically shed half vortex rings that are aligned symmetrically with the vertical plane and inclined mainly at  $45^\circ$  to the wall. Howe *et al.*'s sphere model [83] will therefore be extended to determine the fluctuating lift and drag on a wall-mounted hemisphere, so that the drag dipole noise from a hemispherical roughness element can be evaluated approximately.

Firstly, Howe *et al.*'s model [83] of lift and drag fluctuations on a sphere is introduced succinctly in Section 6.2 summarising the main points of the derivation for completeness of the idea. Then we formulate the theory of drag dipole noise from hemispherical bosses on an otherwise flat plate in Section 6.3 and present two alternative approaches of determining the spectrum of the unsteady drag, *i.e.* Glegg *et al.*'s drag model [61] for relatively large roughness elements (Region II in Figure 2.3) and the wall-mounted hemisphere model developed in this work for very large roughness elements (the upper section of Region III). Section 6.4 presents numerical predictions for the unsteady lift and drag during the initial stages of vortex formation, and preliminary assessments of the drag dipole noise and its comparison with the scattering noise.

## 6.2 Howe *et al.*'s Sphere Model of Unsteady Forces

### 6.2.1 Analytical model of vortex shedding

In the analytical model, Howe *et al.* [83] consider a rigid sphere of radius  $R$  situated in the presence of a nominally steady, incompressible flow at speed  $U$  in the positive

$x$ -direction. The centre of the sphere is at the origin of the Cartesian coordinates  $(x, y, z)$ . The wake flow is turbulent owing to the sufficiently high Reynolds number, and its dominant characteristics are modelled by a sequence of vortex rings depicted schematically in Figure 6.1. The rings are shed from the sphere quasi-periodically at frequency  $f_0$  and Strouhal number  $f_0 D/U \sim 0.2$ , where  $D = 2R$  is the diameter of the sphere.

The vortex rings are assumed to translate in the mean stream direction with their centres on the  $x$ -axis at a constant convection velocity  $U_c \approx 0.7U$ . The  $n$ th ring has radius  $a$  and circulation  $\Gamma$  (see Figure 6.1); its normal  $\mathbf{n}_n$  to the plane of the ring makes an angle  $\theta_n$  ( $0 \leq \theta_n \leq \pi/2$ ) with the positive  $x$ -axis, and  $\varphi_n$  is denoted as the azimuthal angle between the  $y$ -direction and the plane defined by the  $x$ -axis and  $\mathbf{n}_n$ . As the ring tip is convected downstream, the arc increases in length with its attachment points to the sphere moving around  $z = 0$  to the separation points A and B, as illustrated in Figures 6.1 and 6.3. If shedding starts for the  $n$ th ring at time  $t = t_n$ , it is complete when  $t = t_n + \delta t_n$ , where  $\delta t_n$  denotes the duration of shedding,

$$\delta t_n = 2a \sin \theta_n / U_c, \quad (6.1)$$

and the position of the centre of this ring on the  $x$ -axis is

$$x_n(t) = U_c(t - t_n) + \sqrt{R^2 - a^2 \cos^2 \theta_n} - a \sin \theta_n, \quad t > t_n. \quad (6.2)$$

As pointed out by Howe *et al.* [83], the proposed shedding mechanism can produce quasi-periodic and potentially large-amplitude fluctuations in the "lift" force.

### 6.2.1.1 The surface forces

According to Howe [80], the net force exerted on the sphere in the  $i$ -direction in incompressible flow can be expressed as

$$F_i(t) = \rho_0 \int \nabla X_i \cdot (\boldsymbol{\omega} \wedge \mathbf{v}) d^3 \mathbf{x} - \eta \oint_S (\boldsymbol{\omega} \wedge \nabla X_i) \cdot d\mathbf{S}, \quad (6.3)$$

where  $\rho_0, \eta$  are the mean density and shear viscosity of the fluid;  $\mathbf{v}(\mathbf{x}, t)$  is the fluid velocity, and  $\boldsymbol{\omega} \equiv \text{curl } \mathbf{v}$  is the vorticity; the auxiliary function

$$X_i = x_i \left( 1 + \frac{R^3}{2|\mathbf{x}|^3} \right) \quad (6.4)$$

coincides with the velocity potential of an ideal flow past the sphere that has unit speed in the  $i$ -direction at large distances from the sphere. The surface integral in Equation (6.3) represents the surface force produced by the viscous skin friction and can be discarded at high Reynolds numbers. Thus, the net force can be obtained by

$$F_i(t) = \sum_{n=-\infty}^{\infty} F_{in}(t), \quad (6.5)$$

where  $F_{in}(t)$  denotes the force component attributable to the  $n$ th vortex ring,

$$\begin{aligned} F_{in}(t) &= 0, & t < t_n \\ &= \rho_0 \int \nabla X_i \cdot (\boldsymbol{\omega}_n \wedge \mathbf{v}) d^3\mathbf{x}, & t > t_n, \end{aligned} \quad (6.6)$$

and  $\boldsymbol{\omega}_n(\mathbf{x}, t)$  is the vorticity distribution of the  $n$ th ring.

To evaluate the volume integral in Equation (6.6), Howe *et al.* [83] assume the cross-section of the vortex ring core to be infinitesimal, and to fix ideas they consider the case in which the  $n$ th ring is orientated with its normal  $\mathbf{n}_n$  in the  $(x, y)$ -plane (*i.e.*  $\varphi_n = 0$ ). If  $\xi$  is defined as the angle measured from the lower point of intersection of the ring and the  $(x, y)$ -plane (where  $y < 0$ , see Figure 6.3),  $s = a\xi$  denotes the

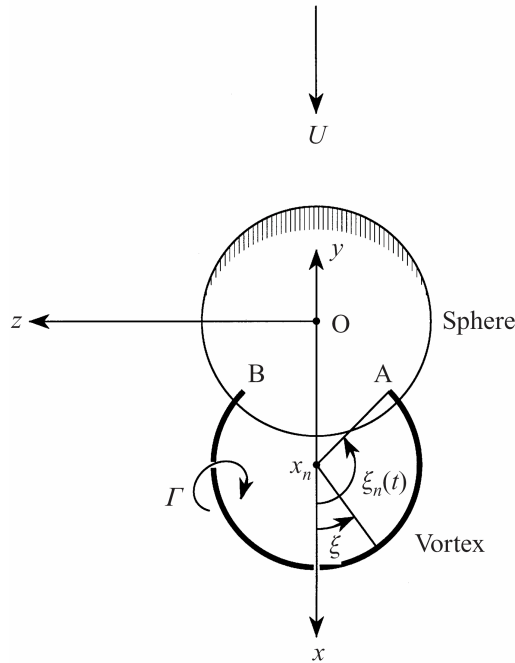


Figure 6.3: View from downstream and above of a vortex ring separating from the sphere at A and B when  $\varphi_n = 0$ . The angle  $\xi_n(t)$  determines the total arc length  $2a\xi_n(t)$  of the shed vortex during separation (Howe *et al.* [83]).

curvilinear distance along the axis of the core in the right-handed sense with respect to  $\mathbf{n}_n$ . The instantaneous velocity  $\mathbf{v}$  must satisfy the no-slip boundary condition on the sphere, but Howe *et al.* take  $\mathbf{v} = (U_c, 0, 0)$  on the ring to account for uniform convection of the vortex at constant speed  $U_c$  in the  $x$ -direction, so that

$$(\boldsymbol{\omega}_n \wedge \mathbf{v}) d^3 \mathbf{x} = \Gamma U_c (0, \cos \xi, \cos \theta_n \sin \xi) a d\xi, \quad (6.7)$$

and hence

$$F_{in}(t) = \rho_0 U_c \Gamma a \int_{-\xi_n(t)}^{\xi_n(t)} \left( \cos \xi \frac{\partial X_i}{\partial y} + \cos \theta_n \sin \xi \frac{\partial X_i}{\partial z} \right) d\xi, \quad t > t_n. \quad (6.8)$$

In the above formula the integral bounds are taken as

$$\begin{aligned} \xi_n(t) &= \pi, & t > t_n + \delta t_n \\ &= \frac{\pi}{2} + \sin^{-1} \left[ \frac{x_n^2(t) + a^2 - R^2}{2ax_n(t) \sin \theta_n} \right], & t_n < t < t_n + \delta t_n, \end{aligned} \quad (6.9)$$

and the derivatives  $\partial X_i / \partial y$ ,  $\partial X_i / \partial z$  are evaluated on the vortex ring at the integration point given by

$$\mathbf{x} = (x_n(t) + a \sin \theta_n \cos \xi, -a \cos \theta_n \cos \xi, -a \sin \xi). \quad (6.10)$$

### 6.2.1.2 The unsteady lift and drag

When  $\varphi_n = 0$ , it is evident by symmetry that  $\mathbf{F}_n$  of the  $n$ th vortex ring can be resolved into a "lift" in the  $y$ -direction and a drag in the  $x$ -direction. The mean lift must vanish, but the root-mean-square lift is the same in all directions transverse to the mean flow, and may be evaluated in the  $y$ -direction by setting

$$X_i = X_y \equiv y \left( 1 + \frac{R^3}{2|\mathbf{x}|^3} \right) \quad (6.11)$$

in Formula (6.8). When  $\varphi_n \neq 0$ , the component of the lift  $\mathcal{L}_n$  in the  $y$ -direction can be obtained by first evaluating it for  $\varphi_n = 0$  and then multiplying by  $\cos \varphi_n$ , yielding

$$\mathcal{L}_n = \rho_0 U_c \Gamma a \cos \varphi_n \mathcal{F}_n(t - t_n), \quad (6.12)$$

$$\begin{aligned} \mathcal{F}_n(t - t_n) &= 0, & t < t_n \\ &= \int_{-\xi_n(t)}^{\xi_n(t)} \cos \xi \left[ 1 + \frac{R^3 (x_n^2(t) + 2ax_n(t) \cos \xi \sin \theta_n + a^2 (1 - 3 \cos^2 \theta_n))}{2(x_n^2(t) + 2ax_n(t) \cos \xi \sin \theta_n + a^2)^{5/2}} \right] d\xi, & t > t_n. \end{aligned} \quad (6.13)$$

On the other hand, the drag  $\mathcal{D}_n$  produced by the  $n$ th vortex ring is independent of  $\varphi_n$ . Taking  $X_i = X_x$  in Formula (6.8) yields

$$\mathcal{D}_n = \rho_0 U_c \Gamma a \mathcal{G}_n(t - t_n), \quad (6.14)$$

$$\begin{aligned} \mathcal{G}_n(t - t_n) &= 0, \quad t < t_n \\ &= \frac{3aR^3 \cos \theta_n}{2} \int_{-\xi_n(t)}^{\xi_n(t)} \frac{(x_n(t) + a \cos \xi \sin \theta_n) d\xi}{(x_n^2(t) + 2ax_n(t) \cos \xi \sin \theta_n + a^2)^{5/2}}, \quad t > t_n. \end{aligned} \quad (6.15)$$

## 6.2.2 The lift and drag spectra

### 6.2.2.1 The mean drag

Howe *et al.* [83] then simulate periodic vortex shedding from the sphere by assuming that the  $n$ th vortex ring starts to form at time  $t_n = n\tau$ , where  $\tau \equiv 1/f_0$  and  $f_0 \sim 0.2U/D$ . The mean drag can be written in the form

$$\langle \mathcal{D}_n(t) \rangle = \rho_0 U_c \Gamma a \sum_{n=-\infty}^{\infty} \langle \mathcal{G}_n(t - t_n) \rangle, \quad (6.16)$$

where the angle brackets denote an ensemble average of the train of vortex rings. Introduce the Fourier transform of  $\mathcal{G}_n(t)$ ,

$$\hat{\mathcal{G}}_n(\omega) = \frac{1}{2\pi} \int_0^{\infty} \mathcal{G}_n(t) e^{i\omega t} dt, \quad (6.17)$$

and thus the mean drag (6.16) becomes

$$\langle \mathcal{D}_n(t) \rangle = \rho_0 U_c \Gamma a \int_{-\infty}^{\infty} \sum_{n=-\infty}^{\infty} \langle \hat{\mathcal{G}}_n(\omega) \rangle e^{-i\omega(t-n\tau)} d\omega. \quad (6.18)$$

The mean value  $\langle \hat{\mathcal{G}}_n(\omega) \rangle$  is independent of  $n$ , and the Fourier expansion [96]

$$\sum_{n=-\infty}^{\infty} e^{-i\omega n\tau} = \frac{2\pi}{\tau} \sum_{m=-\infty}^{\infty} \delta\left(\omega - \frac{2\pi m}{\tau}\right) \quad (6.19)$$

therefore gives

$$\langle \mathcal{D}_n(t) \rangle = \frac{2\pi \rho_0 U_c \Gamma a}{\tau} \sum_{m=-\infty}^{\infty} \langle \hat{\mathcal{G}}_n(2\pi m f_0) \rangle e^{-i2\pi m f_0 t}, \quad (6.20)$$

which shows how the ensemble-average drag varies with time at the fundamental shedding frequency  $f_0$ . The time-averaged drag  $\overline{\mathcal{D}}$  is thus obtained as

$$\overline{\mathcal{D}} = \frac{2\pi \rho_0 U_c \Gamma a}{\tau} \langle \hat{\mathcal{G}}_n(0) \rangle \equiv \frac{\rho_0 U_c \Gamma a}{\tau} \int_0^{\infty} \langle \mathcal{G}_n(t) \rangle dt. \quad (6.21)$$

Combining  $\overline{\mathcal{D}} = C_D \frac{1}{2} \rho_0 U^2 A^\dagger$  and Equation (6.21), the circulation  $\Gamma$  can be expressed in terms of the mean drag coefficient  $C_D$  of the sphere:

$$\frac{\Gamma}{UR} = \frac{\pi C_D R U}{2 a U_c} \left/ \frac{1}{\tau} \int_0^\infty \langle \mathcal{G}_n(t) \rangle dt. \right. \quad (6.22)$$

### 6.2.2.2 The spectra of lift and drag fluctuations

The time-dependent lift experienced by the sphere in the  $y$ -direction is given by

$$\mathcal{L}(t) = \rho_0 U_c \Gamma a \sum_{n=-\infty}^{\infty} \cos \varphi_n \mathcal{F}_n(t - t_n). \quad (6.23)$$

Evidently the mean lift vanishes since  $\langle \cos \varphi_n \rangle = 0$ . When successive vortices are statistically independent,  $\langle \cos \varphi_n \cos \varphi_m \rangle = \frac{1}{2} \delta_{nm}$  and the mean-square lift becomes

$$\begin{aligned} \langle \mathcal{L}^2(t) \rangle &= \frac{(\rho_0 U_c \Gamma a)^2}{2} \sum_{n=-\infty}^{\infty} \langle \mathcal{F}_n^2(t - t_n) \rangle \\ &= \frac{(\rho_0 U_c \Gamma a)^2}{2} \iint_{-\infty}^{\infty} \sum_{n=-\infty}^{\infty} \langle \hat{\mathcal{F}}_n(\omega) \hat{\mathcal{F}}_n^*(\omega') \rangle e^{-i(\omega - \omega')(t - n\tau)} d\omega d\omega', \end{aligned} \quad (6.24)$$

where  $\hat{\mathcal{F}}_n(\omega)$  is the Fourier transform of  $\mathcal{F}_n(t)$  as in Equation (6.17). As before, the ensemble average  $\langle \hat{\mathcal{F}}_n(\omega) \hat{\mathcal{F}}_n^*(\omega') \rangle$  does not depend on  $n$ , so that the expansion (6.19) (with  $\omega$  replaced by  $\omega - \omega'$ ) leads to a time-averaged, mean-square lift

$$\overline{\mathcal{L}^2} = \frac{\pi(\rho_0 U_c \Gamma a)^2}{\tau} \int_{-\infty}^{\infty} \langle |\hat{\mathcal{F}}_n(\omega)|^2 \rangle d\omega. \quad (6.25)$$

The one-sided frequency spectrum of the lift  $\Phi_L(\omega)$  satisfying

$$\overline{\mathcal{L}^2} = \int_0^\infty \Phi_L(\omega) d\omega \quad (6.26)$$

is therefore obtained as

$$\Phi_L(\omega) = (\rho_0 U_c \Gamma a)^2 \frac{2\pi}{\tau} \langle |\hat{\mathcal{F}}_n(\omega)|^2 \rangle. \quad (6.27)$$

Similarly, the frequency spectrum  $\Phi_D(\omega)$  of the unsteady drag

$$\mathcal{D}'(t) = \mathcal{D}(t) - \langle \mathcal{D} \rangle \quad (6.28)$$

---

<sup>†</sup> $A = \pi R^2$  is the frontal area of the sphere.

is defined such that

$$\overline{\mathcal{D}^2} = \int_0^\infty \Phi_D(\omega) d\omega, \quad (6.29)$$

$$\Phi_D(\omega) = (\rho_0 U_c \Gamma a)^2 \frac{4\pi}{\tau} [\langle |\hat{\mathcal{G}}_n(\omega)|^2 \rangle - |\langle \hat{\mathcal{G}}_n(\omega) \rangle|^2]. \quad (6.30)$$

The remaining averages in the spectra (6.27) and (6.30) are to be taken over all possible orientations  $\theta_n$  of the vortex rings.

### 6.2.3 Comparison of prediction and measurement

Towing tank measurements were conducted by Howe *et al.* [83] to validate the theoretical model. The unsteady lift and drag on a sphere of diameter 7.62 cm were measured in water at four different towing speeds of 10, 15, 20 and 25 cm/s, corresponding to Reynolds numbers ranging from about 7000 to 17000. Details of the construction of the apparatus and the experimental procedure can be found in Howe *et al.* [83], Wang [154] and Wang *et al.* [155]. As shown in Figures 6.4, the solid circles represent average measured values of the normalized lift and drag spectra:

$$G_L(f) = 2\pi \Phi_L(\omega) \quad \text{and} \quad G_D(f) = 2\pi \Phi_D(\omega), \quad (6.31)$$

which ensure that

$$\overline{\mathcal{L}^2} = \int_0^\infty G_L(f) df \quad \text{and} \quad \overline{\mathcal{D}^2} = \int_0^\infty G_D(f) df. \quad (6.32)$$

Also shown in Figure 6.4(a) are the low-frequency lift spectrum (open squares) of Willmarth and Enlow [159] (1969) averaged over the very high Reynolds numbers of 4.84, 8.26, 16.46,  $16.67 \times 10^5$ .

The solid and broken curves in Figure 6.4 are the predictions of  $G_L(f)$  and  $G_D(f)$  determined by Equations (6.27) and (6.30). In these formulae the Fourier transforms  $\hat{\mathcal{F}}_n(\omega)$ ,  $\hat{\mathcal{G}}_n(\omega)$  and the circulation  $\Gamma$  involve double integrals with respect to  $\xi$  and  $t$  which must be evaluated numerically. Here we use the five-point Gauss-Legendre quadrature with adjustable subintervals as for the numerical integrations in Section 3.4.2. The number of subintervals increases exponentially from 200 to 2000 over the range of Strouhal number,  $10^{-4} \leq fD/U \leq 10^2$ , to ensure sufficient accuracy at high frequencies. To validate the reliability of our numerical



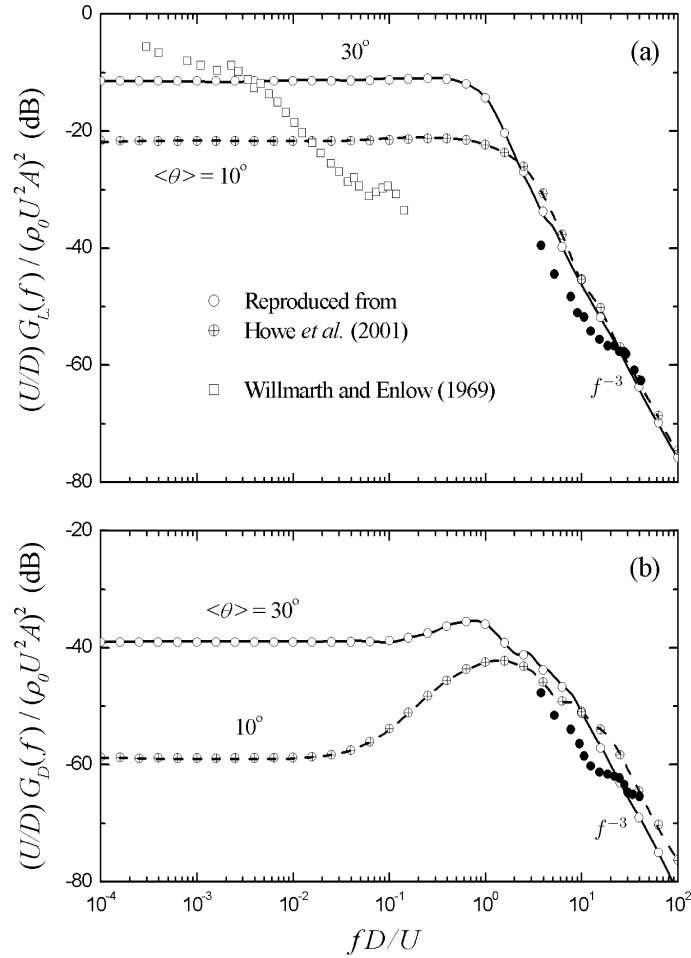


Figure 6.4: Measured and predicted (a) lift spectrum and (b) drag spectrum. ●●● averaged measured values for  $Re = 6680, 10020, 13360, 16700$ . — —,  $\circ \oplus$  predictions for the two cases  $\langle \theta \rangle = 10^\circ, 30^\circ$  when averaging is performed over  $0.9 < \theta_n / \langle \theta \rangle < 1.1$  and  $a = 0.7R$ ,  $U_c = 0.7U$ ,  $C_D = 0.4$  (reproduced from Howe *et al.* [83]).

code, we have reproduced the original lift and drag spectra of Howe *et al.* [83] (curves) and plotted our results as scatter points in Figure 6.4.

In addition, permissible vortex orientations  $\theta_n$  are assumed to be uniformly distributed over the interval  $0.9 < \theta_n / \langle \theta \rangle < 1.1^\dagger$ , where  $\langle \theta \rangle$  is the mean orientation angle and the two cases  $\langle \theta \rangle = 10^\circ, 30^\circ$  are shown in Figure 6.4. Average values have been computed using an ensemble of 100 vortex rings. Following Howe *et al.* [83], the drag coefficient  $C_D = 0.4$  has been taken which is appropriate over the whole

<sup>†</sup>The original interval given by Howe *et al.* [83] is  $0.5 < \theta_n / \langle \theta \rangle < 1.5$ . However, although the lift spectra are only weakly dependent on the extent of the range spanned by  $\theta_n$ , the integration of the drag spectra is sensitive to the interval of  $\theta_n / \langle \theta \rangle$ . We have validated through recalculation that it is actually the interval  $0.9 < \theta_n / \langle \theta \rangle < 1.1$  that is able to reproduce the predictions of  $G_D(f)$  in Figure 6.4, and have confirmed with the authors through personal communication that this is in fact what they used.

subcritical region where  $Re > 10^3$  [130]; and the value  $a = 0.7R$  is used for the radius of the shed vortices because the simplicity of Howe *et al.*'s analytical model and the relative insensitivity of their predictions to the ratio  $a/R$  suggest that this nominal value is probably representative of a high-Reynolds-number wake of reduced width immediately behind the sphere [83].

As can be seen in Figure 6.4, at high Strouhal numbers both sets of theoretical curves decrease like  $f^{-3}$ , independently of  $\langle\theta\rangle$ , and this is close to the trend of the experimental data. Howe *et al.* [83] then conclude from the remarkable accord in the absolute levels between prediction and measurement that the proposed model is correct in principle if not in detail, inasmuch as the high-frequency behaviour of the spectra is governed by the initial stages in the shedding of a vortex structure. Predictions at lower frequencies ( $fD/U < 1$ ) are more critically dependent on the assumed statistics of the vortex rings, but nonetheless exhibit an acceptable level of agreement with the early lift measurements made by Willmarth and Enlow [159]. This sphere model of high Reynolds number will be extended to a wall-mounted hemisphere model in Section 6.3.3 to enable the prediction of noise generated by very large roughness elements.

## 6.3 Drag Dipole Noise

### 6.3.1 Theoretical formulation

We now consider the sound generated by enhanced drag fluctuations on the wall which result from local vortex shedding from each roughness element. The physical process is assumed to be the same as noise from the unsteady loads on rigid, stationary objects in a steady flow and so each individual roughness element behaves as a drag dipole. Therefore the acoustic field radiated by the unsteady forcing exerted on the solid boundary can be derived from the classical FW-H equation [53] as:

$$p(\mathbf{x}, \omega) = \oint_{S(\mathbf{y})} \frac{\partial G(\mathbf{x}, \mathbf{y}, \omega)}{\partial y_i} n_j p_{ij}(\mathbf{y}, \omega) dS(\mathbf{y}), \quad (6.33)$$

where  $S$  denotes the rigid rough surface defined by  $y_2 = \xi(y_1, 0, y_3)$  and  $\mathbf{n}$  is the normal vector of  $S$ . The rough surface is formed by a number of rigid hemispherical bosses of radius  $R$  over the plane  $y_2 = 0$ , and the pressure fluctuations are subject to the rigid boundary condition  $\partial p / \partial y_n = 0$  everywhere on the surface.

To determine the sound field, we introduce the half free space Green's function in the frequency domain:

$$G(\mathbf{x}, \mathbf{y}, \omega) = \frac{-e^{i\omega|\mathbf{x}-\mathbf{y}|/c}}{2\pi|\mathbf{x}-\mathbf{y}|} \quad (6.34)$$

which satisfies the boundary condition

$$\frac{\partial G}{\partial y_2} = 0 \quad \text{on the plane} \quad y_2 = 0. \quad (6.35)$$

We assume that the roughness height  $R$  is much less than the acoustic wavelength (*i.e.* compact roughness elements,  $kR < 1$ ) and that the far-field observer  $\mathbf{x}$  is situated at a distance much greater than  $R$ , so that the derivatives of the Green's function,  $\partial G / \partial y_i$ , are uniform over the hemispherical elements. Therefore the surface integral of the acoustic field (6.33) becomes

$$p(\mathbf{x}, \omega) = -\frac{\partial G(\mathbf{x}, \mathbf{y}_O, \omega)}{\partial x_i} \oint_{S(\mathbf{y})} n_j p_{ij}(\mathbf{y}, \omega) dS(\mathbf{y}); \quad (6.36)$$

herein the reciprocal relationship

$$\frac{\partial G}{\partial x_i} = -\frac{\partial G}{\partial y_i} \quad (6.37)$$

is used and  $\mathbf{y}_O = (0, 0, 0)$ .

In the above integral (6.36),  $p_{ij}$  represents the compressive stress tensor on the surface,

$$p_{ij} = (p - p_0)\delta_{ij} - \sigma_{ij}, \quad (6.38)$$

where  $\sigma_{ij}$  is the viscous stress tensor, and the notation is adopted that  $p_{ij}$  is in the  $i$ -direction acting on a surface with the normal in the  $j$ -direction. We apply a no-slip condition so that the Reynolds stress can be set to zero on the wall. There are two categories of  $p_{ij}$  components that can contribute to this integral. The first is comprised of the normal stress components  $p_{11}, p_{22}, p_{33}$  which account for the contributions from the fluctuating surface pressures, and the second is from the

shear stress components  $p_{12}, p_{13}, p_{23}$ , etc. We can define the force vector

$$f_i = -n_j p_{ij} = -n_i(p - p_0) + n_j \sigma_{ij} \quad (6.39)$$

which represents the force per unit area externally applied on the fluid by the rigid roughness bosses. As we will discuss later, generally the force components  $f_2, f_3$  normal to the direction of flow either cancel out or can be neglected, and so we can limit consideration to the drag fluctuations in the  $x_1$ -direction.

For  $\mathbf{x}$  in the far field, the half free space Green's function can be approximated as

$$G(\mathbf{x}, \mathbf{y}, \omega) \approx \frac{-e^{ik|\mathbf{x}| - ik\mathbf{x}\cdot\mathbf{y}/|\mathbf{x}|}}{2\pi|\mathbf{x}|}, \quad (6.40)$$

and its derivative in the  $x_1$ -direction is approximated by

$$\frac{\partial G}{\partial x_1} \approx ikx_1 \frac{e^{ik|\mathbf{x}| - ik\mathbf{x}\cdot\mathbf{y}/|\mathbf{x}|}}{2\pi|\mathbf{x}|^2}. \quad (6.41)$$

Substituting Equations (6.39) and (6.41) into the surface integral (6.36), we obtain the far-field acoustic frequency spectrum as

$$p(\mathbf{x}, \omega) = \frac{ik \cos \theta e^{ik|\mathbf{x}|}}{2\pi|\mathbf{x}|} \int_{S(\mathbf{y})} f_1(\mathbf{y}, \omega) dS(\mathbf{y}), \quad (6.42)$$

where  $\cos \theta = x_1/|\mathbf{x}|$  denotes the dipole directivity.

If the surface has  $N$  roughness elements located at  $\mathbf{x}_m = (x_{m1}, 0, x_{m3})$  which cause a fluctuating drag  $\mathcal{D}_m(\omega)$ , the ensemble drag force is

$$f_1(\mathbf{y}, \omega) = \sum_{m=1}^N \mathcal{D}_m(\omega) \delta(y_1 - x_{m1}) \delta(y_3 - x_{m3}). \quad (6.43)$$

If the roughness elements are large enough that they mostly lie in the logarithmic layer or the outer region, we would expect that the drag on each roughness element is determined by vortex shedding from the element in isolation. The unsteady drag on each individual element is uncorrelated and thus the aggregate power spectrum of the far-field sound can be obtained by adding up the sound radiation from each roughness drag dipole, *i.e.*

$$P_D(\mathbf{x}, \omega) = \left( \frac{k \cos \theta}{2\pi|\mathbf{x}|} \right)^2 \sum_{m=1}^N \Phi_{Dm}(\omega), \quad (6.44)$$

where  $\Phi_{Dm}(\omega)$  is the spectrum of the drag fluctuations on each element.

### 6.3.2 Glegg *et al.*'s drag model

Glegg *et al.* [61] (2007) have recently investigated noise generation owing to enhanced shear stress fluctuations by relatively large roughness elements contained in the logarithmic layer (Region II in Figure 2.3). In this case the normal stress components  $p_{11}$  and  $p_{33}$  can be first neglected in the integral (6.36) due to the relatively small surface irregularities. The contribution from the pressure fluctuations  $p_{22}$  at the wall, identified as the source mechanism of sound scattering, has been discussed via a different approach in Chapter 3 and would not be repeated here. In addition, the shear stress component  $p_{21}$  does not contribute to the integral either, because the far-field approximated Green's function (6.40) satisfies

$$\frac{\partial G}{\partial x_2} \approx 0 \quad \text{on} \quad x_2 = 0. \quad (6.45)$$

The unsteady forces are hence associated with the skin friction drag arising from the viscous shear stresses tangential to the wall. In this work, Glegg *et al.* [61] assume that the shear stresses  $p_{31}, p_{32}$  normal to the flow direction are negligible<sup>†</sup> and consider only the shear stress  $p_{12}$  in the drag direction.

In Equation (6.44) the unsteady drag spectrum  $\Phi_{Dm}$  on the roughness bosses needs to be determined to evaluate the far-field acoustic pressure spectrum  $P_D(\mathbf{x}, \omega)$ . To do this Glegg *et al.* [61] suggested using existing semi-empirical techniques for estimating the noise from bluff bodies. As pointed out by Glegg *et al.* [61], the most work in this area so far has been the investigation of the noise from splitter plates in flow ducts. In Nelson and Morfey's work [114], for example, they related the unsteady drag spectrum of a splitter plate to the steady drag. Glegg *et al.* [60] then successfully applied these results to estimate the noise from bluff bodies on wind turbine blades. In the very recent work by Glegg *et al.* [61], the same approach was used to give a first estimate of the roughness drag spectrum and will be summarised below.

The concept of Glegg *et al.*'s approach [60] is to define the unsteady loading as the product of the steady loading and a loading spectrum:

$$\Phi_{Dm}(\omega) = \overline{\mathcal{D}}_m F(St), \quad (6.46)$$

<sup>†</sup>According to tensor symmetry the shear stress components  $p_{13}, p_{23} \approx 0$ , too.

where  $\overline{\mathcal{D}}_m$  is the steady drag on each roughness element; the spectrum  $F(St)$  is a function of the Strouhal number

$$St = \frac{\omega d_m}{2\pi U_m}, \quad (6.47)$$

defined for each element with the element width  $d_m$  and the local velocity  $U_m$  that it is exposed to. Glegg *et al.* [60] gave  $F(St)$  in the form:

$$F(St) = 8.6 \times 10^{-7} \frac{d_m}{U_m} St^{-3}. \quad (6.48)$$

However, this formula is based on the measurements of Nelson and Morfey [114] which consider Strouhal numbers  $St > 0.1$  only. The results presented by Beranek [14] suggest a spectral peak at a Strouhal number of 0.2 rather than the monotonic decrease with Strouhal number in Equation (6.48). Glegg *et al.* [61] then proposed to use the formula

$$F(St) = 8.6 \times 10^{-7} \frac{d_m}{U_m} \frac{125(5St)^2}{[1/4 + (5St)^2]^{5/2}} \quad (6.49)$$

which matches the spectra in Nelson and Morfey [114] and Beranek [14] and has a peak at the frequency  $\omega \sim 0.4\pi U_m/d_m$ .

The scaling of the spectrum function (6.49) leads to the concept of a friction frequency defined as

$$\omega_\tau = \text{Ex} \left[ \frac{U_m}{d_m} \right] = \text{Ex} \left[ \frac{\mathcal{A}U_m}{h_m} \right], \quad \mathcal{A} = \text{Ex} \left[ \frac{h_m}{d_m} \right], \quad (6.50)$$

where  $h_m$  is the roughness height;  $\mathcal{A}$  denotes the expected aspect ratio of the roughness elements and reduces to unity in the case of hemispherical bosses. The Strouhal number then becomes  $St = \omega/2\pi\omega_\tau$ . The expected steady loading on each roughness element, as estimated by Glegg *et al.* [61], is  $\tau_w S/N$  where  $\tau_w = \rho_0 u_\tau^2$  is the surface shear stress and  $S$  is the surface area. Therefore the unsteady drag spectrum may be represented by the aggregate drag of  $N$  elements,

$$\sum_{m=1}^N \Phi_{Dm}(\omega) = N(\tau_w S/N)^2 S_F(\omega), \quad (6.51)$$

where

$$S_F(\omega) = \text{Ex}[F(St)] \quad (6.52)$$

is an expected spectrum function. It appears in Equation (6.51) that the sum of the drag spectrum  $\Phi_{Dm}$  scales as  $1/N$  for a given shear stress. However  $\tau_w$  also increases with the number of elements and so the actual level of  $\sum \Phi_{Dm}$  is proportional to  $N$ .

From Equations (6.44–6.51) the far-field radiated noise spectrum due to the drag fluctuations can be obtained as

$$P_D(\mathbf{x}, \omega) = \left( \frac{\cos \theta}{\pi |\mathbf{x}| c} \right)^2 \frac{\tau_w^2 S^2}{16N} \omega_\tau \Omega_\tau^2 \tilde{S}_F(\Omega_\tau), \quad (6.53)$$

$$\tilde{S}_F(\Omega_\tau) = 8.6 \times 10^{-7} \frac{125(5\Omega_\tau/2\pi)^2}{[1/4 + (5\Omega_\tau/2\pi)^2]^{5/2}}, \quad (6.54)$$

where  $\Omega_\tau = \omega/\omega_\tau$ . The noise spectrum is dependent on the friction velocity  $u_\tau$  and the local velocity  $U_m$ . In the logarithmic layer  $U_m$  will increase with roughness height  $h_m$  and Glegg *et al.* [61] suggested to use the formula by Schlichting [130]:

$$U_m = u_\tau \left( 8.5 + 5.75 \log_{10} \frac{h_m}{2k_s} \right), \quad (6.55)$$

where the length scale  $k_s$  is determined by Blake [17] from the roughness defect deficit. Glegg *et al.* [61] expected that typically  $k_s \approx 2h_m$  and thus  $U_m \sim 5u_\tau$ .

Glegg *et al.* [61] then calculated a preliminary case of  $P_D(\mathbf{x}, \omega)$  for an aspect ratio of  $\mathcal{A} = 2$  and compared it to Howe's empirical spectrum (3.41) [82] of the sound scattering mechanism. As have been mentioned in Section 2.3.3.3, they found that the peak frequency of Howe's spectrum is about twice that of the shear stress noise spectrum and that the scattering mechanism dominates the sound radiation by  $\sim 46$  dB<sup>†</sup>. For larger roughness elements Glegg *et al.* [61] suggested to approximate the local velocity by outer variables as

$$U_m = U(h_m/2\delta_{99})^{1/7} \approx 15u_\tau. \quad (6.56)$$

However, since this scaling of flow parameters is suspect for roughness elements this large they speculated that estimating the level for this noise source is probably unreasonable.

<sup>†</sup>This order may need be corrected to  $\sim 40$  dB. Glegg *et al.* failed to include the sound reflected by the surface, in that they used a free space Green's function in the derivation of the acoustic field [61]. Accordingly, the factor 16 in Equation (6.53) should be replaced by 4 and so the spectral level of the shear stress noise is augmented by a factor of 4.

### 6.3.3 Wall-mounted hemisphere model

In this section, we consider the drag dipole noise due to very large hemispherical roughness elements that protrude far beyond the logarithmic layer (*i.e.* in the upper section of Region III, see Figure 2.3). The Reynolds number is generally very high for hemispheres this large and so we discard the shear stress components of  $p_{ij}$  due to the viscous skin friction in the surface integral (6.36). To evaluate the contribution from the normal stress components, *i.e.* the fluctuating surface pressures  $p_{11}$ ,  $p_{22}$  and  $p_{33}$ , we will modify the sphere model proposed by Howe *et al.* [83] (see Section 6.2) to attain the unsteady surface forces on a wall-mounted hemisphere in a nominally steady, incompressible flow. To be consistent with the sphere model, here we follow the coordinates  $(x, y, z)$  that correspond to the notation  $(x_1, x_2, x_3)$  used in the derivation of the acoustic field in Section 6.3.1.

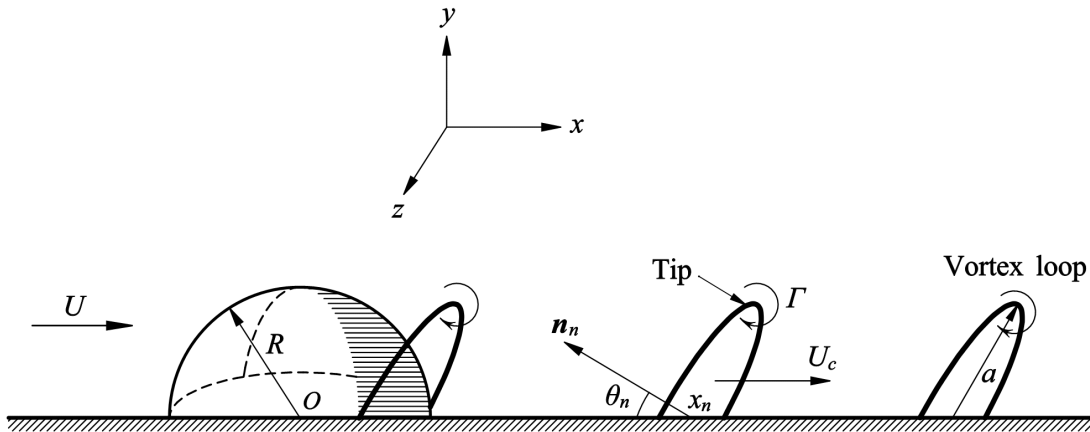


Figure 6.5: Schematic of vortex shedding from a wall-mounted hemisphere modelled by a sequence of vortex semi-circular arcs.

Figure 6.5 depicts schematically the periodic vortex shedding from a rigid hemisphere placed on a flat plate. Compared with the vortex shedding from a sphere in Figure 6.1, only one half of the vortex ring is able to be formed in Figure 6.5 due to the restriction of the plate plane, leading to the development of a succession of vortex semi-circular arcs in the hemisphere wake. Indeed, Acarlar and Smith [1] have observed periodically shed hairpin vortices generated by a surface hemispherical protuberance within a developing laminar boundary layer. As a crude model of gross oversimplification, these hairpin vortices could



be approximated by the “vortex semi-circular arcs” of radius  $a$  as illustrated in Figure 6.5. In a more general view of the problem, the length  $a$  would be interpreted as the radius of curvature of the initial thread of the large-scale hairpin-like vortex loops that are periodically shed from the hemisphere.

Because the sphere in free space is now replaced by a hemisphere in half free space, some parameters described in Section 6.2 must be accordingly modified for the wall-mounted hemisphere model. Under these circumstances the formation and translation of the vortex loops are restricted due to the existence of a supporting plate, which mitigates somewhat the randomness of the varying vortex orientations. Firstly, we redefine  $\theta_n$  as the angle between the normal  $\mathbf{n}_n$  to the plane of the  $n$ th vortex loop and the negative  $x$ -axis. In the wake of the hemisphere, permissible vortex loops are aligned with the tip of the vortex downstream (see Figure 6.5), *i.e.*  $0 \leq \theta_n \leq \pi/2$ . According to the experimental observations and numerical simulations of the hairpin-type vortices developed on a flat plate (see Section 6.1.2), it might be appropriate to use the mean orientation angle  $\langle \theta \rangle \approx 45^\circ$  for the vortex loops shed from a surface hemisphere.

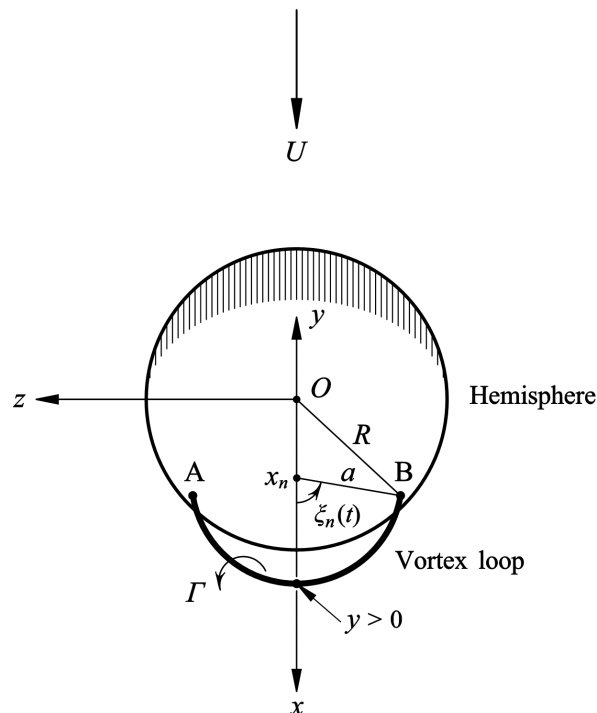


Figure 6.6: View from downstream and above of a vortex loop separating from the hemisphere at the intersection points A and B,  $\varphi_n \equiv 0$  (modified from Figure 6.3).

Figure 6.5 illustrates the situation when one nascent vortex semi-circular arc is formed and is about to separate from the hemisphere. After the vortex is released by the hemisphere, we have

$$\xi_n(t) = \pi/2 \quad \text{for} \quad t > t_n + \delta t_n. \quad (6.57)$$

At earlier times  $\xi_n(t)$  is the angle illustrated in Figure 6.6, determined by the points of intersection (labelled A and B) of the vortex loop with the hemisphere surface. The formula of  $\xi_n(t)$  is still given by Equation (6.9) and it is obvious that

$$\xi_n(t) < \pi/2 \quad \text{for} \quad t_n < t < t_n + \delta t_n. \quad (6.58)$$

However, the duration of shedding  $\delta t_n$  for the  $n$ th loop is not  $a \sin \theta_n / U_c$  by simply dividing Equation (6.1) by 2. When the shedding is complete  $\xi_n(t) = \pi/2$  and it is evident from Equation (6.9) and Figure 6.6 that the position of the centre of this vortex loop on the  $x$ -axis reduces to

$$x_n(t) = \sqrt{R^2 - a^2}, \quad t = t_n + \delta t_n. \quad (6.59)$$

Substituting this expression into Equation (6.2), we obtain the duration of shedding for the vortex semi-circular arc as

$$\delta t_n = (a \sin \theta_n + \sqrt{R^2 - a^2} - \sqrt{R^2 - a^2 \cos^2 \theta_n}) / U_c. \quad (6.60)$$

Since the vortex loops are now formed above the plate plane, in Figure 6.6 the direction of  $\Gamma$  is reversed compared to that in Figure 6.3, and the angle  $\xi$  should be measured from the “higher” point of intersection of the loop and the  $(x, y)$ -plane (where  $y > 0$ ). Thus the integration point given in Equation (6.10) becomes

$$\mathbf{x} = (x_n(t) + a \sin \theta_n \cos \xi, a \cos \theta_n \cos \xi, -a \sin \xi). \quad (6.61)$$

Moreover, the hemisphere halves the frontal area ( $A = \pi R^2 / 2$ ) and this may affect the value of the circulation  $\Gamma$  in Equation (6.22) which now takes the form:

$$\frac{\Gamma}{UR} = \frac{\pi C_D R U}{4 a U_c} \left/ \frac{1}{\tau} \int_0^\infty \langle \mathcal{G}_n(t) \rangle dt. \quad (6.62)$$

However, the integral in the denominator  $\int_0^\infty \langle \mathcal{G}_n(t) \rangle dt$  also decreases by a factor  $\sim 2$  due to the halved maximum angle  $\xi_n(t)$  (*i.e.*  $\pi \rightarrow \pi/2$ ), and hence the value of  $\Gamma$  is almost unchanged for the hemisphere model.

We now evaluate the unsteady surface forces exerted on the hemisphere. Generally, the contribution  $\mathbf{F}_n$  of the  $n$ th vortex loop to the net force on the hemisphere can be resolved into three components  $F_{1n}$ ,  $F_{2n}$  and  $F_{3n}$  in which the components of the lift  $\mathcal{L}_n$  and the drag  $\mathcal{D}_n$  (i.e.  $F_{1n}$  and  $F_{2n}$ ) have been derived in Equations (6.12) and (6.14), respectively. The force component  $F_{3n}$  that is transverse to the flow and tangential to the plate is obtained by taking

$$X_i = X_z \equiv z \left( 1 + \frac{R^3}{2|\mathbf{x}|^3} \right) \quad (6.63)$$

in Equation (6.8) and multiplying by  $\sin \varphi_n$ . Owing to the confinement of the plate plane, we assume that the wake behind the hemisphere appears more like an attached turbulent boundary layer than the free-sphere case. Therefore the vortex loops in Figure 6.5 can be modelled as symmetric to the  $(x, y)$ -plane resulting in an azimuthal angle  $\varphi_n \approx 0$ , and the transverse force component  $F_{3n}$  is hence neglected. Moreover, when considering the acoustic field due to the fluctuating surface forces on a wall-mounted hemisphere, the image-vortex effects will cause the mutual cancellation of the contribution from the lift component  $F_{2n}$  and double<sup>†</sup> that from the drag component  $F_{1n}$  (see Appendix D.1 for details).

Therefore, the far-field radiated drag dipole noise  $P_D(\mathbf{x}, \omega)$  generated by  $N$  very large hemispherical roughness elements is achieved by substituting the drag spectrum (6.30) into the acoustic spectrum (6.44) to obtain

$$P_D(\mathbf{x}, \omega) = \left( \frac{\cos \theta}{|\mathbf{x}|c} \right)^2 \frac{N\omega^2}{\pi\tau} (\rho_0 U_c \Gamma a)^2 [\langle |\hat{\mathcal{G}}_n(\omega)|^2 \rangle - |\langle \hat{\mathcal{G}}_n(\omega) \rangle|^2], \quad (6.64)$$

where the circulation and the Fourier transform,

$$\Gamma = \frac{C_D A \tau U^2}{2aU_c} \left\langle \int_0^\infty \int_{-\xi_n(t)}^{\xi_n(t)} \frac{(x_n(t) + a \cos \xi \sin \theta_n) d\xi}{(x_n^2(t) + 2ax_n(t) \cos \xi \sin \theta_n + a^2)^{5/2}} dt \right\rangle \quad (6.65)$$

and

$$\hat{\mathcal{G}}_n(\omega) = \frac{3aR^3 \cos \theta_n}{4\pi} \int_0^\infty \int_{-\xi_n(t)}^{\xi_n(t)} \frac{(x_n(t) + a \cos \xi \sin \theta_n) d\xi}{(x_n^2(t) + 2ax_n(t) \cos \xi \sin \theta_n + a^2)^{5/2}} e^{i\omega t} dt, \quad (6.66)$$

must be integrated numerically with respect to  $\xi$  and  $t$  with the modifications given parametrically in Equations (6.57–6.62) applied.

<sup>†</sup>This effect has been included in the half free space Green's function (6.34).

## 6.4 Numerical Prediction

### 6.4.1 Small-time approximation

#### 6.4.1.1 Time dependence

Following Howe *et al.* [83] we first calculate the dependence of the nondimensional lift  $\mathcal{L}_n/\rho_0 U_c \Gamma a \cos \varphi_n$  and drag  $\mathcal{D}_n/\rho_0 U_c \Gamma a$  on the nondimensional time  $U_c(t - t_n)/R$  for the case in which  $a = 0.7R$  and  $\theta_n = \pi/8$ . Figures 6.7(a) and 6.7(b) show the comparison between the sphere and hemisphere models for the unsteady lift and drag, respectively. For the sphere model [83], the lift grows rapidly during the initial stages of shedding, attaining a maximum when about half a vortex ring has been formed; the subsequent vorticity of opposite sign reduces the net circulation around the sphere and causes the lift to decrease. After release at time A the lift decays slowly and becomes negligible when the ring has convected about a sphere radius  $R$  into the wake. For the hemisphere model, the lift grows in a similar way as in the sphere model until half vortex ring is formed at time B. After the half ring is released, the lift first attains a maximum and then decays slowly approaching a constant  $\sim 2$ .

The difference in the lift variations after time B between the two models can be explained by Figure 6.8 which illustrates the variations of  $\xi_n(t)/\pi$  determined by Formula (6.9) and the integrands  $\dot{\mathcal{F}}_n, \dot{\mathcal{G}}_n$  of  $\mathcal{F}_n, \mathcal{G}_n$  in Equations (6.13) and (6.15) with time. Firstly,  $\xi_n(t)$  increases from 0 to  $\pi$  (sphere) or  $\pi/2$  (hemisphere) and maintains this maximum after the vortex is released. For the sphere,  $\dot{\mathcal{F}}_n$  decreases rapidly from shedding and becomes negative when half a vortex ring has been formed. However for the hemisphere,  $\dot{\mathcal{F}}_n$  decays identically as the sphere until half ring is released and becomes negligible afterwards, maintaining positive during shedding. The unaltered sign of  $\dot{\mathcal{F}}_n$  after the formation of the half vortex ring accounts for the slow decay of the lift on the hemisphere after time B, as shown in Figure 6.7(a).

In fact, Acarlar and Smith [1] have observed that a standing vortex would be generated near the leading edge of a hemispherical protuberance on a flat plate, forming a stationary horseshoe-shaped structure passing around the hemisphere. They used the concept of concentration of vorticity to describe the formation

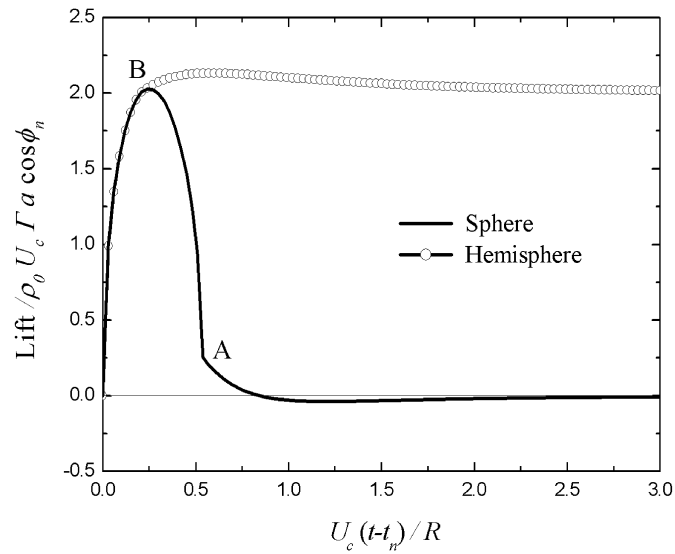
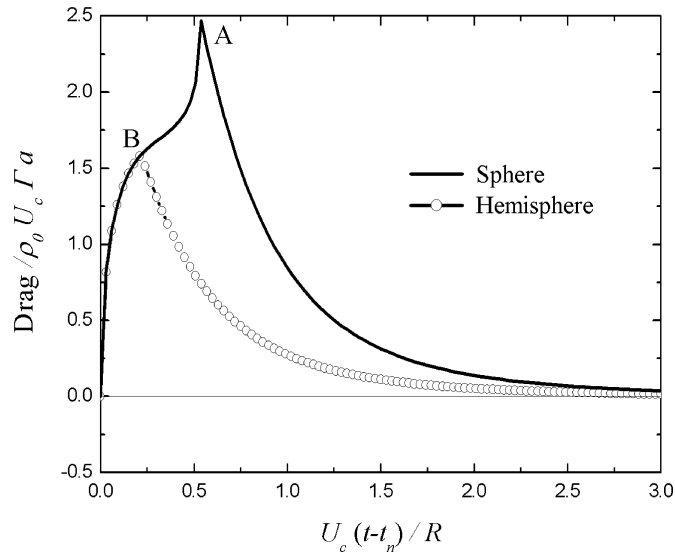
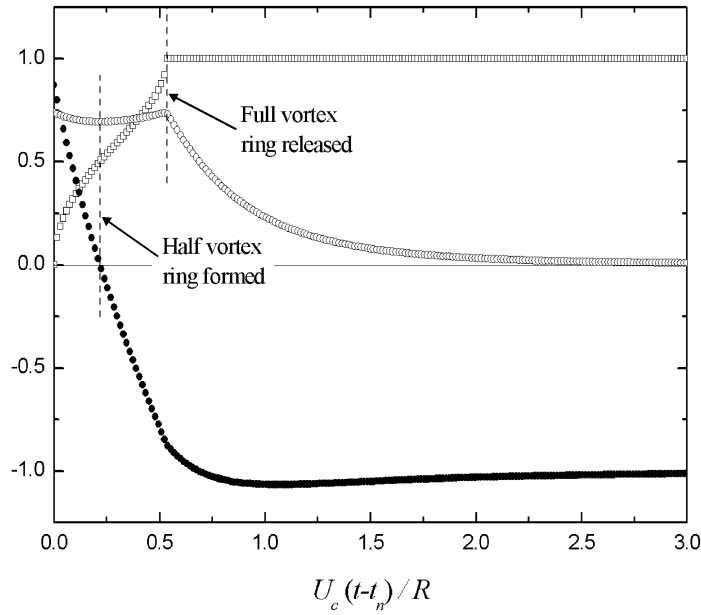
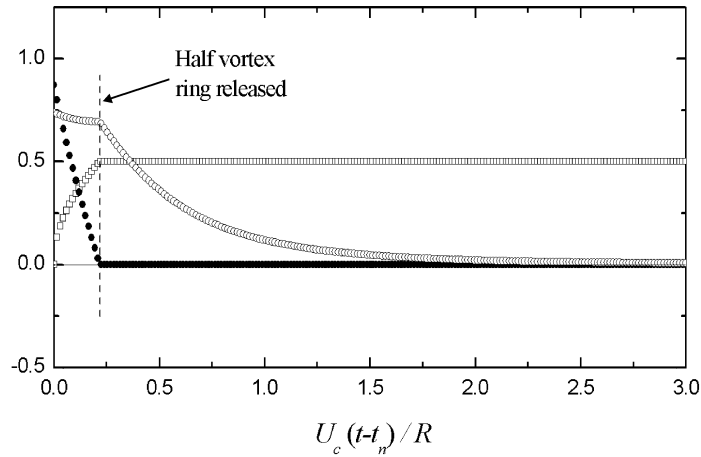
(a)  $\mathcal{L}_n / \rho_0 U_c \Gamma a \cos \varphi_n$ (b)  $\mathcal{D}_n / \rho_0 U_c \Gamma a$ 

Figure 6.7: Variation of the nondimensional lift and drag during shedding from the sphere and hemisphere, respectively, when  $a = 0.7R$ ,  $\theta_n = \pi/8$ . Important time points: A – full vortex ring released from the sphere, and B – half vortex ring released from the hemisphere.

of the standing vortex in the vicinity of the hemisphere, and explained that boundary-layer flows (laminar or turbulent) can be characterized as a shear layer represented by vortex sheets consisting of vortex lines [150]. Initially, as the laminar boundary layer impinges upon the hemisphere, the undisturbed vortex sheets laying below the upstream stagnation point undergo a retardation. The impinging vortex sheets roll up to form the standing vortex [1].



(a) Sphere model



(b) Hemisphere model

Figure 6.8: Variation of  $\xi_n(t)/\pi$  ( $\square \square \square$ ) and the integrands  $\dot{\mathcal{F}}_n$  ( $\bullet \bullet \bullet$ ),  $\dot{\mathcal{G}}_n$  ( $\circ \circ \circ$ ) of Equations (6.13) and (6.15) with the nondimensional time  $U_c(t - t_n)/R$  for the sphere model and hemisphere model, respectively, when  $a = 0.7R$ ,  $\theta_n = \pi/8$ .

According to the observations of Acarlar and Smith [1], the two legs of this standing vortex embrace the succession of hairpin-like half vortex rings shed from the hemisphere and will be elongated by the translation of the hairpin vortices along the plate surface. The vorticity in the leg of the standing vortex is in opposite direction with the vorticity in the adjacent arc of the hairpin vortex. We hence speculate that the counteraction of vorticity between the standing vortex and hairpin vortices could reduce the net circulation around the hemisphere, and

presumably the unsteady lift on the hemisphere as in Figure 6.7(a) would not maintain a positive constant value at large time. The validation of this speculation is suggested as an area of future work.

On the other hand, the drag variations on the sphere and hemisphere are similar in trend. As shown in Figures 6.7(b), the drag increases monotonically until the vortex ring or half vortex ring is released at time A or B; it subsequently decreases slowly and is negligible when the ring or half ring is about a distance of  $3R$  downstream. Curves of the drag of both models coincide with each other before the half vortex ring is formed, and after release they decay at different rates to 0. Figure 6.8 also shows the similar variations of  $\dot{\mathcal{G}}_n$  during shedding for the sphere and hemisphere.

#### 6.4.1.2 High-frequency representation

The above discussions imply that the behaviour of the vortex in the distant wake makes a very limited contribution to the unsteady surface forces except through the lift on the hemisphere. Nevertheless, this considerable lift is unlikely to contribute to the far-field sound pressure as it becomes quasi-steady (*i.e.*  $\partial\mathcal{L}_n/\partial t \approx 0$ ) when  $U_c(t - t_n)/R \gg 1$ . Also lift force is cancelled by equal opposite image in plane surface. Therefore we confine attention to the small-time characteristics of the lift and drag because the high-frequency dependence of their spectra is governed by their behaviour during the initial stages of formation of a vortex structure.

In Appendix D.2 we have derived the approximations of  $\mathcal{F}_n(t)$ ,  $\mathcal{G}_n(t)$  when  $U_c(t - t_n)/R \ll 1$  for the sphere model as:

$$\mathcal{F}_n(t) \approx 3\sqrt{\frac{2U_c(t - t_n)}{a}} \left[ 1 - \left(\frac{a}{R}\right)^2 \cos^2 \theta_n \right] \mathcal{H}, \quad (6.67a)$$

$$\mathcal{G}_n(t) \approx \frac{3a \cos \theta_n}{R} \sqrt{\frac{2U_c(t - t_n)}{a}} \left[ 1 - \left(\frac{a}{R}\right)^2 \cos^2 \theta_n \right]^{1/2} \mathcal{H}, \quad (6.67b)$$

where the auxiliary term

$$\mathcal{H} = \left[ \frac{\sqrt{R^2 - a^2 \cos^2 \theta_n}}{\sin \theta_n (\sqrt{R^2 - a^2 \cos^2 \theta_n} - a \sin \theta_n)} \right]^{1/2}. \quad (6.68)$$

By evaluating the Fourier transforms  $\hat{\mathcal{F}}_n(\omega)$ ,  $\hat{\mathcal{G}}_n(\omega)$  from Equations (6.67) we obtain the high-frequency representations for the spectra of the unsteady lift and drag (see Appendix D.2):

$$\Phi_L(\omega) \sim (\rho_0 U_c \Gamma a)^2 \frac{9U_c}{4\tau a \omega^3} \left\langle \left[ 1 - \left( \frac{a}{R} \right)^2 \cos^2 \theta_n \right]^2 \mathcal{H}^2 \right\rangle, \quad (6.69a)$$

$$\Phi_D(\omega) \sim (\rho_0 U_c \Gamma a)^2 \frac{a^2}{R^2} \frac{9U_c}{2\tau a \omega^3} [\langle |\mathcal{E}|^2 \rangle - |\langle \mathcal{E} \rangle|^2], \quad (6.69b)$$

where

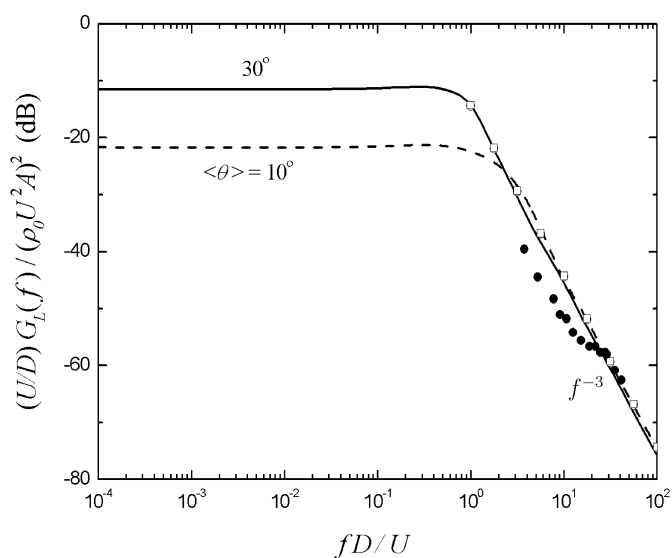
$$\mathcal{E} = -\frac{\sqrt{2}}{2}(1+i) \cos^2 \theta_n \left[ 1 - \left( \frac{a}{R} \right)^2 \cos^2 \theta_n \right]^{1/2} \mathcal{H}. \quad (6.70)$$

Note that Equations (6.67b) and (6.69b) are also valid for the hemisphere model due to its identical initial-stage behaviours of vortex formation with the sphere model.

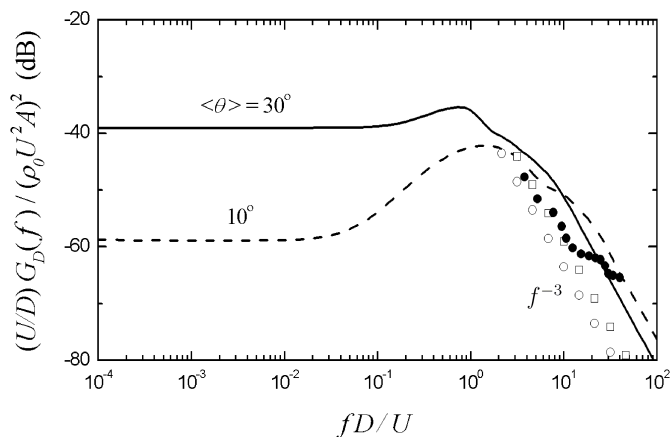
Figures 6.9(a) and 6.9(b) illustrate the comparison between the small-time approximation and numerical integration of the normalized lift and drag spectra  $10 \log_{10} ((U/D)G_L(f)/(\rho_0 U^2 A)^2)$ ,  $10 \log_{10} ((U/D)G_D(f)/(\rho_0 U^2 A)^2)$ , respectively, for the sphere model. Averages have been taken using an ensemble of 100 vortex rings. As shown in Figures 6.9(a), the approximated lift spectra almost coincide with the integrated spectra for the two cases  $\langle \theta \rangle = 10^\circ, 30^\circ$ . Both sets of approximated and integrated predictions decay like  $f^{-3}$  at high frequencies, independently of the value of the mean orientation angle  $\langle \theta \rangle$ .

For the drag spectrum, however, the approximated and integrated curves agree in trend ( $f^{-3}$ ) at high frequencies but not in absolute levels. Nevertheless, the remarkable accord between approximation and experiment in both the trend and absolute levels, particularly in the Strouhal number range  $3 < fD/U \leq 15$ , implies that the high-frequency representation (6.69b) is presumably a good asymptotic approximation for the drag spectrum  $\Phi_D(\omega)$ . When evaluating Equation (6.30) we discovered that the small-time approximation and numerical integration actually yield very close values for either mean square,  $\langle |\hat{\mathcal{G}}_n(\omega)|^2 \rangle$  or  $|\langle \hat{\mathcal{G}}_n(\omega) \rangle|^2$ . However,  $\Phi_D(\omega)$  is determined by the difference between the two mean squares which is numerically sensitive to different methods of evaluation. This numerical error perhaps accounts in part for the discrepancy between the drag spectra obtained by the asymptotic approximation and numerical integration.





(a) Lift spectrum



(b) Drag spectrum

Figure 6.9: Comparison of approximated and integrated predictions of the lift and drag spectra for the two cases  $\langle \theta \rangle = 10^\circ, 30^\circ$  when averaging is performed over  $0.9 < \theta_n / \langle \theta \rangle < 1.1$  and  $a = 0.7R$ ,  $U_c = 0.7U$ ,  $C_D = 0.4$ . Small-time approximations:  $\circ \circ \circ \langle \theta \rangle = 30^\circ$ ,  $\square \square \square \langle \theta \rangle = 10^\circ$ . Numerical integrations: —  $\langle \theta \rangle = 30^\circ$ , - - -  $\langle \theta \rangle = 10^\circ$ . Also shown are  $\bullet \bullet \bullet$  the averaged measured values for  $Re = 6680, 10020, 13360, 16700$  by Howe *et al.* [83]. The sphere model.

In Figure 6.10 are shown the approximated and integrated drag spectra for the hemisphere model. The drag coefficient  $C_D = 0.4$  is taken as the sphere model for Reynolds numbers in the subcritical region. The low-frequency dependence of the drag spectra ( $fD/U < 0.1$ ) in Figure 6.10 agrees with that in Figure 6.9(b) and this should be attributed to the approximate large-time behaviours of the drag when  $U_c(t - t_n)/R > 3$  between the sphere and hemisphere models as shown

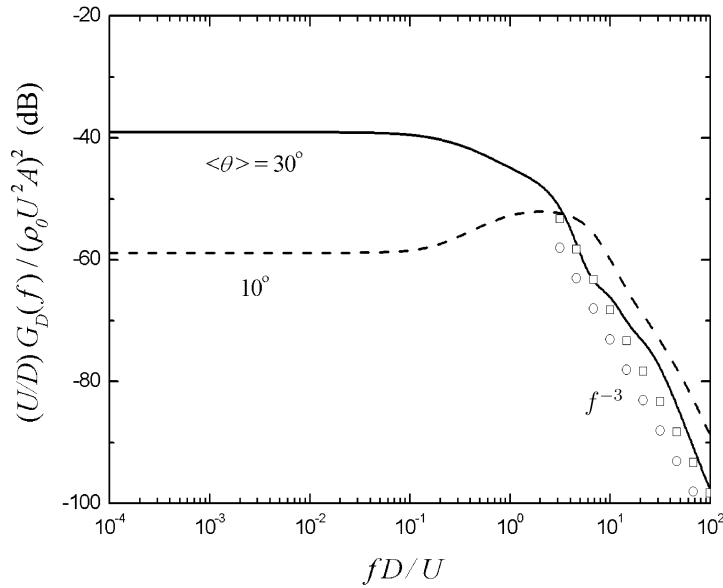


Figure 6.10: Approximated and integrated drag spectra for the two cases  $\langle \theta \rangle = 10^\circ, 30^\circ$  over the interval  $0.9 < \theta_n / \langle \theta \rangle < 1.1$  and  $a = 0.7R$ ,  $U_c = 0.7U$ ,  $C_D = 0.4$ . Small-time approximations:  $\circ \circ \circ \langle \theta \rangle = 30^\circ$ ,  $\square \square \square \langle \theta \rangle = 10^\circ$ . Numerical integrations: —  $\langle \theta \rangle = 30^\circ$ , - - -  $\langle \theta \rangle = 10^\circ$ . The hemisphere model.

in Figure 6.7(b). At high frequencies ( $fD/U > 1$ ), it is shown that the spectral level oscillates slightly for the larger  $\langle \theta \rangle$  ( $30^\circ$ ), and that the discrepancy between small-time approximation and numerical integration still exists, which implies that there is scope to improve the drag spectrum model in accuracy.

## 6.4.2 Noise spectrum

### 6.4.2.1 Nondimensional spectrum

In this section we will present preliminary predictions for surface roughness noise generated by the unsteady drag. Figure 6.11 illustrates the nondimensional noise spectra  $10 \log_{10} ((U/R)^{-1} f^2 G_D(f) / (\rho_0 U^2 A)^2)$  of the sphere model and the hemisphere model, respectively, plotted as a function of  $fR/U$  for the case  $\langle \theta \rangle = 45^\circ$ . The vortex orientation angles  $\theta_n$  are assumed to occupy the interval  $0.75 < \theta_n / \langle \theta \rangle < 1.25$  with  $a = 0.7R$ ,  $U_c = 0.7U$ . The additional term  $f^2$  in the noise spectrum and the large mean orientation angle  $\langle \theta \rangle = 45^\circ$  will intensify the numerical oscillation in spectral levels as shown in Figure 6.10. For this reason, herein we apply a wider interval  $0.75 < \theta_n / \langle \theta \rangle < 1.25$  to somewhat alleviate the oscillations at high

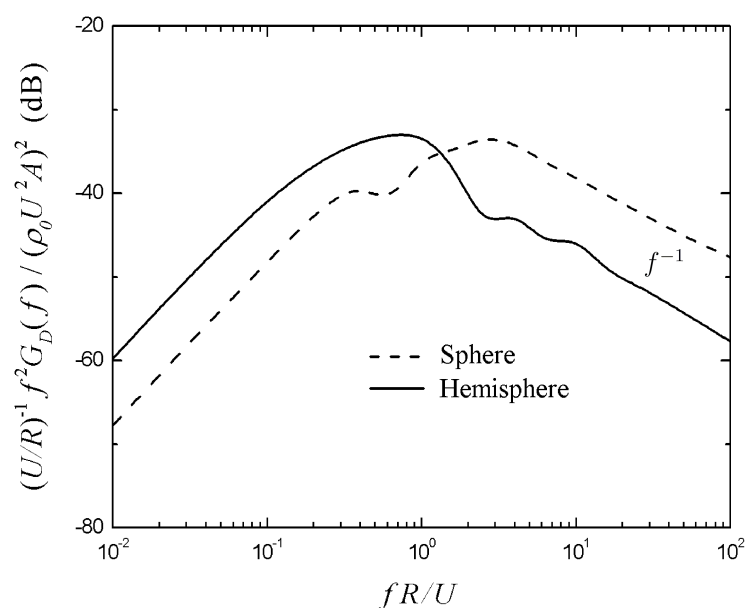


Figure 6.11: Nondimensional drag dipole noise spectra of the sphere and hemisphere models for the case  $\langle \theta \rangle = 45^\circ$  over the interval  $0.75 < \theta_n / \langle \theta \rangle < 1.25$  and  $a = 0.7R$ ,  $U_c = 0.7U$ ,  $C_D = 0.4$ .

frequencies ( $fR/U > 1$ ).

As can be seen from Figure 6.11, the peak frequency of the sphere model occurs at  $fR/U \approx 2.5$ , higher than that of the hemisphere model at  $fR/U \approx 0.7$ . Unlike the spectra of the unsteady force, both the noise spectra of the sphere and hemisphere models decay like  $f^{-1}$  in the high-frequency region and their spectral peaks are at approximate levels. However, when considering far-field radiation the acoustic intensity of the wall-mounted hemisphere will be augmented by a factor of 4 due to the effect of wall reflection and will be about 6 dB higher than that of the sphere in free space.

#### 6.4.2.2 Comparison with the scattering noise

We now compare the two mechanisms of surface roughness noise: the drag dipole noise and the scattering noise, respectively. For the drag dipole noise, the roughness height and roughness density are taken as  $R = 2$  cm,  $\sigma = 0.01$  for the very large but sparsely distributed roughness elements, whereas for the scattering noise we use the three idealized test cases that have been described in Section 5.2.2. As for the Boeing-757 sized aircraft wing (see Section 5.2.1), we select a flat plate

with the dimensions  $L_c = 5$  m,  $L_s = 16.5$  m and a far-field observation point at  $|\mathbf{x}| = 100$  m,  $\theta = \pi/4$ ,  $\phi = 0$ .

Before applying the wall-mounted hemisphere model to the roughness noise prediction, we need to make some restrictive assumptions. Firstly, in the derivation of the far-field drag dipole noise in Section 6.3.1, the roughness elements are assumed to be compact bluff bodies, *i.e.*  $kR < 1$ . The compactness condition can also be written as

$$2\pi MSt < 1, \quad \text{where} \quad St = fR/U. \quad (6.71)$$

As shown in Figure 6.4, if we take  $fD/U = 6$  from the Strouhal number range where the predictions are in good accord with the measurements, the low Mach number  $M = 0.05$  satisfies the compactness condition (6.71), *i.e.*  $2\pi MSt \approx 0.9$ . This Mach number results in a high Reynolds number based on the radius of the hemisphere,  $UR/\nu \approx 2.3 \times 10^4$ , that falls into the subcritical region  $10^3 < Re < 3 \times 10^5$  [130]. Therefore the wall-mounted hemisphere model and the drag coefficient  $C_D = 0.4$  are applicable to this preliminary case.

Moreover, because the hemisphere model of unsteady forces is based on a nominally steady flow, we assume that the roughness elements are located near the leading edge of the plate to achieve an initial laminar boundary layer before the hemispheres. According to the Blasius solution for the laminar boundary-layer flow over a flat plate [42]:

$$\delta = \frac{5.0x_1}{\sqrt{Re_x}}, \quad \text{where} \quad Re_x = \frac{Ux_1}{\nu}, \quad (6.72)$$

the boundary-layer thickness at the streamwise distance  $x_1 = 0.5$  m, for example, is  $\delta \sim 2$  mm, and so these hemispherical roughness elements ( $R = 2$  cm) protrude far beyond the outer region of the boundary layer.

The comparison between the drag dipole noise  $P_D(\mathbf{x}, \omega)$  and the scattering noise  $P_R(\mathbf{x}, \omega)$  in the frequency range  $20$  Hz  $< f < 100$  kHz is shown in Figure 6.12. We see that the noise spectrum of the drag dipole mechanism again decays like  $f^{-1}$  in the high-frequency region ( $f > 1$  kHz). For this test case the drag dipole mechanism shows a spectral peak of about 4 dB, approximate to the spectral peak of Case 1 of the scattering noise. Nonetheless, the slowly decaying spectral level leads to the much

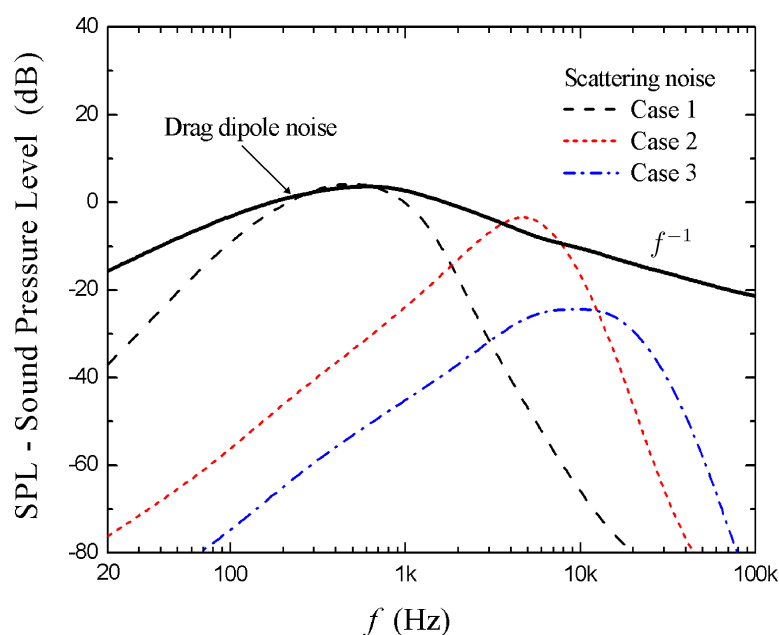


Figure 6.12: Comparison of noise spectra between the drag dipole mechanism and the scattering mechanism. For the drag dipole noise spectrum,  $R = 2$  cm,  $\sigma = 0.01$  for the case  $\langle \theta \rangle = 45^\circ$  over the interval  $0.75 < \theta_n / \langle \theta \rangle < 1.25$  and  $a = 0.7R$ ,  $U_c = 0.7U$ ,  $C_D = 0.4$ . For the scattering noise spectra, Cases 1–3 are defined in Section 5.2.2.

wider spectral peak of the drag dipole noise spectrum than those of the scattering noise spectra, which indicates that the OASPL of the drag dipole noise is higher than those of the scattering noise. This preliminary test case shows that the drag dipole noise of very large roughness elements could be comparable to or even higher than the scattering noise.

## 6.5 Summary

The alternative source mechanism of surface roughness noise, the drag dipole mechanism, has been studied in this chapter additional to the sound scattering mechanism introduced in detail in Chapters 3–5. The aim was to extend the application of the drag dipole mechanism from relatively large roughness elements which has been recently investigated by Glegg *et al.* [61] to very large roughness elements. The theoretical model proposed by Howe *et al.* [83] for the lift and drag fluctuations on a sphere has been modified to determine the unsteady drag on the wall-mounted hemisphere and hence the far-field generated noise.

We first surveyed the relevant work on unsteady forces on a sphere and on hairpin vortices, and decided to model the hairpin vortices behind the hemisphere by a succession of quasi-periodically shed half vortex rings on the basis of Howe *et al.*'s analytical model [83] and Acarlar and Smith's observations [1]. The major derivations of the sphere model of Howe *et al.* [83] were then described briefly to set the scene for the modifications for the hemisphere model. The theoretical formulation of the drag dipole noise has been presented and two models of the unsteady drag spectrum have been introduced. The drag model proposed by Glegg *et al.* aims to evaluate the roughness noise due to relatively large elements in the logarithmic layer, but it is not applicable to larger roughness elements protruding into the outer region.

In this chapter, we have developed a wall-mounted hemisphere model from Howe *et al.*'s sphere model [83] to account for the very large roughness elements that protrude far beyond the logarithmic layer. The characteristics of the unsteady lift and drag during the initial stages of vortex formation have been numerically predicted for both the sphere and hemisphere, and their high-frequency approximations have been derived. The drag dipole noise spectrum has been preliminarily assessed by comparing to the scattering noise spectra using the idealized test cases in Chapter 5. It has been shown that this noise source by very large roughness elements can be as significant as the scattering noise particularly in the OASPL.

# Chapter 7

## Beamforming Correction for Dipole Measurement

### 7.1 Introduction

THE conventional beamforming algorithm normally assumes monopole propagation characteristics to steer the focus of the phased array. Although such beamforming techniques work well in locating monopole-like sources with uniform directivities, they can perform poorly when used to reconstruct directional noise sources such as dipoles. In fact, for many aeroacoustic systems the noise sources arise from fluctuating loading forces and these are principally of dipole type. Therefore array measurements can be misinterpreted if applied directly to aeroacoustic sources without consideration of the source mechanism, particularly if the axes of the dominant dipoles are not in line with the receiver.

Jordan *et al.* [89] demonstrated how the monopole assumption can be problematic for a dipole source. They developed a correction for the phase difference in microphone signals to be compatible with a dipole source, and applied it to measurements of a 30-channel linear array for an aeolian-tone dipole produced by cross flow over a cylinder. The true source location and source energy of the dipole was then retrieved. In Section 4.3.4.2 we have pointed out the inability of the conventional beamforming to directly validate theoretical predictions for dipole-type surface roughness noise. Instead of altering the beamforming algorithm, we processed the numerical simulation through the same algorithm as

the experiment and compared the simulated and measured source maps. Quayle *et al.* [125] have also suggested that a similar mismatch could help explain differences in estimates of source power from two nested arrays. More accurate estimates of aeroacoustic dipoles through array measurements are therefore useful as they can provide insight into the noise generation mechanism, enable the validation of theoretical and numerical models, and assist the development of noise reduction technologies.

The analysis by Jordan *et al.* [89] suggests a technique for dipole correction of microphone array systems which extends the conventional delay-and-sum procedure to a process of delay-analyze-and-sum. The analysis stage adds an examination of the phase characteristics of microphone signals for each focus position and so is recognized as a “signal correction”. The examination process is not very time-consuming for a linear focus region, but it will increase the CPU time quadratically in the case of a 2D focus region, typically with many more grid points. Furthermore, modelling the exact phase alignment of a real acoustic source is difficult due to the inherent nonideal nature of propagation characteristics. A significant drawback of the signal correction is that when extended to a 2D microphone array it is only applicable to one single dipole with known position and direction. This technique therefore limits the main objective of a phased array, which is to localize noise sources.

In this chapter, a beamforming correction to array processing techniques is presented for identifying dipole sources. The main idea is to modify the conventional beamforming algorithm source description to account for the dipole propagation characteristics. This improves the ability of conventional beamforming for estimating dipole sources and extends the technique of Jordan *et al.* [89], yielding a new beamforming algorithm capable of evaluating the true source location and source power of a distribution of dipoles with known orientation. This “dipole-beamforming” algorithm is then applied to numerical simulations and experiments for validation.

We will commence with a theoretical formulation for the far-field sound field of aeroacoustic sources in Section 7.2. The monopole description is based



on Sijtsma [133] to be consistent with the array software used in this work, and the dipole characteristic term is derived. In Section 7.3, two approaches for dipole correction to conventional beamforming techniques, *i.e.* through microphone signals and beamforming algorithm, are described and compared. A dipole-beamforming algorithm is presented by applying the dipole characteristic term to the source definition for correction. Section 7.4 validates these two approaches through numerical simulations and demonstrates the advantages of the beamforming correction. Following validation some results from the application of the beamforming correction to dipole source localization of aeolian tones are presented and discussed in Section 7.5.

## 7.2 Theoretical Formulation

### 7.2.1 The monopole source

An ideal point source with uniform directivity (monopole) is assumed to be located at  $\boldsymbol{\xi}$  in a medium with a uniform flow  $\boldsymbol{U}$ . The acoustic pressure  $p(\boldsymbol{x}, t)$  at the receiver  $\boldsymbol{x}$  satisfies the convective wave equation [133]:

$$\frac{1}{c^2} \left( \frac{\partial}{\partial t} + \boldsymbol{U} \cdot \nabla \right)^2 p(\boldsymbol{x}, t) - \nabla^2 p(\boldsymbol{x}, t) = -q(t) \delta(\boldsymbol{x} - \boldsymbol{\xi}), \quad (7.1)$$

where  $q(t)$  is the monopole source strength in time domain and  $\delta(\boldsymbol{x} - \boldsymbol{\xi})$  is the Dirac delta function. In the frequency domain, Equation (7.1) transforms into the convective Helmholtz equation:

$$\frac{1}{c^2} (i\omega + \boldsymbol{U} \cdot \nabla)^2 p(\boldsymbol{x}, \omega) - \nabla^2 p(\boldsymbol{x}, \omega) = -a(\omega) \delta(\boldsymbol{x} - \boldsymbol{\xi}), \quad (7.2)$$

where  $a(\omega)$  is the Fourier transform of  $q(t)$ .

The solution to Equation (7.1) is

$$p(\boldsymbol{x}, t) = \frac{-q(t - \Delta t_e)}{4\pi \sqrt{(\boldsymbol{M} \cdot \boldsymbol{r})^2 + \beta^2 |\boldsymbol{r}|^2}}, \quad (7.3)$$

where  $\boldsymbol{M} = \boldsymbol{U}/c$  is a vector of mean flow Mach number,  $\boldsymbol{r} = \boldsymbol{x} - \boldsymbol{\xi}$  is the propagation vector from source to receiver,  $\Delta t_e$  is the emission time delay:

$$\Delta t_e = \frac{1}{c\beta^2} \left( -\boldsymbol{M} \cdot \boldsymbol{r} + \sqrt{(\boldsymbol{M} \cdot \boldsymbol{r})^2 + \beta^2 |\boldsymbol{r}|^2} \right), \quad (7.4)$$

and  $\beta^2 = 1 - |\mathbf{M}|^2$ . The frequency-domain form of Equation (7.3), *i.e.* the solution of Equation (7.2), can be expressed as:

$$p(\mathbf{x}, \omega) = \frac{-a(\omega)e^{-i\omega\Delta t_e}}{4\pi\sqrt{(\mathbf{M} \cdot \mathbf{r})^2 + \beta^2|\mathbf{r}|^2}}, \quad (7.5)$$

because

$$\int_{-\infty}^{\infty} p(\mathbf{x}, t)e^{-i\omega t} dt = \frac{e^{-i\omega\Delta t_e} \int_{-\infty}^{\infty} -q(t - \Delta t_e)e^{-i\omega(t - \Delta t_e)} d(t - \Delta t_e)}{4\pi\sqrt{(\mathbf{M} \cdot \mathbf{r})^2 + \beta^2|\mathbf{r}|^2}}. \quad (7.6)$$

## 7.2.2 The dipole source

A dipole source can be modelled as a coherent pair of closely placed monopoles  $q(t)$  with opposite phase at a distance  $l$  apart. The total source strength is

$$\mathbf{F}_{\text{tot}} = -q(t)[\delta(\boldsymbol{\xi}) - \delta(\boldsymbol{\xi} - l)]. \quad (7.7)$$

If the distance  $l = |l|$  is small (*i.e.*  $kl < 1$ ), the total source strength simplifies to

$$\mathbf{F}_{\text{tot}} = -\nabla \cdot [\mathbf{F}(t)\delta(\boldsymbol{\xi})] \quad (7.8)$$

by Taylor expansion, where  $\mathbf{F}(t) = q(t)l$  is the dipole strength vector. Hence for a dipole located in a medium with a uniform flow, the convective wave equation (7.1) becomes:

$$\frac{1}{c^2} \left( \frac{\partial}{\partial t} + \mathbf{U} \cdot \nabla \right)^2 p(\mathbf{x}, t) - \nabla^2 p(\mathbf{x}, t) = -\nabla \cdot [\mathbf{F}(t)\delta(\mathbf{r})], \quad (7.9)$$

and the convective Helmholtz equation in the frequency domain is:

$$\frac{1}{c^2} (i\omega + \mathbf{U} \cdot \nabla)^2 p(\mathbf{x}, \omega) - \nabla^2 p(\mathbf{x}, \omega) = -a(\omega)l\delta(\mathbf{r}). \quad (7.10)$$

Similar to the solution to Equation (7.1) for a monopole, the solution of Equation (7.9) for source  $-\nabla \cdot [\mathbf{F}(t)\delta(\mathbf{r})]$  is:

$$p(\mathbf{x}, t) = -\nabla \cdot \left[ \frac{\mathbf{F}(t - \Delta t_e)}{4\pi\sqrt{(\mathbf{M} \cdot \mathbf{r})^2 + \beta^2|\mathbf{r}|^2}} \right]. \quad (7.11)$$

For a given Mach number vector  $\mathbf{M}$  and dipole source vector  $\mathbf{F}$ , we can express the solution to Equation (7.9) as:

$$\begin{aligned} p(\mathbf{x}, t) &= -\nabla \cdot \left[ \frac{\mathbf{F}(t - \Delta t_e)}{4\pi r \Theta} \right] \\ &= \frac{1}{4\pi \Theta} \left[ \frac{\nabla(r\Theta)}{r^2 \Theta} + \frac{\nabla(\Delta t_e)}{r} \frac{\partial}{\partial t} \right] \cdot \mathbf{F}(t - \Delta t_e), \end{aligned} \quad (7.12)$$

where

$$\Theta = \sqrt{(\mathbf{M} \cdot \mathbf{r}/r)^2 + \beta^2}, \quad (7.13)$$

$$\nabla(r\Theta) = \frac{(\mathbf{M} \cdot \mathbf{r})\mathbf{M} + \beta^2\mathbf{r}}{r\Theta}, \quad (7.14)$$

$$\nabla(\Delta t_e) = \frac{-\mathbf{M} + \nabla(r\Theta)}{c\beta^2}. \quad (7.15)$$

As we are only interested in far-field sound<sup>†</sup>, we discard the first term in the bracket,  $\nabla(r\Theta)/r^2\Theta$ , and obtain the far-field acoustic pressure as:

$$p(\mathbf{x}, t) = \frac{\nabla(\Delta t_e)}{4\pi r\Theta} \cdot \frac{\partial}{\partial t} \mathbf{F}(t - \Delta t_e). \quad (7.16)$$

The Fourier transform of Equation (7.16) is:

$$\begin{aligned} p(\mathbf{x}, \omega) &= \frac{\nabla(\Delta t_e)}{4\pi r\Theta} \cdot i\omega a(\omega) \mathbf{l} e^{-i\omega\Delta t_e} \\ &= \frac{a(\omega) e^{-i\omega\Delta t_e}}{4\pi r\Theta} [i\omega \mathbf{l} \cdot \nabla(\Delta t_e)]. \end{aligned} \quad (7.17)$$

Comparing the above expression with the pressure spectrum of a monopole in Equation (7.5), we obtain the dipole characteristic term representing the ratio between dipole and monopole fields as:

$$\text{DPL} = -i\omega \mathbf{l} \cdot \nabla(\Delta t_e). \quad (7.18)$$

## 7.3 Beamforming Algorithm

### 7.3.1 Conventional beamforming

Following the work of Sijtsma [133], the array processing software stores the measured pressure amplitude in frequency domain in an  $N$ -dimensional vector:

$$\mathbf{p} = [p_1(f), \dots, p_N(f)], \quad (7.19)$$

where  $N$  is the number of array microphones. The cross-power matrix  $\mathbf{C}$  is introduced by:

$$\mathbf{C} = \frac{1}{2} \overline{\mathbf{p}\mathbf{p}^*}, \quad (7.20)$$

<sup>†</sup>This assumption requires  $\omega r/c \gg 1$ , and so may not be satisfied in many phased array installations (e.g. in a closed-return wind tunnel). It is possible to extend the formulation so that the second term in Equation (7.12) is included.

where the overbar denotes an ensemble average or, in practice, the average over the Fourier transforms obtained from discrete time blocks. The assumed source description is put in the “transfer vector”  $\mathbf{g}$ , *i.e.*, its components  $g_n$  are the pressure amplitudes at the microphone location of an ideal source with unit strength. For the case of a monopole in a medium with uniform flow,  $\mathbf{g}$  can be obtained from Equation (7.5) by setting the source strength  $a(\omega) = 1$ , namely

$$g_n = \frac{-e^{-i\omega\Delta t_e}}{4\pi\sqrt{(\mathbf{M} \cdot \mathbf{r})^2 + \beta^2|\mathbf{r}|^2}}. \quad (7.21)$$

The purpose of beamforming is to determine the amplitude  $a$  of sources at grid points. This is done by comparing the measured pressure vector  $\mathbf{p}$  with the transfer vector  $\mathbf{g}$ , for instance through minimization of

$$J = \overline{|\mathbf{p} - a\mathbf{g}|^2}. \quad (7.22)$$

The solution of this minimization problem is:

$$a = \frac{\mathbf{g}^* \mathbf{p}}{|\mathbf{g}|^2}, \quad (7.23)$$

and the source auto-power is:

$$A = \frac{1}{2} \overline{|a|^2} = \frac{1}{2} \frac{\mathbf{g}^* \mathbf{p}}{|\mathbf{g}|^2} \left( \frac{\mathbf{g}^* \mathbf{p}}{|\mathbf{g}|^2} \right)^* = \frac{\mathbf{g}^* \mathbf{C} \mathbf{g}}{|\mathbf{g}|^4}. \quad (7.24)$$

Expression (7.24) is known as *conventional beamforming* [133].

### 7.3.2 Signal correction

As mentioned earlier, conventional beamforming usually assumes monopole sources to enable the minimization solution. Here it is referred to as the *monopole-beamforming* (M-Beam) algorithm. There are two approaches to correct conventional beamforming techniques for dipole source identification. The first approach is to correct the array microphone signals stored in the cross-power matrix  $\mathbf{C}$  before the beamforming procedure, as proposed by Jordan *et al.* [89]. This is essentially a “signal correction” rather than a correction to the beamforming algorithm. The application of this correction is limited for a 2D microphone array

because it is time consuming, not easily processed by computer (due to nonideal phase alignment) and restricted to one single fixed dipole source. Nevertheless, the signal correction method provides a useful validation for the dipole characteristic term which will be used in a corrected beamforming algorithm for dipoles.

If the source strength of a monopole is  $a(\omega) = 1$ , we can model a dipole with two coherent monopoles with the same strength but opposite phase. In this case, the signal correction for the cross-power matrix  $C$  would be

$$C_{mn} = \frac{\frac{1}{2} \overline{p_m p_n^*}}{\text{DPL}_m \text{DPL}_n^*}, \quad (7.25)$$

where the dipole correction term  $\text{DPL}$  is an  $N$ -dimensional vector containing the information of both amplitude and phase for all array microphones, and the suffix denotes the  $m$ th or  $n$ th microphone. If the corrected dipole simulation gives the same source location and source power as the reference monopole simulation, the correction of Equation (7.25) is validated.

### 7.3.3 Beamforming correction

The second approach for estimating dipole source power is to correct the beamforming algorithm itself to account for a dipole source. It is therefore recognized as the “beamforming correction”, and the corrected algorithm is referred to here as the *dipole-beamforming* (D-Beam) algorithm. To implement the beamforming correction, the transfer vector  $g$  for a dipole should be defined by setting the dipole strength  $a(\omega)l = 1$  in Equation (7.17), *i.e.*

$$g_n = \frac{-e^{-i\omega\Delta t_e} \cdot \text{DPL}}{4\pi r \Theta l}, \quad (7.26)$$

and then the beamforming procedure should proceed as normal to represent the true source location and source power for a dipole. With the dipole signature imprinted in the source description, the beamforming correction allows the user to find the true amplitude and location of a suspected dipole.

In principle, it would be possible to determine the most likely orientation and amplitude of dipoles anywhere on the scanning grid. However, for complex

source patterns which might be encountered on an aeroacoustic model, iterations through amplitude and orientation of potential dipoles for each grid point would be computationally expensive. Such a method might also lead to inaccuracies due to insufficient signal-to-noise ratio. For the present method, we assume that the user has some information about likely source orientation and is interested in determining a more accurate estimate of source location and amplitude. A reference dipole direction is therefore required as an input parameter when the D-Beam algorithm is applied. The software divides the region of interest into a number of grid points, and then scans this region point by point for dipoles in the reference direction, estimating the source auto-power using Equation (7.24).

## 7.4 Numerical Simulation

### 7.4.1 Simulation setup

In this section, numerical simulations are performed to validate the two approaches mentioned previously. Figure 7.1 shows a candidate dipole source located in a uniform flow,  $\mathbf{M} = (0.1, 0.0, 0.0)$ , with the dipole distance vector  $\mathbf{l}$  at arbitrary directions. In Figure 7.2 two cases are examined with the dipole aligned parallel to the  $y$ - or  $z$ -axis, referred to as the Y or Z dipole, respectively. The  $y$ - $z$  axes are parallel and normal to the array plane respectively. The source location  $\boldsymbol{\xi}$  and dipole vector  $\mathbf{l}$  for these two test cases are listed in Table 7.1, and Figures 7.2(a) and 7.2(b) show the respective dipole directivity patterns. In each test case, an ideal monopole at the same location with source strength  $a(\omega) = 1$  is also simulated for comparison. As shown in Table 7.1, the dipole size is chosen to be small,  $l = 0.002$  m, to ensure a compact source. Since there is no sound radiation ( $DPL = 0$ ) in the plane normal to a dipole, an offset of source location  $\Delta\xi = 0.005$  m is included in Case 1 to avoid divide-by-zero errors when applying the dipole correction of Equation (7.25).

The simulation array geometry is identical to that of the microphone array system described in Section 4.3.2. The use of both the HF and LF arrays allows estimates over a large frequency range. However, differences in estimates of source power for the same model at common frequencies can be a problem if the sources

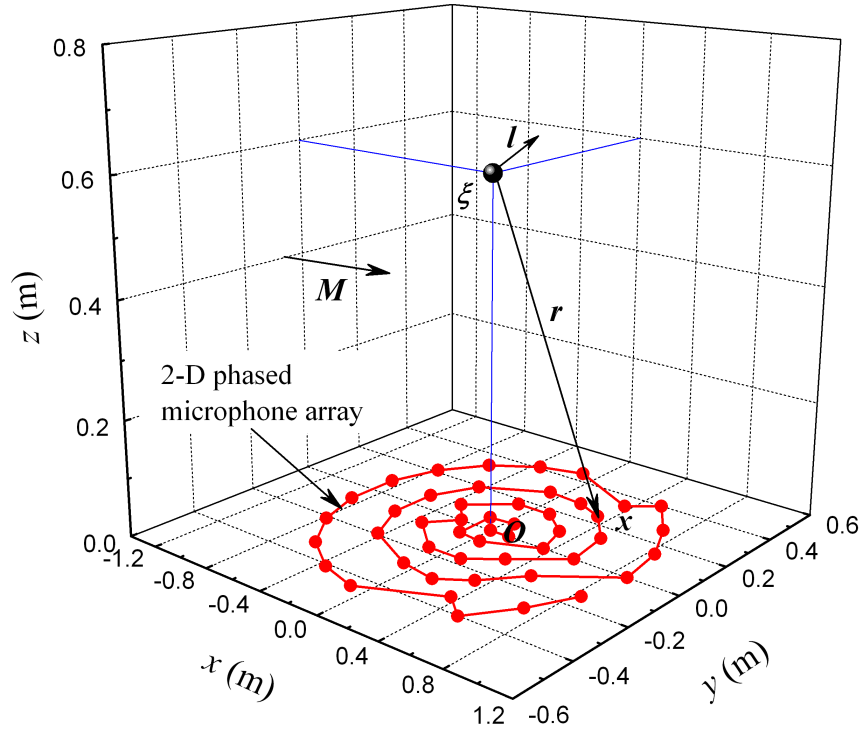


Figure 7.1: Schematic of the simulation for a dipole source.

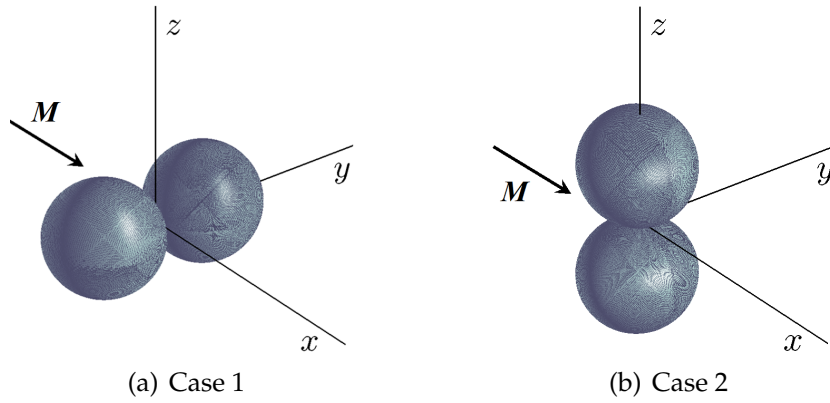


Figure 7.2: Dipole directivities for test cases 1 and 2.

Table 7.1: Source location  $\xi$  and dipole vector  $l$  for test cases 1 and 2.

Case no.	Dipole	$\xi$ (m) <sup>†</sup>	$l$ (m) <sup>‡</sup>
1	Y	(0.0, $\Delta\xi$ , 0.6)	(0.0, $\Delta l$ , 0.0)
2	Z	(0.0, 0.0, 0.6)	(0.0, 0.0, $\Delta l$ )

<sup>†</sup>  $\Delta\xi = 0.005$  m.

<sup>‡</sup>  $\Delta l = 0.002$  m.

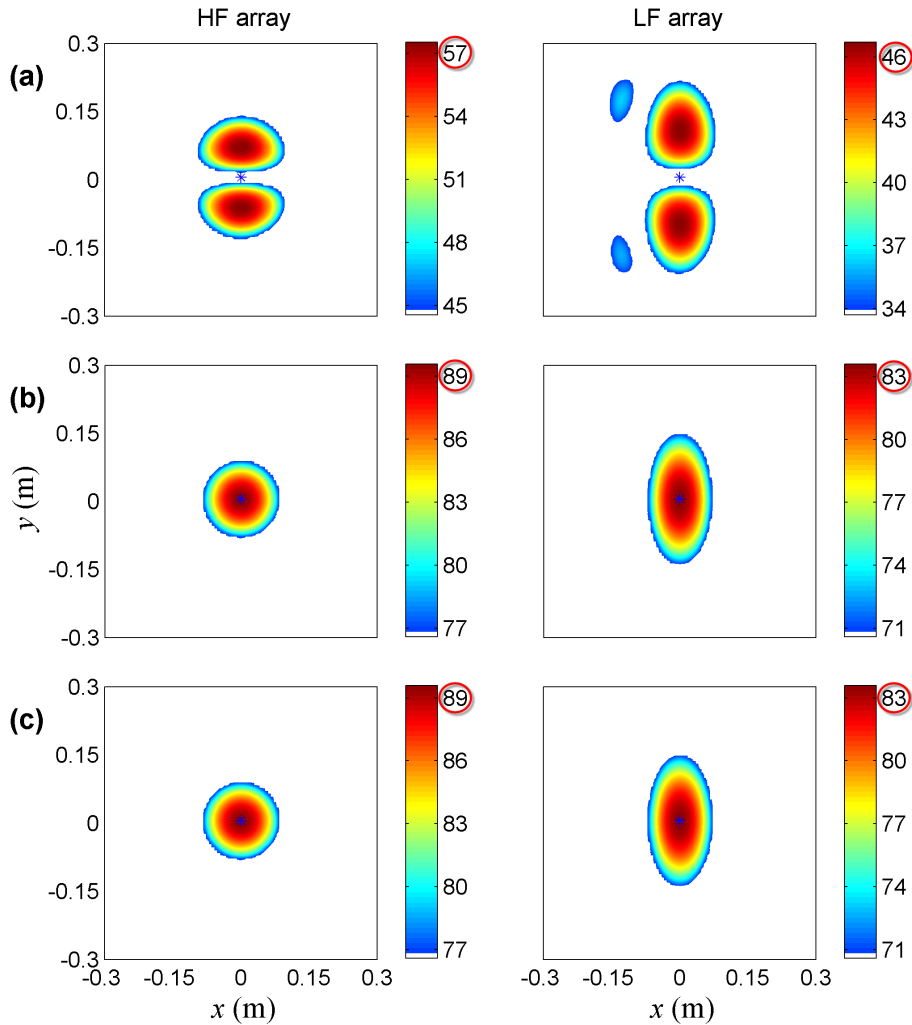


Figure 7.3: Simulated source maps for Case 1: (a) dipole without correction, (b) dipole with signal correction, (c) reference monopole. HF array,  $f = 8000$  Hz; LF array,  $f = 2000$  Hz. Colour bars are in dB.

are not well modelled. Hence for both simulation and experiment we look at information from both arrays. The beamforming source maps are generated in  $1/3$  octave-band frequencies, and the source auto-powers have been converted to SPL in  $\text{dB}^\dagger$  at a reference distance of  $1/\sqrt{4\pi}$  m from the source [133] and in the dipole direction if the D-Beam algorithm is applied.

### 7.4.2 Signal correction

Figures 7.3 and 7.4 show the simulated source maps for Cases 1 and 2 using the signal correction technique. The top row of the figures shows the dipole as

$^\dagger 20 \log_{10}(p/p_{\text{ref}})$ ,  $p_{\text{ref}} = 2 \times 10^{-5}$  Pa.



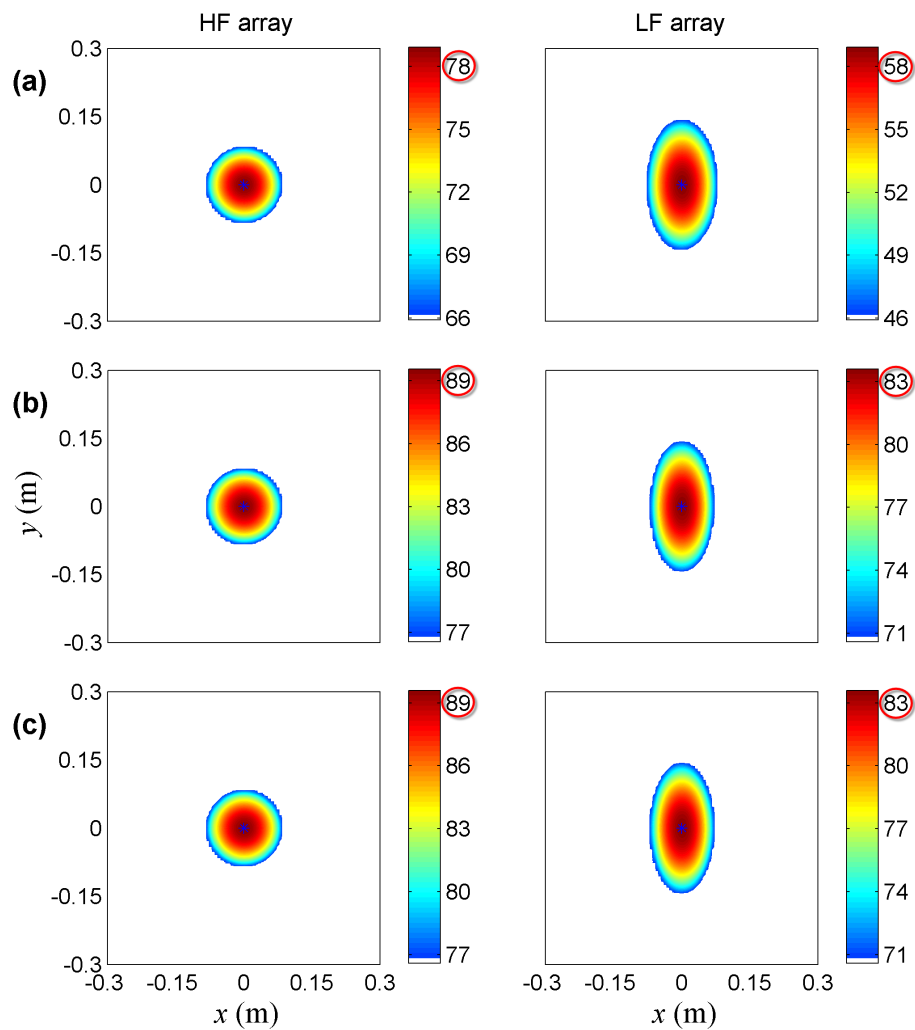


Figure 7.4: Simulated source maps for Case 2: (a) dipole without correction, (b) dipole with signal correction, (c) reference monopole. HF array,  $f = 8000$  Hz; LF array,  $f = 2000$  Hz. Colour bars are in dB.

interpreted by conventional beamforming (M-Beam algorithm), the middle row is the dipole after signal correction, and the bottom row gives the reference monopole with conventional beamforming. For brevity, only the results of 8000 Hz and 2000 Hz are shown for the HF and LF arrays, respectively.

For the Y dipole, Figure 7.3 shows that the dipole source is missed at the true location (marked by an asterisk) by the conventional beamforming because the phase variation in the radiated sound is entirely different from a monopole in directions close to the normal of the dipole vector  $\mathbf{l}$ , *i.e.*, the sign of the acoustic pressure changes across this normal plane. Instead, the sound is interpreted as coming from elsewhere on the scan grid. More striking are the dipole source powers

that are significantly underestimated compared with the reference monopole simulations. As can be found from the colour bars in Figure 7.3, without correction the detected peak source powers are 57.6 dB and 46.7 dB for the HF and LF arrays, respectively, which are about 32 dB and 37 dB lower than those of the reference monopoles used to construct the dipoles.

Conventional beamforming is able to better detect the source at the original dipole location for Case 2 (Figure 7.4), where the radiation of the Z dipole has a phase variation similar to that of a monopole over the area of the arrays. However, the source powers before correction are still much lower than those of the reference monopole, which can be largely accounted for by the relatively small value of the term DPL in the dipole pressure spectrum (7.17). The frequency-dependent DPL also explains the 20 dB difference between the source powers (without correction) detected by the HF and LF arrays because of the different chosen frequencies, 8000 Hz and 2000 Hz, respectively.

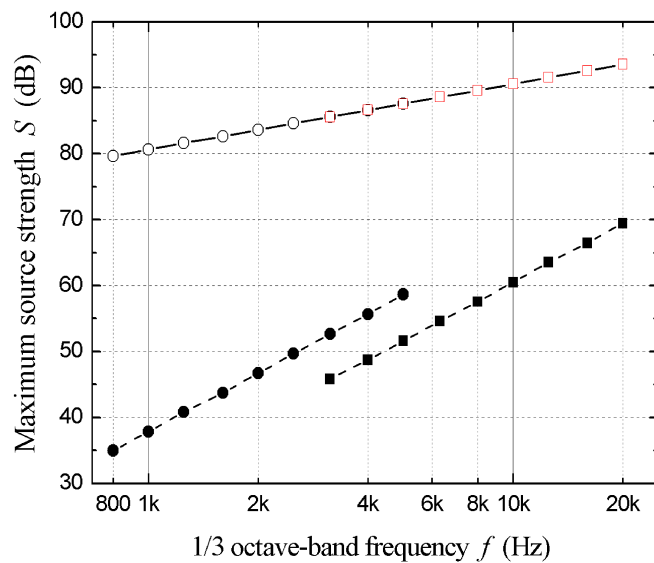
With the signal correction applied, however, the true source maps for a dipole are recovered for both Cases 1 and 2, and they agree with those of the reference monopole in both source pattern and source power, as shown clearly in the middle and bottom rows of Figures 7.3 and 7.4, respectively. This provides confirmation of the validity of the dipole correction form (7.25).

Figure 7.5 shows the variation of the peak source power  $S$  with 1/3 octave-band centre frequency  $f$  for Cases 1 and 2 for both arrays. For a monopole with  $a(\omega)$  independent of frequency,  $S$  scales on  $f$  because the 1/3-octave bandwidth  $B$  varies linearly with  $f$ . Actually,  $S$  should increase by 1 dB between two adjacent 1/3 octave-band centre frequencies  $f_1$  and  $f_2$  because

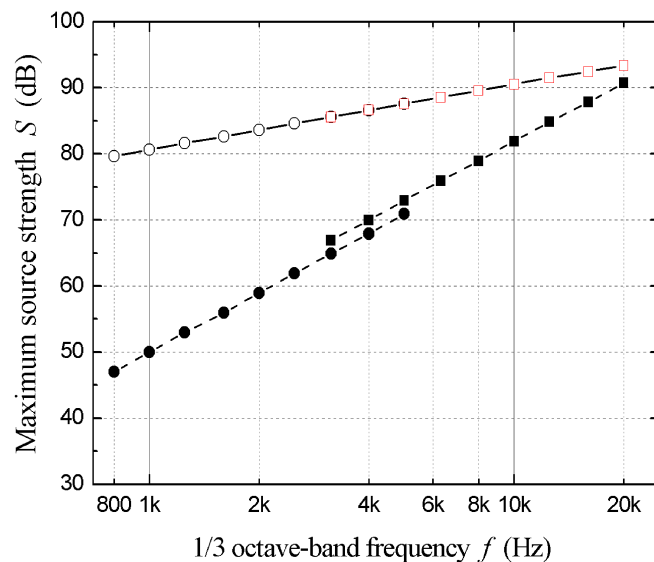
$$\Delta S = 10 \log_{10}(B_2/B_1) = 10 \log_{10}(f_2/f_1) = 10 \log_{10} 2^{1/3} = 1 \text{ dB}, \quad (7.27)$$

and the corrected estimates (solid lines) show this tendency. However, without correction, estimates of  $S$  (solid squares and circles) vary with  $f^3$  in each case because the sound power of a dipole scales on  $\omega^2$  as well as the frequency-dependent 1/3-octave bandwidth  $B$ , so that

$$\Delta S = 10 \log_{10}(f_2^2 B_2 / f_1^2 B_1) = 10 \log_{10}(f_2^3 / f_1^3) = 10 \log_{10} 2 = 3 \text{ dB}. \quad (7.28)$$



(a) Case 1



(b) Case 2

Figure 7.5: Variation of peak source power  $S$  with 1/3 octave-band centre frequency  $f$  for Cases 1 and 2. Dipole without correction: ■ HF array, ● LF array; dipole with signal correction: □ HF array, ○ LF array; ---  $S \sim f^3$ , —  $S \sim f$ .

After correction, estimates of  $S$  (open squares and circles) vary with frequency as  $S \sim f$ , which is simply a 1/3-octave bandwidth dependence. The same relationship is seen for estimates of a monopole with uniform strength. The signal correction also presents the same values of  $S$  at a fixed frequency for the HF and LF arrays, which is in line with the expectation that the algorithm should be independent of array geometry.

### 7.4.3 Beamforming correction

#### 7.4.3.1 Single source

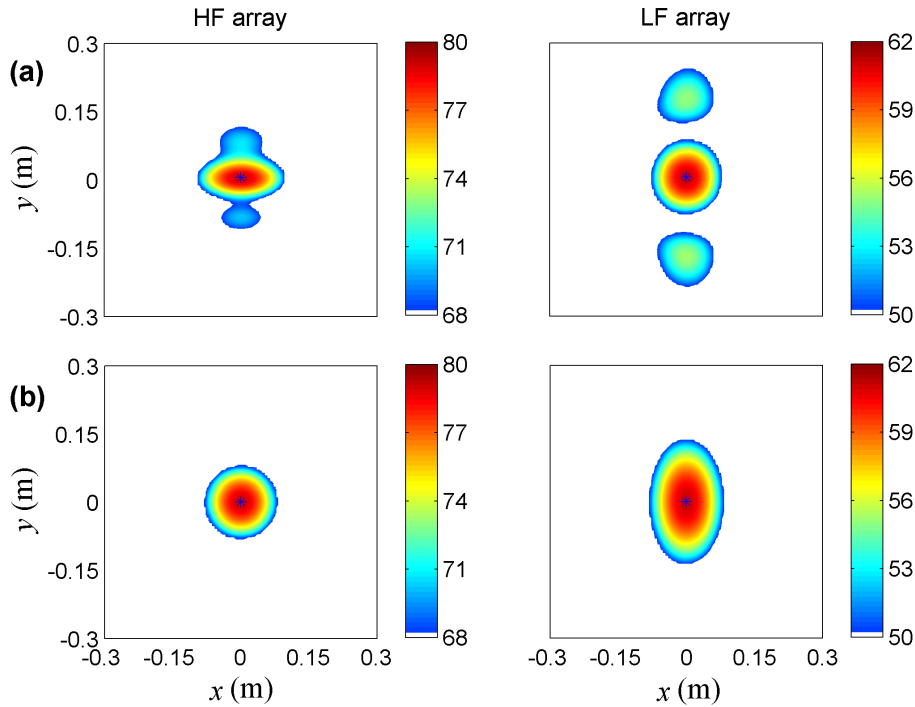


Figure 7.6: Simulated source maps by the D-Beam algorithm: (a) Case 1 and (b) Case 2. HF array,  $f = 8000$  Hz; LF array,  $f = 2000$  Hz. Colour bars are in dB.

With the dipole correction term DPL validated by the signal correction method, we apply the D-Beam algorithm to identify the original dipole source instead of the corrected monopole source as in the middle rows of Figures 7.3 and 7.4. The effect of the beamforming correction on the source maps of Cases 1 and 2 is shown in Figure 7.6. We can see from the corrected algorithm that the main source is correctly placed at the true source location, though low-level side lobes occur away from the main source. Note that the microphone arrays now detect very similar peak source powers  $S$  for both dipole orientations (see Table 7.2).

Comparing the source maps of the signal correction (Figures 7.3 and 7.4) and beamforming correction (Figure 7.6), we see that both techniques are able to recover the true location of a single dipole. However, the signal correction gives the amplitude of the constituent monopoles of the dipole, whereas the beamforming correction directly identifies the amplitude of the dipole. Table 7.3 shows the

Table 7.2: Simulated peak source power  $S$  (dB) by the M-Beam and D-Beam algorithms for Cases 1 and 2. HF array,  $f = 8000$  Hz; LF array,  $f = 2000$  Hz.

Case no.	Dipole	HF array		LF array	
		M-Beam	D-Beam	M-Beam	D-Beam
1	Y	57.55	79.11	46.71	61.10
2	Z	78.92	79.12	58.93	61.12

Table 7.3: Comparison of elapsed CPU time (s) between the signal correction ( $t_s$ ) and beamforming correction ( $t_b$ ). HF array,  $f = 8000$  Hz; LF array,  $f = 2000$  Hz.

Case no.	Dipole	HF array		LF array	
		$t_s$	$t_b$	$t_s$	$t_b$
1	Y	141.7	21.4	41.6	6.8
2	Z	141.8	21.4	41.4	6.7

elapsed CPU time of the two techniques for Cases 1 and 2 on a PC with an Intel Pentium 4 processor of 3.4 GHz clock speed and a 1 GByte RAM. The CPU time is very close in each column of Table 7.3, and it is evident that the signal correction uses much longer CPU time than the beamforming correction, *i.e.*  $t_s \sim 6-7t_b$ , because the signal correction includes a process of delay-analyze-and-sum while the beamforming correction processes the data directly using the D-Beam algorithm. The CPU time varies significantly between the HF and LF arrays due to the different frequencies used. With an identical frequency bandwidth for both arrays ( $\Delta f = 117.2$  Hz, see Section 7.5.1), the higher centre frequency of 1/3 octave-band contains more frequency bands and thus takes longer CPU time to process.

### 7.4.3.2 Multiple sources

One advantage of beamforming correction over signal correction is that it can be used in the case of multiple dipoles. The application of the D-Beam algorithm to simulated multiple sources of 2 Y dipoles in the flow direction and 3 Z dipoles in a triangle is shown in Figure 7.7. At low frequencies the source lobes of multiple dipoles are likely to overlap with one another particularly for the HF array which

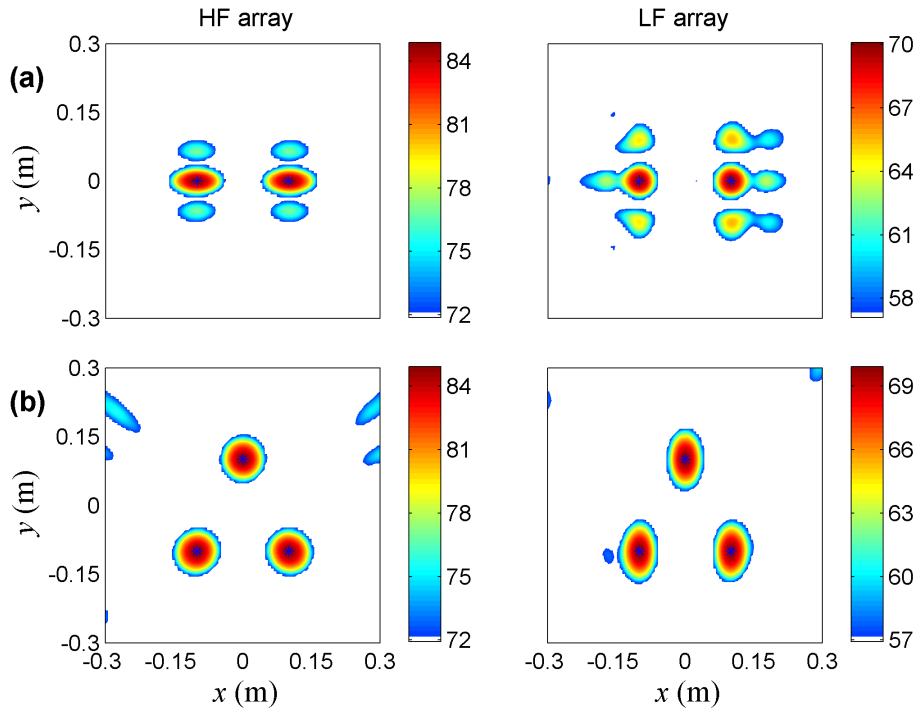


Figure 7.7: Simulated multiple dipole by the D-Beam algorithm: (a) 2 Y  $(0, 1, 0)$  dipoles located at  $(-0.1, 0.0)$  and  $(0.1, 0.0)$ ; (b) 3 Z  $(0, 0, 1)$  dipoles located at  $(0.0, 0.1)$ ,  $(-0.1, -0.1)$  and  $(0.1, -0.1)$ . HF array,  $f = 12500$  Hz; LF array,  $f = 4000$  Hz. Colour bars are in dB.

has a worse resolution. Hence the frequencies have been increased to 12500 Hz and 4000 Hz for the HF and LF arrays, respectively to achieve better resolution so that dipole sources at different locations can be clearly isolated. The source strength is set as  $al = 0.002$  for all dipoles. As can be observed in Figure 7.7, after the beamforming correction each dipole source is detected at the simulated location for all cases. This proves that the D-Beam algorithm is capable of localizing multiple dipoles in spite of different dipole directions, source arrangements and microphone arrays, and therefore it should be of general use in practice.

## 7.5 Experiment

### 7.5.1 Experimental setup

A series of experiments were conducted in the low-speed Markham wind tunnel located at CUED to test the performance of the D-Beam algorithm. Figure 7.8

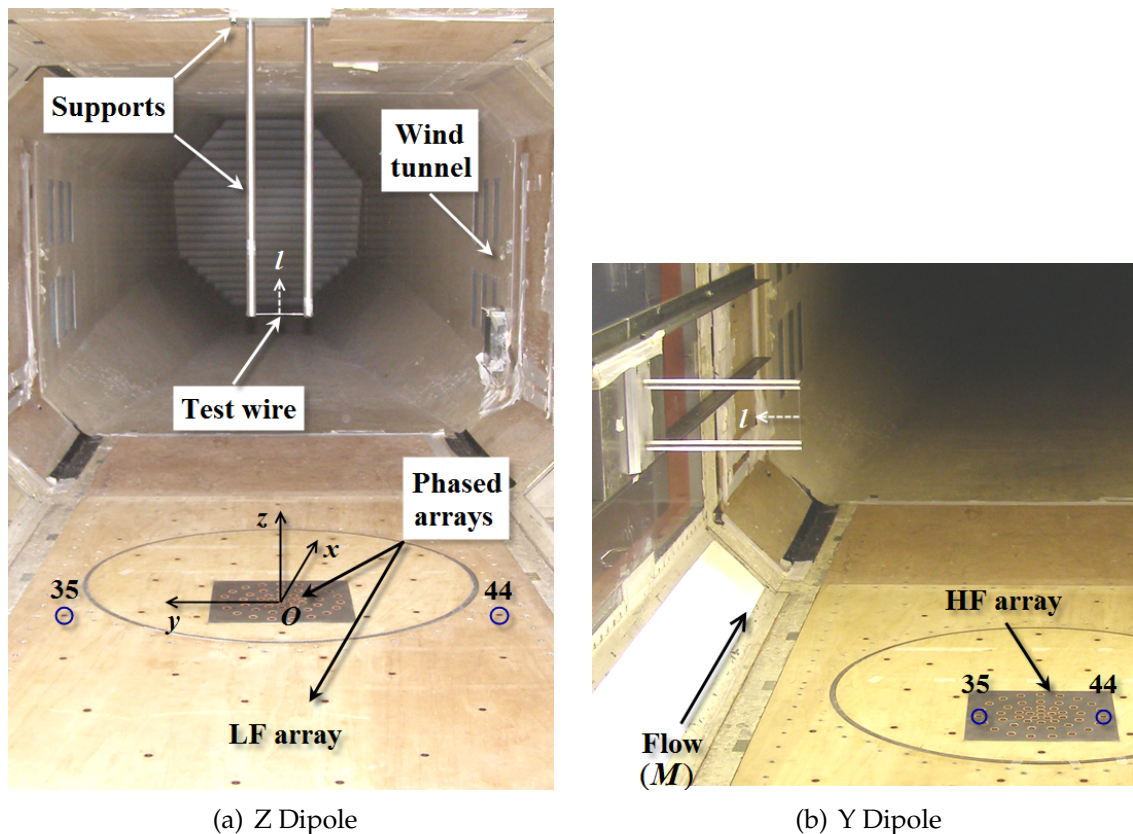


Figure 7.8: Experimental setup for aeolian-tone dipoles in two different directions: Z  $(0, 0, 1)$  and Y  $(0, 1, 0)$ .

illustrates the experimental setup of the wind tunnel, the phased microphone arrays and a test wire with supports. The test wire was 1.5 mm in diameter and aligned perpendicular to the flow in order to generate an aeolian tone, representing a realistic aeroacoustic dipole source. Acoustic measurements were performed at free-stream flow velocities,  $U = 20, 40$  m/s, to obtain aeolian-tone dipole sound at different peak frequencies. The wire was orientated to hopefully obtain dipoles in the Z- and Y-directions as shown in Table 7.4. The “Y dipole” configuration was

Table 7.4: Dipoles in two different directions.

Dipole	Direction	Coordinates of wire centre (m)		
		$x$	$y$	$z$
Z	$(0, 0, 1)$	0.075	0.003	0.60
Y	$(0, 1, 0)$	-0.005	0.465	0.60

moved to the side to provide a better view for the microphone arrays. The support structure included two support rods 10 cm apart and one or two support plates, and was mounted to the tunnel ceiling or side wall.

Measurements were made with both the HF and LF arrays at sampling frequency of 120 kHz or 30 kHz, respectively. Both arrays contain 48 microphones and are flush mounted into the rigid tunnel floor. In the post-processing, the time-domain signals were broken down into 1024 (HF array) or 256 (LF array) data blocks, and each block was Fourier transformed, resulting in frequency-domain signals with bandwidth  $\Delta f = 117.2$  Hz for each array. Narrow-band acoustic beamforming scans were performed to determine source auto-powers as described in Section 7.3. Both monopole (M-Beam) and dipole (D-Beam) source descriptions were examined in each case. For each experiment, a horizontal scan plane was used which intersected the test wire at the midpoint. Finally, source maps were generated by summing the narrow-band data to 1/3 octave-band data, with source auto-powers shown as SPL (dB) at a reference distance of  $1/\sqrt{4\pi}$  m and a reference dipole direction if applicable.

## 7.5.2 Noise spectra

Cross spectra between a pair of microphones are shown in Figure 7.9 for each experimental case together with the noise generated by the support (without the wire) for comparison. Microphones used for the cross spectra are marked by circles in Figures 7.8(a) and 7.8(b) for each array. The aeolian tones are clearly audible around 6000 Hz for the HF array ( $U = 40$  m/s) and 3000 Hz for the LF array ( $U = 20$  m/s), corresponding to a Strouhal number  $\sim 0.225$ . As the spectral peaks span a range of frequencies, 1/3-octave frequency bands were used for beamforming source maps to capture the total acoustic energy of the aeolian tone. In this case, the centre frequencies of 6300 Hz (HF array) and 3150 Hz (LF array) were selected because they cover the frequency bands of 5613–7072 Hz and 2806–3536 Hz, respectively, which are sufficiently large for the spectral peaks of interest.



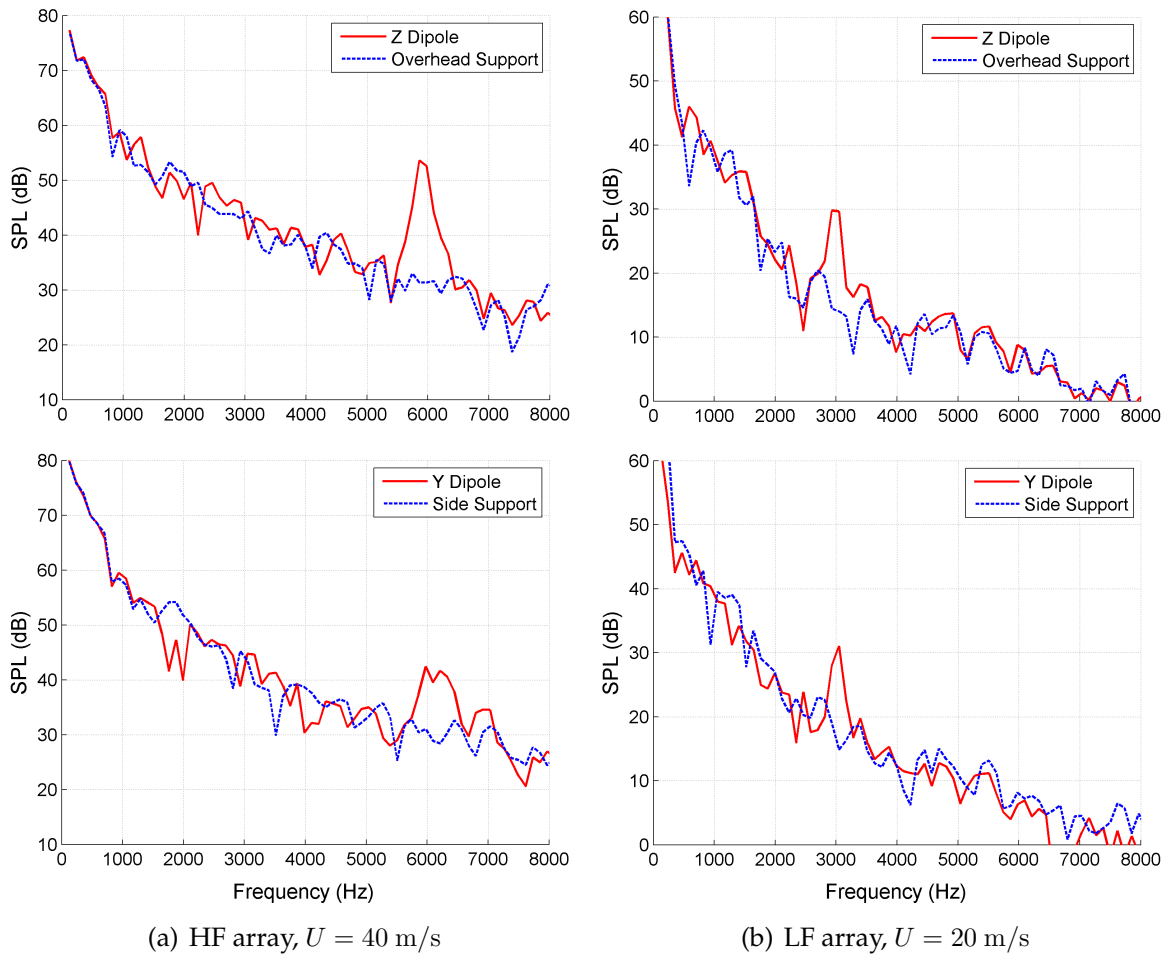


Figure 7.9: Measured cross spectra for dipoles in two different directions: Z  $(0, 0, 1)$  and Y  $(0, 1, 0)$  with measured cross spectra of overhead and side supports for comparison.  $\Delta f = 117.2$  Hz.

## 7.5.3 Beamforming correction

### 7.5.3.1 Simulation

Theoretical simulations were first carried out to examine the performance of the proposed beamforming correction on identifying distributed aeolian-tone dipoles, and to provide a baseline for comparison with experimental results. In Section 4.3.4 we used this method to validate the prediction model for surface roughness noise by comparing the measured and simulated source powers. In this work, however, we are not concerned about the source power itself. Instead, we compare the increase ( $\Delta S_s$ ) in the estimated peak source power  $S$  from the M-Beam algorithm to the

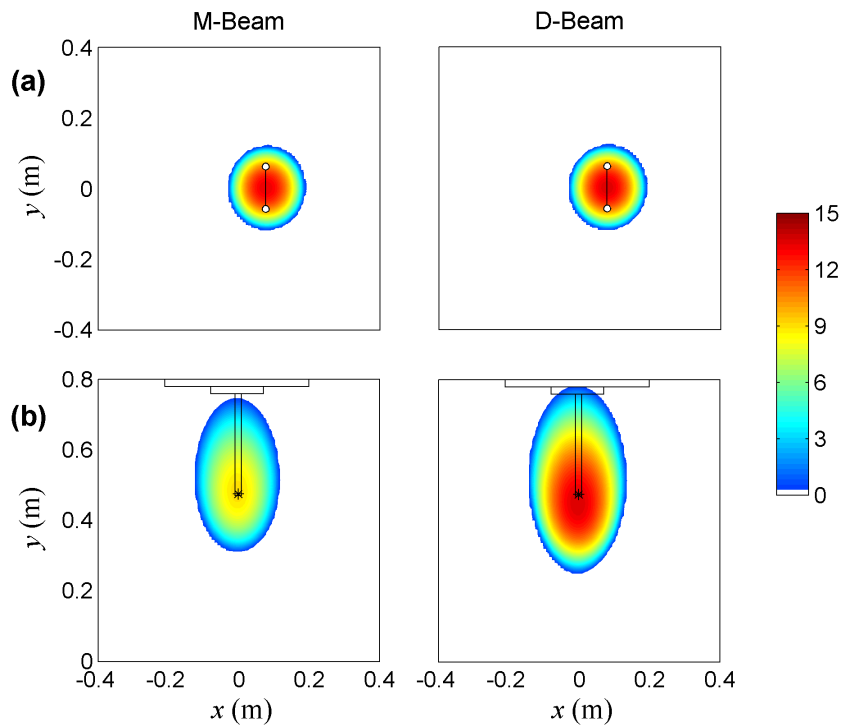
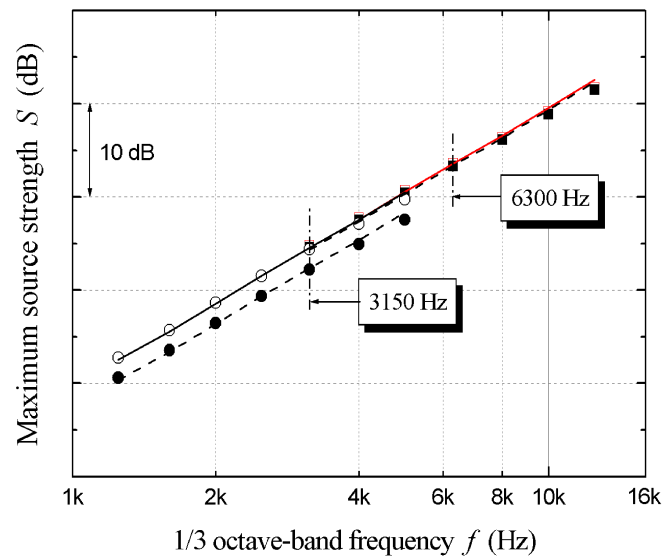


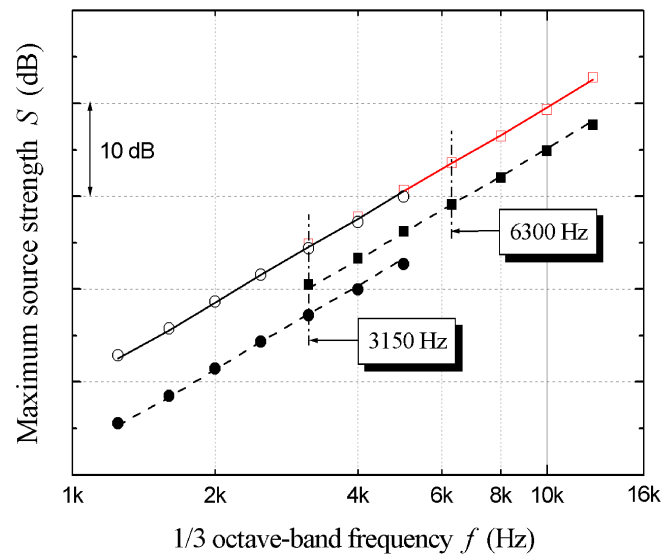
Figure 7.10: Comparison of simulated source maps by the M-Beam and D-Beam algorithms for dipoles in two different directions: (a) Z (0, 0, 1) and (b) Y (0, 1, 0). HF array,  $f = 6300$  Hz. Colour bars are in dB.

D-Beam algorithm. To implement the simulation for the Z and Y dipoles, we assume that 11 identical incoherent dipoles are uniformly distributed in the direction of the wire, and the same value of  $a(\omega)$  is used as the input source strength for both algorithms and both arrays.

Figure 7.10 illustrates the simulated source maps at 6300 Hz by the HF array for the Z and Y dipoles, and the comparison between the M-Beam and D-Beam algorithms. The colour bar on the right restricts the SPL data within the range of 0–15 dB, and the source maps of different dipoles and algorithms are shown on identical scales for comparison. Support structures are also sketched on the source maps. Note that since  $a(\omega)$  has been set equal to some value, these simulated SPL data do not represent the true source powers of the aeolian-tone dipoles and are merely meaningful as relative levels to show the effect of the beamforming correction. In fact, both the M-Beam and D-Beam algorithms detect the true location of the main source for the distributed dipoles. However, only the D-Beam algorithm correctly identifies strength of the Z and Y dipoles, as both dipoles have the similar



(a) Z dipole



(b) Y dipole

Figure 7.11: Variation of simulated peak source power  $S$  with 1/3 octave-band centre frequency  $f$  for the Z and Y dipoles. M-Beam algorithm: ■ HF array, ● LF array; D-Beam algorithm: □ HF array, ○ LF array; ---, —  $S \sim f^3$ .

source powers. The M-Beam algorithm appears to substantially underestimate source strength of the Y dipoles, as anticipated by the earlier simulation (Figure 7.3).

Figures 7.11(a) and 7.11(b) show the variation of  $S$  with 1/3 octave-band centre frequency  $f$ . As expected from Equation (7.28), the simulated  $S$  of the Z and Y dipoles varies as  $f^3$ , independently of the different arrays and algorithms used. After applying the beamforming correction, the estimated peak source powers  $S$

by the HF and LF arrays almost coincide with one another, consistent with the tendency of the ideal individual sources as in Figure 7.5. For the Z dipole, the effect of the beamforming correction is generally small, *i.e.*,  $\Delta S_s \approx 2.2$  dB for the LF array and nearly negligible for the HF array (see Table 7.5). However for the Y dipole, the values of  $S$  increase significantly from the M-Beam algorithm to the D-Beam algorithm by about 7.2 dB (LF array) and 4.6 dB (HF array). This is because for the Z dipole the variation of phase over the microphones is just due to propagation distance and is correctly captured by the M-Beam algorithm. However, for the Y dipole there is an additional phase change due to the dipole directivity.

### 7.5.3.2 Measurement

Figure 7.12 illustrates the measured source maps at 6300 Hz by the HF array for the Z and Y dipoles. The source powers of the aeolian-tone dipoles identified by the M-Beam and D-Beam algorithms are shown in the SPL range of 65–80 dB.

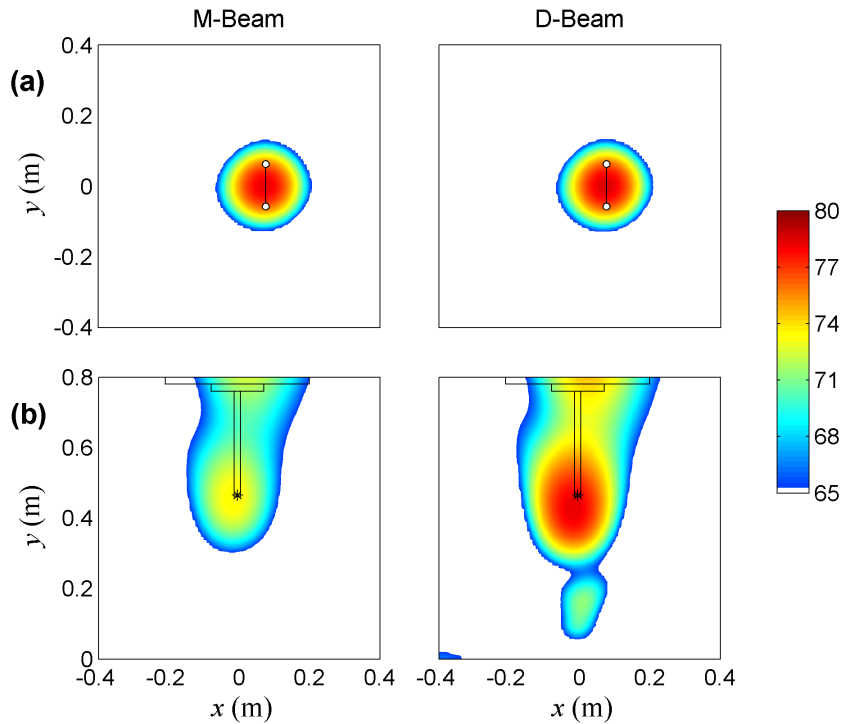


Figure 7.12: Comparison of measured source maps by the M-Beam and D-Beam algorithms for dipoles in two different directions: (a) Z (0, 0, 1) and (b) Y (0, 1, 0). HF array,  $f = 6300$  Hz. Colour bars are in dB.

Comparing Figures 7.10 and 7.12 we see that the simulated and measured source maps show very similar source patterns and similar effects of the beamforming correction. Table 7.5 compares the estimated peak source power  $S$  of the two dipoles, as recorded by both arrays at 6300 Hz and 3150 Hz. For each dipole orientation, the value of  $S$  is given for both the M-Beam and D-Beam algorithms. In each case, the M-Beam algorithm shows a lower estimate of source power. The differences between the M-Beam and D-Beam algorithm are also much greater for the Y dipole, as seen in simulation. In addition, the D-Beam algorithm correctly identifies the wire as producing very similar sound power in both orientations. Corrected source maps are also shown in the right column of Figure 7.12.

Table 7.5: Peak source power  $S$  (dB) of measurement and simulation for the Z and Y dipoles. (a) HF array,  $f = 6300$  Hz; (b) LF array,  $f = 3150$  Hz.

(a)	Measurement			Simulation	
	M-Beam	D-Beam	$\Delta S_m$	$\Delta S_s$	$ \Delta S_m - \Delta S_s $
Dipole					
Z	78.31	78.57	0.26	0.24	0.02
Y	73.59	78.32	4.73	4.57	0.16
(b)	Measurement			Simulation	
	M-Beam	D-Beam	$\Delta S_m$	$\Delta S_s$	$ \Delta S_m - \Delta S_s $
Dipole					
Z	51.73	53.92	2.19	2.16	0.03
Y	48.01	55.18	7.17	7.22	0.05

The difference in measured peak source powers between the M-Beam and D-Beam algorithms is shown in Table 7.5 as  $\Delta S_m$ . Due to the source directivity, the Y dipole shows larger  $\Delta S_m$  because much of its sound radiation is missed without the beamforming correction. In Table 7.5 are also shown the corresponding values of  $\Delta S_s$  obtained from a simplified simulation of the experimental setup. This enables the evaluation of the difference  $|\Delta S_m - \Delta S_s|$ . It indicates that  $\Delta S_m$  agrees with  $\Delta S_s$  fairly well for all cases with the largest discrepancy of 0.16 dB occurring at the Y dipole by the HF array. This suggests that the modelling of the aeolian tones from the wire as a series of incoherent dipoles is realistic and provides a preliminary validation of the D-Beam algorithm for an experimental dipole source.

## 7.6 Summary

It has been shown that conventional beamforming techniques can misinterpret the microphone array measurement for a simple dipole due to the inherent monopole assumption. A correction for the phase differences in microphone signals was presented by Jordan *et al.* [89] and it displayed the capability to recover the source location of a single dipole in the resulting source map. In this chapter, we present a method of modifying the source transfer vector to search the scanning plane for dipole sources. The resulting algorithm is able to identify the source location and amplitude of dipoles with a suspected orientation. This method extends the capability of the “signal correction” by Jordan *et al.* [89] to deal with multiple dipoles for 2D microphone arrays.

In simulations of dipoles normal to the flow, the dipole-beamforming algorithm recovered the true source location and amplitude. For a point dipole, the use of a dedicated dipole beamforming algorithm can lead to large increases in source estimates. For simulations with distributed dipole sources and comparable measurements of aeolian tones, the improvement in estimates of source power with the D-Beam algorithm was less marked. However, the implementation of the new algorithm did allow recovery of the same source strength from different orientations of the same aeolian tone.

Whilst both simulations and measurements have validated the capability of the D-Beam algorithm to improve conventional techniques for identifying dipole sources, the present implementation requires specification of the dipole direction. A potential improvement would be to iterate through different dipole orientations at each point on the scanning grid. However, in many aeroacoustic experiments it may be possible to readily identify the likely dipole orientations by using knowledge of the source mechanisms. In such cases, it is hoped that more accurate estimates of source amplitude can be determined with this method.

# Chapter 8

## Conclusions and Future Work

### 8.1 Summary and Conclusions

THE noise from aircraft has been a significant contributor to the considerable environmental problem of noise pollution that impacts on the population in modern society, and has drawn worldwide concerns especially due to the increasing growth of civil transport aircraft since the 1960s.

With the significant reduction of jet-engine noise levels in recent years, airframe noise has been highlighted, particularly during landing approach when some geometrically complex structural features are exposed to the flow (*i.e.* the “dirty” configuration). These complex components, *e.g.* landing gears, slats and flaps, have been noted to be the dominant sources of airframe noise on modern commercial aircraft and have received sufficient concerns in terms of the noise source mechanisms and noise reduction technologies.

Other sources may also contribute to the airframe noise of aircraft flying in the “clean” configuration, for example the trailing edge and panel vibration. In this thesis, however, we have carried out an investigation into a previously discounted noise source arising from the rough surfaces on aircraft wings and fuselages, as part of the SAI project. The aim was to understand better the noise source mechanisms and to predict the far-field sound radiation produced by surface roughness.

Through the literature review in Chapter 2, we divided the source mechanisms of surface roughness noise into two alternative categories: the sound scattering

mechanism (incoherent and coherent) and the drag dipole mechanism, according to which boundary-layer velocity profile region the roughness elements lie in. In the course of the thesis, we focused on the incoherent sound scattering mechanism for roughness elements confined in the logarithmic layer since previous studies on this mechanism are relatively systematic and mature.

### **Sound Scattering Mechanism**

*Theoretical modelling:* First the theoretical modelling of the incoherent scattering mechanism was based on Howe's diffraction theory [77] of turbulent boundary-layer roughness noise, which has been extended to evaluate the integral of the far-field roughness noise spectrum by means of direct numerical integration instead of asymptotic approximation. Hence we obtained the prediction model by using previous empirical models [25, 26, 31, 43, 140] of smooth-wall wavenumber-frequency spectrum and considering the effects of roughness-enhanced turbulent fluctuations. The numerically predicted roughness noise spectra have shown encouraging agreement with Howe's empirical model [82] and the experimental data by Hersh [71], which provided preliminary validation of the prediction model.

*Experimental validation:* We then conducted acoustic measurements for the radiated sound from two rough plates in an open-jet wind tunnel to experimentally validate the prediction model. The measured noise spectra of the rough plates were above that of a smooth plate in 1–2.5 kHz frequency, and exhibited reasonable amount of agreement with the predicted level. Phased microphone arrays were also applied to the measurement and simulation of surface roughness noise. The source maps measured at three streamwise locations have demonstrated the dipole directivity. Higher source strengths were observed on the rough plates which also enhanced the TE noise. The prediction model was used to describe the strength of a distribution of incoherent dipoles and to simulate the sound detected by the microphone array. Source maps of measurement and simulation have exhibited satisfactory similarities in both source pattern and source strength. All these observations have confirmed the dipole nature of surface roughness noise



and provided further form of validation for the prediction model. It was also shown, however, that there is scope to improve the prediction model in terms of the somewhat underestimated streamwise gradient of source strength and the overestimated SPL at high frequencies. Moreover, hot-wire measurement has determined the suitable value of wake strength which gave the best fit to measured data and has confirmed the validity of the skin friction formula of Mills and Hang [106] for the prediction model.

*Numerical prediction and analysis:* The next step was to apply the validated model to a Boeing-757 sized aircraft wing and the SAI conceptual design SAX-40 with idealized levels of surface roughness. Numerical predictions for both aircraft have shown that the spectral level of roughness noise could exceed that of TE noise at sufficiently high frequencies resulting in the higher roughness noise OASPL, too, and that TE noise was somewhat enhanced as an indirect effect of surface roughness. The parametric studies indicated that roughness height and roughness density are two important parameters having significant effects on roughness noise with the former a more dominant one. The directivity of roughness noise was observed to vary over different roughness levels. In addition, we presented two categories of limiting roughness for SAX-40, one sparse roughness element and the other more uniformly distributed. We showed that provided the surface roughness was less than each of these surface roughness noise would not prevent SAX-40 from meeting its aggressive noise target.

The numerical prediction using the validated theoretical model has demonstrated the potential importance of the noise due to surface roughness as well as its indirect effect of enhancement on the corresponding TE noise. This implies that surface roughness could contribute to the difference in noise levels between the TE noise and the airfoil self noise for current jet aircraft in “clean” configurations, as illustrated in Figure 1.5. Explaining that “gap” was a major motivation of the research carried out in this thesis. This highlights the need to consider carefully the contribution of surface roughness to aircraft noise, which has been previously overlooked, in the design of a low-noise airframe.

### **Drag Dipole Mechanism**

Further to the work based on the incoherent scattering mechanism, we also investigated the drag dipole mechanism and extended it to consider the noise resulting from the unsteady drag on very large roughness elements that protrude into the outer region of the boundary-layer velocity profile. The work was motivated by the analytical model of Howe *et al.* [83] and the observations of Acarlar and Smith [1]. We first modified Howe *et al.*'s sphere model of lift and drag fluctuations and obtained the corresponding wall-mounted hemisphere model. We then applied the unsteady drag on the hemispherical roughness elements to determine the far-field radiated sound. The preliminary comparison of noise spectra between the drag dipole mechanism and the sound scattering mechanism has implied that the drag dipole noise from very large roughness elements has the potential to become a source as significant as the scattering noise.

The relative significance of the two source mechanisms of surface roughness noise, *i.e.* sound scattering and drag dipole, depends on the boundary-layer velocity profile region in which the roughness elements are contained. For roughness elements not protruding beyond the logarithmic layer, the drag dipole noise is generated by enhanced shear stress fluctuations on the wall, and it has been confirmed that in this case surface roughness noise is dominated by the sound scattering mechanism. However, for very large roughness elements that protrude far beyond the logarithmic layer, unsteady drag is principally due to the fluctuation in surface pressures, and the drag dipole noise could be comparable to or even higher than (if the nominally steady flow is replaced by a turbulent flow in the hemisphere model) the noise from sound scattering.

### **Dipole Beamforming Correction**

The remaining work of the thesis was on the beamforming correction for identifying dipoles through microphone array measurements. Jordan *et al.* [89] have shown that conventional beamforming techniques can misinterpret array measurements

when applied directly to reconstruct dipole sources due to the inherent monopole assumption, and they proposed a correction technique for microphone signals to recover the source location of a single dipole.

In this work, we extended the signal correction technique to deal with multiple dipoles for 2D microphone arrays, and developed a new D-Beam algorithm by modifying the source transfer vector which is able to identify both source location and source amplitude of dipoles in a suspected orientation. Numerical simulations of dipoles normal to the flow have validated the capability of the D-Beam algorithm to recover the true dipole sources. Measurements of distributed aeolian-tone dipoles have shown the improvement of array performance in estimates of source power, though less remarkable, after applying the D-Beam algorithm.

The present D-Beam algorithm requires the specification of a reference dipole direction and so it is applicable to a distribution of dipoles yet in a uniform orientation. However, for a complex aeroacoustic system in practice combined with various source types (for example, monopoles and dipoles, or dipoles with different components), the indirect approach of theoretically simulating the source distribution and then comparing the predicted source maps with experimental results, as described in Sections 4.3.4 and 4.3.5, is recommended in the data processing.

## 8.2 Suggestions for Future Work

In order to improve the theoretical models and obtain more accurate predictions, further investigations of interest are recommended as follows:

### Sound Scattering Mechanism

- Due to practical limits on experimental work, the roughness noise spectra were obtained in a very narrow range of flow velocity for only two roughness conditions. A detailed investigation should be carried out into the effects of the parameters  $U, R, \sigma$  on roughness noise spectra to enable a scaling study

with nondimensional variables. An anechoic chamber with jet facility would be ideal for such measurements as it provides very quiet background noise. Far-field sound from the whole rough region should be measured to reduce unnecessary error when comparing prediction and experiment.

- The prediction model could be improved in accuracy particularly at high frequencies, and the underestimated streamwise gradient of roughness noise source strengths over a flat plate should be corrected.
- Computational Fluid Dynamics (CFD) simulations of the turbulent flow field over a rough wall using DNS would improve the understanding of the noise source mechanisms and provide another approach to validating the prediction model. Consideration of roughness elements in various shapes (sphere, cylinder, cube, pyramid, *etc.*), which are more realistic for the surface irregularities on aircraft wings and fuselages, would also be made possible by the CFD simulation.
- Investigate the effects of aircraft configuration when applying the prediction model to current aircraft and SAX-40, for example, the changes in boundary layer development (*i.e.*  $u_\tau$  and  $\delta$ ) due to the existence of surface curvature or other airframe components, *e.g.* high-lift devices, engine nacelles.

### Drag Dipole Mechanism

- The wall-mounted hemisphere model should be experimentally validated by towing tank measurement for the lift and drag fluctuations on the hemisphere and acoustic measurement for the far-field radiated sound. CFD simulations would provide numerical data of pressure fluctuations due to vortex shedding from the roughness element for validation of the hemisphere model.
- The analytical sphere/hemisphere model would need to be refined if it is also desired to incorporate modifications of the flow that occur when the sphere/hemisphere is located in a mean turbulent stream [84], and also in applications where the influence of a neighbouring sidewall (for instance a wind tunnel) is important [83].

- For the hemisphere model, the speculation that the vorticity counteraction between the standing vortex and hairpin vortices could reduce the net circulation around the hemisphere and thus result in negligible unsteady lift at large time should be verified by including the standing vortex in the model.
- Alleviation of the high-frequency oscillation in evaluation of the drag spectrum would improve the accuracy of numerical prediction.
- Consider more test cases for the drag dipole noise prediction.

### **Dipole Beamforming Correction**

- A potential step beyond this work would be to iterate through a range of dipole orientations to identify the most likely direction of dipoles anywhere on the scanning grid, rather than specifying the reference dipole direction in the D-Beam algorithm. However, this optimization is generally tricky and time-consuming, especially if a 3D orientation is proposed.
- The present D-Beam algorithm is not applicable to out-of-flow phased array measurements for an open jet. When shear-layer corrections are made, sound transmission is calculated for different Mach numbers. However, the directivity pattern of dipoles is dependent on Mach numbers, and thus the application of the D-Beam algorithm in this case would produce a lot of ambiguity. A more advanced algorithm capable of identifying aeroacoustic dipoles in an open jet should be developed to enable a direct comparison between measurement and simulation for the array results in Section 4.3.
- Experiments for a realistic individual dipole instead of distributed dipoles would provide a straightforward validation of the D-Beam algorithm in recovering dipole source strengths.



# Appendix A

## Empirical Models for Smooth-Wall Wavenumber-Frequency Spectrum

The wavenumber-frequency spectrum  $\tilde{\Phi}_p$  has been used in the prediction model for the far-field radiated roughness noise. In this appendix, we list several representative empirical models for the wavenumber-frequency spectrum of turbulent boundary-layer pressures on a smooth wall. This is based on the model comparison by Graham [63], but only the formulae and constant values are given for ease of reference. The original notations are accordingly altered to be consistent with the definitions of this thesis.

### A.1 Empirical Models

#### The Corcos Model

$$\tilde{\Phi}_p(\boldsymbol{\kappa}, \omega) = \frac{4\alpha_1\alpha_3}{[\alpha_1^2 + (U_c\kappa_1/\omega - 1)^2][\alpha_3^2 + U_c^2\kappa_3^2/\omega^2]}, \quad (\text{A.1})$$

where  $\alpha_1$  and  $\alpha_3$  are the parameters chosen to yield the best agreement with experiment. Various values for  $\alpha_1$  and  $\alpha_3$  are given in the literature; herein  $\alpha_1 = 0.1$  and  $\alpha_3 = 0.77$  are used as suggested by Graham [63].

#### The Efimtsov Model

$$\tilde{\Phi}_p(\boldsymbol{\kappa}, \omega) = \frac{\omega^2}{U_c^2} \frac{4\Lambda_1\Lambda_3}{[1 + \Lambda_1^2(\kappa_1 - \omega/U_c)^2][1 + \Lambda_3^2\kappa_3^2]}, \quad (\text{A.2})$$

where the correlation lengths,

$$\Lambda_1 = U_c/|\omega|\alpha_1 \quad \text{and} \quad \Lambda_3 = U_c/|\omega|\alpha_3 \quad (\text{A.3})$$

are given by the empirical expressions:

$$\frac{\Lambda_1}{\delta} = \left[ \left( \frac{a_1 Sh}{U_c/u_\tau} \right)^2 + \frac{a_2^2}{Sh^2 + (a_2/a_3)^2} \right]^{-1/2}, \quad (\text{A.4a})$$

$$\frac{\Lambda_3}{\delta} = \left[ \left( \frac{a_4 Sh}{U_c/u_\tau} \right)^2 + \frac{a_5^2}{Sh^2 + (a_5/a_6)^2} \right]^{-1/2}, \quad M < 0.75, \quad (\text{A.4b})$$

$$\frac{\Lambda_3}{\delta} = \left[ \left( \frac{a_4 Sh}{U_c/u_\tau} \right)^2 + a_7^2 \right]^{-1/2}, \quad M > 0.9. \quad (\text{A.4c})$$

In Equations (A.4),  $M$  is the free-stream Mach number, and  $Sh = \omega\delta/u_\tau$  is the Strouhal number. The empirical constants  $a_1$ – $a_7$  are, respectively,

$$\begin{aligned} a_1 = 0.1, \quad a_2 = 72.8, \quad a_3 = 1.54, \quad a_4 = 0.77, \\ a_5 = 548, \quad a_6 = 13.5, \quad a_7 = 5.66. \end{aligned} \quad (\text{A.5})$$

Values for  $\Lambda_3$  when  $0.75 < M < 0.9$  are not given; herein interpolation is used if necessary.

## The Smol'yakov and Tkachenko Model

$$\tilde{\Phi}_p(\boldsymbol{\kappa}, \omega) = 0.974 A(\omega) h(\omega) [F(\boldsymbol{\kappa}, \omega) - \Delta F(\boldsymbol{\kappa}, \omega)], \quad (\text{A.6})$$

where

$$A(\omega) = 0.124 \left[ 1 - \frac{U_c}{4\omega\delta^*} + \left( \frac{U_c}{4\omega\delta^*} \right)^2 \right]^{1/2}, \quad (\text{A.7a})$$

$$h(\omega) = \left[ 1 - \frac{m_1 A}{6.515\sqrt{G}} \right]^{-1}, \quad (\text{A.7b})$$

$$m_1 = \frac{1 + A^2}{1.025 + A^2}, \quad G = 1 + A^2 - 1.005 m_1, \quad (\text{A.7c})$$

$$F(\boldsymbol{\kappa}, \omega) = \left[ A^2 + \left( 1 - \frac{\kappa_1 U_c}{\omega} \right)^2 + \left( \frac{\kappa_3 U_c}{6.45\omega} \right)^2 \right]^{-3/2}, \quad (\text{A.7d})$$

$$\Delta F(\boldsymbol{\kappa}, \omega) = 0.995 \left[ 1 + A^2 + \frac{1.005}{m_1} \left\{ \left( m_1 - \frac{\kappa_1 U_c}{\omega} \right)^2 + \left( \frac{\kappa_3 U_c}{\omega} \right)^2 - m_1^2 \right\} \right]^{-3/2}. \quad (\text{A.7e})$$

Here  $\delta^*$  is the displacement boundary-layer thickness, taken as  $\delta^* = \delta/8$ .



## The Ffowcs Williams Model

$$\tilde{\Phi}_p(\boldsymbol{\kappa}, \omega) = \left( \frac{U_c |\boldsymbol{\kappa}|}{\omega} \right)^2 \frac{4\alpha_1 \alpha_3}{[\alpha_1^2 + (U_c \kappa_1 / \omega - 1)^2] [\alpha_3^2 + U_c^2 \kappa_3^2 / \omega^2]}, \quad (\text{A.8})$$

with the same values for  $\alpha_1$  and  $\alpha_3$  as in the Corcos model.

## The Chase I Model

$$\tilde{\Phi}_p(\boldsymbol{\kappa}, \omega) = \frac{\rho_0^2 \omega^2 u_\tau^3}{U_c^2 \Phi(\omega)} \left( \frac{C_M \kappa_1^2}{[K_+^2 + (b_M \delta)^{-2}]^{5/2}} + \frac{C_T |\boldsymbol{\kappa}|^2}{[K_+^2 + (b_T \delta)^{-2}]^{5/2}} \right), \quad (\text{A.9})$$

where

$$K_+^2 = \frac{(\omega - U_c \kappa_1)^2}{h^2 u_\tau^2} + |\boldsymbol{\kappa}|^2, \quad (\text{A.10a})$$

$$\frac{\Phi(\omega)}{2\pi} = \frac{2\pi h \rho_0^2 u_\tau^4}{3\omega(1 + \mu^2)} (C_M F_M + C_T F_T), \quad (\text{A.10b})$$

$$F_M = \frac{1 + \mu^2 \alpha_M^2 + \mu^4 (\alpha_M^2 - 1)}{[\alpha_M^2 + \mu^2 (\alpha_M^2 - 1)]^{3/2}}, \quad (\text{A.10c})$$

$$F_T = \frac{1 + \alpha_T^2 + \mu^2 (3\alpha_T^2 - 1) + 2\mu^4 (\alpha_T^2 - 1)}{[\alpha_T^2 + \mu^2 (\alpha_T^2 - 1)]^{3/2}}, \quad (\text{A.10d})$$

$$\alpha_{M \text{ or } T}^2 = 1 + (U_c / b_{M \text{ or } T} \omega \delta)^2, \quad (\text{A.10e})$$

$$\mu = h u_\tau / U_c. \quad (\text{A.10f})$$

Based on Chase's recommendations, the empirical constants have values as below,

$$\begin{aligned} C_M &= 0.0745, & C_T &= 0.0475, \\ b_M &= 0.756, & b_T &= 0.378, & h &= 3.0. \end{aligned} \quad (\text{A.11})$$

## The Chase II Model

$$\tilde{\Phi}_p(\boldsymbol{\kappa}, \omega) = \frac{\rho_0^2 \omega^2 u_\tau^3}{U_c^2 \Phi(\omega) [K_+^2 + (b\delta)^{-2}]^{5/2}} \left( C_M \kappa_1^2 + C_T |\boldsymbol{\kappa}|^2 \frac{K_+^2 + (b\delta)^{-2}}{|\boldsymbol{\kappa}|^2 + (b\delta)^{-2}} \right), \quad (\text{A.12})$$

where

$$K_+^2 = \frac{(\omega - U_c \kappa_1)^2}{h^2 u_\tau^2} + |\boldsymbol{\kappa}|^2, \quad (\text{A.13a})$$

$$\frac{\Phi(\omega)}{2\pi} = \frac{2\pi h \rho_0^2 u_\tau^4}{3\omega(1 + \mu^2)} (C_M F_M + C_T F_T), \quad (\text{A.13b})$$

$$F_M = \frac{1 + \mu^2 \alpha^2 + \mu^4 (\alpha^2 - 1)}{[\alpha^2 + \mu^2 (\alpha^2 - 1)]^{3/2}}, \quad (\text{A.13c})$$

$$F_T = \frac{3(1 + \mu^2)(1 + \alpha^2)}{2\alpha^3}, \quad (\text{A.13d})$$

$$\alpha^2 = 1 + (U_c / b \omega \delta)^2, \quad (\text{A.13e})$$

$$\mu = h u_\tau / U_c. \quad (\text{A.13f})$$

The recommended empirical constant values are

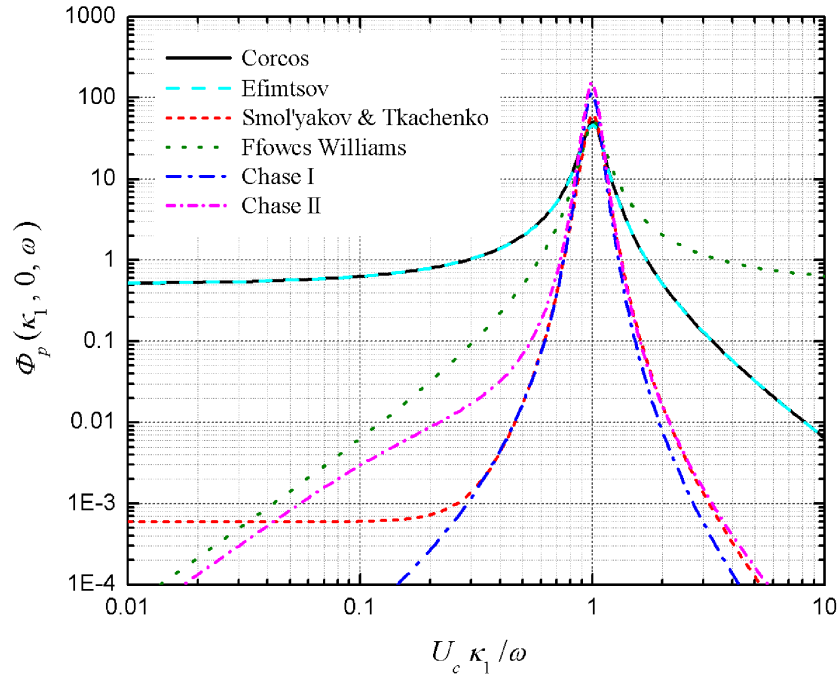
$$\begin{aligned} b &= 0.75, & h &= 3.0, \\ hC_M &= 0.466, & hC_T &= 0.014. \end{aligned} \quad (\text{A.14})$$

## A.2 Prediction

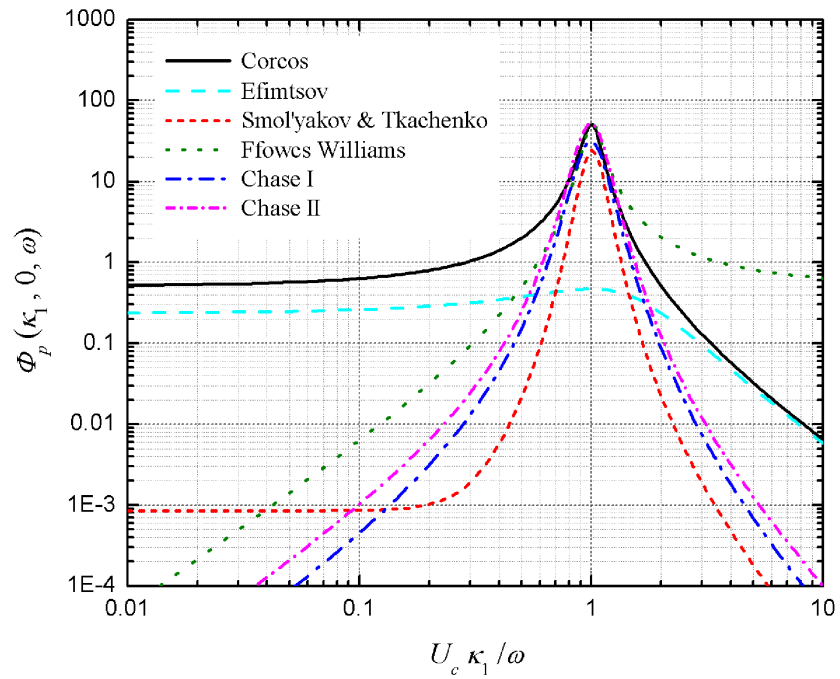
Several representative empirical models to predict the wavenumber-frequency spectrum have been briefly described in Section A.1. In Figures A.1 and A.2 are shown the predictions for streamwise wavenumber-frequency spectra  $\tilde{\Phi}_p(\kappa_1, 0, \omega)$  and spanwise wavenumber-frequency  $\tilde{\Phi}_p(0, \kappa_3, \omega)$ , for Strouhal numbers ( $Sh = \omega \delta / u_\tau$ ) 248 and 24.8, respectively. All dimensional variables in these models can be non-dimensionalized as functions of  $U_c \kappa / \omega$ ,  $Sh$ ,  $U_c / u_\tau$ , and following Graham [63] we have employed

$$\frac{U_c}{u_\tau} = 9.55 Sh^{1/5} \left[ \frac{1 + (6.38 \times 10^{-4} Sh)^2}{1 + (3.98 \times 10^{-3} Sh)^4} \right]^{1/10} \quad (\text{A.15})$$

which is the empirical fit obtained by Efimtsov [43]. The assessments of the empirical models based on Figures A.1 and A.2 can be found in Graham [63] and Ahn [4] and will not be repeated here.



(a)  $Sh = 248$



(b)  $Sh = 24.8$

Figure A.1: Predicted wavenumber-frequency spectra that are plotted against streamwise wavenumber  $\kappa_1$  non-dimensionalized on the convective wavenumber  $\omega/U_c$ , and thus peak round one.

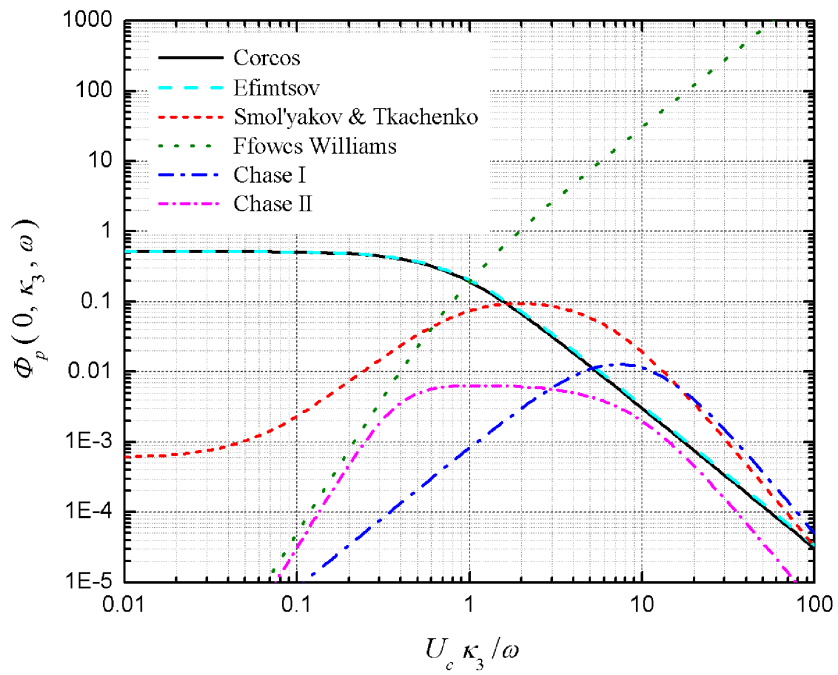
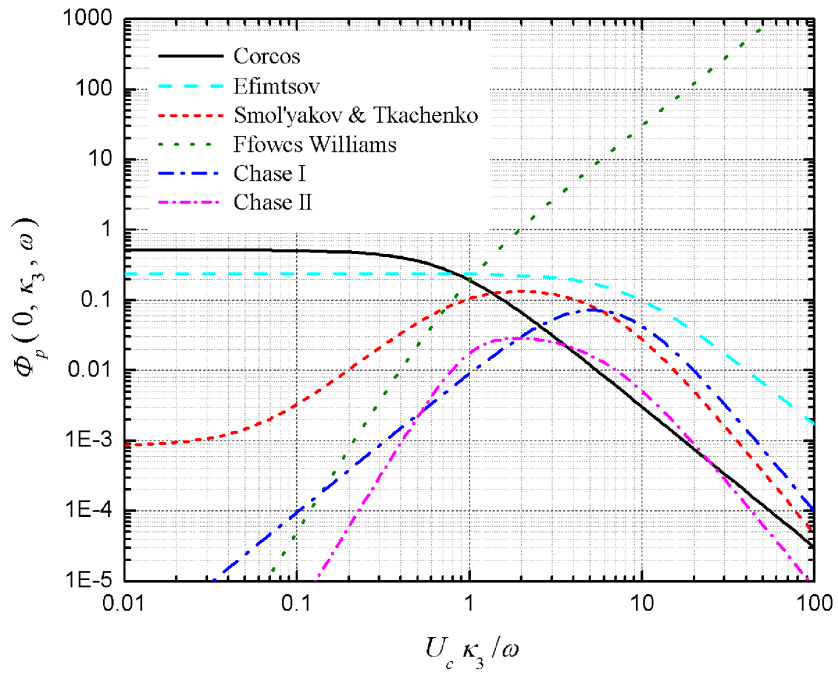
(a)  $Sh = 248$ (b)  $Sh = 24.8$ 

Figure A.2: Predicted spanwise wavenumber-frequency spectra.

## Appendix B

# Discrete Power Spectral Density

In an acoustic experiment, the signal  $p(t)$  is measured for a finite time interval  $T$ , and sampled at  $N$  different times  $t = n\Delta$ , where  $n = 0, 1, \dots, N - 1$  and the time lag  $\Delta = T/N$ . In this case, a discrete Fourier transform of the signal is applied and can be defined by [39]:

$$\begin{aligned}\hat{p}_m &= \frac{1}{N} \sum_{n=0}^{N-1} p(n\Delta) e^{-2\pi imn/N} \\ &= \frac{1}{N} \sum_{l=0}^{N-1} p[(n+l)\Delta] e^{-2\pi im(n+l)/N},\end{aligned}\tag{B.1}$$

where  $\hat{p}_m$  is the frequency spectrum of  $p(t)$ .

The discrete auto-correlation of the signal is

$$P(l\Delta) = \langle p(n\Delta) p[(n+l)\Delta] \rangle,\tag{B.2}$$

and the discrete power spectral density is defined as the discrete Fourier transform of  $P(l\Delta)$ ,

$$\hat{P}_m = \frac{1}{N} \sum_{l=0}^{N-1} P(l\Delta) e^{-2\pi iml/N}.\tag{B.3}$$

$P(l\Delta)$  can be reconstructed from the inverse Fourier transform

$$P(l\Delta) = \sum_{m=0}^{N-1} \hat{P}_m e^{2\pi iml/N},\tag{B.4}$$

and we can see that  $\hat{P}_m$  means the power in the  $m$ th frequency interval.

The power spectral density  $\hat{P}_m$  can be related directly to the Fourier transform of the signal. The ensemble average of the discrete Fourier transforms of  $p(n\Delta)$  and  $p[(n+l)\Delta]$  is given by

$$\begin{aligned}\langle \hat{p}_m \hat{p}_{m'} \rangle &= \frac{1}{N^2} \sum_{n=0}^{N-1} \sum_{l=0}^{N-1} \langle p(n\Delta) p[(n+l)\Delta] \rangle e^{-2\pi i m n / N} e^{-2\pi i m' (n+l) / N} \\ &= \frac{1}{N} \sum_{l=0}^{N-1} P(l\Delta) e^{-2\pi i m' l / N} \cdot \frac{1}{N} \sum_{n=0}^{N-1} e^{-2\pi i (m+m') n / N}.\end{aligned}$$

The double sum in Equation (B.5) can be simplified to

$$\langle \hat{p}_m \hat{p}_{m'} \rangle = \hat{P}_{m'} \delta(m + m'), \quad (\text{B.5})$$

because

$$\frac{1}{N} \sum_{n=0}^{N-1} e^{-2\pi i (m+m') n / N} = \begin{cases} 0 & \text{if } m \neq -m', \\ 1 & \text{if } m = -m'. \end{cases} \quad (\text{B.6})$$

Hence  $\langle \hat{p}_m \hat{p}_{m'} \rangle = 0$  if  $m \neq -m'$ . When  $m = -m'$ , Equation (B.5) becomes

$$\langle \hat{p}_m \hat{p}_{-m} \rangle = \hat{P}_{-m}. \quad (\text{B.7})$$

It is apparent from Equations (B.1) and (B.3) that

$$\hat{p}_{-m} = \hat{p}_m^*, \quad (\text{B.8})$$

and that

$$\hat{P}_{-m} = \hat{P}_m. \quad (\text{B.9})$$

Combining these relationships (B.7–B.9), we obtain

$$|\hat{p}_m|^2 = \hat{P}_m, \quad (\text{B.10})$$

and we can confirm that the discrete power spectral density  $\hat{P}_m$  has the dimension of power  $\text{Pa}^2$ , unlike the dimension  $\text{Pa}^2 \text{ Hz}^{-1}$  for the general power spectral density  $\hat{P}(\omega)$  based on the continuous Fourier transform.

## Appendix C

# Derivation of Skin Friction Coefficient from Hot-Wire Measurement

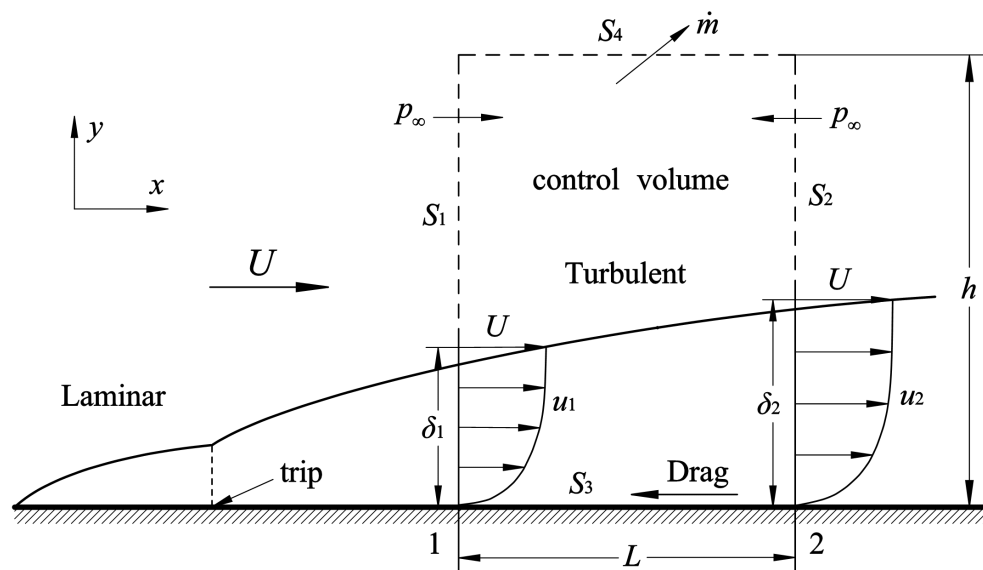


Figure C.1: Schematic of the derivation of  $\bar{c}_f$  from measured mean velocity profiles at two stations along a flat plate.

As shown in Figure C.1, a turbulent boundary layer is developing on a flat plate. The flow is assumed to be inviscid and incompressible with free-stream velocity  $U$ . The mean velocity profiles  $u_1(y)$  and  $u_2(y)$  in the boundary layer are measured at two stations 1 and 2 at a distance  $L$  apart. We take a control volume  $V$  of  $L \times h$  that encloses the two measurement stations at the front and rear boundaries  $S_1$  and  $S_2$ .

Applying momentum conservation to the control volume, we have

$$\underbrace{\int_V \frac{\partial(\rho\mathbf{v})}{\partial t} dV}_{\text{Momentum Rate}} + \underbrace{\oint_S (\rho\mathbf{v})(\mathbf{v} \cdot d\mathbf{S})}_{\text{Momentum Flux}} = - \underbrace{\oint_S p d\mathbf{S}}_{\Sigma \text{ Force}} - \text{Drag}. \quad (\text{C.1})$$

On the left-hand side of the above equation, the first integral denotes the rate of momentum addition in volume  $V$ , and the second integral is the momentum flux across control surfaces  $S_1$ – $S_4$ . If we consider the mean flow in Equation (C.1), the first term of momentum becomes zero; and assuming incompressible flow the second term is simplified to

$$\oint_S \rho_0 \bar{\mathbf{v}} (\bar{\mathbf{v}} \cdot d\mathbf{S}) + \oint_S \underbrace{\overline{\rho_0 \mathbf{v}' (\mathbf{v}' \cdot d\mathbf{S})}}_{\text{Reynolds stress}}, \quad (\text{C.2})$$

in which the momentum flux due to the sufficiently small Reynolds stress fluctuation  $\overline{\rho_0 \mathbf{v}' (\mathbf{v}' \cdot d\mathbf{S})}$  can be discarded.

In the terms of force acting on the control surfaces, the surface integral vanishes because the mean pressure is  $p_\infty$  on  $S_1$ – $S_4$ , and the drag is due to the skin friction on  $S_3$ , *i.e.*

$$\text{Drag} = \int_{S_3} \tau_w dS = \frac{1}{2} \rho_0 U^2 \int_{S_3} c_f dS, \quad (\text{C.3})$$

where  $c_f$  is the local skin friction coefficient at a position on  $S_3$ . Therefore Equation (C.1) simplifies to

$$\oint_S \rho_0 \bar{\mathbf{v}} (\bar{\mathbf{v}} \cdot d\mathbf{S}) = -\frac{1}{2} \rho_0 U^2 \bar{c}_f L, \quad (\text{C.4})$$

where  $\bar{c}_f$  is the average skin friction coefficient over the length of  $S_3$  and is to be derived in this appendix.

In the  $x$ -direction, we take  $\bar{\mathbf{v}} = (u, 0, 0)$  and Equation (C.4) can be expressed as

$$\rho_0 \left( \underbrace{\int_0^h u_2^2 dy - \int_0^h u_1^2 dy}_{S_1, S_2} \right) + \underbrace{\dot{m}U}_{S_4} = -\frac{1}{2} \rho_0 U^2 \bar{c}_f L, \quad (\text{C.5})$$

where  $u_1$  and  $u_2$  denote the mean velocity profiles at Stations 1 and 2, respectively. On the left-hand side of Equation (C.5), the first term describes the momentum flux through the front and rear control surfaces  $S_1$  and  $S_2$ ; and the second term is for the



momentum flux through the control surface  $S_4$ , in which the mass flux is

$$\dot{m} = \rho_0 \left( \int_0^h u_1 \, dy - \int_0^h u_2 \, dy \right). \quad (\text{C.6})$$

For simplicity, we make the usual approximation that  $\partial \bar{p} / \partial y = 0$  across the boundary layer and constant mean velocity beyond  $y = \delta$ . Therefore the integrals of  $u^2$  and  $u$  over the height of the control surfaces  $S_1$  and  $S_2$  split into two parts:

$$\int_0^h u^2 \, dy = \int_0^\delta u^2(y) \, dy + U^2(h - \delta), \quad (\text{C.7a})$$

$$\int_0^h u \, dy = \int_0^\delta u(y) \, dy + U(h - \delta). \quad (\text{C.7b})$$

In the above integrals  $u(y)$  denotes the mean velocity profile in the boundary layer and  $\delta$  is the boundary-layer thickness, both of which can be obtained by experiment. The height of the control volume is recommended to be sufficiently larger than  $\delta$ . In the hot-wire measurement carried out in this research (Section 4.4.2), the value  $h > 3\delta$  is used.

From Equations (C.5–C.7), the average skin friction coefficient  $\bar{c}_f$  between Stations 1 and 2 can be derived, provided that the mean velocity profiles  $u_1(y)$  and  $u_2(y)$  (and hence  $\delta_1$  and  $\delta_2$ ) have been determined through the hot-wire measurement. This method is then applied to the experimental data in Section 4.4.2.2 to compare with  $\bar{c}_f$  predicted by different formulae of skin friction [106, 124].



# Appendix D

## Derivations Related to the Wall-Mounted Hemisphere Model

### D.1 The Image-Vortex Effects

For the vortex shedding from a wall-mounted hemisphere, the effects of the image vortex need to be considered. The image vortex is identical to the original vortex in strength but opposite in orientation, and we will use the prime ' to denote the notations of the image vortex.

Figure D.1 illustrates the  $n$ th vortex loop and its image when separating from the surface of the hemisphere. We can see from Figure D.1 that the circulation  $\Gamma$ , the vorticity  $\omega_n$  and the  $y$ -coordinate of the loop are in opposite directions for the original vortex and the image vortex. The  $(x, y, z)$  coordinates of a point on the vortex loop are determined by

$$\mathbf{x} = (x_n(t) + a \sin \theta_n \cos \xi, a \cos \theta_n \cos \xi, -a \sin \xi), \quad (\text{D.1a})$$

$$\mathbf{x}' = (x_n(t) + a \sin \theta_n \cos \xi, -a \cos \theta_n \cos \xi, -a \sin \xi), \quad (\text{D.1b})$$

which means that  $\mathbf{x}$  and  $\mathbf{x}'$  are opposite in the  $y$ -direction, *i.e.*  $y = -y'$ .

The vorticity vectors  $\omega_n, \omega'_n$  can be expressed as

$$\omega_n = |\omega_n| (\sin \theta_n \sin \xi, -\cos \theta_n \sin \xi, -\cos \xi), \quad (\text{D.2a})$$

$$\omega'_n = |\omega_n| (\sin \theta_n \sin \xi, -\cos \theta_n \sin \xi, \cos \xi), \quad (\text{D.2b})$$

which means that  $\omega_n$  and  $\omega'_n$  are opposite in the  $z$ -direction, *i.e.*  $\omega_{zn} = -\omega'_{zn}$ . Thus

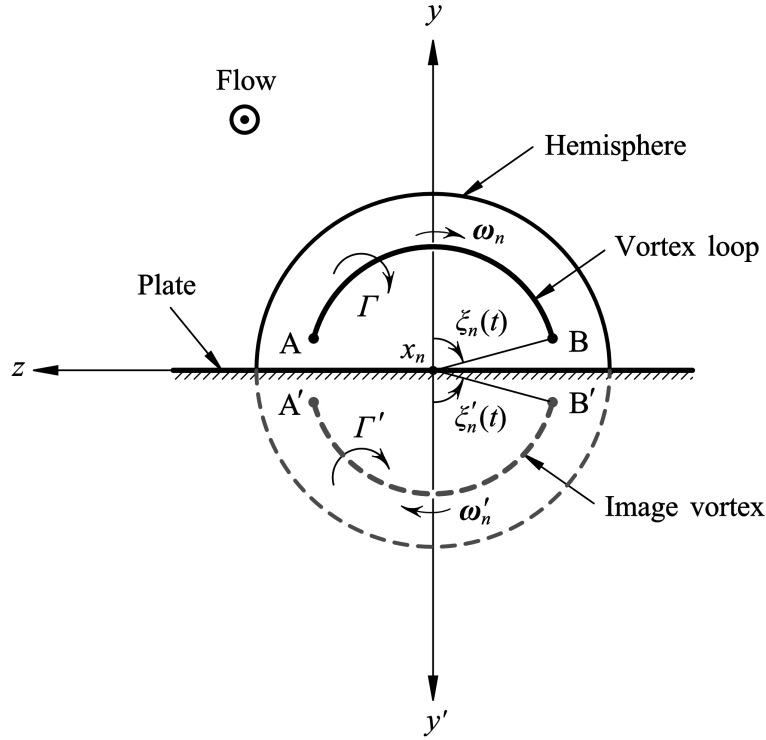


Figure D.1: End view of a vortex loop separating from the hemisphere at the intersection points A and B. Also shown are the images of the vortex loop and the hemisphere (dashed lines).  $\varphi_n \equiv 0$ .

Equation (6.7) becomes

$$(\boldsymbol{\omega}_n \wedge \mathbf{v}) d^3\mathbf{x} = \Gamma U_c(0, -\cos \xi, \cos \theta_n \sin \xi) a d\xi, \quad (\text{D.3a})$$

$$(\boldsymbol{\omega}'_n \wedge \mathbf{v}') d^3\mathbf{x} = \Gamma U_c(0, \cos \xi, \cos \theta_n \sin \xi) a d\xi, \quad (\text{D.3b})$$

for the original vortex and the image vortex, respectively. Herein we have taken  $\mathbf{v} = \mathbf{v}' = (U_c, 0, 0)$  on the vortex loop following the suggestion of Howe *et al.* [83].

To evaluate the force component  $F_{in}(t)$  described in Equation (6.8) we also need to determine the derivatives  $\partial X_i/\partial y$ ,  $\partial X_i/\partial z$ . For the component of the lift  $\mathcal{L}_n$  in the  $y$ -direction, we have

$$\frac{\partial X_y}{\partial y} = \frac{\partial X'_y}{\partial y'} = 1 + \frac{R^3}{2|\mathbf{x}|^3} - \frac{3R^3 y^2}{2|\mathbf{x}|^5}, \quad (\text{D.4})$$

and

$$\frac{\partial X_y}{\partial z} = -\frac{\partial X'_y}{\partial z'} = -\frac{3R^3 y z}{2|\mathbf{x}|^5}. \quad (\text{D.5})$$

Substituting Equations (D.3–D.5) into the expression of  $F_{in}(t)$  (6.6), we obtain

$$\mathcal{L}_n(t) = \rho_0 U_c \Gamma a \int_{-\xi_n(t)}^{\xi_n(t)} \left( -\cos \xi \frac{\partial X_y}{\partial y} + \cos \theta_n \sin \xi \frac{\partial X_y}{\partial z} \right) d\xi, \quad t > t_n. \quad (\text{D.6a})$$

$$\mathcal{L}'_n(t) = \rho_0 U_c \Gamma a \int_{-\xi_n(t)}^{\xi_n(t)} \left( \cos \xi \frac{\partial X'_y}{\partial y'} + \cos \theta_n \sin \xi \frac{\partial X'_y}{\partial z'} \right) d\xi, \quad t > t_n. \quad (\text{D.6b})$$

On the other hand, for the component of the drag  $\mathcal{D}_n$  in the  $x$ -direction, the derivatives of  $X_x$ ,  $X'_x$  are given by

$$\frac{\partial X_x}{\partial y} = -\frac{\partial X'_x}{\partial y'} = -\frac{3R^3 xy}{2|\mathbf{x}|^5}, \quad (\text{D.7})$$

and

$$\frac{\partial X_x}{\partial z} = \frac{\partial X'_x}{\partial z'} = -\frac{3R^3 xz}{2|\mathbf{x}|^5}. \quad (\text{D.8})$$

Similarly, we obtain

$$\mathcal{D}_n(t) = \rho_0 U_c \Gamma a \int_{-\xi_n(t)}^{\xi_n(t)} \left( -\cos \xi \frac{\partial X_x}{\partial y} + \cos \theta_n \sin \xi \frac{\partial X_x}{\partial z} \right) d\xi, \quad t > t_n. \quad (\text{D.9a})$$

$$\mathcal{D}'_n(t) = \rho_0 U_c \Gamma a \int_{-\xi_n(t)}^{\xi_n(t)} \left( \cos \xi \frac{\partial X'_x}{\partial y'} + \cos \theta_n \sin \xi \frac{\partial X'_x}{\partial z'} \right) d\xi, \quad t > t_n. \quad (\text{D.9b})$$

Therefore it can be readily derived from Equations (D.4–D.9) that

$$\mathcal{L}_n(t) = -\mathcal{L}'_n(t) \quad \text{and} \quad \mathcal{D}_n(t) = \mathcal{D}'_n(t). \quad (\text{D.10})$$

This indicates that the acoustic field due to the unsteady lift  $\mathcal{L}_n(t)$  will be cancelled, whereas the acoustic field due to the unsteady drag  $\mathcal{D}_n(t)$  will be doubled by the image vortex.

## D.2 Small-Time Approximations

In the initial stages of the vortex formation when  $U_c(t - t_n)/R \ll 1$ , Equation (6.9) indicates that [83]

$$\xi_n(t) \approx \sqrt{\frac{2U_c(t - t_n)}{a}} \left[ \frac{\sqrt{R^2 - a^2 \cos^2 \theta_n}}{\sin \theta_n (\sqrt{R^2 - a^2 \cos^2 \theta_n} - a \sin \theta_n)} \right]^{1/2}, \quad (\text{D.11})$$

and Equation (6.2) now reduces to

$$x_n(t) \approx \sqrt{R^2 - a^2 \cos^2 \theta_n} - a \sin \theta_n. \quad (\text{D.12})$$

At this early time  $\xi \approx 0$  and Equation (6.13) can be rewritten as

$$\mathcal{F}_n(t - t_n) \approx 2\xi_n(t) \left( 1 + \frac{R^3 \mathcal{A}}{2\mathcal{B}^{5/2}} \right), \quad U_c(t - t_n)/R \ll 1. \quad (\text{D.13})$$

In the above formula the auxiliary terms  $\mathcal{A}$ ,  $\mathcal{B}$  are

$$\mathcal{A} = (x_n(t) + a \sin \theta_n)^2 - 2a^2 \cos^2 \theta_n = R^2 - 3a^2 \cos^2 \theta_n, \quad (\text{D.14a})$$

$$\mathcal{B} = (x_n(t) + a \sin \theta_n)^2 + a^2 \cos^2 \theta_n = R^2. \quad (\text{D.14b})$$

Substituting Equations (D.11) and (D.14) into Equation (D.13), we obtain the small-time approximation of  $\mathcal{F}_n(t)$  as

$$\mathcal{F}_n(t) \approx 3\sqrt{\frac{2U_c(t - t_n)}{a}} \left[ 1 - \left( \frac{a}{R} \right)^2 \cos^2 \theta_n \right] \mathcal{H}, \quad (\text{D.15})$$

where the auxiliary term

$$\mathcal{H} = \left[ \frac{\sqrt{R^2 - a^2 \cos^2 \theta_n}}{\sin \theta_n (\sqrt{R^2 - a^2 \cos^2 \theta_n} - a \sin \theta_n)} \right]^{1/2}. \quad (\text{D.16})$$

Similarly, Equation (6.15) can be rewritten as

$$\mathcal{G}_n(t - t_n) \approx 2\xi_n(t) \frac{3aR^3 \cos \theta_n}{2} \frac{\mathcal{C}}{\mathcal{B}^{5/2}}, \quad U_c(t - t_n)/R \ll 1. \quad (\text{D.17})$$

The auxiliary term  $\mathcal{C}$  is given by

$$\mathcal{C} = x_n(t) + a \sin \theta_n = \sqrt{R^2 - a^2 \cos^2 \theta_n}. \quad (\text{D.18})$$

Substituting the expressions of  $\xi_n(t)$  and  $\mathcal{C}$  into Equation (D.17), we have

$$\mathcal{G}_n(t) \approx \frac{3a \cos \theta_n}{R} \sqrt{\frac{2U_c(t - t_n)}{a}} \left[ 1 - \left( \frac{a}{R} \right)^2 \cos^2 \theta_n \right]^{1/2} \mathcal{H} \quad (\text{D.19})$$

which is the small-time approximation of  $\mathcal{G}_n(t)$ .

We now describe the derivations of  $\hat{\mathcal{F}}_n(\omega)$ ,  $\hat{\mathcal{G}}_n(\omega)$ , the Fourier transforms of the small-time approximations of  $\mathcal{F}_n(t)$ ,  $\mathcal{G}_n(t)$  as defined in Equation (6.17), which will lead to the high-frequency representations of the lift and drag spectra  $\Phi_L(\omega)$ ,  $\Phi_D(\omega)$ . As can be seen from Equations (D.15) and (D.19),

$$\mathcal{F}_n(t), \mathcal{G}_n(t) \propto (t - t_n)^{1/2}, \quad (\text{D.20})$$

and thus the standard integration [96]

$$\int_0^\infty x^n e^{i\omega x} dx = \frac{n!}{(i\omega)^{n+1}} \quad (\text{D.21})$$

implies that the Fourier transform of  $(t - t_n)^{1/2}$  can be evaluated,

$$\frac{1}{2\pi} \int_0^\infty (t - t_n)^{1/2} e^{i\omega(t-t_n)} d(t - t_n) = \frac{1}{2\pi} \frac{\frac{1}{2}!}{(i\omega)^{3/2}}. \quad (\text{D.22})$$

By making use of the properties of the Gamma function,

$$\Gamma(n) = (n - 1)!, \quad (\text{D.23a})$$

$$\Gamma\left(\frac{3}{2}\right) = \frac{1}{2}\sqrt{\pi}, \quad (\text{D.23b})$$

we can rewrite Equation (D.22) as

$$\frac{1}{2\pi} \int_0^\infty (t - t_n)^{1/2} e^{i\omega(t-t_n)} d(t - t_n) = \frac{1}{4\sqrt{\pi}(i\omega)^{3/2}}. \quad (\text{D.24})$$

Therefore the high-frequency representations of the Fourier transforms  $\hat{\mathcal{F}}_n(\omega)$ ,  $\hat{\mathcal{G}}_n(\omega)$  are in the form:

$$\hat{\mathcal{F}}_n(\omega) \sim \frac{3}{4(i\omega)^{3/2}} \sqrt{\frac{2U_c}{\pi a}} \left[ 1 - \left(\frac{a}{R}\right)^2 \cos^2 \theta_n \right] \mathcal{H}, \quad (\text{D.25})$$

$$\hat{\mathcal{G}}_n(\omega) \sim \frac{3a \cos \theta_n}{4R(i\omega)^{3/2}} \sqrt{\frac{2U_c}{\pi a}} \left[ 1 - \left(\frac{a}{R}\right)^2 \cos^2 \theta_n \right]^{1/2} \mathcal{H}. \quad (\text{D.26})$$

Substituting the above formulae (D.25) and (D.26) into (6.27) and (6.30), we obtain the high-frequency representations of the lift and drag spectra:

$$\Phi_L(\omega) \sim (\rho_0 U_c \Gamma a)^2 \frac{9U_c}{4\tau a \omega^3} \left\langle \left[ 1 - \left(\frac{a}{R}\right)^2 \cos^2 \theta_n \right]^2 \mathcal{H}^2 \right\rangle, \quad (\text{D.27})$$

$$\Phi_D(\omega) \sim (\rho_0 U_c \Gamma a)^2 \frac{a^2}{R^2} \frac{9U_c}{2\tau a \omega^3} [\langle |\mathcal{E}|^2 \rangle - |\langle \mathcal{E} \rangle|^2], \quad (\text{D.28})$$

where

$$\mathcal{E} = -\frac{\sqrt{2}}{2}(1+i) \cos^2 \theta_n \left[ 1 - \left(\frac{a}{R}\right)^2 \cos^2 \theta_n \right]^{1/2} \mathcal{H} \quad (\text{D.29})$$

and the ensemble averages are to be taken over all possible values of the vortex orientation  $\theta_n$ .





# Bibliography

- [1] ACARLAR, M. S., AND SMITH, C. R. A study of hairpin vortices in a laminar boundary layer. Part 1. Hairpin vortices generated by a hemisphere protuberance. *Journal of Fluid Mechanics* 175 (1987), 1–41.
- [2] ACHENBACH, E. Experiments on the flow past spheres at very high Reynolds numbers. *Journal of Fluid Mechanics* 54 (1972), 565–575.
- [3] ACHENBACH, E. Vortex shedding from spheres. *Journal of Fluid Mechanics* 62 (1974), 209–221.
- [4] AHN, B.-K. *Modeling Unsteady Wall Pressures beneath Turbulent Boundary Layers*. PhD thesis, Department of Engineering, University of Cambridge, Cambridge, England, 2005.
- [5] AHUJA, K. K., MASSEY, K. C., AND D’AGOSTINO, M. S. A simple technique of locating noise sources of a jet under simulated forward motion. AIAA Paper 98-2359, June 1998.
- [6] AMIET, R. K. Refraction of sound by a shear layer. *Journal of Sound and Vibration* 58, 2 (1978), 467–482.
- [7] ANDREOU, C., GRAHAM, W. R., AND SHIN, H.-C. Aeroacoustic comparison of airfoil leading edge high-lift geometries and supports. AIAA Paper 2007-0230, January 2007.
- [8] BALACHANDAR, R., AND PATEL, V. C. Rough wall boundary layer on plates in open channels. *Journal of Hydraulic Engineering* 128, 10 (2002), 947–951.
- [9] BANDYOPADHYAY, P. Large structure with a characteristic upstream interface in turbulent boundary layers. *Physics of Fluids* 23, 11 (1980), 2326–2327.

- [10] BARLOW, J. B., RAE, W. H., AND POPE, A. *Low-Speed Wind Tunnel Testing*, third ed. John Wiley & Sons Inc., New York, 1999, ch. 8: Use of Wind Tunnel Data: Scale Effects.
- [11] BARSIKOW, B., KING, W. F., AND PFIZENMAIER, E. Wheel/rail noise generated by a high-speed train investigated with a line array of microphones. *Journal of Sound and Vibration* 118, 1 (1987), 99–122.
- [12] BASS, F. G., AND FUKS, I. M. *Wave Scattering from Statistically Rough Surfaces*. Pergamon, Oxford, England, 1979.
- [13] BECKMANN, P., AND SPIZZICHINO, A. *The Scattering of Electromagnetic Waves from Rough Surfaces*. Pergamon, Oxford, England (Reprinted 1987 by Artech House Inc., Norwood, Massachusetts, USA), 1963.
- [14] BERANEK, L. L. *Noise and Vibration Control*. McGraw-Hill Inc., New York, 1971.
- [15] BHAT, W. V. Flight test measurement of exterior turbulent boundary layer pressure fluctuations of Boeing model 737 airplane. *Journal of Sound and Vibration* 14, 4 (1971), 439–457.
- [16] BILLINGSLEY, J., AND KINNS, R. The acoustic telescope. *Journal of Sound and Vibration* 48, 4 (1976), 485–510.
- [17] BLAKE, W. K. Turbulent boundary-layer wall-pressure fluctuations on smooth and rough walls. *Journal of Fluid Mechanics* 44, 4 (1970), 637–660.
- [18] BLAKE, W. K. *Mechanics of Flow-Induced Sound and Vibration*, vol. II: Complex Flow-Structure Interactions. Academic Press, New York, 1986.
- [19] BOEING. General exterior arrangement: 757-200 and 757-300. Webpage, 2002. <http://www.boeing.com/commercial/757family/pf/index.html>.
- [20] BROOKS, T. F., AND HUMPHREYS, W. M. A deconvolution approach for the mapping of acoustic sources (DAMAS) determined from phased microphone arrays. *Journal of Sound and Vibration* 294, 4-5 (2006), 856–879.
- [21] BROOKS, T. F., POPE, D. S., AND MARCOLINI, M. A. Airfoil self-noise and prediction. Tech. Rep. NASA-RP-1218, NASA, 1989.

- [22] BULL, M. K., AND THOMAS, S. W. High frequency wall-pressure fluctuations in turbulent boundary layers. *Physics of Fluids* 19, 4 (1976), 597–599.
- [23] CHANAUD, R. C. Experimental study of aerodynamic sound from a rotating disk. *Journal of the Acoustical Society of America* 45 (1969), 392–397.
- [24] CHAPMAN, D. M. F. A improved Kirchhoff formula for reflection loss at a rough ocean surface at low grazing angles. *Journal of the Acoustical Society of America* 73 (1983), 520–527.
- [25] CHASE, D. M. Modeling the wavevector-frequency spectrum of turbulent boundary layer wall pressure. *Journal of Sound and Vibration* 70, 1 (1980), 29–67.
- [26] CHASE, D. M. The character of the turbulent wall pressure spectrum at subconvective wavenumbers and a suggested comprehensive model. *Journal of Sound and Vibration* 112, 1 (1987), 125–147.
- [27] CHINOY, C. B. Airframe noise prediction. Engineering Sciences Data Unit (ESDU) Item 90023, ESDU International plc., London, June 2003.
- [28] CHOI, H., AND MOIN, P. On the space-time characteristics of wall-pressure fluctuations. *Physics of Fluids* 2, 8 (1990), 1450–1460.
- [29] COLE, L. D. Measurements of sound generated by boundary layer turbulence over smooth and rough surfaces. Tech. Rep. SAD-288E-1942, DTNSRDC Report, July 1980.
- [30] COLEMAN, G. N., KIM, J., AND MOSER, R. D. A numerical study of turbulent supersonic isothermal-wall channel flow. *Journal of Fluid Mechanics* 305 (1995), 159–183.
- [31] CORCOS, G. M. The structure of the turbulent pressure field in boundary-layer flows. *Journal of Fluid Mechanics* 18, 3 (1964), 353–378.
- [32] CRICHTON, D., DE LA ROSA BLANCO, E., LAW, T., AND HILEMAN, J. I. Design and operation for ultra low noise take-off. AIAA Paper 2007-0456, January 2007.

- [33] CRIGHTON, D. G. *Aeroacoustics of Flight Vehicles: Theory and Practice*, vol. 1: Noise Sources. Edited by HUBBARD, H. H. Acoustical Society of America, Woodbury, New York, 1995, ch. Airframe Noise.
- [34] CRIGHTON, D. G., DOWLING, A. P., FLOWCS WILLIAMS, J. E., HECKL, M., AND LEPPINGTON, F. G. *Modern Methods in Analytical Acoustics: Lecture Notes*. Springer-Verlag, London, 1992.
- [35] CURLE, N. The influence of solid boundaries upon aerodynamic sound. *Proceedings of the Royal Society of London A* 231, 1187 (1955), 505–514.
- [36] DARCY, H. *Recherches expérimentales relatives au mouvement de l'eau dans les tuyaux*. Mallet-Bachelier, Paris, 1857.
- [37] DE LA ROSA BLANCO, E., HALL, C., AND CRICHTON, D. Challenges in the silent aircraft engine design. AIAA Paper 2007-0454, January 2007.
- [38] DOUGHERTY, R. P. *Aeroacoustic Measurements*. Edited by MUELLER, T. J. Springer-Verlag, Berlin, 2002, ch. Beamforming in Acoustic Testing.
- [39] DOWLING, A. P., AND FLOWCS WILLIAMS, J. E. *Sound and Sources of Sound*. Ellis Horwood Ltd., Chichester, England, 1983.
- [40] DOWLING, A. P., AND GREITZER, E. M. The Silent Aircraft Initiative – overview. AIAA Paper 2007-0452, January 2007.
- [41] DOWLING, A. P., AND HYNES, T. P. Towards a silent aircraft. *Journal of the Royal Aeronautical Society* 110, 1100 (August 2006), 487–494.
- [42] DUNCAN, W. J., THOM, A. S., AND YOUNG, A. D. *Mechanics of Fluids*, second ed. Edward Arnold Ltd., London, 1970.
- [43] EFIMTSOV, B. M. Characteristics of the field of turbulent wall pressure fluctuations at large Reynolds numbers. *Acoustical Physics* 28, 4 (1982), 289–292.
- [44] ESDU. The mean skin friction coefficient for a rough flat plate with a turbulent two-dimensional boundary layer in compressible adiabatic flow, with application to wedges, cylinders and cones. Engineering Sciences Data

- Unit (ESDU) Aerodynamics Data Item 2c-73016, ESDU International plc., London, 1973.
- [45] ESDU. Evaluation of the attenuation of sound by a uniform atmosphere. Engineering Sciences Data Unit (ESDU) Item 78002, ESDU International plc., London, 1978.
- [46] ESDU. Estimation of lateral attenuation of air-to-ground jet or turbofan aircraft noise in one-third octave bands. Engineering Sciences Data Unit (ESDU) Item 82027, ESDU International plc., London, 1982.
- [47] EVANS, P. An introduction to aircraft noise lateral attenuation. Engineering Sciences Data Unit (ESDU) Lateral Attenuation Manual Item 81035, ESDU International plc., London, November 1981.
- [48] FAA. *Code of Federal Regulations*. Federal Aviation Administration (FAA), Department of Transport, 2002, ch. Appendix A – Aircraft Noise Measurement and Evaluation Under §36.101, 14 CFR Part 36, Noise Standards: Aircraft Type and Airworthiness Certification.
- [49] FARABEE, T. M., AND GEIB, F. E. Measurements of boundary layer pressure fluctuations at low wavenumbers on smooth and rough walls. *Flow Noise Modeling Measurements and Control ASME NCA-Vol. 11*, ASME Noise Control and Acoustics Division, 1991.
- [50] FASZER, A. C. *Effect of Boundary Layer Manipulation on Airframe Trailing-Edge Noise*. PhD thesis, Department of Engineering, University of Cambridge, Cambridge, England, in preparation, 2008.
- [51] FASZER, A. C., AND HILEMAN, J. I. Modelling minimum airframe noise for an all-lifting-body. The 8th ASC-CEAS Workshop, Budapest, Hungary, 11-12 November, 2004.
- [52] FLOWCS WILLIAMS, J. E. Boundary-layer pressures and the Corcos model: a development to incorporate low wavenumber constraints. *Journal of Fluid Mechanics* 125 (December 1982), 9–25.

- [53] FLOWCS WILLIAMS, J. E., AND HAWKINGS, D. L. Sound generation by turbulence and surfaces in arbitrary motion. *Proceedings of the Royal Society of London A* 264, 1151 (1969), 321–342.
- [54] FINK, M. R. Airframe noise prediction method. Tech. Rep. FAA-RD-77-29, Federal Aviation Administration, 1977.
- [55] FISHER, M. J., HARPER-BOURNE, M., AND GLEGG, S. A. L. Jet engine noise source location: The polar correlation technique. *Journal of Sound and Vibration* 51, 1 (1977), 23–54.
- [56] FORTUIN, L. Survey of literature on reflection and scattering of sound waves at the sea surface. *Journal of the Acoustical Society of America* 47 (1969), 1209–1228.
- [57] FRANZONI, L. Assessment of the contribution of panel vibration to airframe noise. *AIAA Journal* 42, 8 (2004), 1522–1528.
- [58] GECKINLI, N. C., AND YAVUZ, D. *Discrete Fourier Transformation and Its Applications to Power Spectra Estimation*. Published in “Studies in Electrical and Electronic Engineering 8”, Elsevier, New York, 1983.
- [59] GILBERT, F., AND KNOPOFF, L. Seismic scattering from topographic irregularities. *Journal of Geophysical Research* 65 (1960), 3437–3444.
- [60] GLEGG, S. A. L., BAXTER, S. M., AND GLENDINNING, A. The prediction of broadband noise from wind turbines. *Journal of Sound and Vibration* 118, 2 (1987), 217–239.
- [61] GLEGG, S. A. L., DEVENPORT, W. J., GRISSONM, D. L., AND SMITH, B. Rough wall boundary layer noise: Theoretical predictions. AIAA Paper 2007-3417, May 2007.
- [62] GOLDSTEIN, S. *Modern Developments in Fluid Dynamics*, vol. 2. Dover Publications, New York, 1965.
- [63] GRAHAM, W. R. A comparison of models for the wavenumber-frequency spectrum of turbulent boundary layer pressures. *Journal of Sound and Vibration* 206, 4 (1997), 541–565.

- [64] GRISSOM, D. L., SMITH, B., DEVENPORT, W. J., AND GLEGG, S. A. L. Rough wall boundary layer noise. AIAA Paper 2006-2409, May 2006.
- [65] GRISSOM, D. L., SMITH, B., DEVENPORT, W. J., AND GLEGG, S. A. L. Rough wall boundary layer noise: An experimental investigation. AIAA Paper 2007-3418, May 2007.
- [66] HAGEN, G. Über den einfluss der temperatur auf die bewegung des wassers in röhren. *Mathematische Abhandlungen der Akademie der Wissenschaften zu Berlin* (1854), 17–98.
- [67] HART, R. W., AND FARRELL, R. A. A variational principle for scattering from rough surfaces. *IEEE Transactions on Antennas and Propagation AP-25* (1977), 708–710.
- [68] HAYES, J. A., HORNE, W. C., SODERMAN, P. T., AND BRENT, P. H. Airframe noise characteristics of a 4.7% scale DC-10 model. AIAA Paper 97-1594, 1997.
- [69] HEAD, M. R., AND BANDYOPADHYAY, P. New aspects of turbulent boundary layer structure. *Journal of Fluid Mechanics* 107 (1981), 297–338.
- [70] HERKES, W. H., AND STOKER, R. W. Wind tunnel measurements of the airframe noise of a high-speed civil transport. AIAA Paper 98-0472, 1998.
- [71] HERSH, A. S. Surface roughness generated flow noise. AIAA Paper 83-0786, April 1983.
- [72] HILEMAN, J. I., REYNOLDS, T. G., DE LA ROSA BLANCO, E., LAW, T. R., AND THOMAS, S. P. Development of approach procedures for silent aircraft. AIAA Paper 2007-0451, January 2007.
- [73] HILEMAN, J. I., SPAKOVSKY, Z. S., DRELA, M., AND SARGEANT, M. A. Airframe design for ‘silent aircraft’. AIAA Paper 2007-0453, January 2007.
- [74] HILEMAN, J. I., THUROW, B., AND SAMIMY, M. Exploring noise sources using simultaneous acoustic measurements in real-time flow visualizations in jets. *AIAA Journal* 40, 12 (2002), 2382–2392.
- [75] HOWE, M. S. Contributions to the theory of scattering by randomly irregular surfaces. *Proceedings of the Royal Society of London A* 337, 1611 (1974), 413–433.

- [76] HOWE, M. S. The role of surface shear stress fluctuations in the generation of boundary layer noise. *Journal of Sound and Vibration* 65 (1979), 159–164.
- [77] HOWE, M. S. On the generation of sound by turbulent boundary layer flow over a rough wall. *Proceedings of the Royal Society of London A* 395, 1809 (1984), 247–263.
- [78] HOWE, M. S. The influence of viscous surface stress on the production of sound by a turbulent boundary layer over a rough wall. *Journal of Sound and Vibration* 104, 1 (1986), 29–39.
- [79] HOWE, M. S. The turbulent boundary-layer rough-wall pressure spectrum at acoustic and subconvective wavenumbers. *Proceedings of the Royal Society of London A* 415, 1848 (1988), 141–161.
- [80] HOWE, M. S. On unsteady surface forces, and sound produced by the normal chopping of a rectilinear vortex. *Journal of Fluid Mechanics* 206 (1989), 131–153.
- [81] HOWE, M. S. Surface pressures and sound by turbulent flow over smooth and rough walls. *Journal of the Acoustical Society of America* 90, 2 (1991), 1041–1047.
- [82] HOWE, M. S. *Acoustics of Fluid-Structure Interactions*. Cambridge University Press, Cambridge, England, 1998, ch. 3: Sound Generation in a Fluid with Rigid Boundaries.
- [83] HOWE, M. S., LAUCHLE, G. C., AND WANG, J. Aerodynamic lift and drag fluctuations of a sphere. *Journal of Fluid Mechanics* 436 (2001), 41–57.
- [84] HUNT, J. C. R., KAWAI, H., RAMSEY, S. R., PEDRIZETTI, G., AND PERKINS, R. L. A review of velocity and pressure fluctuations in turbulent flows around bluff bodies. *Journal of Wind Engineering and Industrial Aerodynamics* 35 (1990), 49–85.
- [85] ICAO. *Convention on International Civil Aviation*, fourth ed. International Civil Aviation Organization (ICAO), Supplement incorporated March 2003, ch. Annex 16 – Environmental Protection, Volume I: Aircraft Noise.
- [86] JIMÉNEZ, J. Turbulent flows over rough walls. *Annual Review of Fluid Mechanics* 36 (2004), 173–196.



- [87] JOHNSON, D. H., AND DUDGEON, D. E. *Array Signal Processing: Concepts and Techniques*. Prentice Hall, London, 1993.
- [88] JOHNSON, T. A., AND PATEL, V. C. Flow past a sphere up to a Reynolds number of 300. *Journal of Fluid Mechanics* 378 (1999), 19–70.
- [89] JORDAN, P., FITZPATRICK, J. A., AND VALIÈRE, J.-C. Measurement of an aeroacoustic dipole using a linear microphone array. *Journal of the Acoustical Society of America* 111, 3 (2002), 1267–1273.
- [90] KIM, J., AND MOIN, P. The structure of the vorticity field in turbulent channel flow. Part 2: Study of ensemble-averaged fields. *Journal of Fluid Mechanics* 162 (1986), 339–363.
- [91] KIM, J., MOIN, P., AND MOSER, R. D. Turbulence statistics in fully-developed channel flow at low Reynolds number. *Journal of Fluid Mechanics* 177 (1987), 133–166.
- [92] KOOK, H., MOEBS, G. B., DAVIES, P., AND BOLTON, J. S. An efficient procedure for visualizing the sound field radiated by vehicles during standardized passby tests. *Journal of Sound and Vibration* 233, 1 (2000), 137–156.
- [93] KROGSTAD, P. A., ANTONIA, R. A., AND BROWNE, L. W. B. Comparison between rough- and smooth-wall turbulent boundary layers. *Journal of Fluid Mechanics* 245 (December 1992), 599–617.
- [94] LAN, J., PREMO, J., ZLAVOG, G., BREARD, C., CALLENDER, B., AND MARTINEZ, M. Phased array measurements of full-scale engine inlet noise. AIAA Paper 2007-3434, May 2007.
- [95] LIGHTHILL, M. J. On sound generated aerodynamically: I. General theory. *Proceedings of the Royal Society of London A* 211, 1107 (1952), 564–587.
- [96] LIGHTHILL, M. J. *An Introduction to Fourier Analysis and Generalised Functions*. Cambridge University Press, Cambridge, England, 1958.
- [97] LILLEY, G. M. The prediction of airframe noise and comparison with experiment. *Journal of Sound and Vibration* 293, 4 (2001), 849–859.

- [98] LISZKA, F. G., AND MCCOY, J. J. Scattering at a rough boundary – extensions of the Kirchhoff approximation. *Journal of the Acoustical Society of America* 71 (1982), 1093–1100.
- [99] LOCKARD, D. P., AND LILLEY, G. M. The airframe noise reduction challenge. Tech. Rep. NASA-TM-2004-213013, NASA, 2004.
- [100] LUERS, J. K. Wing contamination: threat to safe flight. *Astronautics and Aeronautics* 21, 11 (1983), 54–59.
- [101] MANNEVILLE, A., PILCZER, D., AND SPAKOVSKY, Z. Preliminary evaluation of noise reduction approaches for a functionally silent aircraft. *AIAA Journal* 43, 3 (2006), 836–840.
- [102] MARTINEZ, M. M. Microphone polar arc phased array for locating turbofan source noise components. AIAA Paper 2007-3445, May 2007.
- [103] METZLER, S. P. Processes in the wall region of a turbulent boundary layer. Master’s thesis, Department of Mechanical Engineering and Mechanics, Lehigh University, Bethlehem, Pennsylvania, USA, 1982.
- [104] MICHEL, U., BARSIKOW, B., HELBIG, J., HELLMIG, M., AND SCHUTTPELZ, M. Flyover noise measurements on landing aircraft with a microphone array. AIAA Paper 98-2336, June 1998.
- [105] MICHEL, U., AND QIAO, W. Directivity of landing gear noise based on flyover measurements. AIAA Paper 99-1956, May 1999.
- [106] MILLS, A. F., AND HANG, X. On the skin friction coefficient for a fully rough flat plate. *ASME Journal of Fluids Engineering* 105, 3 (1983), 364–365.
- [107] MITTAL, R. Planar symmetry in the unsteady wake of a sphere. *AIAA Journal* 37, 2 (1999), 388–390.
- [108] MOIN, P., AND KIM, J. The structure of the vorticity field in turbulent channel flow. Part 1: Analysis of instantaneous fields and statistical correlations. *Journal of Fluid Mechanics* 155 (1985), 441–464.
- [109] MOIN, P., AND MAHESH, K. Direct numerical simulation: A tool in turbulence research. *Annual Review of Fluid Mechanics* 30 (1998), 539–578.

- [110] MÖLLER, W. Experimentelle untersuchung zur hydromechanick der kugel. *Phys. Z.* 39 (1938), 57–80.
- [111] MORRISON, W. R. B., AND KRONAUER, R. R. Structural similarity for fully developed turbulence in smooth tubes. *Journal of Fluid Mechanics* 39 (1969), 117–141.
- [112] MORSE, P. M., AND INGARD, K. U. *Theoretical Acoustics*. McGraw-Hill Inc., New York, 1968, ch. 8: The Scattering of Sound.
- [113] NARAYANAN, S., BARBER, T. J., AND POLAK, D. R. High subsonic jet experiments: Turbulence and noise generation studies. *AIAA Journal* 40, 3 (2002), 430–437.
- [114] NELSON, P. A., AND MORFEY, C. L. Aerodynamic sound production in low speed flow ducts. *Journal of Sound and Vibration* 79, 2 (1981), 263–289.
- [115] NIKURADSE, J. Strömungsgesetze in rauhen rohren. *VDI-Forschungschafft* 361 (1933). English translation: Laws of flow in rough pipes. NACA-TM-1292, 1950.
- [116] OGILVY, J. A. Wave scattering from rough surfaces. *Reports on Progress in Physics* 50 (1987), 1553–1608.
- [117] OGILVY, J. A. *Theory of Wave Scattering from Random Rough Surfaces*. Adam Hilger, New York, 1991.
- [118] PERRY, A. E., LIM, T. T., AND TEH, E. W. A visual study of turbulent spots. *Journal of Fluid Mechanics* 104 (1981), 387–405.
- [119] PHILIPS, O. M. The intensity of aeolian tones. *Journal of Fluid Mechanics* 1 (1956), 607–624.
- [120] PIET, J. F., AND ELIAS, G. Airframe noise source localization using a microphone array. AIAA Paper 97-1643, May 1997.
- [121] PIET, J. F., ELIAS, G., AND LEBIGOT, P. Localization of acoustic source from a landing aircraft with a microphone array. AIAA Paper 99-1811, May 1999.

- [122] PIMENTA, M. M., MOFFAT, R. J., AND KAYS, W. M. The turbulent boundary layer: An experimental study of the transport of momentum and heat with the effect of roughness. Tech. Rep. No. HMT-21, Thermosciences Division, Department of Mechanical Engineering, University of Stanford, California, USA, May 1975.
- [123] PLAS, A. P., MADANI, V., SARGEANT, M. A., GREITZER, E. M., HALL, C. A., AND HYNES, T. P. Performance of a boundary layer ingesting propulsion system. AIAA Paper 2007-0450, January 2007.
- [124] PRANDTL, L., AND SCHLICHTING, H. Resistance law of rough plates. *Werft-Reederei-Hafen* 15, 1 (1934), 1–4.
- [125] QUAYLE, A. R., DOWLING, A. P., BABINSKY, H., GRAHAM, W. R., AND LIU, Y. Phased array measurements from landing gear models. AIAA Paper 2007-3463, May 2007.
- [126] QUAYLE, A. R., DOWLING, A. P., BABINSKY, H., GRAHAM, W. R., AND SIJTSMA, P. Landing gear for a silent aircraft. AIAA Paper 2007-0231, January 2007.
- [127] ROGALLO, R. S., AND MOIN, P. Numerical simulation of turbulent flows. *Annual Review of Fluid Mechanics* 16 (1984), 99–137.
- [128] SAKAMOTO, H., AND HANIU, H. A study on vortex shedding from spheres in uniform flow. *Transactions of ASME: Journal of Fluids Engineering* 112 (1990), 386–392.
- [129] SCHEWE, G. On the structure and resolution of wall-pressure fluctuations associated with turbulent boundary layer flow. *Journal of Fluid Mechanics* 134 (1983), 311–328.
- [130] SCHLICHTING, H. *Boundary Layer Theory*, seventh ed. McGraw-Hill Inc., New York, 1979.
- [131] SCHULTZ, M. P., AND FLACK, K. A. Outer layer similarity in fully rough turbulent boundary layers. *Experiments in Fluids* 38, 3 (2005), 328–340.

- [132] SHIN, H.-C., GRAHAM, W. R., SIJTSMA, P., ANDREOU, C., AND FASZER, A. C. Implementation of a phased microphone array in a closed-section wind tunnel. *AIAA Journal* 45, 12 (2007), 2897–2909.
- [133] SIJTSMA, P. *Advances in Aeroacoustics and Applications*. Edited by ANTHOINE J., AND HIRSCHBERG, A. VKI (von Kármán Institute) Lecture Series 2004-05, March 2004, ch. Experimental Techniques for Identification and Characterisation of Noise Sources.
- [134] SILLER, H. A., ARNOLD, F., AND MICHEL, U. Investigation of aero-engine core noise using a phased microphone array. AIAA Paper 2001-2269, 2001.
- [135] SINGER, B. A., AND JOSLIN, R. D. Metamorphosis of a harpin vortex into a young turbulent spot. *Physics of Fluids* 6, 11 (1994), 3724–3736.
- [136] SKUDRZYK, E. J., AND HADDLE, G. P. Noise production in a turbulent boundary layer by smooth and rough surfaces. *Journal of the Acoustical Society of America* 32, 1 (1960), 19–34.
- [137] SMITH, C. R., AND WALKER, J. D. A. On the dynamics of near-wall turbulence. *Philosophical Transactions of The Royal Society of London* 336 (1991), 131–172.
- [138] SMITH, M. J. T. *Aircraft Noise*. Cambridge University Press, Cambridge, England, 1989.
- [139] SMOL'YAKOV, A. V. Noise of turbulent boundary layer flow over smooth and rough plates at low Mach numbers. *Acoustical Physics* 47, 2 (2001), 218–225.
- [140] SMOL'YAKOV, A. V., AND TKACHENKO, V. M. Model of a field of pseudosonic turbulent wall pressures and experimental data. *Acoustical Physics* 37, 6 (1991), 627–631.
- [141] SPALART, P. R. Direct numerical simulation of turbulent boundary layer up to  $r_\theta = 1410$ . *Journal of Fluid Mechanics* 187 (1988), 61–98.
- [142] TAM, R., BELOBABA, P., POLENSKE, K. R., AND WAITZ, I. Assessment of silent aircraft-enabled regional development and airline economics in the UK. AIAA Paper 2007-0455, January 2007.

- [143] TANEDA, S. Experimental investigation of the wake behind a sphere at low Reynolds numbers. *Journal of the Physical Society of Japan* 11 (1956), 1104–1108.
- [144] TANEDA, S. Visual observations of the flow past a sphere at Reynolds numbers between  $10^4$  and  $10^6$ . *Journal of Fluid Mechanics* 85 (1978), 187–192.
- [145] THE CAMBRIDGE-MIT INSITITUTE. The ‘Silent’ Aircraft Initiative. Website, 2006. <http://silentaircraft.org>.
- [146] THEODORSEN, T. Mechanism of turbulence. 2nd Midwest Conference on Fluid Mechanics, The Ohio State University, Columbus, Ohio, USA, 1952.
- [147] THOMAS, S. P., AND DOWLING, A. P. A dynamical model and controller for the silent aircraft: the effect of maneuvering on noise. AIAA Paper 2007-0866, January 2007.
- [148] TOMBOULIDES, A. G., AND ORSZAG, S. A. Numerical investigation of transitional and weak turbulent flow past a sphere. *Journal of Fluid Mechanics* 416 (200), 45–74.
- [149] UNIVERSITY OF STANFORD. AA241 aircraft design: Course notes. Webpage, 1999. <http://adg.stanford.edu/aa241/noise/noise.html>.
- [150] UTAMI, T., AND UENO, T. *Lagrangian and Eularian Measurement of Large Scale Turbulence by Flow Visualizing Techniques*. Published in “Flow Visualization”. Edited by ASANUNRA, T. Hemisphere, New York, 1979.
- [151] VENKATESH, S. R., POLAK, D. R., AND NARAYANAN, S. Beamforming algorithm for distributed source localization and its application to jet noise. *AIAA Journal* 41, 7 (2003), 1238–1246.
- [152] VON KÁRMÁN, T. Turbulence and skin friction. *Journal of the Royal Aeronautical Society* 1 (1934), 1–20.
- [153] WAGNER, R. J. Shadowing of randomly rough surfaces. *Journal of the Acoustical Society of America* 41 (1967), 138–147.
- [154] WANG, J. *Hydrodynamic lift and drag fluctuations on a sphere*. PhD thesis, The Pennsylvania State University, Pennsylvania, USA, 1999.

- 
- [155] WANG, J., LAUCHLE, G. C., AND HOWE, M. S. Flow-induced force fluctuations on a sphere at high strouhal number. *Journal of Fluids and Structures* 17 (2003), 365–380.
- [156] WEST, G. S., AND APELT, C. S. Measurements of fluctuating pressures and forces on a circular cylinder in the Reynolds number range  $10^4$  to  $2.5 \times 10^5$ . *Journal of Fluids and Structures* 7 (1993), 227–244.
- [157] WILLMARTH, W. W. Wall pressure fluctuations beneath turbulent boundary layer. *Journal of the Acoustical Society of America* 28 (1956), 1048–1053.
- [158] WILLMARTH, W. W. Pressure fluctuations beneath turbulent boundary layers. *Annual Review of Fluid Mechanics* 7 (1975), 13–38.
- [159] WILLMARTH, W. W., AND ENLOW, R. L. Aerodynamic lift and moment fluctuations of a sphere. *Journal of Fluid Mechanics* 36 (1969), 417–432.
- [160] WILLMARTH, W. W., AND WOOLDRIDGE, C. E. Measurements of the fluctuating pressure at the wall beneath a thick turbulent boundary layer. *Journal of Fluid Mechanics* 14 (1962), 187–210.
- [161] WILLSHIRE, B. *Doing the Wright Stuff: 100 Years of Aviation and the Environment*. NASA, 2003, ch. Quiet Aircraft Technology Program.
- [162] ZIERKE, W. C. A physics-based means of computing the flow around a maneuvering underwater vehicle. Tech. Rep. TR 97-002, The Pennsylvania State University Applied Research Laboratory, Pennsylvania, USA, 1997.